Strategies towards Redshifted Hemithioindigo Photoswitches & Development of a Semi-Automated Photochemical Screening Platform

Krell-Jørgensen, Mikkel

Publication date:
2022

Document Version
Publisher's PDF, also known as Version of record

Strategies towards Redshifted Hemithioindigo Photoswitches & Development of a Semi-Automated Photochemical Screening Platform

PhD Thesis

Mikkel Poul Vestergaard Krell-Jørgensen

DEPARTMENT OF CHEMISTRY

TECHNICAL UNIVERSITY OF DENMARK

Faculty:	DTU Chemistry, Technical University of Denmark
Department:	Department of Chemistry
Author:	Mikkel Poul Vestergaard Krell-Jørgensen
Academic advisor:	Luca Laraia
Title:	Strategies towards Redshifted Hemithioindigo Photoswitches & Development of a Semi-Automated Photochemical Screening Platform
Submitted:	07/07/2022

PREFACE

This thesis has been submitted to DTU Chemistry at the Technical University of Denmark in order to obtain the PhD degree in chemistry. The work has been carried out at the Department of Chemistry, Technical University of Denmark in the period from 03 June 2019 to 30 June 2022. The work presented has been performed by the author under the supervision of Associate Professor Luca Laraia.

This PhD thesis is divided into 3 main chapters that all have light as an external stimulus to trigger or control events in its focus.

In Chapter **3**, light is used to control geometry and properties of new artificial photoswitch analogues based on the hemithioindigo scaffold. By systematically extending the π-conjugation of the core electronic system, a programmable bathochromic shift is obtained. This strategy guided the synthesis of new potential photoswitches absorbing light in the red region of the electromagnetic spectrum. Furthermore, one photoswitch even displayed light-induced switching in the near-infrared window, which is a desired trait for use in biological settings.

In Chapter **4**, light is used to mediate chemistry of natural product-like small molecules via photochemical [2+2] cycloadditions in both flow and batch setups. The design of a modular flow microreactor encompassing the possibility of running either electro- or photochemistry in addition to the progress towards its fabrication using additive manufacturing is presented. An inexpensive, open-source microreactor might benefit the research community in general by encouraging its incorporation to the common repertoire of tools available, and help clear the misconception that it requires niche knowledge and expensive equipment to approach this field.

Finally, in Chapter **5**, light is once more intended to mediate chemistry, but in a semi-automated plate-based approach. In this context, the development of an inexpensive medium-throughput semi-automated photochemical screening platform performed in microplates is described. This enabled rapid discovery of optimal reaction conditions for photochemical [2+2] cycloadditions intended for an alkaloid-inspired natural product-like compound library, and complements one-at-a-time classical batch reactions greatly.

The projects described herein are individual projects, and chapters have therefore been separated by numbering of chemical structure. The computational calculations for the manuscript in Chapter **3** were provided by our collaborators. However, the supporting information on this is not disclosed in this thesis, despite the manuscript referring to it. Figures, schemes and tables in the manuscript are continuous from Chapter **3**.

Mikkel Poul Vestergaard Krell-Jørgensen

July 2022

ACKNOWLEDGMENTS

First and foremost, I would like to extend my deepest gratitude to my supervisor, Luca Laraia. You have a spirit unlike anyone I have ever met in my academic career that always makes you see the bright side of life. I have often joked about it, but it is really true, around you the glass is always half full, which is an extremely positive trait to possess as a supervisor that advice and guide young researchers like myself in their early career where doubt may settle in at times. I knew that I could always knock on your door to ask for your opinion on a matter, and the answer would always be the same: "Of course, please come in." Thank you for taking the time, giving me the trust and opportunity besides the countless hours of scientific discussion. You inspire me not only professionally, but also personally, and I will always cherish the days with you as my mentor.

To my fantastic group members, thank you for creating an amazing atmosphere and environment to thrive in. It is quite unique to have a group of people where all bond so well. You made going to work fun and extremely pleasant. I could always count on you if I needed a spare hand or help in general, and I love you for that. I hope we will stay in touch in the future when everybody go their separate ways. Know that if you ever need a place to stay when visiting Copenhagen years from now, I will await you with open arms.

A huge thank you to my two partners in crime, whom contributed to two very different projects, Magnus Grage Bonnevie and Nina Ræbild Hamburger. Magnus contributed with synthesis and analysis of many key photoswitches, while Nina developed the entire data analysis tool that was used in the photochemical screening platform. You helped me realise this PhD thesis, and for this I am forever grateful to you both.

To our two collaborators on the photoswitch project, Habiburrahman Zulfikri and Asmus Ougaard from the University of Iceland, thank you a lot of for providing all the computational calculations needed to guide and support the project. You always had a ton of great ideas, and it certainly developed the project into something bigger than initially intended from the onset. I think we achieved some fantastic results together. Also a thank you to Jacob Thomas Shelley from the Rensselaer Polytechnic Institute for discussions and advice regarding the MS in connection to the photochemical screening platform.

We PhD students are fortunate to have many great and skilled employees working at the department to keep things running smoothly. To our lab-technician Phillip Charlie Johansen, of whom I had the pleasure of bothering more than a few times when instruments did not want to do as told, I sincerely appreciate your time and efforts. My thanks and appreciation also to the NMR-team, Charlotte Held Gotfredsen and Kasper Enemark-Rasmussen, for setting up methods and running countless experiments for me. To everybody at the engineer and service center, thank you guys for your exceptional work and daily assistance with repair of equipment in addition to providing me with new glassware when I needed it. I would also like to thank the many staff members involved in ordering chemicals, and what-else was needed in the laboratory, in addition to washing the massive amount of glassware that I used throughout my three years. To the IT-team and administrative personal, thank you very much for always having the answer to all the obscure problems I sometimes encountered and had no idea how to solve. To our departmental director, Erling Halfdan Stenby, my sincere gratitude for allowing us PhD students to speak our minds and for always listening, it makes a difference.

To my dear friends and family with no idea of what I have been doing in the past many years, but always had to endure my endless blabbering about work, thank you from the bottom of my heart for all your love and support. It did not go unnoticed, and I love you for it.

I saved the most important person in my life for last. Her contribution to this PhD thesis is not noticed by others, but is without a doubt invaluable. You have supported me unconditionally throughout this entire endeavor, and always believed in me. I often worked late hours, and you fully supported my choice to do so even when you really wanted me at home and around. I could not wish for a more perfect life companion. If I had to dedicate this thesis to anyone, it would be you. Tuoi, I love you with all my heart and cannot wait to embark on our round-the-world trip together, where the two of us will share an adventure of a lifetime.

ABSTRACT

Light has found numerous uses as an external stimulus to trigger or control events in photochemical applications, such as the spatial geometry and properties of molecular photoswitches in addition to mediating chemistry in drug discovery as exemplified in this thesis.

Molecular photoswitches comprise a class of photochromic molecules able to interconvert reversibly between a stable and metastable isomer upon absorption of incident light, which can be exploited similar to an "ON"/"OFF" switch to control biological functions, or as a system to store solar thermal energy. A limitation with current molecular photoswitches is the need for low-wavelength UV light to initiate the switching process, as the associated energy is sufficiently high to cause photodegradation of the switch itself, but also of the surrounding material, which for biological applications is less favourable. Redshifting the wavelengths of absorption towards the low-energy red part of the visible electromagnetic spectrum through molecular tailoring serves as a viable strategy in developing new and improved systems. In this context, it enabled the development of hemithioindigo photoswitches with improved photophysical properties in which the absorption was substantially redshifted to facilitate switching with near-infrared light, which is of great value for future applications in photopharmacology.

Light may also be employed to conveniently mediate chemistry, and in connection to this, multiple microfluidic photoreactors were designed and fabricated employing 3D printing technology to allow photochemical transformations in flow. However, despite the many advantageous of performing photo-chemistry in flow, it cannot provide the same throughput in terms of screening many reaction conditions in parallel as other systems might offer.

Therefore, a simple and inexpensive semi-automated photochemical screening platform was developed and applied to expedite the discovery of new photochemical transformations. It enabled parallel screening of reactions in 96-well microtitre plates to discover the most optimal reaction conditions facilitating product formation. This high-throughput experimentation approach far outcompetes the discovery capabilities of the classical one-at-a-time batch approach used as a standard for chemical synthesis when comparing rates of output. In this context, the platform was exploited to discover a new triplet-sensitized photochemical [2+2] cycloaddition reaction that will later set up the synthesis of an alkaloid-inspired natural product-like compound library, with potential applications in drug discovery.

RESUMÉ

Lys som en ekstern stimulus anvendes i dag til mange forskellige formål. I fotokemiske applikationer kan det blandt andet bruges til at udløse eller styre forløbet af en proces, som dikterer den rumlige struktur eller egenskaberne af en molekylær lyskontakt. Derudover kan lys anvendes til at facilitere kemiske reaktioner, som blandt andet kan anvendes i udviklingen af nye lægemidler. Begge eksempler er illustreret i denne afhandling.

Molekylære lyskontakter omfatter en klasse af lysabsorberende molekyler, der reversibelt er i stand til at skifte mellem en stabil og metastabil tilstand, når den absorberer lys. Det kan udnyttes på samme måde som en "TÆND"/"SLUK"-kontakt til blandt andet at kontrollere biologiske funktioner eller som et system til at lagre solenergi. Eksisterende molekylære lyskontakter er dog på nuværende tidspunkt begrænset af, at ultraviolet lys er det eneste, som tillader denne proces. Dette er uheldigt eftersom energien associeret med ultraviolet lys er så kraftig, at den molekylære lyskontakt samt det omkringliggende materiale i anvendelsesomgivelserne bliver nedbrudt, hvilket hæmmer anvendelses-mulighederne i biologiske systemer. For at løse dette problem og udvikle nye og forbedrede molekylære lyskontakter kan man for eksempel rødforskyde de absorberende bølgelængder til den rødlige del af det elektromagnetiske spektrum, hvor energien af lyset er lavere. Med denne strategi udviklede vi således hemithioindigo molekylære lyskontakter med forbedrede fotofysiske egenskaber. Absorptionen var tilstrækkeligt rødforskudt til at tillade brugen af nær-infrarødt lys, hvilket er af stor værdi for fremtidige anvendelser inden for fotofarmakologi.

Som tidligere nævnt kan lys også bruges til at facilitere kemiske reaktioner, og i denne forbindelse brugte vi 3D printning til at fremstille mikroreaktorer, der skulle anvendes til fotokemiske transformationer i kontinuerligt strømmende væsker. Selvom der er mange fordele ved at lave kemi på denne måde, så er det ikke særligt effektivt, hvis formålet er at teste mange reaktionsbetingelser samtidigt, hvilket vi senere blev interesseret i.

Vi udviklede derfor en simpel og billig semi-automatiseret platform til fotokemi, og anvendte den til opdagelsen af nye fotokemiske transformationer. Platformen gjorde det muligt at teste reaktioner i plader med 96 forskellige reaktionsbetingelser, og dermed hurtigt konkludere hvilke betingelser der var de mest optimale i forhold til produktdannelse. Denne metode er langt mere effektiv end det man kan opnå med den klassiske en-af-gangen batch metode, der bruges som standard ved kemisk syntese, når man sammenligner hastigheden for undersøgelse af nye reaktioner. Platformen blev brugt til at fremskynde processen for opdagelsen af en ny triplet-exciteret fotokemisk [2+2] cykloaddition, der senere skal bruges til at syntetisere et alkaloid-inspireret naturstof-lignende kemisk bibliotek til udviklingen af nye lægemidler.

Chapter 3: Redshifted Hemithioindigo Photoswitches.

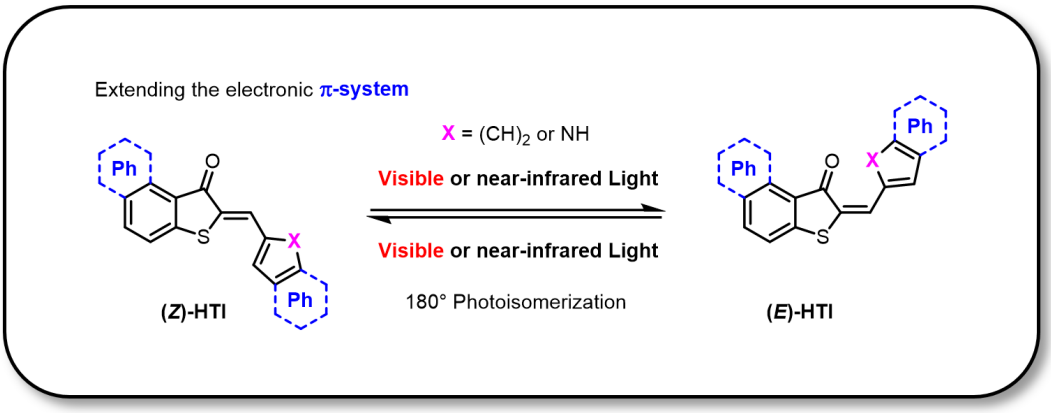

Chapter 4: Microreactors Coupled with Electro- & Photochemistry.

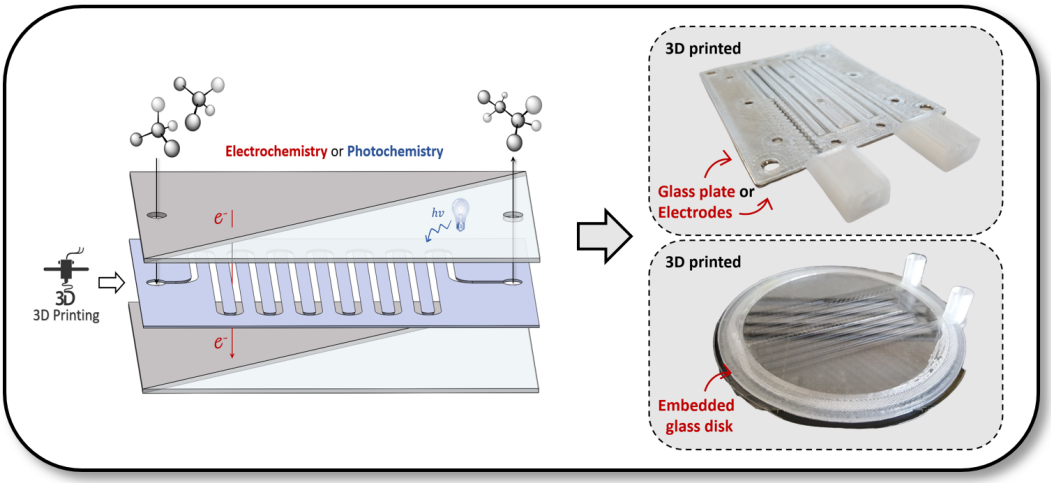

Chapter 5: High-Throughput Photochemical Screening Platform.

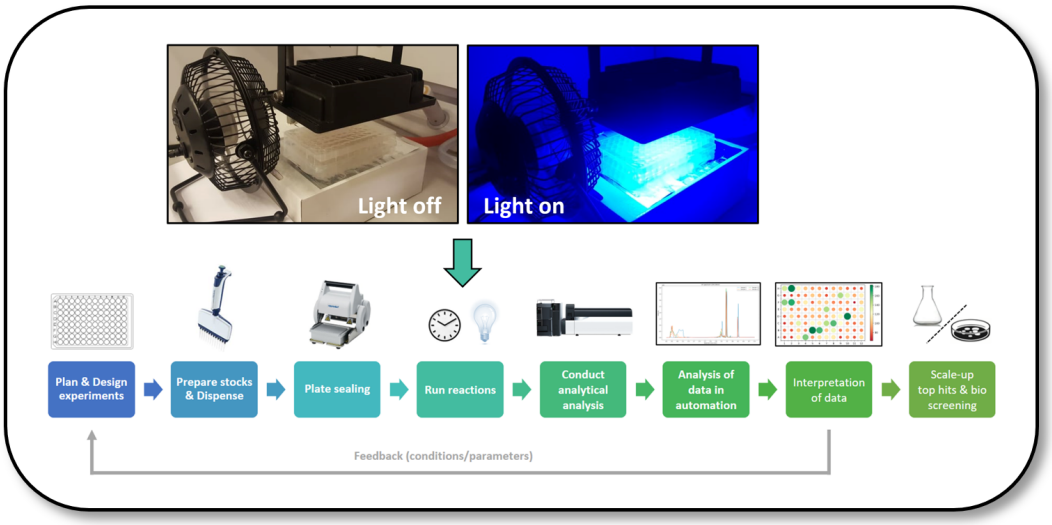

LIST OF ABBREVIATIONS

2PP	Two-photon polymerization
3D	Three dimensional
ABS	Acrylonitrile butadiene styrene
ACN	Acetonitrile
AM	Additive manufacturing
ANOVA	Analysis of variance
API	Active pharmaceutical ingredient
aq.	Aqueous
Ar	Aryl
A.u.	Arbitrary unit
BAF	1,3-Dimethyl barbituric activated furan
β-Gal	β-Galactosidase
Boc	*tert*-Butoxycarbonyl
BP	Benzophenone
Bpy	2,2'-Bipyridine
br	Broad
CAD	Computer-aided design
CASPT2	Complete active space with second-order perturbation theory
CASSCF	Complete active space self-consistent field
cat.	Catalyst
CI	Conical intersection
Cmpd	Compound
COSY	Correlated spectroscopy
CT	Charge transfer
d	Doublet
DAE	Diarylethene
DASA	Donor-acceptor Stenhouse adducts
DBU	1,8-Diazabicyclo[5.4.0]undec-7-ene
DCM	Dichloromethane
DCVC	Dry column vacuum chromatography

DESI	Desorption electrospray ionization
DF	Degrees of freedom
DFT	Density functional theory
DIPEA	*N*,*N*-Diisopropylethylamine
D.I.Y.	Do-it-yourself
DKP	2,5-Diketopiperazine
DMA	Dimethylacetamide
DMF	Dimethylformamide
DMSO	Dimethyl sulfoxide
DSPE	1,2-Distearoyl-sn-glycero-3-phosphatidylethanolamine
Dtbbpy	4,4'di-*tert*-Butyl-2,2'-dipyridyl.
DTE	Dithienylethene
E	Energy
EDG	Electron donating group
EPR	Enhanced permeability and retention
Equiv.	Equivalent(s)
ESIPT	Excited state intramolecular proton transfer
EWG	Electron withdrawing group
FDM	Fused deposition modelling
FEP	Fluorinated ethylene propylene
$GABA_AR$	Ionotropic γ-aminobutyric acid receptor A
GC	Gas chromatography
Hex	Hexane
HMBC	Heteronuclear multiple bond correlation
HOMO	Highest occupied molecular orbital
HPLC	High-performance liquid chromatography
HRMS	High-resolution mass spectroscopy
HSA	Human serum albumin
HSQC	Heteronuclear single quantum coherence
HTE	High-throughput experimentation
HTI	Hemithioindigo
hv	Light

Hz	Hertz
IC	Internal conversion
IHB	Intramolecular hydrogen bond
IPA	Isopropyl alcohol
iPr	*iso*-propyl
IQR	Interquartile range
IR	Infrared
ISC	Intersystem crossing
ISTD	Internal standard
ITX	2-Isopropylthioxanthone
J	Coupling constant in hertz
LOC	Lab-on-a-chip
Lambda	Wavelength λ
LOX	Lipoxygenase
LUMO	Lowest unoccupied molecular orbital
M	Metallacycle or molar
m	Multiplet
MAF	Meldrum's activated furan
MALDI	Matrix-assisted laser desorption/ionization
MC	Merocyanine
MISER	Multiple injections in a single experimental run
MMA	9-Mesityl-10-methylacridinium tetrafluoroborate
MO	Molecular orbital
Molar abs	Molar absorption coefficient (ε)
mPEG	Poly(ethylene glycol) methyl ether
MRI	Magnetic resonance imaging
MS	Mass spectrometry
MTP	Microtitre plate
NaN	Not a number
NIR	Near-infrared light
NMO	*N*-Methylmorpholine *N*-oxide
NMR	Nuclear magnetic resonance

NP	Nanoparticle
OD	Optical density
PBS	Phosphate buffered saline
PDT	Photodynamic therapy
PEG	Polyethylene glycol
PES	Potential energy surface
PETG	Polyethylene terephthalate glycol
Ph	Phenyl
PhMe	Toluene
PIFA	Phenyliodine bis(trifluoroacetate)
PLA	Polylactic acid
PP	Polypropylene
ppm	Parts per million
Ppy	2-Phenylpyridine
ps	Picosecond
PSS	Photostationary state selectivity
PTFE	Polytetrafluoroethylene
Q	Quartet
QY	Quantum yield Φ
R	Arbitrary group
Redox	Oxidation-reduction
R_f	Retention factor
RGB	Red-green-blue
rt	Room temperature
s	Singlet
S_0	Ground electronic state
S_1	First electronic excited state
S_2	Second electronic excited state
SAR	Structure-activity relationship
SLA	Stereolithography
SP	Spiropyran
STD	Standard deviation

STL	Standard tessellation language
STORM	Super-resolution imaging technique
T	Temperature
t	Triplet
TBAF	Tetra-*n*-butylammonium fluoride
TDDFT	Time-dependent density functional theory
TEA	Triethylamine
TEMPO	(2,2,6,6-Tetramethyl-piperidin-yl)oxy
TfOH	Trifluoromethanesulfonic (triflic) acid
THF	Tetrahydrofuran
TLC	Thin layer chromatography
TMS	Trimethylsilane
TS	Transition state
Ts	Tosyl
TX	Thioxanthone
UV	Ultraviolet
Vis	Visible
VR	Vibrational relaxation
X	Xanthone
Å	Ångstrøm

TABLE OF CONTENTS

A LIGHT TEASER

Light is a marvellous source of energy. It also happens to be the only form of energy visible to the human eye. It consists of electromagnetic radiation or photons produced when an object's atoms heat up, as is the case of stars like our sun. Photons travel at an incredible 299.792.458 m/s (the speed of light *in vacuo*) as waves in tiny discrete quantized packets of energy. Being the fastest entity in our universe, it only takes a little more than eight minutes for light to travel from the sun to earth, which spans a distance of 150 million kilometres or between continents on earth in less than a blink of an eye.[1]

From the early days of campfire making by Homo erectus a million years ago to the famous kite in a thunderstorm experiment by Benjamin Franklin in 1752, humankind now has light on demand in versions ranging from regular light bulbs to powerful lasers. Using light as an external stimulus is advantageous over other stimuli, because it is non-invasive over a wide range of wavelengths, and displays high spatial and temporal precision when delivered. Unlike additives, there is no need for its removal afterwards, which simplifies the process and lowers the cost. Furthermore, it is possible to tune the wavelength and intensity of light to match the intended application. With this in mind, light has found numerous uses as an external stimulus to trigger or control events in photochemical applications.

In nature, plants, algae and cyanobacteria make use of light when they transforms light energy from the sun into chemical energy as carbohydrates synthesized from water and carbon dioxide in a process known as photosynthesis, which is pivotal to life developing on earth. Another magnificent example of a biological system evolved to use light as stimulus is our vision. In the eye of vertebrates is located a photoresponsive receptor called rhodopsin that consists of a trans-membrane protein named opsin and a retinal molecule covalently linked via a lysine residue. Retinal is the responsible component for absorbing light, and when this occurs, *cis* retinal is transformed into *trans* retinal triggering a series of downstream events that eventually leads to the brain receiving visual information through neural signals. It is incredible to imagine that photoisomerization (or photoswitching) of such a small entity allow us to distinguish between two million distinct colours.

Taking inspiration from the very sophisticated strategies developed by nature to control such specific tasks as exemplified here, research on artificial switches as well as the general concept of using light as an external stimulus to control chemical interactions and events has exploded over the past few decades. Its future prospects are immense and the journey, relatively speaking, has only just begun.

1. INTRODUCTION TO PHOTOCHEMISTRY

Photochemistry is the branch of chemistry, which relates to the absorption of light energy (photons) by matter to facilitate photophysical and photochemical processes. Although light seems insignificant and harmless for the most part, it possess a considerable amount of energy, which can be utilized to control interactions of matter in order to afford new chemical entities. The specific energy of photons is given by the Planck-Einstein relation.[2] Under normal conditions, molecules reside in the ground electronic state to occupy the stationary state of lowest energy. Upon light absorption, a transient state is generated known as an excited sate. Electronically excited molecules display fundamentally different physical and chemical properties than the corresponding ground states. It is from this excited state that photochemical transformations are realised. Employing light to induce chemical transformations in some instances has the advantage of making non-feasible thermal reactions achievable, while demonstrating perfect atom economy. Furthermore, light is practical to work with and simple to operate. Hence, it is easy to grasp the current surge of interest in photochemistry. There exist two fundamental principles for photochemical transformations;[2] the Grotthuss-Draper law, which states that only light absorbed by a chemical entity can induce a photochemical change, and the Stark-Einstein law, which states that the primary act of light absorption is a one-quantum process. Accordingly, for each photon of light absorbed, only one molecule is excited. The efficiency with which a given photochemical transformation occurs is given by the quantum yield that defines the number of events per incident absorbed photon.

The Planck-Einstein relation:

$$E = h\nu = hc/\lambda$$

Perspective: Light radiation of wavelength 300 nm, effectively translates to an energy equivalent of 95 kcal/mol or about 1500°C when absorbed by matter.

In general, we divide photochemical transformations into the following sub-types:

Photo-dissociation:	AB + $h\nu$ → A* + B*
Photo-induced rearrangement/isomerization:	A + $h\nu$ → B
Photo-addition:	A + B + $h\nu$ → AB
Photo-substitution:	A + BC + $h\nu$ → AB + C
Photo-redox reaction:	A + B + $h\nu$ → A^- + B^+

Asterisk (*) indicates excited species

The most commonly employed photoswitchable systems as described in chapter **2** and further discussed in chapter **3**, exert their function through either photo-addition or photo-induced isomerization processes. In addition, the photochemical [2+2] cycloaddition reactions studied in chapter **4** and **5** likewise follow a photo-addition mechanism for which an elaborated theoretical discussion can be found later in this chapter.

1.1 THE LIGHT ABSORPTION PROCESS

The development of the quantum theory in the early twentieth century allowed predictions relating to the properties and behaviour of matter and light.[2] The electrons in matter display both wavelike and particle-like properties with quantised energies. When the oscillating electromagnetic radiation encounters an appropriate chromophore, the group responsible for light absorption in a molecule, an electron (provided adequate energy) is promoted to a higher-energy excited state. This electronic transition entails that the chromophore undergoes an electric dipole transition and the energy of the photon becomes part of the total energy of the excited state molecule.

1.1.1 JABLONSKI DIAGRAM

The electronic states in a molecule and the photophysical processes accompanying its excitation with light can be illustrated with an energy state diagram, also known as a Jablonski diagram (**Figure 1.1**). When an incident photon of adequate energy is absorbed by a molecule, a singlet ground state (S_0) electron is promoted to a higher electronic energy state (S_1-S_n) of the same multiplicity, due to conservation of angular momentum.[3] This absorption is a very fast process and takes place on the femtosecond scale.[2] The transition can be to any vibrational level (v_n) within an electronic excited state, and depends on the respective energy of the incident photon absorbed. Excess vibrational energy is dissipated as vibrational relaxation (VR) through rapid collision with the surrounding medium to produce molecules in the lowest vibrational level (v_0) of a particular electronic energy state (S_n).

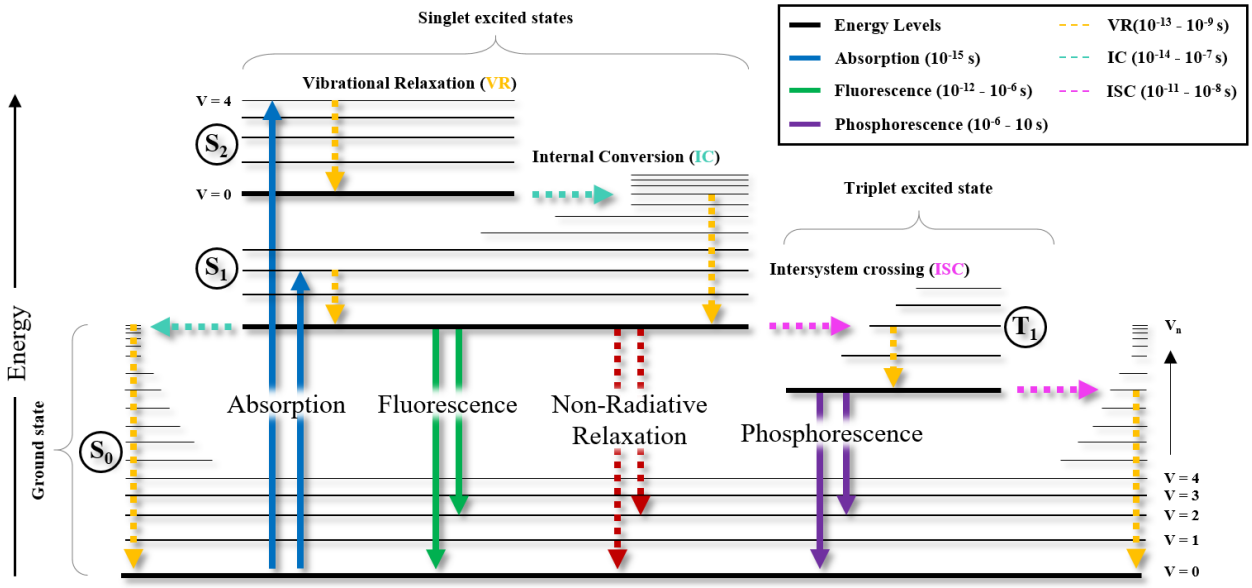

Figure 1.1. *Energy state diagram (Jablonski diagram) illustrating excited state photophysical processes. Coloured solid arrows are radiative transitions and dashed arrows non-radiative transitions. Black bars are different electronic states. Black horizontal lines are different vibrational energy levels. Time scales from B. Wardle.*[2]

Subsequently, non-radiative internal conversion (IC) between vibronic states (v_n) of the same total energy (isoenergetic states) and multiplicity takes place. This transition is much faster between the upper excited states as they are exceedingly closer in energy, which means that no other processes than internal conversion and vibrational relaxation is observed for excited states higher than the first excited state (S_1). The rate of internal conversion decreases exponentially as the energy gap increases between electronic states (the energy gap law).[3] Hence, irrespective of which upper excited state is initially produced by photon absorption, conversion will always proceed to the lowest vibrational level of S_1 (or T_1), where a number of processes may then compete effectively with similar rate constants. This observed behaviour is in accordance with Kasha's rule, which states that luminescence and photochemical transformations in general originate from the lowest vibrational level of S_1 (or T_1).[2]

Spontaneous emission of light in the form of fluorescence, thus leads to deexcitation of the molecule and regeneration of the ground state (S_0). Alternatively, non-radiative intersystem crossing (ISC) between isoenergetic states of different multiplicity affords the excited triplet state (T_1). However, this process is spin-forbidden by the spin selection rule as it requires the spin of the electron to change during the electronic transition.[2] Nevertheless, spin-orbit couplings with other electrons or with a nuclei in the molecule affects the orbital motion of the electron enough to give singlet states some triplet character and vice versa. This allows mixing of the states in which the spin selection rule is not rigidly applied, and makes transitions between states of different multiplicity weakly allowed. Molecules containing atoms of high atomic mass will experience a larger degree of spin-orbit couplings and show enhanced singlet to triplet transition (the heavy atom effect).[2] The excited triplet state (T_1) is lower in energy than that of the corresponding excited singlet state (S_1) in accordance with Hund's rule, which states that when two unpaired electrons occupy different orbitals, there is a minimum energy repulsion between the electrons when their spins are parallel.[2]

Vibrational relaxation followed by reverse intersystem crossing or phosphorescence thus results in the regeneration of the electronic ground state (S_0). However, as it requires a spin flip to re-populate the ground state per Pauli Exclusion Principle, which states the no two electrons in the same atom can have identical values for all four quantum numbers, both processes become spin-forbidden (spin selection rule).[2] Consequently, triplet states display very long excited state lifetimes relative to the time scale of other photophysical processes as the probability for proceeding transitions are very low. Thereby, allowing enough time for photochemical transformations to take place. This includes energy transfer to a molecule in the surrounding medium as exemplified by photosensitizers. Photosensitizers typically display intense excitation with subsequent rapid relaxation to the corresponding excited triplet state. This excited triplet state energy may be transferred to another molecule of adequate triplet state energy level via triplet-triplet energy transfer, essentially facilitating excitation of molecules that would otherwise not be feasible through standard absorption processes.

1.1.2 THE FRANCK-CONDON PRINCIPLE

The Franck-Condon Principle assumes that electronic transitions take place without any geometrical changes in the molecule, due to the small time scale relative to molecular motion. The heavy nuclei in the vibrating molecule is therefore considered to be fixed during the transition compared to the much lighter electrons.[2] Hence, the stationary nuclear framework gives rise to vertical electronic transitions (Franck-Condon transitions) in response to absorption of an incident photon (**Figure 1.2a-b**).

Furthermore, the most intense absorptions occur when the initial and final wavefunctions (ψ and ψ^*) most closely resemble one another (**Figure 1.2a-b**). Thus the greater the overlap (Franck-Condon factor), the greater the probability of an electronic transition.[2] The molar extinction coefficient is thus proportional to the probability of a given transition. In addition, the different radiative transitions results in an absorption spectrum with bands at lower wavelengths than the corresponding emission spectrum (**Figure 1.2c**).

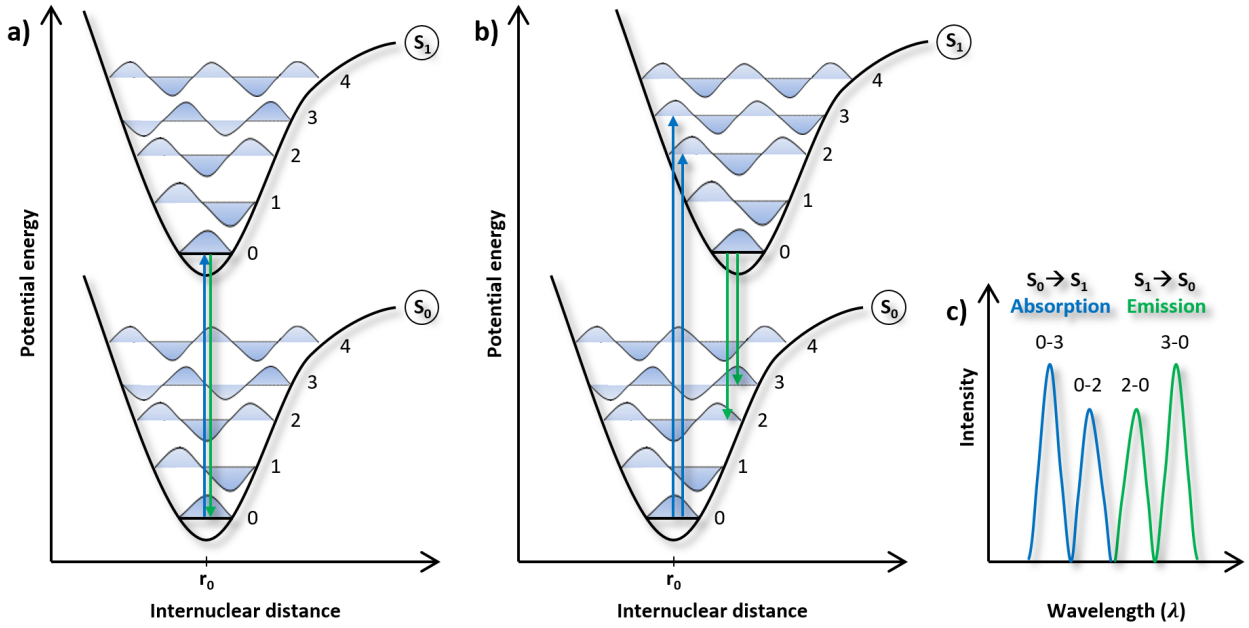

Figure 1.2. *Morse potentials illustrating Franck-Condon vertical electronic transitions with the greatest probability of absorption from S_0 (v = 0). Absorption (blue arrow) and fluorescence (green arrow). (a) Both electronic states have similar geometries with coincident internuclear minima. (b) The excited state has a larger internuclear distance than the ground state. (c) Corresponding absorption and emission spectra.*

1.2 THE PATHWAY OF PHOTOCHEMICAL REACTIONS

The potential energy of a molecular system can be visualized with a reaction profile diagram displaying the potential energy changes occurring during the chemical reaction (**Figure 1.3**). Modelling photochemical reactions requires at least two energy surfaces, whereas one is the ground state surface and the other the corresponding excited state surface.

All photochemical reactions that begin and end on the ground state potential energy surface (PES) involve a crossing, also commonly referred to as a funnel, from the excited state to the ground state.[2] The excited species travels along the reaction coordinate until it reaches a minimum in which the excited state PES resembles the ground state PES in both energy and geometry. From this point, the pathway of the photochemical reaction may proceed along the excited state PES or cross to continue the transformation into product (P) as a thermal process. For many reactions the equations for the two PES in the region of the crossing resembles the geometrical shape of two cones touching or nearly touching, and is thus referred to as a conical intersection (CI).[2] Reactions where the product is formed after the ground state has been reached are said to be diabatic. However, if the excited species proceeds along the excited state PES to generate the excited state product (P*), which subsequently decays to afford the product (P), it is an adiabatic reaction. Reactions with a concerted (single-step) process to give the product (P) includes pericyclic reactions with cyclic transition states, and will be discussed in the following section for photochemical [2+2] cycloadditions. However, the reaction profile may proceed through reactive intermediate(s) in either the ground state or excited state PES (I or I*). The latter includes the reactions of ketones and radical species.[2]

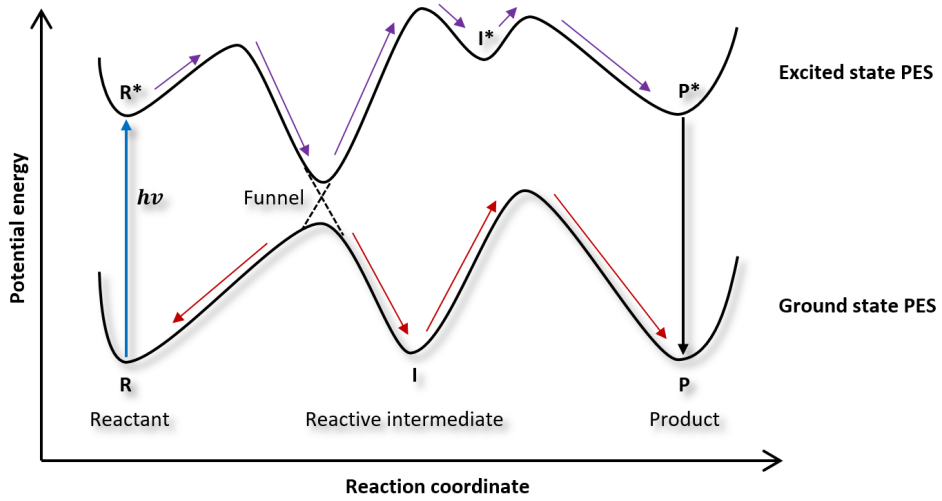

Figure 1.3. Schematic representation of a photochemical reaction profile diagram with ground state and excited state potential energy surfaces (PES). The arrows represent the course of the molecule moving along the reaction coordinate in the excited state (purple) and ground state (red). Adapted from B. Wardle.[2]

Excited state molecules are more reactive than the corresponding ground state molecules as the excited species have electrons in antibonding molecular orbitals, while the bonds are longer and weaker. Furthermore, excited species may afford energy-rich and strained molecules at low temperatures, which would otherwise not be feasible via a thermal process, due to decomposition. In addition, selective excitation is often possible with monochromatic light of appropriate wavelength (energy) with increased control of the reaction. The stereochemical outcome can also be very different for a photochemical reaction versus a thermal reaction as exemplified by electrocyclic reactions. Lastly, excited state species are better electron donors and acceptors than ground state species leading to very different redox properties between the two states. Photochemistry is therefore in many aspects, a powerful method.

1.3 PHOTOCHEMICAL [2+2] CYCLOADDITION

The cyclobutane motif can be found in a variety of complex natural products and pharmaceutical drugs (**Figure 1.4**) that exhibit versatile biological activity from cytotoxicity,[4] antifungal,[4,5] anti-HIV,[4,6] antimicrobial,[4,7] antiviral[4] and immunosuppressive effects.[4] It comprises a strained 4-membered cyclic system that introduces significant 3-dimensionality into the scaffold, which is important in order to increase the complexity (FSP^3 = fraction of SP^3 hybridized carbons/total carbon count) of molecules. Its incorporation into small-molecule drugs may therefore have a positive effect on the pharmaceutical properties and aid hit-to-lead fragment screening campaigns in developing new biologically active compounds.[8,9]

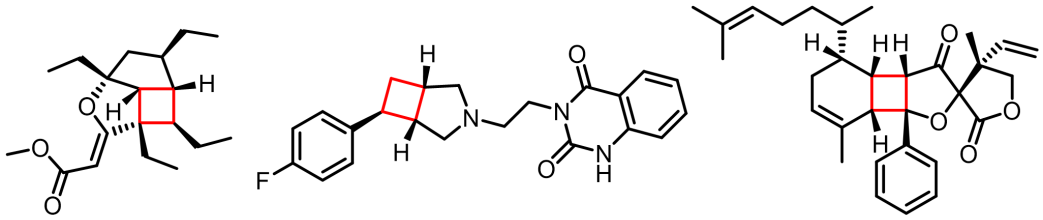

1 **Hippolachnin A** *Antifungal*

2 **Belaperidone** *Antischizophrenia agent*

3 **Biyouyanagin A** *Anti-HIV activity*

Figure 1.4. *Representation of biologically active compounds containing a cyclobutane motif in its core. Compounds 1 and 3 are natural products.*[5,6,10]

The preparation of cyclobutanes is conveniently achieved through an atom-economic cycloaddition reaction. In general, a cycloaddition is a chemical reaction that combines two or more unsaturated components with the formation of a cyclic adduct and a net reduction of the bond multiplicity. Most cycloaddition reactions are concerted with a pericyclic transition state, and hence do not involve any intermediate. It permits carbon-carbon bond formation without employing neither nucleophiles nor electrophiles. The Woodward-Hoffmann notation is generally the most encountered and accepted way to describe the interacting system, and is based on the number of electrons, rather than carbons, involved in forming the product.[11] Thus, the familiar Diels-Alder reaction is a [4+2] cycloaddition reaction (**Scheme 1.1**). Furthermore, it is an example of a thermal cycloaddition with the reactants following only the ground state PES to afford the product.

Thermal cycloadditions typically have $(4n + 2)$ π electrons participating in the reaction, while photochemical cycloadditions have $(4n)$ π electrons participating, for some integer n.[11] All cycloaddition reactions that are not allowed thermally, are allowed photochemically and vice versa. Whether a cycloaddition reaction is allowed thermally or photochemically, can be explained from an orbital symmetry point of view.

Bond formation is suprafacial if both σ bonds form on the same side of the π system (*syn* fashion), and antarafacial if the two σ bonds form on the opposite sides of the π system (*anti* fashion) (**Figure 1.5**).[12] Naturally, it requires a two-component unsaturated system with each alkene coupling partner comprising

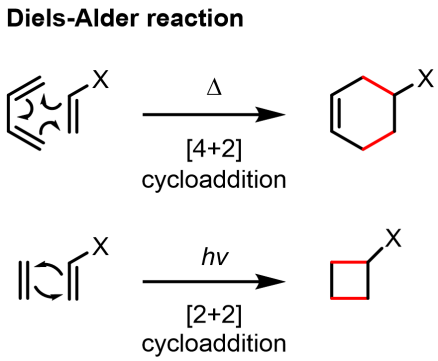

Scheme 1.1. General cycloaddition reactions between two alkenes with X as an arbitrary group.

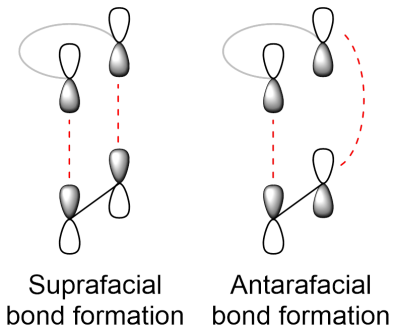

Figure 1.5. The two modes of orbital overlap for the simultaneous formation of two σ bonds, suprafacial and antarafacial.

two interacting π electrons to make a cyclobutane ring structure. Thermal conditions do not allow this [2+2] cycloaddition reaction, due to incompatible orbital symmetry in the binding mode, and an antarafacial approach is not feasible, due to the geometric constraints of the small ring. However, it does take place under photochemical conditions with an orbital symmetry-allowed suprafacial approach. Thus, the problem with incompatible symmetry is solved photochemically by converting one alkene into an excited state species (**Figure 1.6**). Mixing of the orbitals have a net result of three electrons going down in energy and only one that goes up, which favours bonding. If one alkene is bonded to a conjugated group such as an enone, this alone is excited while the other alkene remains in the ground state.

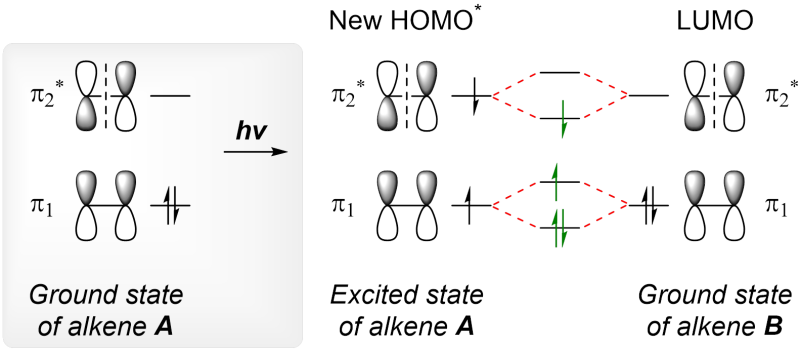

Figure 1.6. Photochemical [2+2] cycloaddition reaction between excited alkene A and ground state alkene B.

The same Woodward-Hoffmann selection rules governing its formation, also prevent the strained 4-membered ring structure from thermally reverting back to the two alkene starting materials, and since the system has lost its π bonds it cannot absorb light to do it photochemically either.

2. INTRODUCTION TO PHOTOSWITCHES

There exist many photochromic molecules known to date. Therefore, to simplify the vast field of photoresponsive systems, the following sections will discuss molecular photoswitches based on the type of chemical reaction involved when induced with light and the core chemical structure that makes up its photoswitch family. Furthermore, elegant examples on the use of photoswitches in applications as powerful tools to control units or unlock entirely new functions are presented to illustrate the future prospects of this fascinating area of research. First, however, a short introduction to the definition, scientific terminology and parameters used to describe photoswitches.

2.1 MOLECULAR PHOTOSWITCHES

Molecular photoswitches comprise a class of photochromic molecules able to interconvert reversibly between their stable A and metastable isomer(s) B upon absorption of incident light in at least one direction (**Figure 2.1.**). We typically refer to this as photoisomerization or simply photoswitching. Subjecting the system to light (P-type photochromism) or by means of thermal relaxation (T-type photochromism), depending on the thermal barrier, returns the initial isomer A (**Figure 2.1.**).[13] The two isomers (or states) show different physicochemical properties including absorption spectra. For the most part, photoisomerization is accomplished in a controlled manner by selection of appropriate wavelengths ranging from visible to near-infrared (NIR) light. Typically, absorption of electromagnetic radiation occurs at higher wavelengths (redshifted) for the metastable isomer B as compared to the stable isomer A, λ_{max}(B) > λ_{max}(A). This phenomenon is referred to as positive photochromism, whereas the opposite is negative or inverse photochromism.[13] Most prevalent photoswitches involve unimolecular reactions in systems with two molecular states, but systems with more states exist.[14]

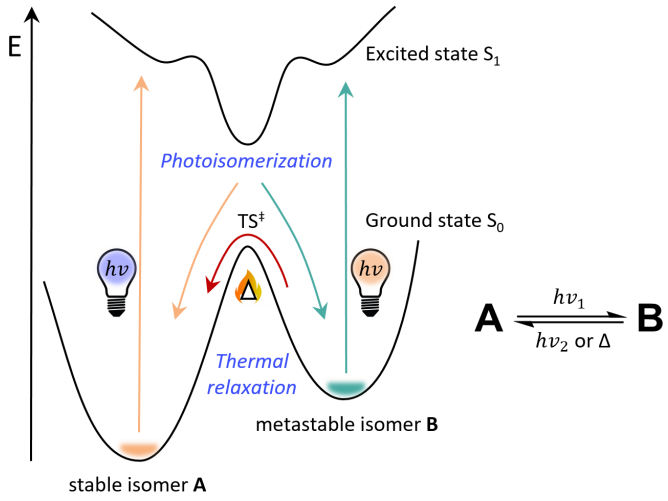

Figure 2.1. *Schematic representation of a photoisomerization between two molecular states (A and B) and their potential energy surfaces. Orange/green arrows show isomerization induced by light, whereas the red arrow by thermal relaxation. Inspiration from A. Goulet-Hanssens.*[14]

2.2 DESIGNING THE OPTIMAL PHOTOSWITCH

Several parameters are essential to consider when designing the optimal photoswitch and the importance of each depends in large by the intended use in an application. An overview of the most significant and commonly encountered experimental parameters in the literature is given in **Table 2.1**. In general, all parameters are associated with either addressability, efficiency, thermal stability or reliability.[15]

Addressability pertains to the specific wavelength used to excite the photoswitch, represented by absorption maxima, which has to be compatible with the material surrounding it. The use of high energy (low wavelength) light to initiate excitation may result in degradation of the material. Hence, many strategies aim at redshifting the absorption profile to minimize material damage in addition to enhanced penetration depth, making the photoswitch more applicable. Furthermore, the absorption spectra of the different isomers should not overlap completely allowing excitation of each state independently with good band separation.

Table 2.1. *Most significant and commonly encountered parameters of photoswitches in the literature.*

Parameter	SI unit	Description of measurement
Absorption maximum (λ_{max})	nm	The wavelength of maximum absorption
Band separation ($\Delta\lambda$)	nm	The difference in wavelength between absorption maximum of each isomer
Cyclability (Z_{50})	$-$	The number of cycles required to reduce the initial absorbance at a specific wavelength by 50%
Emission maximum (λ_{em})	nm	The wavelength of maximum emission
Half-life ($\tau_{1/2}$)	$seconds - years$	The time necessary for thermal back isomerization of 50% of the metastable isomer in the dark at a specific temperature
Isosbestic point	nm	The wavelength at which the total absorbance of a sample does not change
Molar absorption coefficient (ε)	$L \cdot mol^{-1} \cdot cm^{-1}$	The intensity of absorption at a specific wavelength
Oscillator strength (f)	$-$	The probability of absorption or emission of electromagnetic radiation
Quantum yield (Φ)	$-$	The number of occurring events per absorbed photon
Stokes shift	nm	The difference in wavelength between absorption and emission maxima

Efficiency is typically evaluated by the degree of photoconversion when switching the system back and forward, where (near) quantitative isomerization in both directions is favoured. Furthermore, the ability to absorb a photon by each state in the system should be high in terms of quantum yields. Fast photoisomerization aided by high quantum yields and good band separation helps prevent potential degradation from prolonged irradiation with light.

Thermal stability refers to the rate of thermal back isomerization of the metastable isomer displayed by the thermal half-life, which should allow enough time for the switch to exert its function.

Finally, reliability concerns the ability of a photoswitch to undergo many forward and backward switching cycles without significant degradation, and is evaluated through cyclability.

For a two state system, one cycle under well-defined conditions corresponds to system A photochemically transforming into system B, following its return photochemically or thermally to system A. In an ideal situation, this cycle via photoisomerization is quantitative. However, sideproducts accumulate with time caused by chemical photodegradation most often involving oxidation. This loss in performance over time, due to degradation of the photoswitch is termed fatigue. When describing colours or absorbance, the term photobleaching is more appropriate. A robust system able to undergo many switching cycles is fatigue resistant.

Another important experimental parameter is the photostationary state. For a reversible photochemical system induced by light, the photostationary state is the steady state where rates of formation and disappearance are equal for all isomers. Hence, when discussing photostationary state selectivity (PSS), it denotes the ratio typically as a percentage of each entity at steady state after irradiation with light of a specific wavelength. Efficient systems should have a high PSS in both switching directions.

According to Wiedbrauk and Dube (2015), photoswitches need to fulfil a variety of special requirements to be useful for applications.[16] An important consideration when making switches for applications is that irradiation with light should produce a specific and distinct change in the molecule, such as isomerization, pericyclic reaction or tautomerization, and is typically the basis for how photoswitches are classified.

2.3 CLASSIFICATION OF PHOTOSWITCHES

One way to classify molecular photoswitches is by the type of chemical reaction involved in the light induced isomerization. For the most part, these belong to hydrogen transfer, cycloaddition, homolytic or heterolytic bond dissociation, *E*/*Z* isomerization and electrocyclization reactions.[15] As the latter two constitute by far the most explored types to date, the focus will be on these.

E/*Z* isomerization involves the isomerization of a central π double bond, which is formally broken upon excitation with light. It introduces a large structural change in the molecule accompanied by a change in physicochemical properties. The mechanism of isomerization proceeds either via a “one-bond-flip” turning over half of the molecule or through a ”hula-twist” with simultaneous conformational isomerization of a small C-H unit.[17]

Electrocyclization reactions involve six conjugated π-electrons in a triene system that upon excitation performs a pericyclic ring-opening, ring-closing reaction. The resulting change in spatial geometry may vary a lot depending on the location of the interacting bonds in the system. It is, however, often accompanied by a dramatic change in electronic configuration among other properties, albeit the most prominent and physically observable change is that one state is often coloured and the other completely colourless.

Indigos, stilbenes, azobenzenes and hydrazones are examples on the first type, whereas diarylethenes, spiropyrans, fulgides and donor-accepter Stenhouse adducts are examples of the second type (**Figure 2.2**). Most photoswitches of the *E/Z* isomerization type display T-type photochromism, whereas electrocyclization types are often bistable molecules and therefore predominantly exhibit P-type photochromism. Sometimes photoswitches are categorizes based on T- or P-type photochromism.

Incorporation of photoswitchable molecules into materials enables the development of molecular photo-responsive systems. Activating the system with light of appropriate wavelength delivers a selective and reversible response. This is an advantageous strategy as the system can be switched "ON"/"OFF" or perform two different functions on demand. Consequently, photoswitches have sparked great interest as promising tools within photopharmacology,[18–20] optical data,[14,21,22] energy storage systems,[23–25] guest-host complexes,[26–28] self-healing materials,[29–31] molecular motors[32–35] and photomechanical polymers[30,36] to name a few in recent decades.

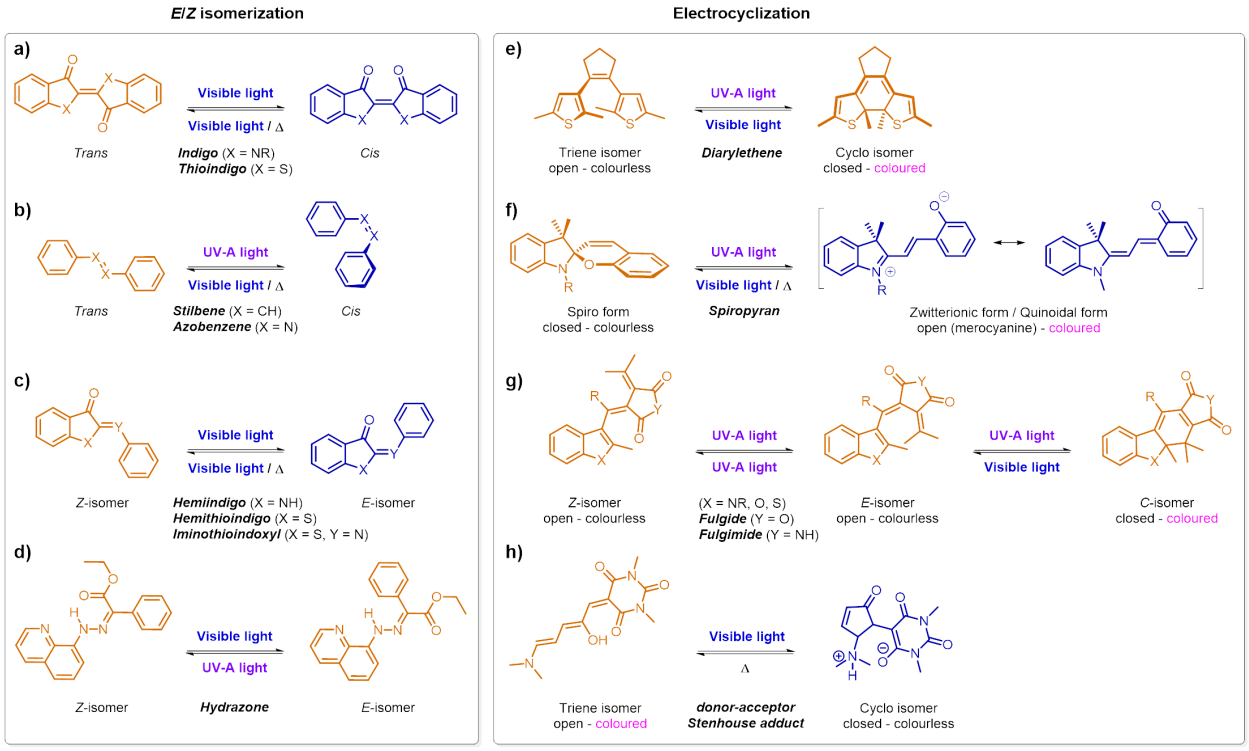

Figure 2.2. *Overview of photoresponsive molecules classified into either E/Z isomerization or electrocyclization types. Orange colours represent stable states whereas blue colours metastable states of the photoswitches.*

2.3.1 *E*/*Z* ISOMERIZATION TYPES

INDIGO/THIOINDIGO

The indigo and thioindigo family of photoswitches belong to the *E*/*Z* isomerization type (**Figure 2.2a**). It was observed already in the middle of the last century that these compounds exhibit photochromism, and were well-characterized as dyes decades ago.[37–39] The parent indigo is not a photoswitch in itself, due to an excited state intramolecular proton transfer (ESIPT) from the indole-NH onto the carbonyl moiety, which results in its deexcitation. However, N-substituted derivatives of indigo undergo efficient *E*/*Z* isomerization when irradiated with orange-to-red light.[37,40,41] With absorption maxima of both isomers in the visible region, these derivatives are attractive for soft material applications, as the lower excitation energy needed minimizes material damage. Furthermore, indigo photoswitches display negative photochromism allowing for enhanced penetration depth.[13,15,42] A limitation is that the metastable *Z* isomer is often short-lived and requires pump-probe experiments to be studied as is the case of N,N'-dimethylindigo that readily relaxes to its *E* isomer (T-type photochromism).[42,43] However, molecular tailoring have managed to improve thermal half-lives while maintaining red light photoswitching. [40]

Thioindigo is the sulphur-analogue of the parent indigo (**Figure 2.2a**), and likewise absorbs light in the visible spectrum, albeit slightly blueshifted, while displaying negative photochromism. Although it resembles the photoswitches of its nitrogen-containing counterpart, key differences exist. It shows reversible photoswitching with visible light (P-type photochromism), but is limited by very low solubility in almost all conventional organic solvents unless accounted for by suitable substituents.[43] Recently, a sulfonated thioindigo derivative displayed reversible photoswitching in water, which may open up possibilities towards making thioindigo photoswitches relevant in biological applications. [44]

Besides giving name to a distinct hue of blue, dyeing clothes or as a food additive, neither derivatives of indigo nor thioindigo have found much use as photoswitches in applications relevant to highlight here. I will therefore focus on the better alternatives available to date.

STILBENE/AZOBENZENE

Stilbene is arguably the most studied model for photochemistry, whereas azobenzene may be the most utilized photoswitch to date and among the first reported molecular photoswitch to undergo reversible light induced *E*/*Z* isomerization.[15][45,46] They both consist of a double bond linking two terminal aryl moieties (**Figure 2.2b**). They are simple in structure and can be accessed from inexpensive starting materials in one or two synthetic steps. Irradiation with UV light induces a reversible *trans* → *cis* isomerization of the double bond via a $\pi \rightarrow \pi^*$ excitation.[15,47] Consequently, a large change in molecular geometry results, which significantly reduces the distance between the two phenyl moieties leading to an increased dipole moment and a considerable free volume change in the material.[14,45] The return to the *trans* isomer of azobenzene is typically achieved with either visible light irradiation inducing the $n \rightarrow \pi^*$ electronic transition or thermally (T-type photochromism) with relatively short half-lives depending on substituents, due to a small 10 kcal/mol difference in energy between the two states.[47,48] In contrast, stilbene is bistable

and shows reverse photoswitching with UV light (P-type photochromism), due to a large thermal energy barrier of 41-46 kcal/mol between the two states.[48]

The need for UV light to induce isomerization is a noteworthy disadvantage for both of these families as surrounding material will non-selectively absorb the high energy light and likely degrade. Furthermore, azobenzenes often display incomplete reverse isomerization, due to overlapping $n \rightarrow \pi^*$ bands in the visible region.[15] By increasing the separation of the $n \rightarrow \pi^*$ electronic transitions through molecular design, several research groups have managed to develop near quantitative reversible photo-isomerization of azobenzene derivatives with visible light irradiation.[47,49–52] Thereby addressing both major drawbacks.

Azobenzene photoswitches have been employed in a rich number of applications, and is the most utilized when it comes to biological applications.[53,54] An attractive example includes restoring visual function in retinas of blind animal models through photoswitchable control of light-gated ion-channels by Gaub and co-workers (2014).[55,56]

Another intriguing example involves smart materials like supramolecular photochromic hydrogels, where light triggers a reversible dissipation of the gel resulting in the release of encapsulated cargo molecules in biological systems (**Figure 2.3a-b**).[57] In this way, Karcher and Pianowski (2018) were able to release unmodified antibiotic, anticancer and anti-inflammatory compounds from hydrogels with green light irradiation.[57] The authors further validated the system by inhibiting bacterial cell growth with ciprofloxacin as the released encapsulated antibiotic cargo under green light (**Figure 2.3c**).[57]

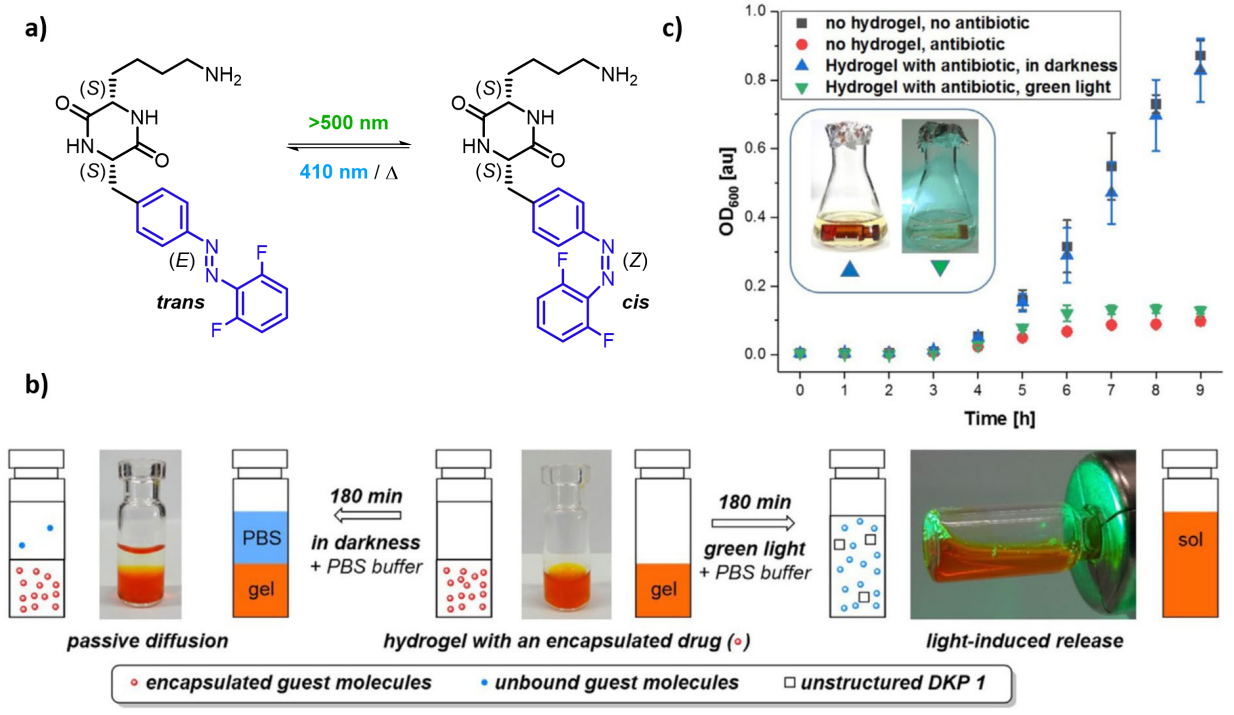

Figure 2.3. Green light induced drug release from hydrogels. (a) Reversible E/Z photoisomerization of the fluorinated azobenzene hydrogelator. (b) Schematic representation of the cargo encapsulation and release process in the irradiated and non-irradiated gel sample. (c) Growth curves of bacterial cell cultures exposed to ciprofloxacin-loaded hydrogel samples. Adapted from J. Karcher & Z. Pianowski.[57]

HEMITHIOINDIGO

Hemithioindigo-based photoswitches have not seen much attention when compared to the more well-established classes like azobenzene, spiropyran and diarylethene. However, derivatives of this family have become increasingly more popular in recent years, due to their distinct and very interesting physico-chemical properties.[37]

Hemithioindigos (HTIs) consist of half a thioindigo connected to half a stilbene fragment via a double bond, which when induced with visible light in both switching directions (typically >430 nm) undergoes a reversible photoisomerization between the stable *Z* isomer and metastable *E* isomer (**Figure 2.2c**). The thermal energy barrier between isomers of HTI derivatives is significantly higher (typically >27 kcal/mol) than the most commonly used azobenzenes (≤25 kcal/mol),[16] essentially rendering HTIs very bistable P-type photoswitches. Furthermore, the *E* isomers are bathochromically shifted with good band separation to the *Z* isomers (typically 20-30 nm) allowing high PSS (>95%) even for analogues with low quantum yields.[16] Photoisomerization around the double bond is extremely fast (typically low ps range) in both switching directions.[58] For this reason, not often is radiative deexcitation processes such as fluorescence or phosphorescence observed to any great extent. Lastly, they are highly fatigue resistant photochromic compounds that have shown cyclability values past the orders of thousands. All of these properties combined make HTI-based photoswitches ideal candidates for light induced applications including in biological systems. However, light-induced intermolecular [2+2] cycloaddition of the central double bond, especially at high photoswitch concentrations, is a potential concern for their reliability observed at times. In conjunction with their often-lower solubility when compared to indigoids like the hemiindigo photoswitches, it can make for an unfortunate cocktail.

HTI-based photoswitches have started to see the light in recent times and found their way into different applications such as machine-like systems comprising complex motion,[59,60] information processing,[61] photoresponsive guests-host complexes,[28,62,63] unidirectional molecular motors[64–70] with high solvent dependent behaviour [32,71] and photopharmacology.[72–76] The latter exemplified by Lougheed and co-workers (2004) that managed to initialize large changes in peptide secondary structure by photoswitching an HTI derivative incorporated into a β-hairpin motif (**Figure 2.4a**).[77] Light induced isomerization to the metastable *E* isomer resulted in an almost instant loss of hydrogen bonds within the β-hairpin.

In similar manner, new modes of controlling biological functions associated with secondary peptide or protein structures can be visualized with light activated HTI-based photoswitches. Furthermore, Herre and co-workers (2006) exploited the close resemblance between ebselon, a known lipoxygenase (LOX) inhibitor, and the parent HTI photoswitch to switch "ON" inhibition of the enzyme with light (**Figure 2.4b**).[78] LOX enzymes catalyse the peroxidation of polyunsaturated fatty acids and are involved in orchestrating a variety of biological processes for example skin barrier formation, cell differentiation and immunity.[79] Its biological modulation is however important, as LOXs have also shown to be involved in diseases such as asthma, atherosclerosis, osteoporosis and inflammatory diseases.[16] The *E* configuration of the HTI-derivative exhibited a 33-fold greater inhibition (IC_{50} = 21 uM) when compared to its *Z* isomer in vitro, highlighting that photochromic compounds might be developed as potential drugs for inflammatory skin diseases.[78]

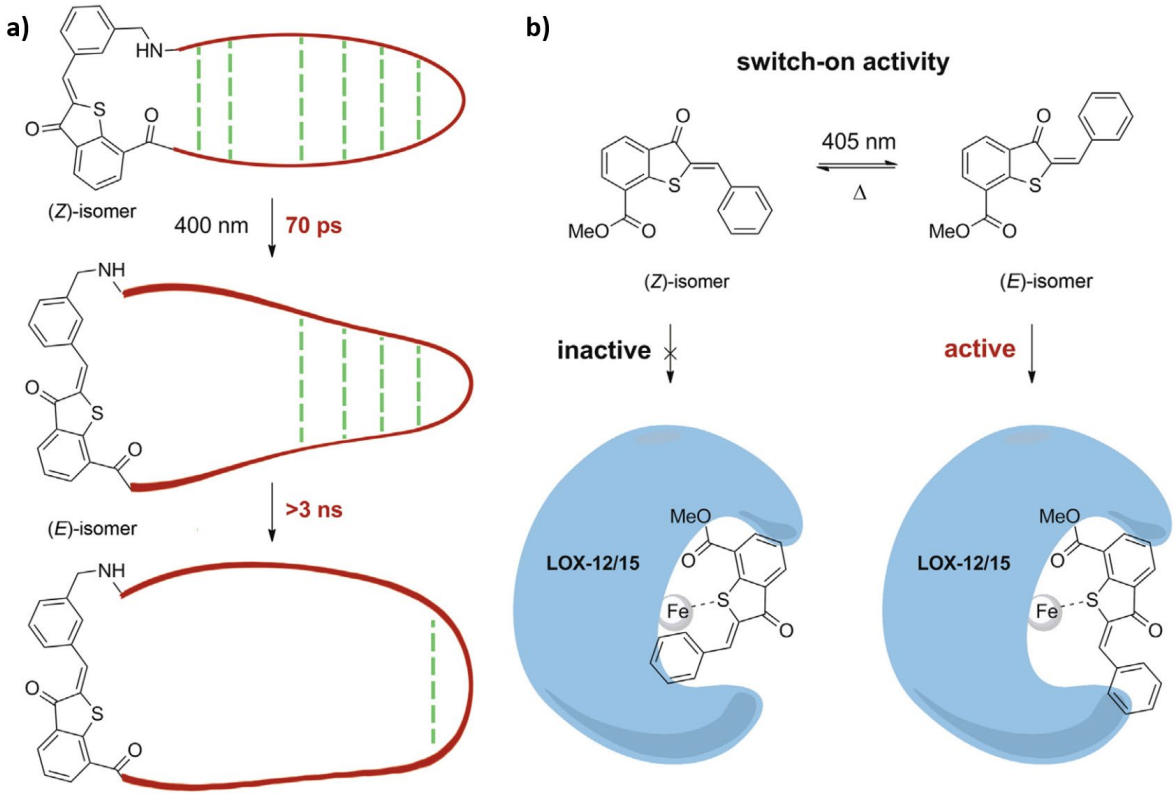

Figure 2.4. *Biological applications of HTI photoswitches. (a) HTI-modified β-hairpin peptide forming multiple hydrogen bonds that upon photoisomerization of the HTI to its E configuration gets disrupted resulting in an altered secondary structure of the peptide. (b) HTI derivative displaying photoinducible inhibition of the lipoxygenase LOX-12/15. While the thermodynamically stable Z isomer is virtually inactive, the E isomer binds the enzyme strongly. Adapted from S. Wiedbrauk & H. Dube.*[16]

HYDRAZONE

Hydrazone switches are multi-stimuli responsive systems characterized by the triatomic structure C=N-N. It is unique in that the C=N double bond can undergo *E*/*Z* isomerization triggered by either pH,[80–83] metal ions[84–86] or light.[87–89] When the isomerization is triggered photochemically, the metastable *Z* isomer is obtained using visible light (typically about 440 nm), whereas the reverse isomerization happens with UV light (band separation >100 nm) or thermally. Recently, P-type hydrazones displaying thermal bistability were discovered (**Figure 2.2d**).[90] The previous generation of acylhydrazones contained a rotor (upper) pyridyl moiety able to form an intramolecular hydrogen bond to the carbonyl group, but only when in the stable *E* configuration, hindering efficient isomerization and resulting in relatively low thermal half-lives (minutes to days). By replacing this with a phenyl moiety incapable of making this bond (**Figure 2.2d**), efficient photoswitching from the now stable *Z* isomer to the metastable *E* isomer occurs with good PSS (76-95%) and quantum yields (2-10%). The thermal half-lives improved to an impressive 255 years.[88] Upon further introduction of a stator (lower) 8-aminoquinolinyl moiety resulting in an increased thermal barrier,

due to a new intramolecular hydrogen bond with the pyridyl group in the lower half of the molecule, a thermal half-life of an astonishing 2700 years was obtained.[88]

Hydrazone-based photochromic compounds, however, still suffer from low wavelength absorption making its potential use in biological applications limited. For this reason, hydrazones have mainly found their use in supramolecular chemistry with mostly chemical inputs for switching.[87,88] An elegant example by Kassem and co-workers involves moving cargo like a molecular robotic arm a distance of 2 nm to either of two platform sites by carefully controlling the amount of acid in the surrounding environment.[91] Another intriguing example involves hydrogels based on acylhydrazones with intrinsic self-healing and tissue-adhesive properties by Yu and co-workers.[92] Furthermore, achiral hydrazone-containing polymers integrated into liquid crystals were shown to impose macroscopic chirality of flat ribbons through photogenerated mechanical strain (**Figure 2.5**).[93] The photogenerated handedness of the ribbons doped in the liquid crystals depended on which of the two sides that was illuminated with UV light. This highlights an example of setting soft matter in motion and adds to the prospects of polymer photoactuation.

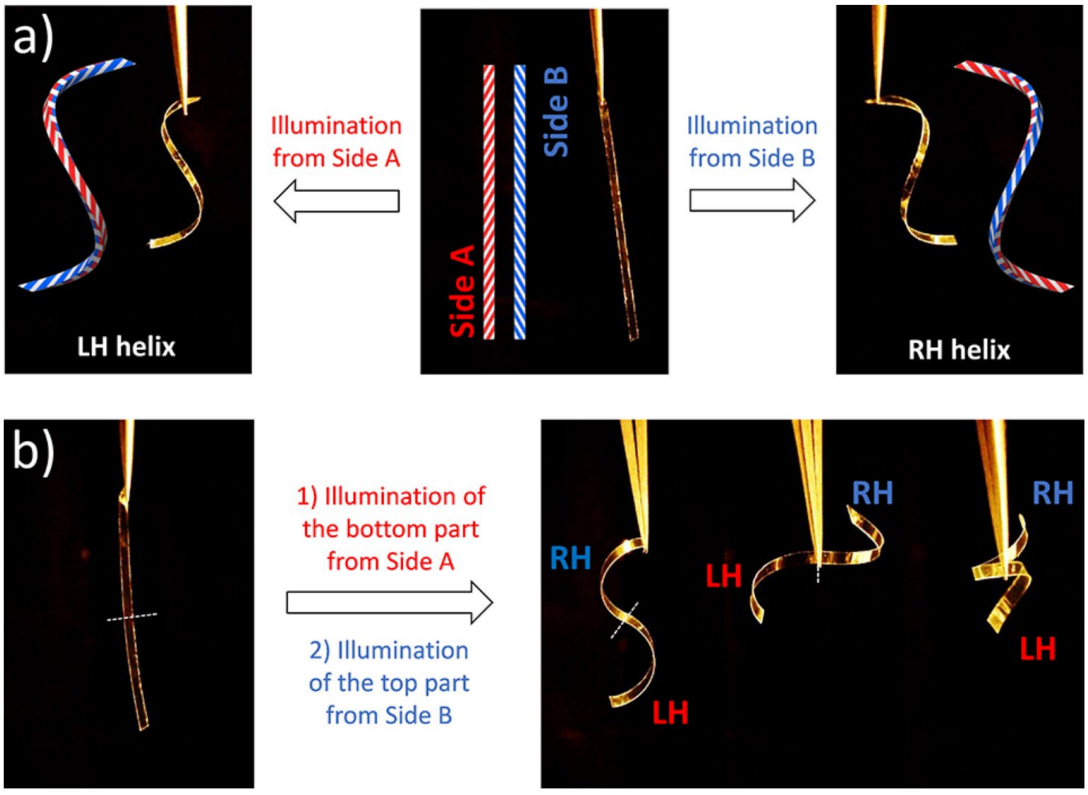

Figure 2.5. *Macroscopic chirality of flat ribbons introduced by a gradient of mechanical strain. The white sripes indicate molecular orientation in the sample. The colours, red and blue, represents opposite sides of the ribbons to help guide the eye. LH and RH indicate left- and right-handedness, respectively. (a, b) The ribbons doped in a liquid crystal integrating a hydrazone-containing polymer responds mechanically to illumination with UV light resulting in chiral deformation. Reproduced from A. Ryabchun et al.*[93]

2.3.2 ELECTROCYCLIZATION TYPES

DIARYLETHENE

Dithienylethenes (DTEs) or generally diarylethenes (DAEs) are photochromic compounds belonging to the electrocyclization class of photoswitches. They can be considered derivatives of stilbene. The core structure typically consists of two thiophene rings bridged by an ethene unit to assemble a hexatriene system (**Figure 2.2e**). The ethylene is typically a cyclic olefin to avoid unwanted *Z* → *E* isomerization. Irradiation of the colourless open form with UV light results in a reversible ring-closure to the coloured cyclic form through a photochemical pericyclic reaction. Photocyclization to the closed form generates a fully delocalized π-conjugated system that despite only small geometrical changes to the structure results in large changes to electronic properties and flexibility. Hence, DAEs are considered very promising photoswitchable components for optoelectronic devices.[15] The reverse ring-opening reaction can be triggered with visible light (typically above 450 nm) and often proceeds quantitatively, due to the open form not absorbing in the visible region.[43,94] In addition, DAEs exhibit thermal bistability, and thus P-type photochromism, because the photochemically allowed conrotatory ring-closure is thermally forbidden for many derivatives of 5-membered heterocycles according to the Woodward-Hoffman rules.[43] A drawback of DAEs, besides the need for UV light to induce isomerization, is that the synthesis can be challenging for derivatives that is more complex and possess asymmetry.[95] Furthermore, DAEs at times exhibit low fatigue resistance, due to photoinduced oxidation and rearrangement side reactions.[43]

Diarylethene is a popular switching system and has been studied in a large variety of applications ranging from inspiring supramolecular guest-host and self-assembly materials,[93,96–99] photodynamic-immunotherapy,[100] programmable sensing materials,[101] smart inks,[102] light-harvesting systems,[103] to bioluminescence imaging[104] and optoelectronic devices.[95]

Reversible generation of singlet oxygen ($^1O_2$) in a precise and programmable manner with light stimulus is in great demand and a potential strategy for photodynamic therapy (PDT).[105] Qin and co-workers (2019) developed a new dual-stage metallacycle (M) incorporating DAE photochromic switches and porphyrin photosensitizers with proximal placements of both functional entities for efficient intramolecular energy transfer (**Figure 2.6a**).[106] Efficient generation of singlet oxygen from the porphyrin photosensitizer occurs when the DAE units are in the ring-open form (O-M), in contrast to the ring-closed form (C-M) where an energy transfer from the porphyrin entity to the DAE unit takes place effectively quenching the process. The generation of singlet oxygen can be selectively controlled by irradiation with either UV or visible light. Furthermore, by embedding the dual-stage metallacycle within the hydrophobic interior of nanoparticles (O-NPs and C-NPs), the authors were able to remotely control the off-on switching of singlet oxygen generation in vitro and in vivo as anti-tumour treatments (**Figure 2.6b**). This strategy may lead to a potential clinical treatment of cancer in the future.

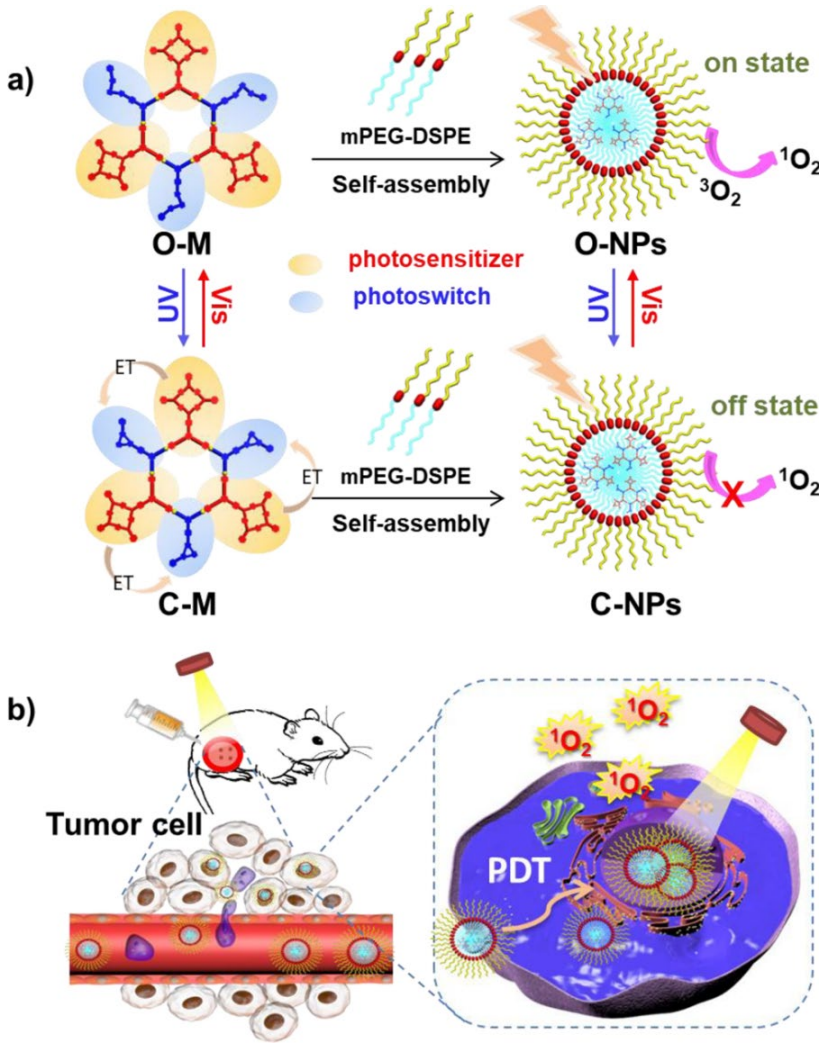

Figure 2.6. Schematic representations of light-controlled singlet oxygen generation using a dual-stage metallacycle for cancer therapy. (a) When the DAE units have a ring-closed configuration, the metallacycle (C-M) exhibit no generation of singlet oxygen in contrast to the ring-open configuration (O-M). Embedding the metallacycle into NPs (C-NPs and O-NPs) allows for efficient light-induced switching between off-on states. (b) Illustration of O-NPs accumulation in tumour tissue followed by enhanced permeability and retention (EPR) effect and photodynamic therapy (PDT) effect. Adapted from Y. Qin et al.[106]

SPIROPYRAN

Spiropyran-based photoswitches present another very popular and old family of photochromic molecules that follows a 6π electrocyclization mechanism when isomerized. The core scaffold comprises an indoline and a chromene moiety connected via a spiro-carbon atom with the two parts oriented perpendicular to one another (Figure 2.2f). The parent ring-closed spiro isomer (SP) is colourless whereas the ring-open merocyanine isomer (MC) is coloured. Spiropyran-based switches are multi-stimuli responsive systems that can be triggered with a whole range of stimuli, including heat, pH, electrons and light, which makes them

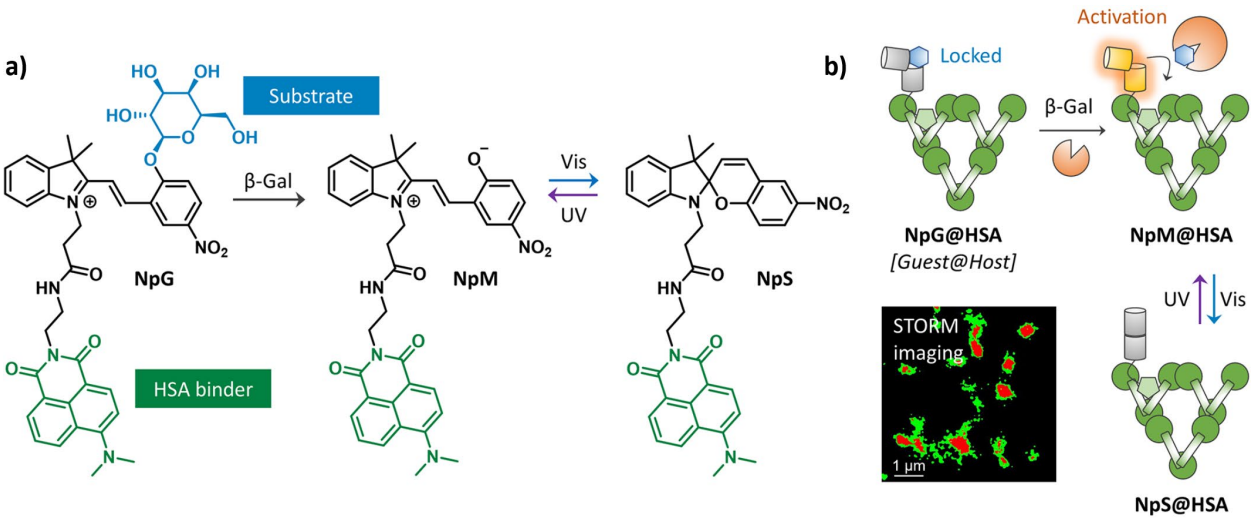

Figure 2.7. *Schematic representation of a spiropyran-based β-galactosidase (β-Gal)-responsive photochromic fluorescent probe for super-resolution bioimaging and determination of subcellular distribution of β-Gal activity between cell lines. (a) Substrate hydrolysis (blue) by β-Gal enzyme to activate fluorescence of the probe. Subsequent reversible photoswitching from fluorescent active NpM to fluorescent inactive NpS. (b) NpG specifically designed to bind human serum albumin (HSA) through the naphthalimide fluorescent linker (green) forms a protein-probe complex NpG@HSA enabling cellular uptake. Subsequently, β-Gal hydrolyses the galactose substrate (blue) and activates the fluorescence of the NpM@HSA complex. Super-resolution imaging technique (STORM) monitors the precise location of the enzymatic biomarker β-Gal in senescent cells. Illumination with UV-Visible light switches the system ON/OFF. Adapted from X. Chai et al.*[107]

prominent candidates for a large variety of applications.[43,108,109] Ring-opening following UV light irradiation (typically 320 nm) proceeds via a carbon-oxygen heterolytic bond cleavage with a subsequent *Z* → *E* isomerization. The MC isomer consists of an extended π-conjugated system featuring two resonance structures, i.e. zwitterionic and quinoidal. Switching back to the SP isomer is accomplished with visible light irradiation (typically 500-600 nm) of the MC isomer or thermally through spontaneous relaxation in the dark (T-type photochromism). The reason for its on-going popularity as a switch originates in large from the substantial change in structural geometry (orthogonal vs. planar), electronic structure (non-conjugated vs. conjugated π-system) and dipole moment ($\Delta\mu > 10$ D).[109] However, the need for UV light to induce ring-opening in conjunction with fast thermal relaxation, low fatigue resistance due to photodegradation via triplet excited states, and aggregation of the ring-open MC isomer due to poor solubility, pose significant drawbacks for its use in numerous applications.[15]

Spiropyrans have found use in a variety of applications, but is probably most famous for its contribution to photochromic ophthalmic lenses, which darken in the sun and bleach in dim light.[110] Additionally, one very neat feature of spiropyrans is the interconversion between a charged and a neutral species greatly influencing solubility in different media. Hence, the SP form can be solubilized in uncharged liposomes, which is in contrast to the MC form.[111] Furthermore, the SP form can pass membranes and be switched inside living cells.[112,113] X. Chai and co-workers (2020) recently reported a β-galactosidase (β-Gal)-responsive photochromic fluorescent probe that allowed the intracellular distribution of β-Gal to be

monitored (**Figure 2.7a-b**).[107] The spiropyran-based photoresponsive probe containing naphthalimide and a galactose sugar moiety directly attached to the phenol ring of the MC isomer, forms a protein-probe complex with human serum albumin (HSA) ensuring aqueous solubility and good cellular uptake. The galactose moiety is hydrolysed by β-galactosidase inside the cells resulting in a localized increase in red fluorescence, due to the formation of free MC isomers ("on state"). Subsequent irradiation with visible light quenched fluorescence by photoisomerization to the SP isomers ("off state"). The clever design exploits the selective fluorescence of spiropyrans to set up a versatile imaging platform suitable for illuminating the precise location of disease-specific biomarkers in various cellular processes.[107]

FULGIDE/FULGIMIDE

Fulgides and fulgimides are an established class of photochromic compounds undergoing electrocyclization reaction.[114] The scaffold consists of a heteroaromatic moiety connected via an exocyclic double bond to either a succinic anhydride (Y = O) to give a fulgide, or a succinimide (Y = NR) to assemble a fulgimide (**Figure 2.2g**). A second exocyclic double bond completes the 1,3,5-hexatriene structure. The ring-open *Z* isomer is colourless, and may undergo reversible *Z* → *E* isomerization upon irradiation with UV light (typically 360-420 nm).[43] However, this process is often very inefficient, as the two configurational isomers show significant overlapping of their excitation spectra. Further irradiation with UV light induces an irreversible (under the same conditions) conrotatory electrocyclization of the *E* isomer to the ring-closed coloured isomer, which essentially functions as a photochemical sink. The large extended π-conjugated system delocalized throughout several ring-structures makes the ring-closed isomer absorb light at higher wavelengths into the visible region. Both fulgides and fulgimides are P-type photochromic compounds, thus in order to return to the *E* isomer, visible light (typically 450-600 nm) irradiation of the ring-closed isomer initiates the electrocyclic ring-opening.[43] Smaller substituents (R groups) such as a methyl in the bridging part allow for facile *E* → *Z* isomerization, while larger substituents such as an isopropyl does not.[43] Fulgimides display bathochromically shifted absorptions compared to fulgides, and both are more hydrophilic and thus more soluble in organic and aqueous solvents than DAEs.[43]

Fulgide and fulgimide-based photoswitches have been reported for a wide range of applications such as switchable polymer films,[115,116] unidirectional molecular motors,[117] molecular keypad locks,[118] molecular logic gates[119] and photopharmacology.[120–122] In a recent study, Ustler and co-workers (2020) demonstrated that an ionotropic γ-aminobutyric acid receptor A ($GABA_AR$) could be reversibly inhibited by Fulgazepam, an iso-fulgimide-based benzodiazepine derivative (**Figure 2.8**).[120] Photoswitching of the inactive open *E* isomer results in $GABA_A$-mediated current amplitudes (potentiation of the receptor) by the closed *C* isomer. Importantly, Fulgazepam was shown to work both in vitro and in vivo with no toxicity displayed in zebrafish opening up possibilities of dissecting the mechanisms of GABAergic neurotrans-mission at high spatiotemporal resolution.

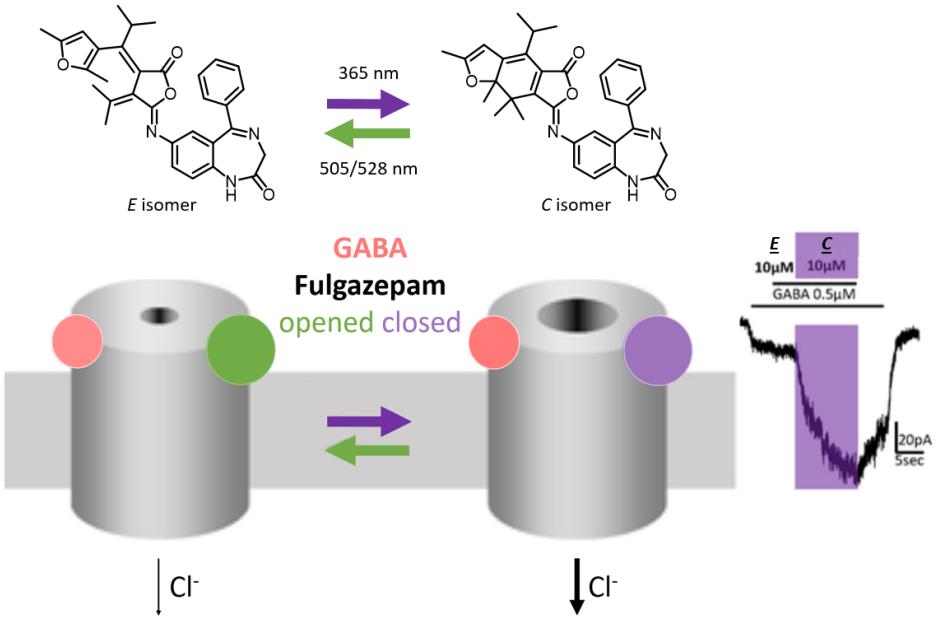

Figure 2.8. *Schematic representation of the reversible inhibition of ionotropic γ-aminobutyric acid receptors ($GABA_ARs$) by an iso-fulgimide derivative of benzodiazepine, Fulgazepam. Illumination with UV-Visible light enables selective potentiation of the receptor in vitro and in vivo. Adapted from K. Ustler et al.*[120]

DONOR-ACCEPTOR STENHOUSE ADDUCT

Donor-acceptor Stenhouse adducts (DASAs) is a novel family of photoswitches first described in 2014.[123] However, they quickly gained interest and already now exist in a third generation with alterations to the donor and acceptor part of the molecule. In general, the core structure consists of an electron donor moiety connected via a conjugated triene bridge with an oxygen on C_2, to an electron acceptor moiety (**Figure 2.2h**). Thereby making DASAs push-pull systems. First generation DASAs typically contained dialkylamines as the donor, while the acceptor was Meldrum's acid or 1,3-dimethyl barbituric acid. The donor part was replaced a few years later by secondary anilines or functionalized indoles, whereas more strongly electron withdrawing carbon acids were introduced in place of the acceptor moiety in the third generation. The acceptor is installed via a simple Knoevenagel condensation to inexpensive furfural, and the donor introduced by subsequent ring-opening of the activated furan core with a nitrogen nucleophile through a series of rearrangements reminiscent of the (aza)-Piancatelli rearrangement.[124] The elongated, hydrophobic and strongly coloured triene isomer absorbs visible light (typically 450-700 nm) to afford the more compact, hydrophilic and colourless cyclic isomer through electrocyclization.[36,125] DASA display negative photochromism with no electronic transitions of the cyclic isomer above 300 nm. Furthermore, it readily relaxes with short half-lives in the dark (typically within minutes), effectively rendering DASA a T-type photochromic switch.[43,125]

As a result of the above-mentioned features, DASA photochromic compounds have been extensively studied in the field of drug delivery systems,[126] surface micro-pattern photolithography,[127] switchable polymer films,[128–130] liquid crystals,[131] molecular motors,[132] chemosensing,[133] molecular logic gates[134] and supramolecular assembly of NPs.[135] Diaz and co-workers (2017) exploited that Meldrum's activated furan (MAF) or 1,3-dimethyl barbituric activated furan (BAF) could function as simple and versatile colorimetric chemosensors for the detection of sub ppm levels of amines in solutions, on solid supports and as vapours (**Figure 2.9a-d**).[133] The sensing mechanism of the system follows the general design and synthesis principle of DASAs, thus when a nitrogen nucleophile is present, it reacts with the MAF (or BAF), and the DASA photochromic compound is formed in its triene state, which is highly coloured. The detection limit is less than 1 ppm, making it among the most sensitive, all organic, colorimetric tests for amines to date.[133] The system is conveniently selective for primary and secondary amines in the presence of competing nucleophiles, hence the method can be useful as stains for TLC, monitoring of peptides for solid-phase synthesis, peptidomimetics, food spoilage applications and drug detection.

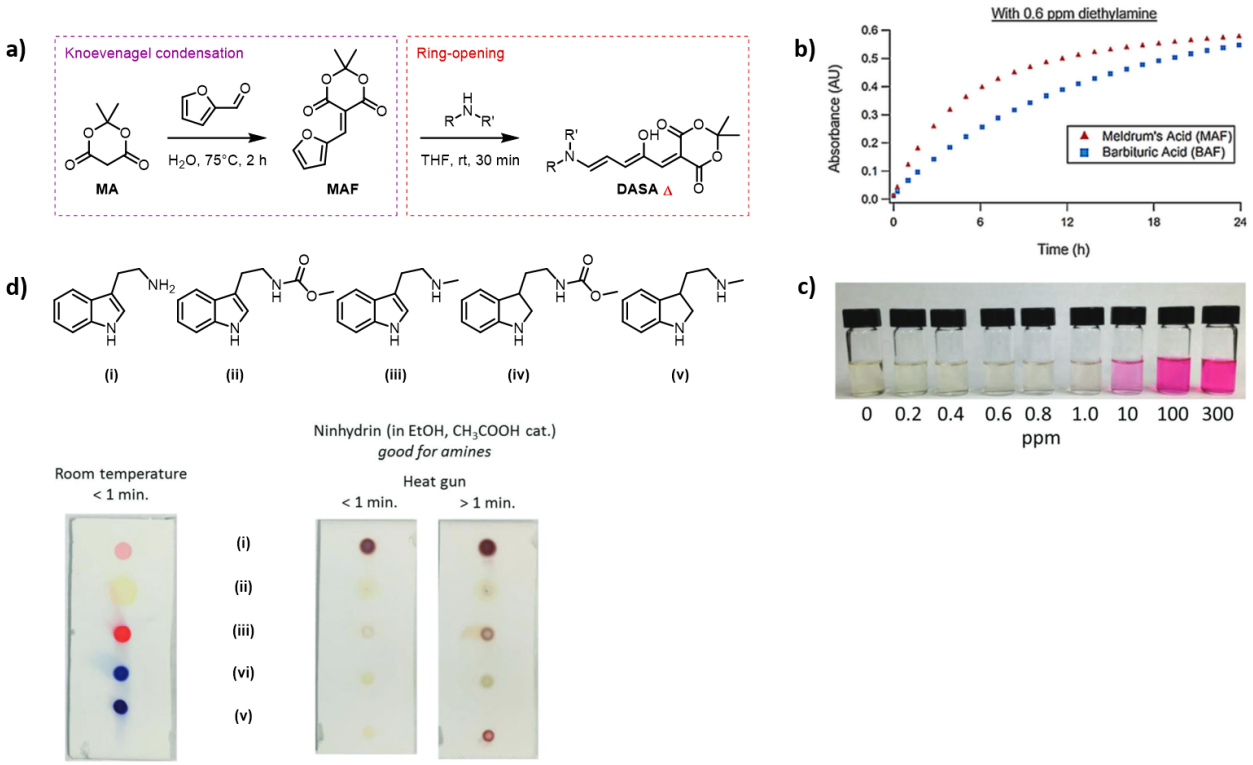

Figure 2.9. *Colorimetric chemosensing of 1° and 2° amines with activated furans utilizing the donor-acceptor Stenhouse adduct (DASA) synthetic route. a) DASA synthesis. b) Comparison of acceptors with respect to their response to diethylamine (monitored in THF at 532 nm). c) DASA formation in ppm visible to the naked eye. d) TLC stain developed from this method demonstrated with compounds* ***i-v*** *and comparison to conventional ninhydrin staining. Adapted and merged from M. Lerch et al.*[124] *and Y. Diaz et al.*[133]

2.4 METHODS TO REDSHIFT ABSORPTION SPECTRA

Circumventing the need for UV light irradiation to drive photoisomerization and thereby switching events, is of immense value to reduce undesirable radiation damage from occurring, and to increase applicability. One viable strategy involves indirect photoexcitation via energy transfer from triplet photo-sensitizers.[47] The sensitizer absorbs photons at higher wavelengths, and thus drives photoisomerization of the switch through (non)trivial energy transfer. Another method employs indirect excitation via photoinduced electron transfer from a sensitizer, thereby driving isomerization through (photo)redox catalytic cycles.[47] The most direct approach, however, is through appropriate HOMO-LUMO gap engineering with the purpose of redshifting the absorption profile of the photochromic compound to the far end of the visible or NIR region of the electromagnetic spectrum.[43,47] This may be achieved either by extending the π conjugation of the system, and/or through strengthening of the push-pull system by introducing donor/acceptor substituents across the isomerizable bond(s).

2.4.1 EXTENDING π-CONJUGATION & PUSH-PULL SYSTEMS

Atomic p orbitals can be combined either in phase or out of phase to create new molecular orbitals (MOs). The new MOs will be lower and higher in energy depending on the bonding character (bonding vs. antibonding) and the number of nodes, a region of space around a nucleus where the probability of finding an electron is zero (**Figure 2.10**).

In the example of ethene with only one π bond, two atomic p orbitals have combined to create two new MOs denoted π_1 and π_2^* (**Figure 2.10**). One is lower in energy (π_1), because its lobes are in phase resulting in constructive interference of the wave functions, and thereby a MO that is bonding in character. The other is higher in energy (π_2^*), because its lobes are out of phase giving rise to destructive interference and a node, which results in a MO that is antibonding in character. Antibonding MOs are marked with an asterisk. The two π electrons are placed in the lowest MO according to the *aufbau* principle. The s orbitals are excluded for simplicity and are often ignored in photochemical events. Following the same principle, the MO energy level diagram of butadiene is made up from four atomic p orbitals that is combined to create four MOs housing four π electrons. A stabilizing effect occurs from extending the π conjugation of the system, due to delocalization of the π electrons across the entire π system. Accordingly, two bonding MOs in addition to two antibonding MOs results, where two are lower and two are higher in energy when compared to the highest occupied molecular orbital (HOMO) and lowest unoccupied molecular orbital (LUMO) of ethene.

In like manner, MO energy level diagrams of higher order polyenes such as octatetraene can be created, and it becomes clear that the HOMO-LUMO energy gap is being correspondingly lowered. The difference in energy between the frontier MOs (HOMO and LUMO) translates to the minimum energy needed to excite the system by promotion of an electron from the ground state (S_0) to the first excited state (S_1). Excitation partly breaks the π bond and thus allows a compound to isomerize via a non-thermal process. Therefore, the more extended a π conjugated system, the smaller the energy transition between the HOMO and the LUMO, and hence the longer the wavelength of light absorption (redshifting) given the

inverse proportionality between the energy of a photon (E) and its wavelength (λ) from the Planck-Einstein relation.

Push-pull systems facilitate another method to tune HOMO-LUMO energy gaps to redshift absorbance. Introducing an electron-donating group (EDG) and/or an electron-withdrawing group (EWG) in conjugation with the π system of a chromophore creates an electronic push-pull effect, where charge from the donor is delocalized into and across the π system to the acceptor. Hence, the π conjugated system acts as a bridging unit between the push and the pull electronic effect. Typically, a dialkylamine substituent is installed as the EDG, while a nitro substituent serves well as the EWG. The contributing high energy level HOMO and low energy level LUMO p orbitals of the donor and acceptor respectively, not only extend π conjugation, but also minimize bond length alternation of the system. Furthermore, increasing the charge transfer (CT), and thereby the strength of the push-pull system, leads to an increase in the degree of frontier MO localization. Consequently, the HOMO/LUMO energy gap is lowered and a redshift in absorbance is observed. Both the length of the conjugation pathway between the donor and acceptor, and their relative positioning determines the magnitude of the bathochromic shift, thus it is worth considering these when designing a photoswitch.

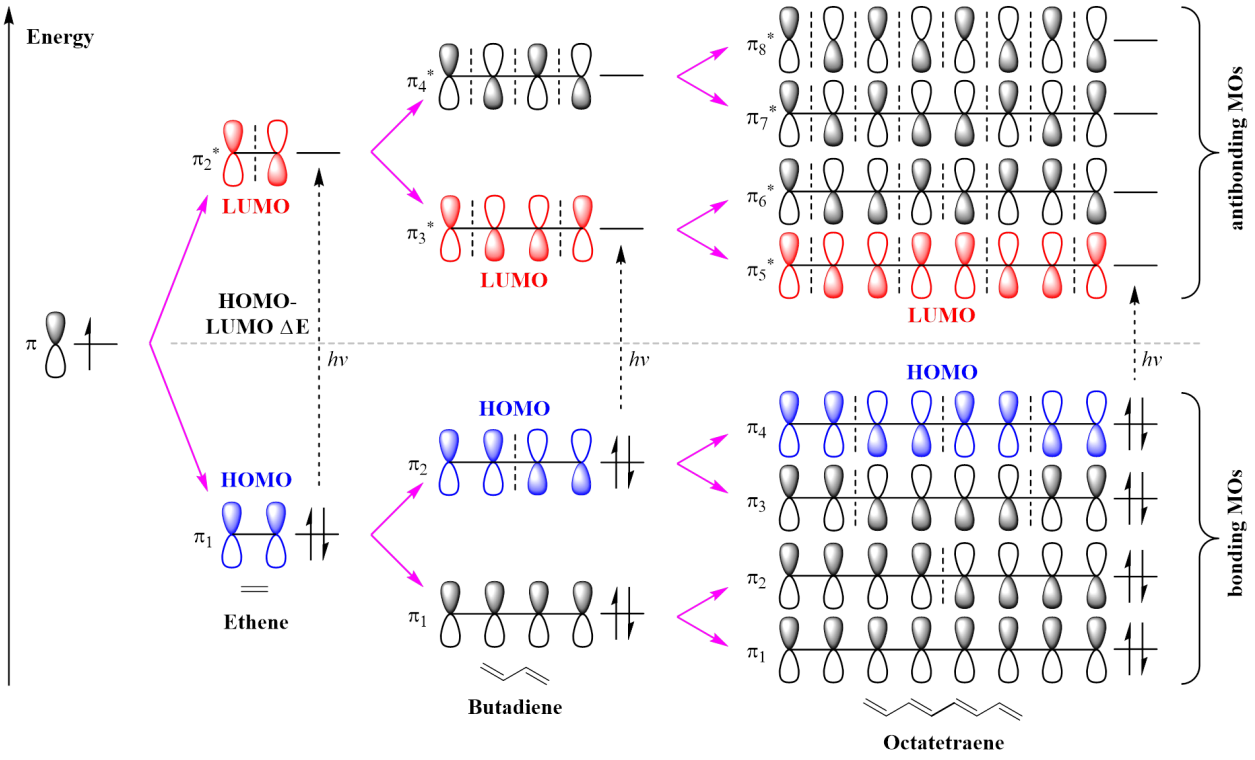

Figure 2.10. Schematic representation of the molecular orbital (MO) energy level diagrams showing only the p-orbitals belonging to ethene, butadiene and octatetraene. The energy (gap) to promote (excite) an electron from the highest occupied molecular orbital (HOMO) in blue to the lowest unoccupied molecular orbital (LUMO) in red is reduced for systems with more extended π conjugation.

3. REDSHIFTED HEMITHIOINDIGO PHOTOSWITCHES

Many photochromic compounds as discussed and highlighted (*vide supra*) unfortunately require illumination with UV light for its photoisomerization in at least one switching direction, which likely affects both addressability and reliability of the photoswitches negatively. It is of special importance in photo-pharmacology as soft material readily degrades by low wavelength radiation. In addition, long wavelength light travels further, and hence redshifting the absorbance allows activation of photoswitchable pharmaceuticals to take place in deeper lying tissue increasing applicability. However, redshifting the absorbance of a system as outlined (*vide supra)* often comes at the cost of a lowered thermal stability and at times efficiency, due to lowered thermal barrier of the metastable isomer and overlapping transition bands used to induce isomerization, respectively. Furthermore, complexity of the synthesis is likely to increase making it challenging and time consuming to investigate new analogues. Solubility of the photoswitch, especially in aqueous solutions, may also decrease dramatically per virtue of introducing further π-conjugation, as rigidity and planarity tend to cause aggregation. Therefore, replacing carbon atoms with heteroatoms, or installing adequate donor-acceptor substituents may alleviate or counter these effects. Additionally, *in silico* modelling is a convenient tool, and more or less standard practice today, to aid predictions of molecular tailoring worth pursuing with the aim of redshifting the absorbance while maintaining thermal bistability. Altogether, it is no straightforward task to redshift the absorption wavelength of photochromic compounds without severely affecting other key properties like absorption band separation, half-life or pharmacological properties. Redshifted bistable photoswitches are however, in high demand, and their development may give a vital push in the field from tool compounds and proof-of-concept to photoswitchable pharmaceuticals.

3.1 BACKGROUND

Many classes and families of photoswitchable compounds have already undergone extensive theoretical and experimental studies with several aimed at extending the absorption spectra towards the red or NIR region of the electromagnetic spectrum.[125]

With regard to HTI-based photoswitches, studies investigating the effects of introducing electron withdrawing and donating substituents in conjugated positions to the π system was performed by Dube *et al.* (2014 and 2017).[58,61] The authors thereby created push-pull frameworks displaying increased bathochromic shifts depending on the strength of the donor and its position in the thioindigo and stilbene fragment (**Figure 3.1a**-**b**). In the first generation of HTI substrates, both the *ortho* and *para* position of the stilbene fragment were investigated with a series of donor substituents varying from the weak *para* methyl (not included in the figure) to the strong *para* dimethylamine substituent (**5**) (**Figure 3.1a**).[58] This resulted in $\pi\pi^*$ transition bands (S_0-S_1) with absorption maxima that were increased from 433-457 nm to 484-513 nm with good QYs 5-23% (**Figure 3.1a**, **1**-**5**). Strong donor substituents led to smaller HOMO-LUMO excitation energies through stabilization of the first excited state (S_1), albeit the effect was smaller for *ortho* substitutions. Additionally, a julolidine HTI derivative (**6**) where the phenyl moiety of the stilbene fragment was replaced, generated the most redshifted and efficient photoswitch in the series (*Z* isomer: 514 nm, QY: 20%; *E* isomer: 545 nm, QY 33%).

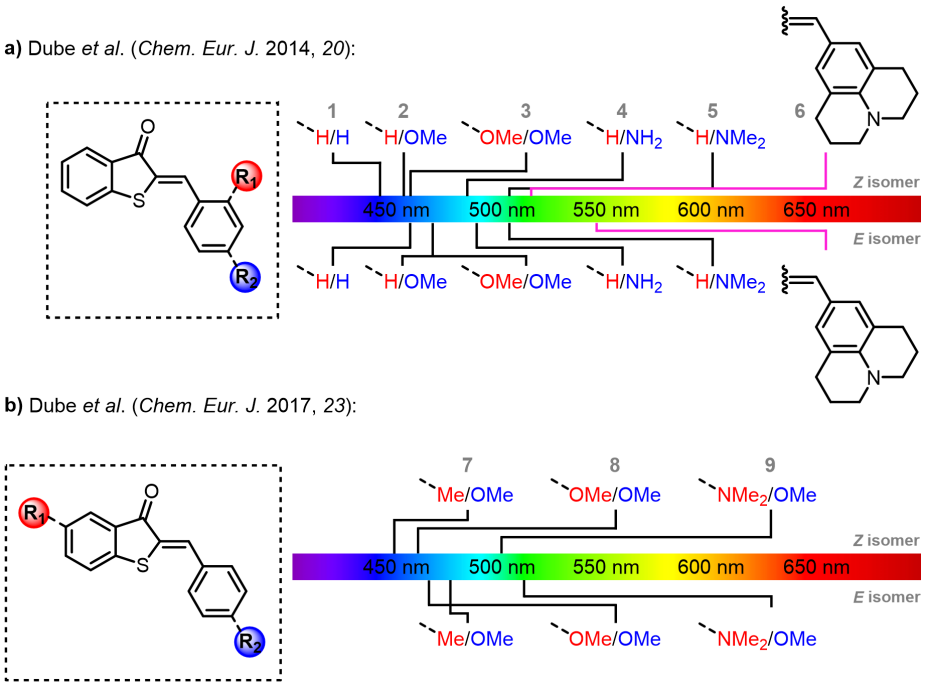

Figure 3.1. *Introduction of electron withdrawing and donating substituents in conjugated positions of hemithioindigos (HTIs) to create a push-pull system and extend the absorption spectra towards the red region of the electromagnetic spectrum. Wavelength of maximum absorption (S_0-S_1 transition) recorded in CH_2Cl_2 from Dube et al.*[58,61]

Interestingly, the rate of photoisomerization in both switching directions was shown to increase with respect to the strength of the donor substituent (up to a limit), following a Hammett correlation study.[58] However, a rate limit was observed in which the trend reversed with stronger donors than the *para* amino substituent (**4**). Hence, the rate of photoisomerization decreased from 2.4 ps to 29 ps when strong electron donors such as the dimethylamine (**5**) or julolidine (**6**) were introduced into the *para* position of the stilbene unit. The second excited state (S_2) is strongly polarized with positive charge distribution in the stilbene fragment. Donors in the *para* position of the stilbene, thus lowers the barrier (crossing point) between the (S_1 → S_2) excited states, resulting in accelerated photoisomerization with a conical intersection from the S_2 excited state. However, for very strong donors (**5**-**6**), the (S_1) excited state is concomitantly stabilized, and the absorption is therefore redshifted, albeit with slower kinetics, due to a higher barrier between the (S_1 → S_2) excited states.

The observed changes in excitation energies is a consequence of a significantly altered charge distribution in the first optically accessible excited state (S_1).[58] The HOMO-LUMO orbitals are distributed over the whole molecule for weak electron donating substituents with little to no LUMO contribution at the sulphur atom (**1**-**3**). For strong donors (**4**-**6**), the HOMO and HOMO-1 orbitals mix and become localized at the stilbene and thioindigo fragments, respectively. Hence, a charge separation from the localized HOMO to the delocalized LUMO is induced when strong donor substituted HTIs are excited, resulting in a stabilizing effect of the (S_1) excited state. The electron density shifts from the stilbene to the thioindigo fragment. The

thermal bistability is, however, simultaneously lowered significantly (half-life of **6** = 9 min), due to the thermal energy barrier decreasing from >26 kcal/mol (**2**) to <22 kcal/mol (**6**). This essentially renders derivatives with strong electron donor capacity in the *para* position of the stilbene non-ideal.[61]

In a second generation of redshifted HTIs, the thermal bistability problem was circumvented by introducing electron donating substituents at the *para* position to the sulphur atom in the thioindigo fragment while maintaining the methoxyl in the stilbene (**Figure 3.1b**).[61] The thermal energy barrier remained high (>25.7 kcal/mol) with half-lives of days to 1 month. The ineffective electronic communication with the isomerizable double bond by the thioindigo donating substituents prevented it from affecting the thermal isomerization, thus the intrinsic high thermal barrier that HTIs possess was preserved. While the weak methyl donor (**7**) in this series did not produce a noticeably redshift in absorption, the strong dimethylamine donor (**9**) afforded a large bathochromic shift (43-47 nm) with an absorbance close to and above 500 nm. The strength of the donor, however, also displayed a negative trend in molar extinction coefficients for the HTI derivatives (**7**-**9**). Additionally, the authors exploited the basic amine of (**6**) to develop a molecular digital information processing system, where protonation was used as a second input to alter the responsiveness of the switch to light.

Dube *et al.* demonstrated the effectiveness of the push-pull strategy in redshifting the absorbance of HTI-based photoswitches into the green region of the visible spectrum, while maintaining thermal bistability.[58,61] Furthermore, the strength of the electronic donating substituent in the *para* position of the stilbene fragment was observed to greatly influence both thermal stability in conjunction with the photoisomerization kinetics.

Newhouse *et al*. (2017) expanded the push-pull strategy with structural modifications to the HTI scaffold that further included extending the π conjugation of the system (**Figure 3.2a**-**b**).[136] Replacing the phenyl group of the HTI core with a series of aromatic heterocycles produced large bathochromic shifts (absorbance >500 nm) (**Figure 3.2a**). In addition, it was discovered that the electron rich pyrrole (**14**), capable of making an intramolecular hydrogen bond to the benzothiophenone ketone in its *E* isomer, resulted in selective and quantitative photoisomerization (PSS >97%) of either isomer with a large band separation (>40 nm). This hydrogen bond was expected to stabilize the LUMO leading to a smaller HOMO-LUMO energy gap in the *E* isomer, thus increasing band separation. The intramolecular hydrogen bond is supported by theoretical calculations, reductions in stretching frequencies by IR and from the observations that neither thiophene nor furan displayed high band separations (<20 nm). Furthermore, the *Z* to *E* isomerization of a nitrogen methylated analogue of (**14**) could not be observed by UV-Vis spectroscopy, presumably due to a steric clash between the methyl and the ketone, which disfavoured relaxation from the excited state to the *E* isomer.

A second series of structural modifications, where the π conjugation of the system was extended by arylation in the 5'-position of the pyrrole, further redshifted the absorbance (488-613 nm) and increased band separations (59-67 nm) while maintaining near quantitate PSS (>88%) for most of the HTIs (**15**-**18**) (**Figure 3.2a**). The julolidine analogue (**18**) displayed absorbance into the red region (670 nm) of the visible spectrum, however, the thermal half-life was only 0.3 hours at 80°C with a low PSS for the reverse photo-isomerization (62%). In addition, the reliability for the most redshifted compounds in the series (**17**-**18**) was not exceptional, and displayed photobleaching with significant loss of absorbance (1-5%) per cycle.

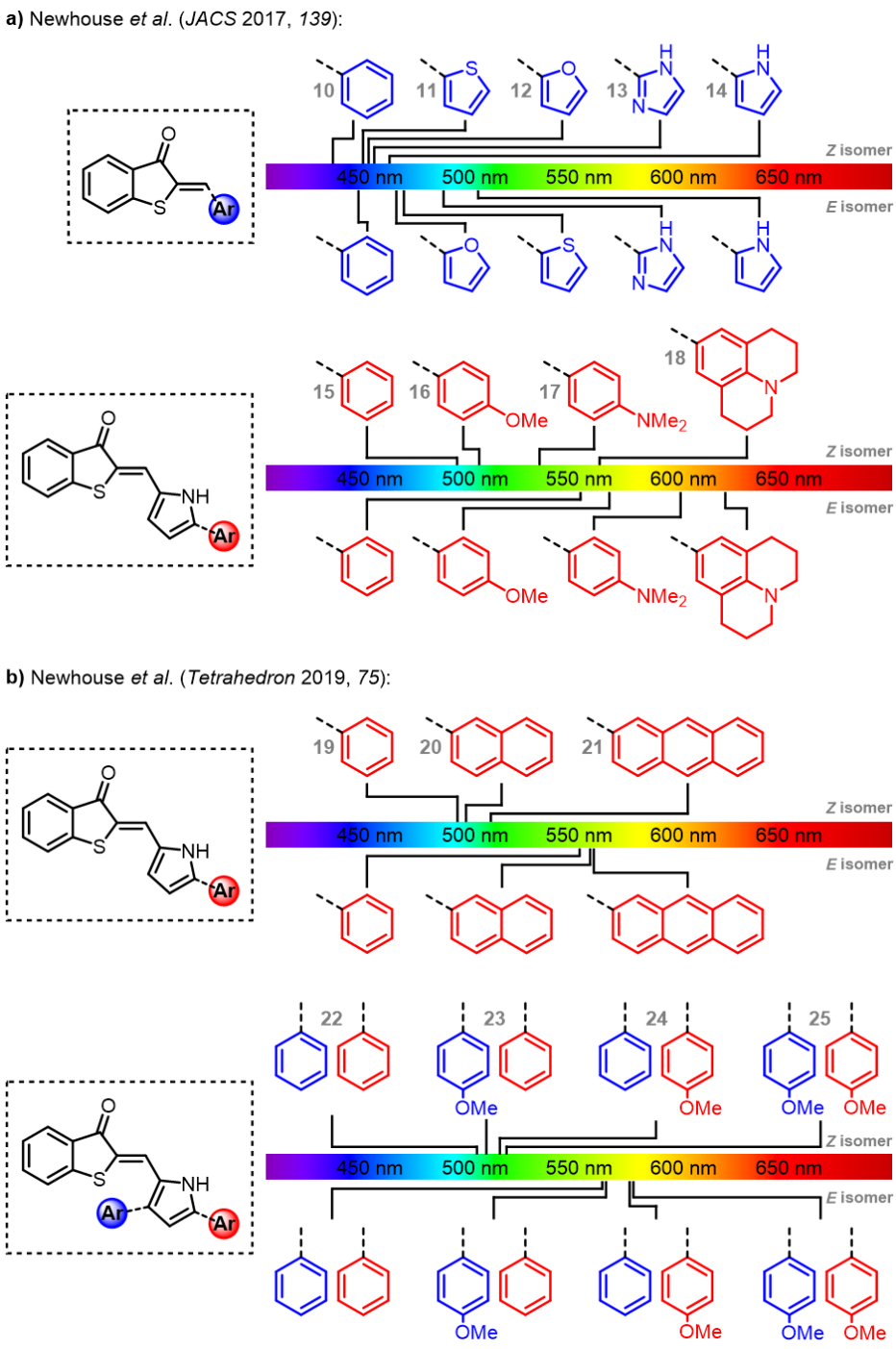

Figure 3.2. *Extension of π conjugation and introduction of electron donating substituents in conjugated positions in hemithioindigos (HTIs) to create a push-pull system and extend the absorption spectra towards the red region of the electromagnetic spectrum. Wavelength of maximum absorption (S_0-S_1 transition) recorded in CH_2Cl_2 from Newhouse et al.*[136,137]

Subsequently, Newhouse *et al.* (2019) reported a study addressing the reliability concerns resulting from the electron rich amino substituted HTI substrates.[137] Hence, a second generation of compounds were synthesized and evaluated varying the 5-position of the pyrrole with increasingly extended π conjugated systems in order to redshift the absorbance (**Figure 3.2b**). The distinct trend followed that the more extended systems afforded the most redshifted spectra, which was in line with the expected.

The 2-naphthyl analogue (**20**) displayed a 4-5 nm bathochromic shift, whereas the 2-anthracenyl analogue (**21**) resulted in a 6-16 nm increase in absorption maxima compared to the 5'-phenyl derivative (**19**). Interestingly, the shorter end-to-end 1-naphthyl and 9-antracenyl analogues (not included in the figure) exhibited hypsochromic shifts to shorter wavelengths than the 5'-phenyl derivative (**19**). The HTI-based photoswitches in the series displayed redshifted spectra (*Z* isomers: 491-507 nm, *E* isomers: 550-556 nm), albeit with a slightly worse PSS (88%) when the π system was extended with an anthracene (**21**).

Therefore, another series of compounds exploring 3,5'-diaryl substituted pyrroles were prepared with electron donating methoxy groups in the *para* positions of the aryl moieties (**22**-**25**) (**Figure 3.2b**). This afforded bathochromic shifts of 24-26 nm for the methoxy substituted 3,5'-diphenyl analogue (**25**) when compared to the 5'-phenyl derivative (**19**). The 3,5'-diaryl substituted pyrroles (**22**-**25**) were also considerably more soluble in organic solvents, and allowed for convenient observation and quantitation of the photoisomerization via ^{1}H NMR spectroscopy. Selective photoisomerization in both directions with blue and amber light was achieved (PSS >95%)

Compounds with 4,5'-diaryl substituted pyrroles were also investigated, but provided poor properties. Out-of-plane steric distortion between the groups led to slightly diminished conjugation, while computational studies only observed minimal LUMO coefficients on the 4'-aryl groups, suggesting that this position is electronically isolated from the system.

Pyrrole HTIs are very efficient photochromic compounds, due to an intramolecular hydrogen bond induced by the proximity of the pyrrole NH of the *E* isomer to the ketone. Furthermore, it is evident from the results by Newhouse *et al.* that extending the π conjugation of the system is a viable strategy to obtain even larger bathochromic shifts.[137] In combination with electron donating substituents, HTI-based photoswitches having absorption profiles in the yellow to red region of the electromagnetic spectrum were developed, which is a great achievement for pushing applicability of HTIs as photoswitchable pharmaceuticals in the future.

3.2 PROJECT OUTLINE

Although impressive studies have been reported that accomplished sufficiently redshifted absorption spectra to enable red and near-infrared light photoisomerization of hemithioindigo-derived photoswitches, decoupling the affected thermal stability and reliability is still an unsolved issue.

Therefore, to address this issue and close the current gap to see hemithioindigos employed with higher chance of success in various applications including biological, we aimed at exploring the effects resulting from phenyl-fused π-extension of the parent hemithioindigo. In a systematic approach, we want to evaluate the effects in both directions of the scaffold, as this has not been investigated before (Scheme 3.1). Extending the π-system results in a decreased HOMO-LUMO energy gap and consequently an increase in excitation wavelength. Accordingly, photoswitching may be facilitated with lower-energy light, which benefits the surrounding material that experience non-selective radiation damage. Furthermore, following the recent discovery of the promising pyrrole-substituted hemithioindigo, it would be interesting to adopt the same strategy with this alternative scaffold to give access to new redshifted photoswitches encompassing quantitative photoisomerization, while displaying high thermal stability and reliability (Scheme 3.1).

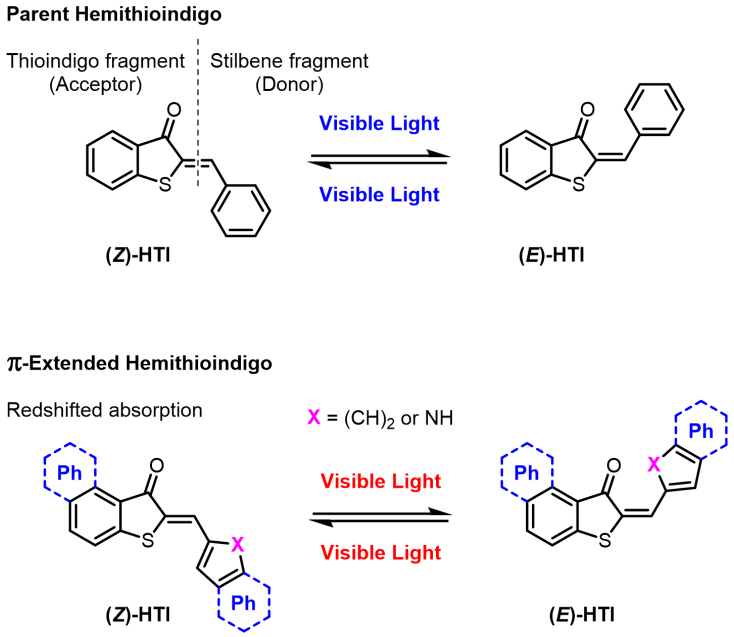

Scheme 3.1. *π-Extension of the hemithioindigo and pyrrole-substituted hemithioindigo scaffold to achieve redshifted photoswitches.*

3.3 MANUSCRIPT

The following section contains the photoswitch project written as a manuscript-based chapter.

Programmable Synthesis of Redshifted and Thermally Bistable One-Way Quantitative Hemithioindigo-derived Photoswitches Enabled by Isomer-Specific Excited State Intramolecular Proton Transfer

Mikkel Krell-Jørgensen, Habiburrahman Zulfikri, Magnus Grage Bonnevie, Asmus Ougaard Dohn and Luca Laraia

Abstract: Hemithioindigo (HTI)-derived photoswitches have recently emerged as a promising class of *E*/*Z*-type photoswitches with potential applications in photopharmacology, optical data storage, and as molecular machines. However, drawbacks currently include low thermal stability, photobleaching and the ability to tune the directionality and reversibility of the isomerisation. By systematically extending the π-conjugation in both the thioindigo and stilbene fragment of the HTI scaffold, we identified bistable indole-containing HTIs with one-way quantitative photoswitching properties, in addition to a thermally bistable bipyrrole-containing HTI, which displays large band separation and bidirectional near-quantitative photoisomerization in the near-infrared window. Supported by state-averaged CASPT2/CASSCF calculations, we propose a mechanism for the observed one-way photoswitching that involves an isomer-specific excited state intramolecular proton transfer (ESIPT). These results have significant implications in the design of HTI-based photoswitches as low energy light can be employed to facilitate selective light-induced isomerisation without the concerns of either photobleaching or photodegradation of the surrounding material in an application.

1. Introduction

Molecular photoswitches comprise a class of photochromic compounds able to interconvert reversibly between configurational isomers when subjected to light of appropriate wavelength. This photoisomerization reaction allows access to (functional) isomers that often display large changes in structural geometry and photochemical properties including distinctive absorption spectra. For this reason, they have received considerable attention in the preceding decade with potential applications in drug-delivery and photopharmacology,[18,43,48,55,138] optical data[139,140] and solar thermal energy storage systems,[23,24] guest-host complexes[27,141,142] and as molecular machines[33,35,64] to name a few. However, most photoswitches require low wavelength irradiation to initiate excitation and drive photoisomerization events in at least one switching direction, which results in undesirable and non-selective radiation damage of the surrounding material.[47] Therefore, a viable strategy involves appropriate HOMO-LUMO gap engineering with the purpose of redshifting the absorption profile to allow activation within the phototherapeutic window (650-900 nm).[143] Furthermore, long wavelength irradiation provides the additional advantage of enhanced tissue penetration, and hence, a more comprehensive control of photoswitchable pharmaceuticals with a broader scope of applications.[144]

Hemithioindigos (HTIs) are an exceptional family of *E*/*Z*-type photoswitches that intrinsically display fast and fatigue resistant photoisomerization, high thermal bistability and importantly strong visible light absorption for both isomeric states.[16] In addition, the large change in structural geometry and end-to-end distance induced by the *E*/*Z* photoisomerization can be exploited to gain photoresponsive control of material properties and biological functions as illustrated for other *E*/*Z*-type photoswitchable families.[43,145] Accordingly, these properties make hemithioindigos very attractive candidates for phototherapeutics if the absorption spectra can be redshifted into the highly sought-after phototherapeutic window.

The initial efforts of developing redshifted hemithioindigo photoswitches relied on push-pull frameworks with strong electron donating groups, but suffered from poor thermal bistability down to minutes besides reduced efficiency as the strength of the electron donor was increased.[58,61] The more promising recently developed hemithioindigos with arylpyrrole moieties replacing the phenyl group of the stilbene fragment allowed an isomer-specific intramolecular hydrogen bond (IHB) between the pyrrole N-H and the thioindigo ketone to facilitate selective and quantitative photoisomerization.[136,137] However, further redshifting by increasing the size of the aryl group through extension of the π-system in the 5' position of the pyrrole or electron donating ability similarly resulted in decreased thermal barriers with half-lives down to a few hours or minutes and with slightly decreased efficiency for the $E \rightarrow Z$ photoisomerization.[136] Furthermore, the reliability for these compounds were suboptimal displaying photobleaching with significant loss of absorbance (1-5%) upon repeated irradiation.[136] Although considerable contribution in generating selective and bidirectional fully-visible (green-red) light switching of hemithioindigos in either direction has already been carried out, a further redshifting of the absorption spectra, especially for the $Z \rightarrow E$ direction, is still of high value. For photoswitchable therapeutics, it is ideal to have selective light-induced activation within the phototherapeutic window. Key challenges that remain includes decoupling the affected thermal stability and reliability that concurrently transpire when redshifting the absorption spectra.

Herein, we report the effects of systematic phenyl-fused π-extension in both directions of the parent hemithioindigo, which led to the discovery of redshifted and thermally bistable hemithioindigo photoswitches, in addition to one-way quantitative indole-containing hemithioindigos enabled by an unexpected isomer-specific excited state intramolecular proton transfer. Additionally, a thermally bistable bipyrrole-containing hemithioindigo, which displays bidirectional near-quantitative photoisomerization using near-infrared light (660 nm) in solvents with a wide range of polarities, is reported as a new viable strategy towards photoswitchable therapeutics based on the hemithioindigo scaffold.

2. Results and Discussion

2.1 Syntheses of photoswitches

A programmable bathochromic shift was predicted in response to systematic phenyl-fused π-extension of the parent hemithioindigo scaffold. This approach to redshift the absorption profile rely on a decreased HOMO-LUMO energy gap (typically $S_0 \rightarrow S_1$ transition for HTIs) through increased delocalized stabilization of π-orbitals in the molecule. To adequately evaluate the effect, we decided to extend the system in both the stilbene and thioindigo fragment. Three series of compounds comprising nine HTI analogues (**10**-**18**) in total (Scheme 3.2) were prepared in two-five synthetic steps from cheap readily available starting materials using previously reported methods[136,137,146–148] (see Support Information). Substitution of arylthiols **1**-**2** with 2-bromoacetic acid afforded the corresponding arylthioacetic acids **3**-**4**. Subsequently, intramolecular Friedel-Crafts type acylation catalysed by triflic acid to initiate ring-closure, allowed access to thioindigo building blocks **5**-**6** in good yields (57-85% over two steps). To our surprise, the non-linear fused regioisomer **5** obtained. It was decided to continue with the non-linear derivative as trends could be explored just as successfully. Coupling with various aldehydes via aldol condensations catalysed by piperidine resulted in the corresponding HTI photoswitches **10**-**18** in varying yields (26-88%). Bipyrrole aldehyde **9** was the only non-commercially available aldehyde that had to be prepared. This was accomplished in two synthetic steps via PIFA-mediated oxidative homo coupling of pyrrole **7** to give bipyrrole **8** (39% yield) following a Vilsmeier-Haack formylation under stoichiometric control to afford aldehyde **9** (29% yield).

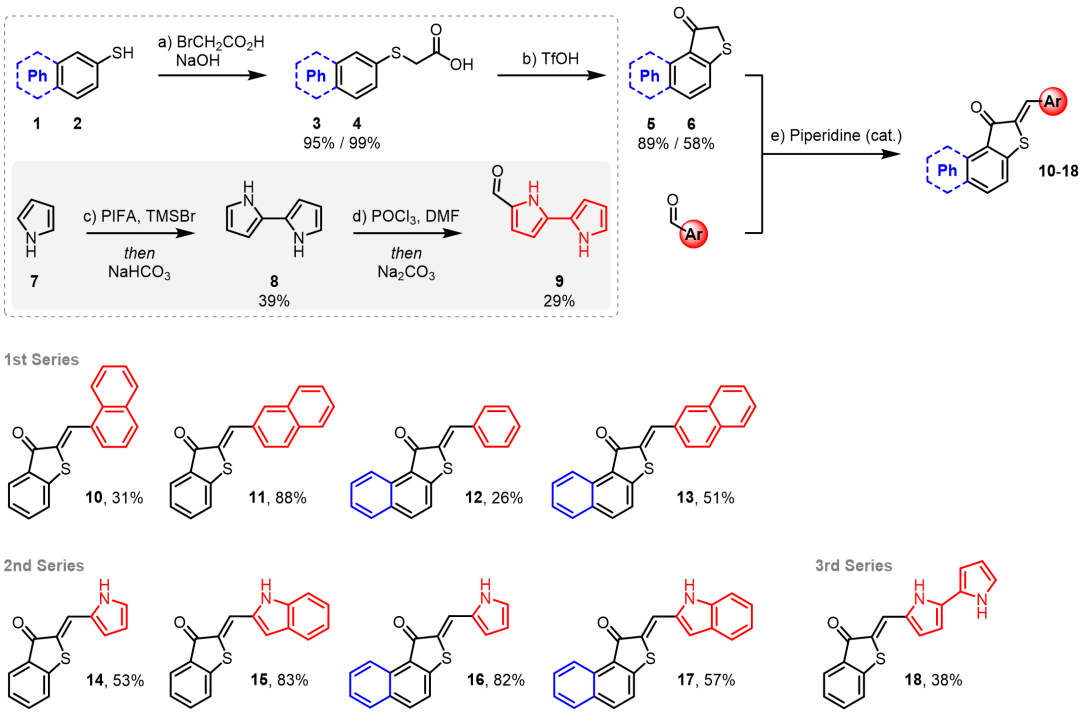

***Scheme 3.2**. Overview and synthesis of π-extended hemithioindigo analogues to enable redshifted absorption profiles. PIFA = phenyliodine(III) bis(trifluoroacetate), TfOH = trifluoromethane sulfonic acid.*

2.2 Evaluation of 1st series photoswitch properties

Supported by initial time-dependent density-functional theory (TDDFT) calculations, we expected a redshifted trend in response to the size of the π-system when substituting either phenyl moiety in the parent unmodified hemithioindigo with a naphthalene (Figure 3.3). The parent HTI displays low wavelength absorption maxima (λ_{max}) of 433/444 nm (*Z*/*E*-isomer) in DCM.[136] As anticipated, separate substitution of phenyl moieties led to noteworthy changes in absorption maxima of analogues **10**-**12** when compared to the parent HTI (Figure 3.3). The larger end-to-end analogue **11** showed favourable photochemical properties compared to its regioisomer **10**, which is why we decided to continue with substitution in the 2-position. Interestingly, extension of the thioindigo fragment in **12** (scaffold B) compared to the stilbene fragment in **10**-**11** (scaffold A) afforded absorption maxima, which are significantly more redshifted (Figure 3.4). The band separation was likewise increased, but it did not translate into improved photostationary state selectivity. The experimentally observed redshifted trend in the first series of analogues is apparent by further installing naphthalenes in place of both phenyl moieties in parallel manner to give analogue **13** with absorption maxima (λ_{max}) of 461/467 nm (*Z*/E-isomer). This is a remarkable increase of 23-28 nm when compared to the absorption maxima of the parent hemithioindigo photoswitch. Furthermore, all analogues in this series displayed excellent bistability with thermal half-lives of the metastable isomers in the orders of days to months. However, the redshifted absorption came at the cost of reduced photostationary state selectivity with minimal band separations. In addition, further extension of the catacondensed polycyclic hydrocarbon system would likely impose solubility issues prompting the need to install solubilising groups to counteract the effect and overall result in complex syntheses.

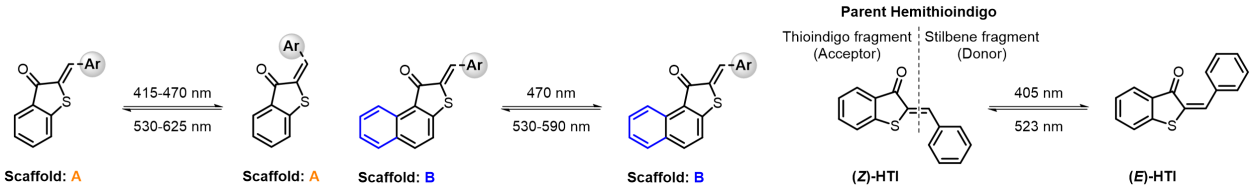

Cmpd	Scaffold	Ar	λ_{max}	$\Delta\lambda$	ε (molar abs)	λ_{max} (calcd)	$\Delta\lambda$ (calcd)	f (calcd)	PSS [light source]	$T_{1/2}$ (half-life)
10	A		447 nm (Z) 450 nm (E)	3 nm	11170 $L \cdot mol^{-1} \cdot cm^{-1}$ (Z) 4697 $L \cdot mol^{-1} \cdot cm^{-1}$ (E)	450 nm (Z) 484 nm (E)	34 nm	0.29 (Z) 0.17 (E)	86% E [470 nm] 86% Z [530 nm]	8.6 days
11	A		445 nm (Z) 451 nm (E)	6 nm	17496 $L \cdot mol^{-1} \cdot cm^{-1}$ (Z) 10385 $L \cdot mol^{-1} \cdot cm^{-1}$ (E)	441 nm (Z) 479 nm (E)	38 nm	0.36 (Z) 0.22 (E)	82% E [415 nm] 96% Z [530 nm]	50 days
12	B		451 nm (Z) 460 nm (E)	9 nm	7188 $L \cdot mol^{-1} \cdot cm^{-1}$ (Z) 4412 $L \cdot mol^{-1} \cdot cm^{-1}$ (E)	456 nm (Z) 481 nm (E)	25 nm	0.12 (Z) 0.08 (E)	77% E [470 nm] 89% Z [530 nm]	>63 days
13	B		461 nm (Z) 467 nm (E)	6 nm	11661 $L \cdot mol^{-1} \cdot cm^{-1}$ (Z) 7327 $L \cdot mol^{-1} \cdot cm^{-1}$ (E)	465 nm (Z) 493 nm (E)	28 nm	0.22 (Z) 0.14 (E)	75% E [470 nm] 87% Z [530 nm]	>77 days
14	A		457 nm (Z) 503 nm (E)	46 nm	25770 $L \cdot mol^{-1} \cdot cm^{-1}$ (Z) 21391 $L \cdot mol^{-1} \cdot cm^{-1}$ (E)	449 nm (Z) 476 nm (E)	27 nm	0.48 (Z) 0.32 (E)	96% E [415 nm] 97% Z [530 nm]	>23 days
15	A		468 nm (Z) 516 nm (E)	48 nm	21655 $L \cdot mol^{-1} \cdot cm^{-1}$ (Z) 16991 $L \cdot mol^{-1} \cdot cm^{-1}$ (E)	471 nm (Z) 506 nm (E)	35 nm	0.68 (Z) 0.48 (E)	>99% E [415 nm] 5% Z [530 nm]	>158 days
16	B		478 nm (Z) 513 nm (E)	35 nm	17476 $L \cdot mol^{-1} \cdot cm^{-1}$ (Z) 17676 $L \cdot mol^{-1} \cdot cm^{-1}$ (E)	464 nm (Z) 479 nm (E)	15 nm	0.51 (Z) 0.37 (E)	88% E [470 nm] 74% Z [530 nm]	>55 days
17	B		486 nm (Z) 526 nm (E)	40 nm	25121 $L \cdot mol^{-1} \cdot cm^{-1}$ (Z) 24333 $L \cdot mol^{-1} \cdot cm^{-1}$ (E)	487 nm (Z) 510 nm (E)	23 nm	0.72 (Z) 0.51 (E)	>99% E [470 nm][c] 25% Z [590 nm][c]	41 days
18	A	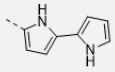	519 nm (Z)[a] 581 nm (E)[a] 537 nm (Z)[b] 589 nm (E)[b]	62 nm 52 nm	27300 $L \cdot mol^{-1} \cdot cm^{-1}$ (Z)[a] 25676 $L \cdot mol^{-1} \cdot cm^{-1}$ (E)[a] 35927 $L \cdot mol^{-1} \cdot cm^{-1}$ (Z)[b] 26733 $L \cdot mol^{-1} \cdot cm^{-1}$ (E)[b]	509 nm (Z) 541 nm (E) 510 nm (Z)[b] 539 nm (E)[b]	32 nm 29 nm	1.02 (Z) 0.64 (E) 1.02 (Z)[b] 0.64 (E)[b]	87% E [470 nm][c] **90% Z [625 nm]**[c]	>10 days

Figure 3.3. *Properties of π-extended hemithioindigo photoswitches (33 μM in CH_2Cl_2). Half-lives in PhMe. [a] THF [b] DMSO [c] ^1H NMR in THF-H_8 with solvent suppression.*

2.3 Evaluation of 2nd series photoswitch properties

We therefore opted to explore the more attractive pyrrole-substituted hemithioindigos known for their redshifted absorption spectra and excellent photostationary state selectivity.[136] Hence, employing the same strategy of fused aromatics in both directions (*vide supra*), we observed significant improvements in photochemical properties for HTI analogues **14**-**17** compared to the first series **10**-**13** (Figure 3.3). It is evident from the experimental observations that the strategy is effective with an observed systematic bathochromic shift between 6-21 nm in **10**-**17** for every phenyl-fused π -extention added to the HTI system (Figure 3.3 and 3.4. The large band separations (35-48 nm) in the second series enabled selective and quantitative photoisomerization to produce the corresponding *E*-isomers. However, the extended pyrrole HTI **16** displayed reduced properties of band separation, molar absorption and photostationary state selectivity. The theoretical oscillator strength and band separation for this analogue were also lower, inline with experiments. Interestingly, extension of the thioindigo fragment in **16** (scaffold B) compared to the stilbene fragment with an indole **15** (scaffold A) afforded significant red-shifting for

Z-**16**, which in contrast was observed for the *E*-isomer in the first series (*vide supra*). However, combined with the observed blueshift for the *E*-isomer, it resulted in the aforementioned decrease in band separation for analogue **16**. The extended indole-substituted HTI **17** displayed absorption maxima (λ_{max}) of 486/526 nm (*Z*/*E*-isomer), which is an impressive 53-82 nm or 23-29 nm redshift compared to the parent HTI and pyrrole-substituted HTI **14**, respectively. It was sufficiently redshifted to allow for photoisomerization with 590 nm orange light. Importantly, thermal stability remained extremely high above 23 days to more than 5 months for analogues **14**-**17**, which for similarly redshifted HTIs in the literature lies in the range of minutes to hours. To our surprise, the indole-containing analogues only displayed quantitative photoisomerization in one direction. Hence, no wavelengths in hand (up to 660 nm light) facilitated backswitching in DCM to produce the *Z*-isomer that could only be realised thermally equivalent to T-type photoswitches (see Section 4, Supporting Information). We therefore performed a solvent screen to investigate if solvent effects were responsible for the observed lack of bidirectional photoswitching (see Section 4, Supporting Information). Six common solvents were selected possessing varying relative permittivity including polar protic and aprotic properties. Both analogues displayed a similar trend with no backswitching observed in any solvent except in iPrOH/DMSO for the less extended indole HTI **15** and in DMSO for the extended indole HTI **17**. However, it required extensive irradiation for more than 60 minutes with 590 nm light as the only effective wavelength to produce any substantial change in absorption spectra. Thus, the thermal stability of both analogous was determined in DMSO to exclude that the specific back isomerization did not result from thermal relaxation as the development of heat from prolonged irradiation likely accelerate this process. A thermal half-life of approximately 78 hours was determined for the less extended indole HTI **15** in DMSO, and therefore did not provide a conspicuous explanation on the nature of the slow back isomerization. The thermal stability was not analysed in iPrOH. In contrast, a thermal half-life of only 112 min was determined for the extended indole HTI **17**, whereby back isomerization could be attributed to thermal relaxation leaving this analogue a one-way quantitative photoswitch. As we were unable to evaluate the extended indole analogue **17** by HPLC, due to slight solubility issues in *n*-hexane/iPrOH mixtures of the *Z*-isomer, we decided to determine the photostationary state selectivity by NMR in THF. Accordingly, the *Z*-isomer was obtained in 25% PSS after prolonged irradiation with 590 nm orange light, which was unexpected given no photoisomerization was observed at low µM concentrations in THF when analysed by UV-Vis spectroscopy. Hence, it appears concentration dependent, while the evolution of heat likely accelerated the rate of thermal isomerization.

2.4 Excited-State Intramolecular Proton Transfer

We hypothesized that an isomer-specific excited state intramolecular proton transfer (ESIPT) between the indole N-H and the thioindigo ketone specific to the *E*-isomer allowed by proximity led to deexcitation, and thereby prevented photoisomerization. Interestingly, the parent indigo, displays ESIPT between the indigo N-H and the ketone preventing photoisomerization of the thermodynamically stable *E*-isomer, which is why indigos are *N*-substituted to mitigate the ESIPT deexcitation pathway and turn them into photoswitches.[37,40,41] To investigate the possibility of an ESIPT event, we sought to theoretical computations where relative electronic energies of the ground state S_0 and bright excited states S_1 and S_2 were calculated at the CASPT2/CASSCF level of theory relative to the O-H bonding distance of the less extended indole HTI **15** as the reference compound (Figure 3.5 and Supporting Information). From these results, we discover that the resultant S_1 coordinate is barrierless with no crossing point

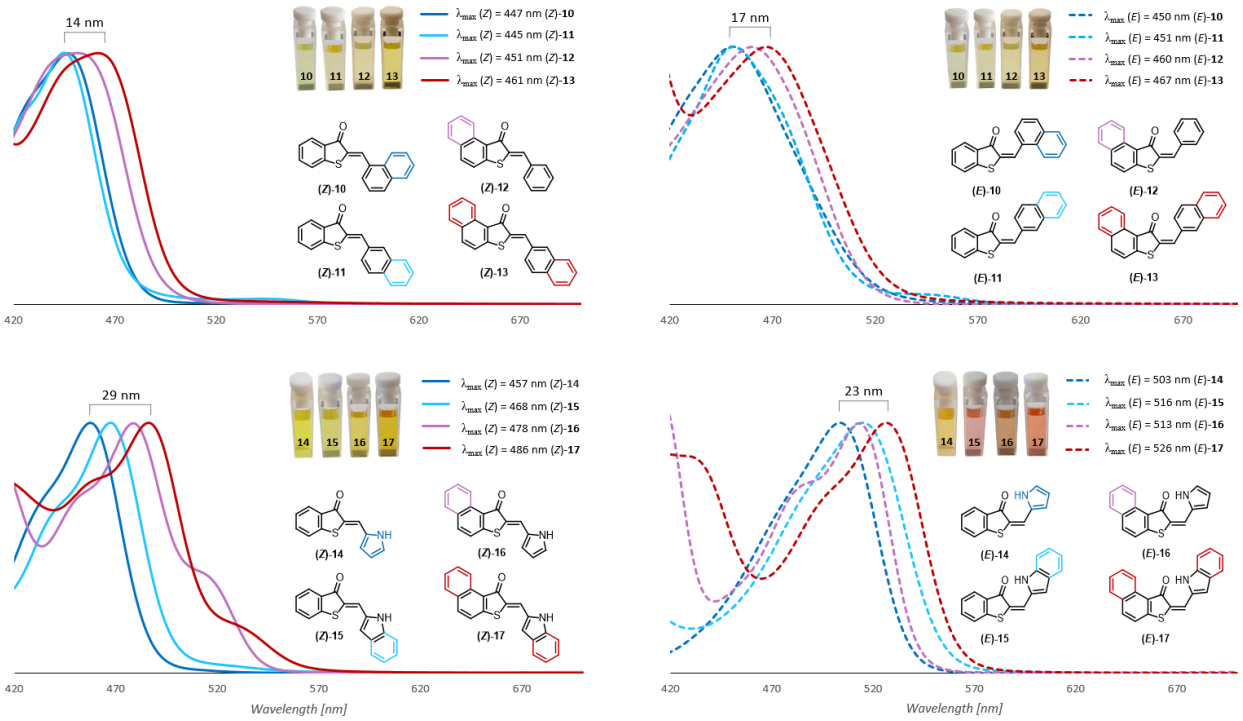

Figure 3.4. *Normalized UV-Vis spectra (33 μM in CH_2Cl_2) displaying the redshifted trend in π-extended hemithioindigo photoswitches visible to the naked eye. Solid lines (Z-isomers). Dashed lines (E-isomers).*

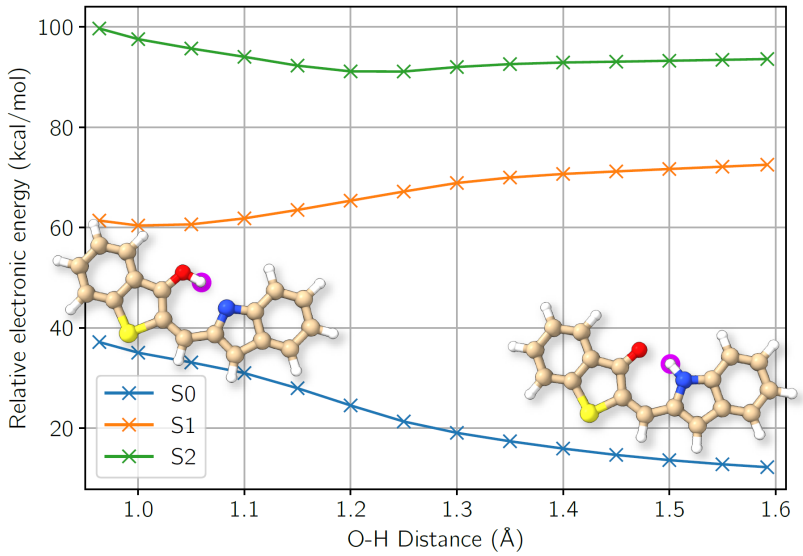

Figure 3.5. *Isomer-specific excited state intramolecular proton transfer (ESIPT) of indole-substituted HTI E-**15** preventing light-induced isomerization to the Z-isomer. Localization of the proton (purple). CASPT2/CASSCF level of theory in the gas phase.*

to the upper and lower states defined. As expected, the relative electronic energy in the ground state S_0 of *E*-**15** is substantially lower for the geometry where the proton is closer to or situated at the indole-nitrogen atom. However, in the first excited state S_1, we observe an energy minimum corresponding to the geometry in which the proton is closer to or situated at the carbonyl oxygen of the thioindigo ketone with a staggering energy difference of 12 kcal/mol when scanning the O-H distance. As it is likely the same event governing the one-way photoswitching property of both indole-containing analogues given their structural and electronic similarity, we predict that an isomer-specific ESIPT with formation of the enol tautomer in the excited state prevents bidirectional photoswitching. Hence, this may explain why polar protic and aprotic solvents like iPrOH, THF and DMSO seem to influence photoswitching of the *E*-isomers. Ground state solvation through hydrogen-bonding interactions may stabilize the proton at the indole-nitrogen that when excited lead to general photoisomerization.

These results have significant implications as indole-containing analogues exhibiting isomer-specific ESIPT can be exploited as a design principle for redshifted and thermally bistable quantitative one-way photoswitches based on the hemithioindigo scaffold. The benefits of such systems resemble that of systems displaying inverse photochromism. Activation to the meta-stable isomer may be induced with light of longer wavelengths allowing enhanced penetration depth into tissue without the concern of reverse photoisomerization affecting the selectivity or damage of the soft material. Interestingly, as these indole-analogues do not exhibit light-induced photoisomerization in both directions and also do not readily relax to the thermally more stable isomer, they can neither be classified as P-type nor T-type photoswitches. Although their slow relaxation may be the only argument to still classify them as the latter.

2.5 Evaluation of 3rd series photoswitch properties

In our continue search to develop redshifted HTIs while maintaining the desired properties of the intramolecular H-bonding that the pyrrole ring provided, we were inspired to develop a new strategy based on conductive pyrrole-containing oligomers. Guided by TDDFT calculations, a 65-69 nm bathochromic shift in absorption maxima (λ_{max}) was predicted for every pyrrole unit added to the pyrrole HTI (see Supporting Information). Furthermore, the oscillator strengths were predicted to increase from below 0.5 to above 1.0 indicating that these systems might be very efficient. However, the theoretical calculations also predicted that the favourable photochemical properties did not follow higher orders of oligomers, as a limit that would see the trend reverse lies somewhere in between that of a tripyrrole and a hexapyrrole-substituted HTI (see Supporting Information). With theoretical computations to support our strategy, a third series comprising only of bipyrrole HTI **18** connected in a 2,2'- fashion was prepared (*vide supra*) and evaluated for its photochemical properties against pyrrole HTI **14** (Figure 3.3). As predicted, we observed a substantial 60-65 nm bathochromic shift in absorption maxima (λ_{max}) from extending the pyrrole to a bipyrrole. In addition, band separations were improved to 50-70 nm depending on the solvent (**Figure 3.6a** and Section 4, Supporting Information). However, the *Z*-isomer of bipyrrole HTI **18** displayed poor solubility in solvents with lower relative permittivity like *n*-Hex, PhMe and DCM, which necessitated pro-longed mixing time. We therefore reported absorption maxima in THF and DMSO, whereas photostationary state selectivity was performed with NMR spectroscopy in THF. We were pleased to discover that the bipyrrole HTI **18** provided near-quantitative photoisomerization with high selectivity (87-90% PSS) using red light irradiation (Figure 3.3). Photoswitching was even possible in the near-

infrared window (660 nm) to effectively photoisomerize the *E*-isomer to the *Z*-isomer, due to the highly redshifted absorption spectra. This was further demonstrated in a range of solvents where absorption maximum exceeded 600 nm in a mixture of *n*-Hex/iPrOH (9:1) (**Figure 3.6a** and Section 4, Supporting Information). Interestingly, a large solvatochromic effect was observed of approximately 30-40 nm depending on if for example acetone or *n*-Hex in mixture with iPrOH was used as the solvent (**Figure 3.6a-b** and Section 4, Supporting Information). Finally, thermal stability was determined to be above 10 days while a fatigue study estimated an approximate 1% loss of absorbance per cycle using 470/625 nm light irradiation for 2-3 min intervals (**Figure 3.6c** and Section 4, Supporting Information), essentially rendering bipyrrole HTI **18** bistable.

3. Conclusion

We have described the effects following systematic phenyl-fused π-extension of the parent unmodified hemithioindigo (HTI) scaffold to discover redshifted HTI photoswitches. Accordingly, these HTI analogues displayed excellent bistability with thermal half-lives of days to months. The selectivity was generally high, but further extension led to a reduced photostationary state selectivity below 80% with minimal band separation that did not improve. We decided not to explore more extended systems, due to concerns regarding solubility and to avoid complex syntheses. Instead, we opted to investigate the effects of extending the pyrrole-substituted HTI known for its excellent bidirectional quantitative photoisomerization properties. Extended analogues of this system not only displayed increased thermal stability up to at least 5 months, which is a great improvement compared to similar redshifted HTIs in the litera-

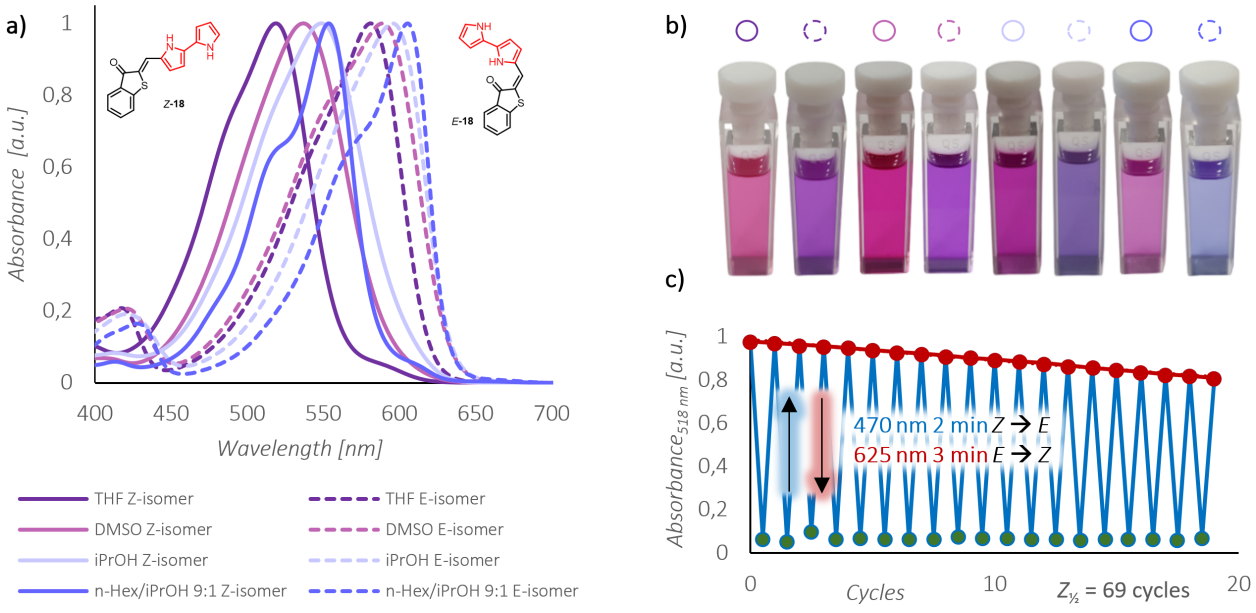

Figure 3.6. *Photochemical properties of oligomer-inspired bipyrrole-substituted HTI **18**. (a) Photoisomerization of the Z-isomer (solid lines) in the near-infrared window (660 nm) afforded the E-isomer (dashed lines) in a range of organic solvents (33 µM). Absorption maximum exceeds 600 nm. (b) Solvatochromism visible to the naked eye. Circles above cuvettes (colour and solid/dash line) indicate solvent (c) Photobleaching experiment (33 µM in THF).*

ture, but also kept its intrinsic large band separation between 35-48 nm. An impressive 53-82 nm or 23-29 nm redshift was produced in response to parallel π-extension compared to the parent HTI and pyrrole-substituted HTI, which allowed photoisomerization with 590 nm orange light. A systematic cumulative bathochromic shift between 6-21 nm was obtained for every phenyl-fused π-extention added to the HTI system, indicating the effectiveness of the strategy. Surprisingly, the indole-substituted HTI analogues in this series displayed quantitative photoisomerization to afford the corresponding *E*-isomers, but the reverse isomerization was only realised through thermal relaxation. Supported by theoretical calculations, we predicted an isomer-specific intramolecular proton transfer between the indole N-H and the thioindigo ketone leading to deexcitation in the S_1 excited state and preventing backswitching with light. This may be exploited as a design principle to allow photoisomerization to the active *E*-isomer with light of longer wavelength resulting in an enhanced penetration depth into tissue without concerns of lowered selectivity or photodegradation taking place. Lastly, guided by theoretical calculations, an oligomer-inspired bipyrrole-substituted HTI was discovered with excellent thermal stability, near-quantitative photoisomerization and improved band separation above to 60 nm. Effective photoswitching with 660 nm light in the near-infrared window was accomplished, of importance to therapeutic applications, due to the significantly redshifted absorption spectra with absorption maximum above 600 nm. Furthermore, solvatochromism was observed for the bipyrrole HTI analogue that did, however, display lowered solubility of the *Z*-isomer in less polar organic solvents. Photobleaching was determined to about 1% per cycle in THF, which is not a substantial loss, but an improvement would be beneficial. Theoretical calculations predicted further redshifting of about 60 nm for the addition of another electron-rich pyrrole moiety, and will be subject to further study. However, this added bathochromic effect would likely see the absorption maximum of the *Z*-isomer move into the red region of the visible spectrum, which for now still has not been achieved for any HTI. Additionally, a tripyrrole perhaps π-extended, following the presented strategy, with incorporation of suitable solubilising groups to achieve water solubility, might with the notably large geometric change conferred by double-bond photoisomerization, make a promising new class and candidate for many relevant biological applications.

Acknowledgements

The authors would like to thank Kasper Enemark-Rasmussen (DTU Chemistry) for help with NMR measurements and DTU/HI for financial support. H. Zulfriki and A. O. Dohn thanks the Icelandic Research Fund for support, grant 196279-051.

Keywords: Excited State Intramolecular Proton Transfer • Hemithioindigo Photoswitch • Photochromism • Redshift • Solvatochromism

Appendix A. Supporting information

Author information

Mikkel Krell-Jørgensen[ǂ]
Habiburrahman Zulfikri[ǂǂ]
Magnus Grage Bonnevie[ǂ]
Asmus Ougaard Dohn[ǂǂ]
Luca Laraia[ǂ]*

[ǂ]Department of Chemistry, Technical University of Denmark, Kemitorvet 207, 2800, Kgs Lyngby, Denmark.
[ǂǂ]Faculty of Physical Sciences, University of Iceland.
*Correspondence to luclar@kemi.dtu.dk

Notes

The authors declare no competing financial interest.

3.4 FUTURE PERSPECTIVES

A compound intended for application in a biological system requires a certain amount of lipophilicity to ensure membrane permeability or binding to the target of interest, while possessing adequate hydrophilicity to enable sufficient water-solubility. As previously described (*vide supra*), the tri-pyrrole HTI is an interesting candidate for a new and promising photoswitch if its properties, especially solubility, can be improved. The unmodified scaffold comprises an extended hydrocarbon system to which an oligomer of pyrroles is linked. The molecule is therefore prone to impose solubility issues, which prompts the need to install solubilizing groups to counteract the effect.

The most common chemical approach is to attach solubilizing moieties, such as charged or polar groups to the structure, and thereby increase water-solubility.[43] In most cases, the charged groups employed consist of phosphates, phosphonates, sulfonates and ammonium. However, it is important to also consider the counter ion and the location of the group(s) installed to gain the most from this strategy, as both of these affect the lattice energy. Installing groups in locations that disrupt planarity or symmetry influence the molecules tendency to stack, which in turn increases the solubility. The drawback, however, is that it may result in less efficient photoswitches as the π-conjugation in the system favours planarity for a better overlap of orbitals. Hence, it is best to install groups in locations that doesn't weaken the conjugation or aromaticity of the system to a significant extent. Alternatively, installing non-ionic polar groups or incorporating electronegative heteroatoms into the scaffold increases the dipole moment of the molecule, and thereby its propensity to interact with water.[43] Heteroatoms also introduce hydrogen bond donors/acceptors that can interact with the solvent to further improve the solubility profile. The most commonly employed heteroatoms to replace carbons are nitrogen and oxygen, while polyethylene glycol (PEG) chains or the oxetanyl sulfoxide moiety can be encountered as well. Other methods include salt formation, replacing linear- with branched alkyl chains, following a prodrug strategy or attaching a bioactive ligand or substrate that is inherently water-soluble.

Suggested modifications to the tri-pyrrole HTI **19** to circumvent poor solubility is given in Scheme 3.3. It is partly inspired by a similar HTI system, where a tri-methoxy substituted HTI demonstrated water-solubility.[74] A methoxy group oriented out of plane in the photoswitchable core distorted planarity and prevented the

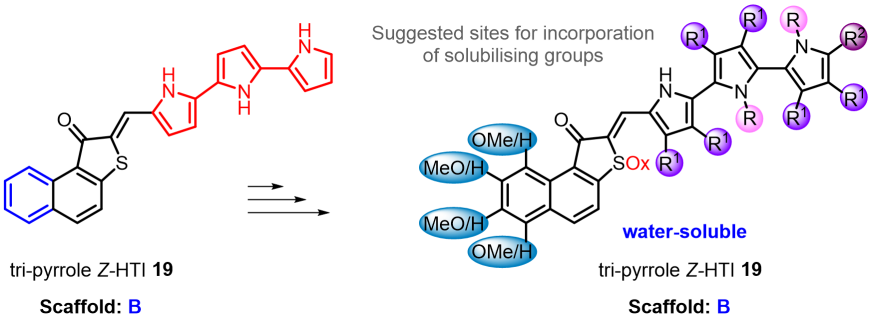

Scheme 3.3. *Increasing water-solubility of the π-extended tri-pyrrole HTI by incorporating solubilising groups or oxidising the thioindigo sulphur.*

molecules from π-stacking, which disabled aggregate formation and increased water-solubility. The other sites are selected for their relative ease of modification. Importantly, the pyrrole directly attached to the thioindigo fragment should not be substituted on the nitrogen in order to preserve the isomer-specific intramolecular hydrogen bond as this facilitates selective and quantitate photoisomerization.[136] Incorporating the solubilising groups early in the design phase is typically most practical by for instance buying starting materials where the substituents are already in place.

3.5 APPENDIX A: SUPPORTING INFORMATION

Supplementary Information

Programmable Synthesis of Redshifted and Thermally Bistable One-Way Quantitative Hemithioindigo-derived Photoswitches Enabled by Isomer-Specific Excited State Intramolecular Proton Transfer

Mikkel Krell-Jørgensen,[‡] Habiburrahman Zulfikri,[‡‡]
Magnus Grage Bonnevie,[‡] Asmus Ougaard Dohn[‡,‡‡] and Luca Laraia[‡]

Department of Chemistry, Technical University of Denmark, Kemitorvet 2800 Kongens Lyngby, DK

Department of Physics, Technical University of Denmark, Fysikvej 2800 Kongens Lyngby, DK

Faculty of Physical Sciences, University of Iceland, IS

TABLE OF CONTENTS

1 General directions

Chemical reactions were carried out under an inert atmosphere of nitrogen or argon using solvents of HPLC grade or anhydrous solvents (MeCN, DCM, DMF, DMSO, Et_2O, THF and PhMe) obtained from a PureSolv system (Innovative Technology, Tronyx). Synthesis was performed in the dark or reaction equipment was wrapped with aluminium foil to shield it from light. Commercially available reagents were used as received from Sigma Aldrich, Combi-Blocks, Fisher Scientific, Strem or Merck without further purification. Reactions were monitored by thin layer chromatography (TLC) and/or reversed-phase ultra-performance liquid chromatography mass spectrometry (RP-UPLC-MS).

Analytical TLC was performed on Merck aluminum sheets covered with silica gel (60 F_{256}). The plates were visualized using UV-light or stained by dipping in a developing agent followed by gentle heating. $KMnO_4$ stain was used as developing agent [3 g in H_2O (300 mL), K_2CO_3 (20 g) and 5% aqueous NaOH (5 mL)].

Column chromatography was performed using Merck Si 60A (40-63 μm) silica gel for flash column chromatography (FCC) and Merck Si 60A (15-40 μm) silica gel for dry column vacuum chromatography (DCVC).

Characterization of new compounds were done by TLC, NMR, MS (ESI), HRMS (ESI), melting point, UV-Vis spectroscopy, fluorescence spectroscopy and/or HPLC retention time (byproducts were not fully characterized).

Structural assignments were made for new compounds using a combination of 2D NMR techniques when relevant (gCOSY, DQF-COSY, HSQC, HMBC, H2BC, 2D NOESY). For the recording of ^{1}H NMR and ^{13}C NMR either a 400 MHz Bruker Ascend with a Prodigy CryoProbe and Avance IIIHD NanoBay console, 400 MHz Bruker UltraShield Plus with a Room Temperature Broadband ^{19}F Observe (RT BBFO) SmartProbe and Avance III console, 800 MHz Bruker Ascend refitted with a TCI (Triple Resonance NMR 'Inverse') CryoProbe and Avance IIIHD console, or 800 MHz Oxford instruments refitted with a TCI CryoProbe and Avance III console was used. Measurements were performed with a sample temperature of 25°C unless otherwise stated. The chemical shifts (δ) are reported in parts per million (ppm) and the coupling constants (*J*) in Hz. Spectra were referenced using the residual solvent peaks of the respective solvents; DMSO (δ 2.50 ppm for ^{1}H NMR DMSO-d_5 and δ 39.52 ppm for ^{13}C NMR DMSO-d_6), $CDCl_3$ (δ 7.26 ppm for ^{1}H NMR $CHCl_3$ and δ 77.16 ppm for ^{13}C NMR $CDCl_3$), MeOD (δ 3.31 ppm for ^{1}H NMR CHD_2OD and δ 49.00 ppm for ^{13}C NMR CD_3OD), DCM (δ 5.32 ppm for ^{1}H NMR $CHDCl_2$ and δ 54.00 ppm for ^{13}C NMR CD_2Cl_2). When THF-H_8 was used as NMR solvent, a double solvent suppression of the proton signals was performed. The following abbreviations were used to report peak multiplicities: s = singlet, bs = broad singlet, d = doublet, dd = doublet of doublets, ddd = doublet of doublets of doublets, dt = doublet of triplets, t = triplet, td = triplet of doublets, tt = triplet of triplets, q = quartet, dq = doublet of quartets, m = multiplet. $CDCl_3$ was treated with K_2CO_3 and filtered before use.

Analytical RP-UPLC-MS (ESI) was performed on an S2 Waters AQUITY RP-UPLC system equipped with a diode array detector using a Thermo Accucore C18 column (d 2.6 μm, 2.1 x 50 mm; column temp: 50°C; flow: 1.0 mL/min). Eluents A (0.1% HCO_2H in H_2O) and B (0.1% HCO_2H in MeCN) were used with a linear gradient (5% B to 100% B) in 2.4 min or 4.8 min and then held for 0.1 min at 100% B (total run time: 2.6 min or 5.0 min). Injection volume was 2 μL. The LC system was coupled to a Single Quadrupole Detector (SQD) 1 or SQD2 mass spectrometer.

UHPLC-HRMS analyses were measured on an Agilent Infinity 1290 UHPLC system (Agilent Technologies, Santa Clara, CA, USA) equipped with a diode array detector. Separation was obtained on an Agilent Poroshell 120 phenyl-hexyl column (d 2.7 μm, 2.1 × 250 mm; column temp: 60°C; flow: 0.35 mL/min). Eluents A (20 mM HCO_2H in H_2O) and B (20 mM HCO_2H in MeCN) were used with a linear gradient (40% B

to 100% B) in 3 min and then held for 5 min at 100% B, returned to 40% B in 0.1 min and held for the remaining 2 min. An injection volume of 0.1 µL was used. MS detection was performed in positive detection on an Agilent 6545 Quadrupole Time-Of-Flight (QTOF) MS equipped with Agilent Dual Jet Stream electrospray ion source with a drying gas temperature of 250°C, gas flow of 8 L/min, sheath gas temperature of 300°C and flow of 12 L/min. Capillary voltage was set to 4000 V and nozzle voltage to 500 V. Mass spectra were recorded as centroid data for *m*/*z* 50–1000, with an acquisition rate of 10 spectra/s. Lock mass solution in 70:30 MeOH:H_2O was infused in the second sprayer using an extra LC pump at a flow of 15 µL/min using a 1:100 splitter. The solution contained 1 µM tributylamine (Sigma-Aldrich) and 10 µM Hexakis(2,2,3,3-tetrafluoropropoxy)phosphazene (Apollo Scientific Ltd., Cheshire, UK) as lock masses. The $[M + H]^+$ ions (*m*/*z* 186.2216 and 922.0098 respectively) of both compounds were used.

Melting points were obtained using a Stuart SMP30 melting point apparatus.

UV-Vis spectroscopy was measured on an Analytik Jena Specord® 210 PLUS double beam spectrophotometer using precision cells 108B-QS made of quartz Suprasil with a 10 mm light path from Hellma® Analytics. Measurements were calibrated against air and pure dry solvent used to dissolve the respective samples to give a final concentration of 33 µM. Absorption wavelengths (λ) are reported in nm and the extinction coefficients (ε) in $L \cdot mol^{-1} \cdot cm^{-1}$. Unless otherwise stated, all included spectra were obtained after irradiation with the respective wavelength and photostationary state at 25°C. Spectra of (*Z*)-isomers are generally reported for non-irradiated samples to get as close to pure (*Z*)-isomer (dark state) composition.

UV-Vis thermal relaxation spectroscopy was obtained similarly to UV-Vis spectroscopy. The relaxation of the metastable (*E*)-isomer to its stable (*Z*)-isomer was determined by measuring the absorption every 5 minutes for 10 hours at 28°C in the respective dry solvent. The sample was kept dark inside in the instrument. Lambda max (λ_{max}) or representative wavelengths (λ) with a significant change between isomers were used to calculate thermal relaxation. Occasionally, a low change in observed relaxation resulted in weak exponential fit. For these instances, half-lives $T_{1/2}$ were reported as worst case (lowest value) and not necessarily for the total 10 hours as indicated by the respective graphs.

Fluorescence spectroscopy were recorded on a Perkin Elmer LS-55 fluorescence spectrophotometer using precision cells 101-QS made of quartz Suprasil with a 10 mm light path from Hellma® Analytics. Measurements were calibrated against air and pure dry solvent used to dissolve the respective samples to give a final concentration of 33 µM. Emission wavelengths (λ) are reported in nm. Unless otherwise stated, all included spectra were obtained after irradiation with the respective wavelength and photostationary state at 25°C.

Photoirradiation was carried out with LEDs purchased from Thorlabs (M340L4 (340 nm), M365L2 (365 nm), M415L4 (415 nm), M470L4 (470 nm), M530L3 (530 nm), M590L4 (590 nm), M625L4 (625 nm) and M660L4 (660 nm)) with collimator (SM2F32-A) and power supply/driver (LEDD1B) to focus the light beam and control the current, respectively.

HPLC quantification of photostationary state (PSS) composition was performed with samples prepared in DCM (2 mg/mL) and irradiated (1 Amp) with respective LEDs in borosilicate glass HPLC vials purchased from Fischer Scientific (fischerbrand 11525884), unless otherwise stated. An Aliquot (0.25 mL) of the sample was transferred to a new HPLC vial and the DCM removed with a flow of nitrogen while the sample was kept dark. A solvent mixture of *n*-hexane/iPrOH (1:1) was added to give the final concentration (0.5 mg/mL). The samples were measured using Waters 2695 Alliance Separations module HPLC with a ChiralPak AD-H column (5 µm, 250 x 4.6 mm) and a Waters 2996 PhotoDiode Array (PDA) detector. For details regarding

the eluent system (*n*-hexane/iPrOH), see the results for each measured photoswitch. The same eluent system used for HPLC quantification of the respective photoswitch was also used in determining the isosbestic point of that photoswitch by UV-Vis spectroscopy. The composition was determined as area under the curve. Chromatograms are representatives.

NMR photoisomerization was achieved by irradiating an NMR sample of the respective compound in the respective deuterated solvent (unless otherwise stated) for 30 min in a 3 mm NMR standard tube using LEDs with wavelengths as described for the UV-Vis spectroscopy data of that compound. The *Z*/*E* ratio was determined by ^{1}H NMR integration of the singlet enone β-proton or the pyrrole/indole-NH.

^{1}H NMR thermal relaxation spectroscopy was obtained similarly to the NMR photoisomerization. The relaxation of the metastable (*E*)-isomer to its stable (*Z*)-isomer was monitored by ^{1}H NMR with spectra recorded every one hour for 24 hours (y-axes) and the integral of the pyrrole/indole-NH of the (*E*)-isomer plotted vs. time. The sample was kept dark inside the instrument at a constant temperature of 24°C. Occasionally, a low change in observed relaxation resulted in weak exponential fit. For these instances, half-lives $T_{1/2}$ were reported as worst case (lowest value) and not necessarily for the total 24 hours as indicated by the respective graphs.

2 General procedures

General procedure A: Coupling of HTI (or derivatives) with mono-aldehydes

To a heat gun-dried reaction vessel evacuated with inert atmosphere was added hemithioindigo (or derivative) (1 equiv.) dissolved in benzene (0.10-0.30 M). Aldehyde (0.9-1 equiv.) and piperidine (1-2 drops) were added and the reaction vessel transferred to a pre-warmed oil bath (40 or 100°C) and stirred for the indicated time before cooling to room temperature. A saturated aqueous NH_4Cl solution (10 mL) was added and the aqueous phase extracted with EtOAc (3 x 10 mL). The combined organic extracts were washed with brine, dried over anhydrous Na_2SO_4, filtered and concentrated under reduced pressure by rotary evaporation. Purification by flash column or dry column vacuum chromatography on silica gel afforded the corresponding mono-substituted photoswitch.

General procedure B: Coupling of HTI (or derivatives) with mono-aldehydes

To a heat gun-dried reaction vessel evacuated with inert atmosphere was added hemithioindigo (or derivative) (1 equiv.) dissolved in PhMe (0.14-0.25 M). Aldehyde (0.8-1 equiv.) and piperidine (1-2 drops) were added and the reaction vessel transferred to a pre-warmed oil bath (40 or 100°C) and stirred for the indicated time before cooling to room temperature. *n*-Hexane (5 mL) was added and the reaction vessel transferred to an ice bath (0°C) for 30-45 min. The precipitate was filtered, washed with cold *n*-hexane until the filtrate ran clear and dried under high vacuum to afford the corresponding mono-substituted photoswitch.

3 Specific reaction procedures for intermediates and building blocks

Thiophenoxy acetic acid (4)

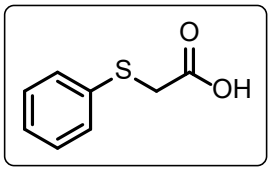

To a 100 mL round-bottomed flask were added deionized H_2O (30 mL), 2-bromoacetic acid (1.99 g, 14.3 mmol, 1.0 equiv.) and thiophenol (1.47 mL, 14.3 mmol, 1.0 equiv.). 6 M aqueous NaOH (5.0 mL, 30.0 mmol, 2.1 equiv.) was added at room temperature and the solution stirred for 22 h. The solution was acidified with dilute 1 M aqueous HCl and extracted with EtOAc (3 x 30 mL). The combined organic extracts were dried over anhydrous Na_2SO_4, filtered and concentrated under reduced pressure by rotary evaporation to afford the title compound **4** (2.39 g, 4.21 mmol, 99%) as a white solid.

The data is in accordance with previously reported work.[147]

TLC: R_f = 0.50 (1:1 EtOAc/*n*-heptane + 1% AcOH)

LCMS (ESI) $[M]^-$ *m/z* calcd for $C_8H_7O_2S^-$: 167.0172 , *m/z* found: 166.83 $[M]^-$

R_t: 1.04 min (total run time: 2.6 min), purity >99%

^{1}H NMR (400 MHz, $CDCl_3$): δ 10.22 (s, 1H), 7.49 – 7.41 (m, 2H), 7.38 – 7.31 (m, 2H), 7.31 – 7.27 (m, 1H), 3.70 (s, 2H)

^{13}C NMR (101 MHz, $CDCl_3$): δ 175.9, 134.6, 130.2, 129.3, 127.4, 36.7

Hemithioindigo (6)

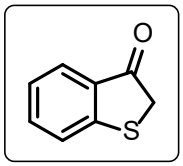

To an oven-dried reaction tube were added thiophenoxy acetic acid **4** (1.92 g, 11.4 mmol, 1.0 equiv.) and DCM (20 mL, 0.570 M). The solution was purged with nitrogen for 5 min. Triflic acid (5.0 mL, 56.6 mmol, 5.0 equiv.) was carefully added and the reaction tube transferred to a pre-warmed oil bath set to 40°C and stirred for 44 h. The reaction mixture was allowed to cool to room temperature before carefully poured into icy H_2O (200 mL). The aqueous phase was extracted with EtOAc (2 x 100 mL) and the combined organic extracts were washed with a saturated aqueous $NaHCO_3$ (100 mL) and brine (50 mL), dried over anhydrous Na_2SO_4, filtered and concentrated under reduced pressure by rotary evaporation to afford the title compound **6** (1.09 g, 6.66 mmol, 58%) as an orange solid.

Important note: Store in a freezer under inert atmosphere to prevent oxidation and prolong shelf life.

The data is in accordance with previously reported work.[136]

TLC: R_f = 0.80 (1:1 EtOAc/*n*-heptane + 1% AcOH)

LCMS (ESI) $[M+H]^+$ *m/z* calcd for $C_8H_7OS^+$: 151.0212 , *m/*z found: 150.86 $[M+H]^+$

R_t: 1.11-1.21 min (total run time: 2.6 min), purity >90%

^{1}H NMR (400 MHz, $CDCl_3$): δ 7.78 (d, *J* = 6.7 Hz, 1H), 7.55 (t, *J* = 7.6 Hz, 1H), 7.43 (d, *J* = 8.0 Hz, 1H), 7.22 (t, *J* = 7.4 Hz, 1H), 3.80 (s, 2H)

^{13}C NMR (101 MHz, $CDCl_3$): δ 200.2, 154.4, 135.8, 131.1, 126.8, 124.9, 124.8, 39.4

(2-Naphthylthio)acetic acid (3)

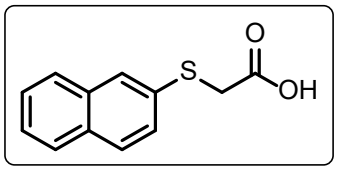

To a 100 mL round-bottomed flask were added deionized H_2O (30 mL), EtOH (20 mL), 2-bromoacetic acid (2.00 g, 14.4 mmol, 1.0 equiv.) and 2-naphthalenethiol (2.00 mL, 14.5 mmol, 1.0 equiv.). 6 M aqueous NaOH (5.0 mL, 30.0 mmol, 2.1 equiv.) was added at room temperature and the solution stirred for 4.5 h. The reaction mixture was filtered and the filtrate acidified with dilute 2 M aqueous HCl. Another filtration was performed and the residues combined, washed with *n*-heptane (3 x 20 mL) and concentrated under reduced pressure by rotary evaporation to afford the (naphthylthio)acetic acid **3** (2.99 g, 13.7 mmol, 95%) as a white solid.

TLC: R_f = 0.45 (1:1 EtOAc/*n*-heptane + 1% AcOH)

LCMS (ESI) $[M+H]^+$ *m/z* calcd for $C_{12}H_{11}O_2S^+$: 219.0474 , *m/z* found: 218.91 $[M+H]^+$

R_t: 1.41 min (total run time: 2.6 min), purity >90%

^{1}H NMR (400 MHz, CD_3OD): δ 7.81 – 7.71 (m, 4H), 7.48 – 7.35 (m, 3H), 3.73 (s, 2H)

^{13}C NMR (101 MHz, CD_3OD): δ 175.7, 136.4, 135.4, 133.0, 129.2, 128.6, 128.0, 127.6, 127.5, 126.4, 39.0

^{1}H NMR (400 MHz, DMSO-d_6): δ 7.82 (d, *J* = 8.1 Hz, 1H), 7.78 (d, *J* = 3.6 Hz, 1H), 7.76 (d, *J* = 3.1 Hz, 1H), 7.72 (bs, 1H), 7.46 (ddd, *J* = 8.2, 6.8, 1.4 Hz, 1H), 7.43 – 7.36 (m, 2H), 3.67 (s, 2H)

^{13}C NMR (101 MHz, DMSO-d_6): δ 170.2, 136.4, 133.5, 130.6, 127.8, 127.5, 126.7, 126.5, 125.9, 125.0, 123.4, 38.1

Naphtho[2,1-b]thiophen-1(2H)-one (5)

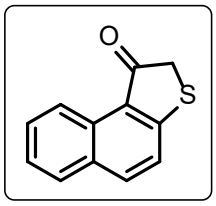

To an oven-dried reaction tube were added (2-naphthylthio)acetic acid **3** (1.00 g, 4.58 mmol, 1.0 equiv.) and DCM (7.0 mL, 0.654 M). Triflic acid (2.0 mL, 22.9 mmol, 5.0 equiv.) was carefully added, the solution purged with Ar for 5 min and the reaction tube transferred to a pre-warmed oil bath set to 40°C and stirred for 22 h. The reaction mixture was allowed to cool to room temperature before carefully poured onto icy H_2O (100 mL). The aqueous phase was extracted with DCM (3 x 30 mL) and the combined organic extracts were washed with a saturated aqueous $NaHCO_3$ (30 mL) and brine (30 mL), dried over anhydrous Na_2SO_4, filtered and concentrated under reduced pressure by rotary evaporation to afford the title compound **5** (0.816 g, 4.08 mmol, 89%) as a dark orange solid.

Important note: Store in a freezer under inert atmosphere to prevent oxidation and prolong shelf life.

TLC: R_f = 0.38 (1:6 EtOAc/*n*-heptane)

LCMS (ESI) $[M+H]^+$ *m/z* calcd for $C_{12}H_9OS^+$: 201.0369 , *m/*z found: 200.93 $[M+H]^+$

R_t: 1.59 min (total run time: 2.6 min), purity >98%

^{1}H NMR (400 MHz, DMSO-d_6): δ 10.65 (s, 1H, enol-OH), 9.10 (d, *J* = 8.3 Hz, 1H), 7.99 (dd, *J* = 8.0, 1.4 Hz, 1H), 7.88 (d, *J* = 8.7 Hz, 1H), 7.78 (d, *J* = 8.7, 1H), 7.63 – 7.57 (m, 1H), 7.57-7.51 (m, 1H), 6.67 (s, 1H)

^{13}C NMR (101 MHz, DMSO-d_6): δ 151.9, 135.6, 130.9, 129.2, 128.0, 126.0, 125.4, 125.1, 125.1, 123.6, 121.6, 98.5

Note: NMR spectroscopy in DMSO-d_6 resulted in the enol tautomer.

1H,1'H-2,2'-Bipyrrole (8)

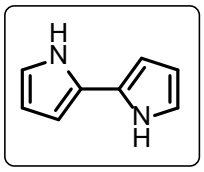

To an oven-dried round-bottomed flask were added pyrrole (0.52 mL, 7.49 mmol, 1.0 equiv.) in DCM (100 mL, 0.0745 M), PIFA (1.07 g, 2.48 mmol, 0.33 equiv.) and TMSBr (0.65 mL, 4.97 mmol, 0.66 equiv.) at -78°C. The reaction mixture was stirred for 80 min, allowed to slowly heat to room temperature and saturated aqueous $NaHCO_3$ (120 mL) was added. This was stirred vigorously for 30 min. The aqueous phase was extracted with DCM (5 x 30 mL) and the combined organic extracts were dried over anhydrous Na_2SO_4, filtered and concentrated under reduced pressure by rotary evaporation. Purified by DCVC (5% to 25% EtOAc in *n*-hexane with 1% increments) to afford the title compound **8** (192 mg, 3.73 mmol, 39%).

The data is in accordance with previously reported work.[149]

LCMS (ESI) $[M+H]^+$ *m/z* calcd for $C_8H_9N_2^+$: 133.0760 , *m/*z found: 132.95 $[M+H]^+$

R_t: 1.08 min (total run time: 2.6 min), purity >99%

^{1}H NMR (400 MHz, $CDCl_3$): δ 8.31 (bs, 2H,), 6.81 – 6.71 (m, 2H), 6.29 – 6.19 (m, 4H)

^{13}C NMR (101 MHz, $CDCl_3$): δ 126.1, 117.7, 109.6, 103.7

1H,1'H-[2,2'-Bipyrrole]-5-carbaldehyde (9)

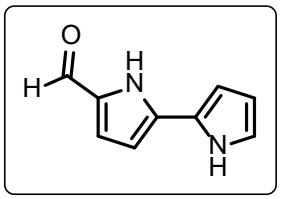

To an oven-dried round-bottomed flask was added bipyrrole **8** (151 mg, 1.14 mmol, 1.0 equiv.) and DMF (7.5 mL, 0.152 M). The solution was cooled to 0°C, and $POCl_3$ (0.10 mL, 1.07 mmol, 1.0 equiv.) was added using a Hamilton syringe. The reaction mixture was stirred at 0°C for 2 h and saturated aqueous Na_2CO_3 (40 mL) was added. The mixture was heated to 70°C for 30 min, cooled to room temperature and filtered. The residue was washed with H_2O, cold MeOH, cold Et_2O and cold *n*-pentane to afford the title compound **9** (52.6 mg, 0.328 mmol, 29%) as a crystalline green-yellow solid.

Data is in accordance with previously reported work.[148]

TLC: R_f = 0.52 (1:1 EtOAc/*n*-heptane)

LCMS (ESI) $[M+H]^+$ *m/z* calcd for $C_9H_9N_2O^+$: 161.0709 , *m/*z found: 160.94 $[M+H]^+$

R_t: 1.00 min (total run time: 2.6 min), purity >99%

^{1}H NMR (400 MHz, DMSO-d_6): δ 11.97 (s, 1H), 11.23 (s, 1H), 9.34 (s, 1H), 7.00 (d, *J* = 3.9 Hz, 1H), 6.88 (q, *J* = 2.1 Hz, 1H), 6.75 – 6.70 (m, 1H), 6.53 (d, *J* = 3.9 Hz, 1H), 6.11 (q, *J* = 3.1, 2.5 Hz, 1H)

^{13}C NMR (101 MHz, DMSO-d_6): δ 177.4, 134.6, 132.0, 123.5, 119.9, 109.2, 107.5, 106.2

Note: There is one quaternary carbon signal missing from the ^{13}C NMR spectrum.

4 Specific reaction procedures and analyses of photoswitches

(*Z*)-2-(Naphthalen-1-ylmethylene)benzo[b]thiophen-3(2H)-one (10)

Prepared according to general procedure A.

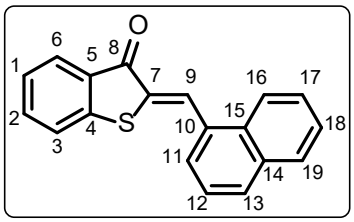

Hemithioindigo **6** (109 mg, 0.727 mmol, 1.0 equiv.), benzene (4.0 mL, 0.182 M), 1-naphthaldehyde (1.04 mL, 0.726 mmol, 1.0 equiv.). The aldehyde was added in two portions with stirring for 45 min under N_2 at 100°C in between. Stirring continued for 2 h at 100°C and 17 h at room temperature. Purified by flash column chromatography (0% to 15% EtOAc in *n*-heptane) to afford the title compound (*Z*/*E*)-**10** (64.3 mg, 0.223 mmol, 31%) as an orange solid.

TLC: R_f = 0.38 (1:6 EtOAc/*n*-heptane)

LCMS (ESI) $[M+H]^+$ *m/z* calcd for $C_{19}H_{13}OS^+$: 289.0682 , *m/*z found: N/A $[M+H]^+$

R_t: 3.39 min (total run time: 5.2 min), purity >99%

^{1}H NMR (800 MHz, CD_2Cl_2): δ 8.71 (s, 1H, **H-9**), 8.27 (d, *J* = 8.4 Hz, 1H), 7.98 (d, *J* = 7.1 Hz, 1H), 7.97 – 7.96 (m, 1H), 7.96 – 7.95 (m, 1H), 7.94 (d, *J* = 8.0 Hz, 1H), 7.65 – 7.57 (m, 4H), 7.54 (dd, *J* = 7.9, 1.8 Hz, 1H), 7.34 (td, *J* = 7.4, 1.6 Hz, 1H)

^{13}C NMR (101 MHz, CD_2Cl_2): δ 188.5, 147.0, 135.9, 134.3, 133.7, 132.8, 132.0, 131.4, 131.2, 130.1, 129.4, 128.2, 127.6, 127.4, 127.1, 126.2, 126.0, 124.6, 124.1

HRMS-ESI $[M+H]^+$ *m/z* calcd for $C_{19}H_{13}OS^+$: 289.0682 , *m/*z found: 289.0678 $[M+H]^+$ (ppm error: -1.34)

(*E*)-**10**:

^{1}H NMR (400 MHz, CD_2Cl_2): δ 7.98 (m, 1H), 7.96 – 7.90 (m, 3H), 7.88 (s, 1H, **H-9**), 7.74 (ddd, *J* = 7.7, 1.4, 0.7 Hz, 1H), 7.63 – 7.56 (m, 2H), 7.56 – 7.52 (m, 2H), 7.51 – 7.48 (m, 1H), 7.26 (ddd, *J* = 8.1, 7.2, 1.0 Hz, 1H)

Note: A 1:5 (*Z*/*E*)-ratio was observed for (*E*)-**10** by ^{1}H NMR.

UV-Vis spectroscopy

HTI 1-naphthalene (**10**) (33 µM in DCM)

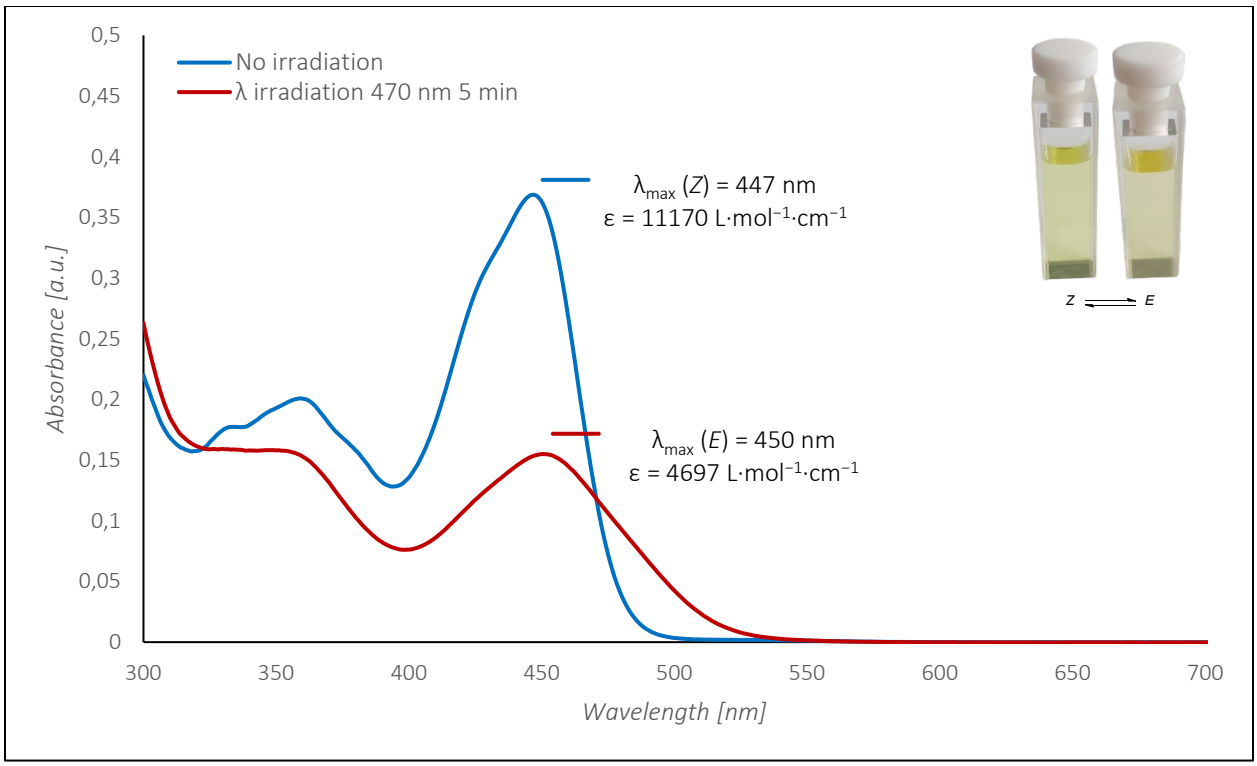

HTI 1-naphthalene (**10**) (33 µM in *n*-hexane/iPrOH 9:1)

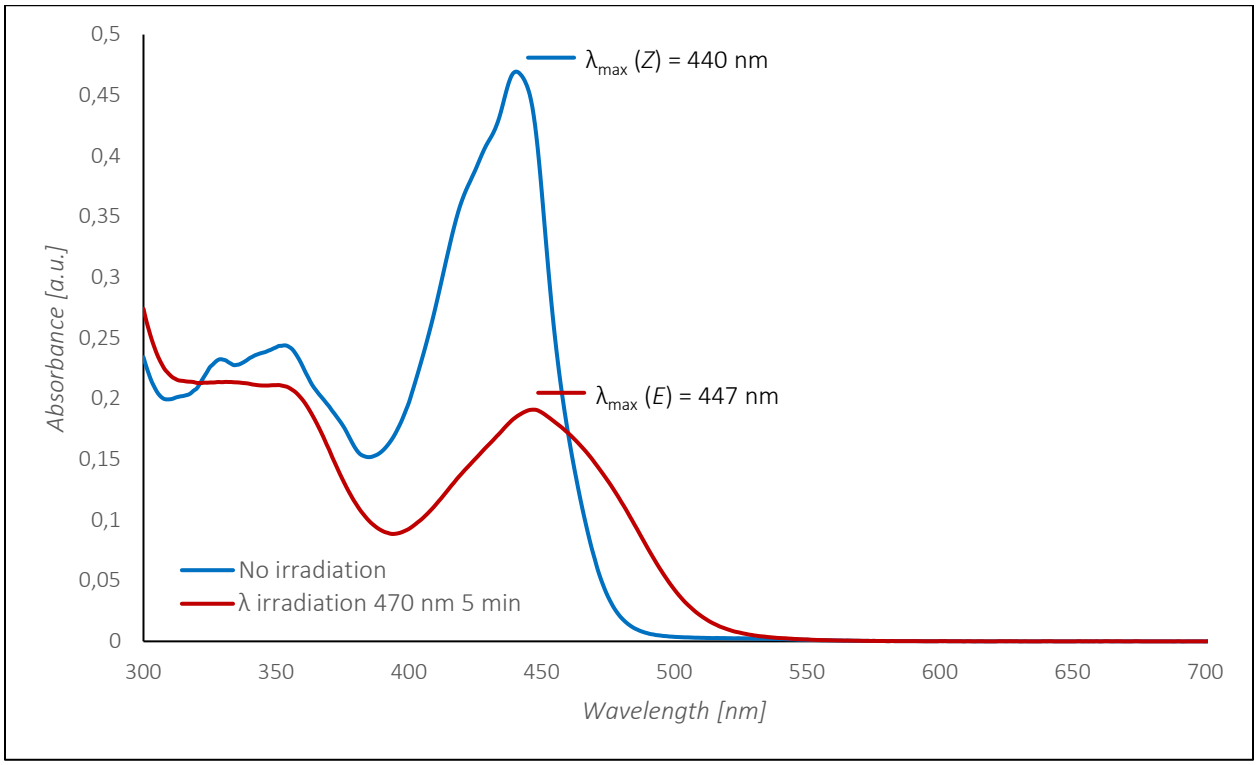

HTI 1-naphthalene (**10**) (33 μM in PhMe)

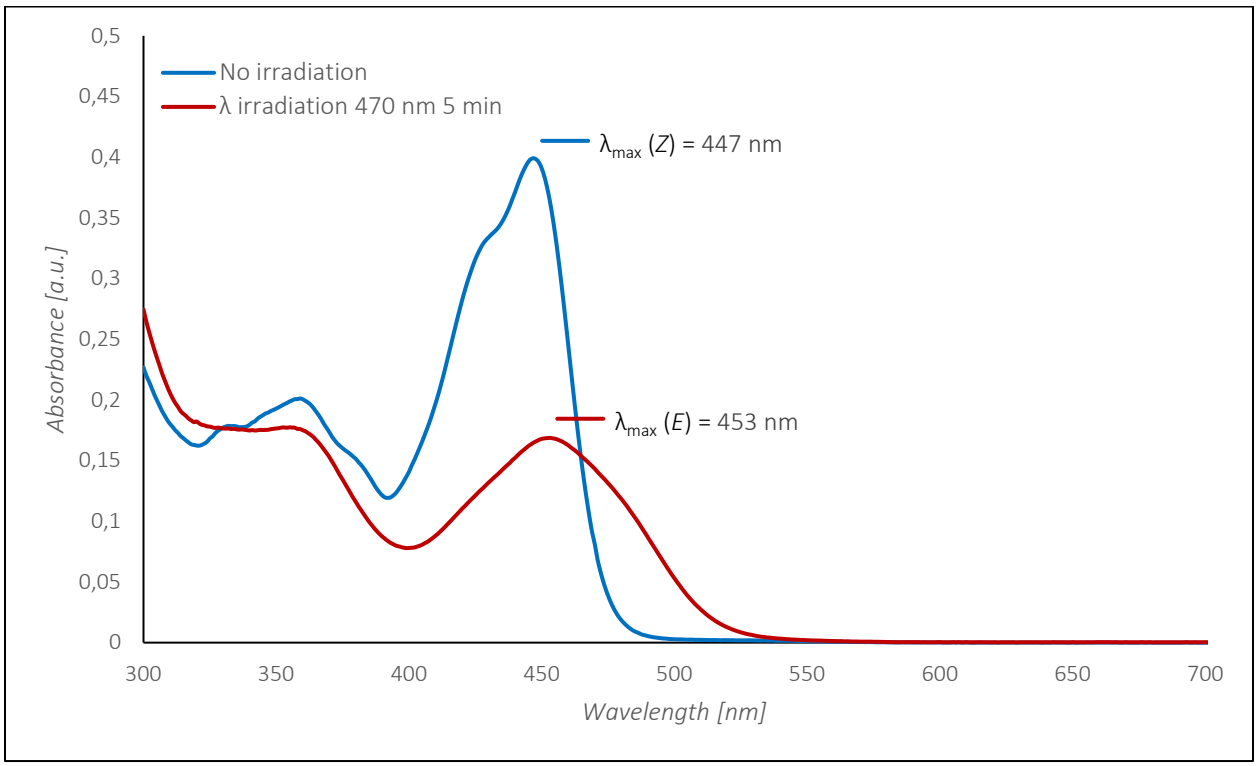

UV-Vis thermal relaxation spectroscopy

HTI 1-naphthalene (**10**) (33 μM in PhMe)

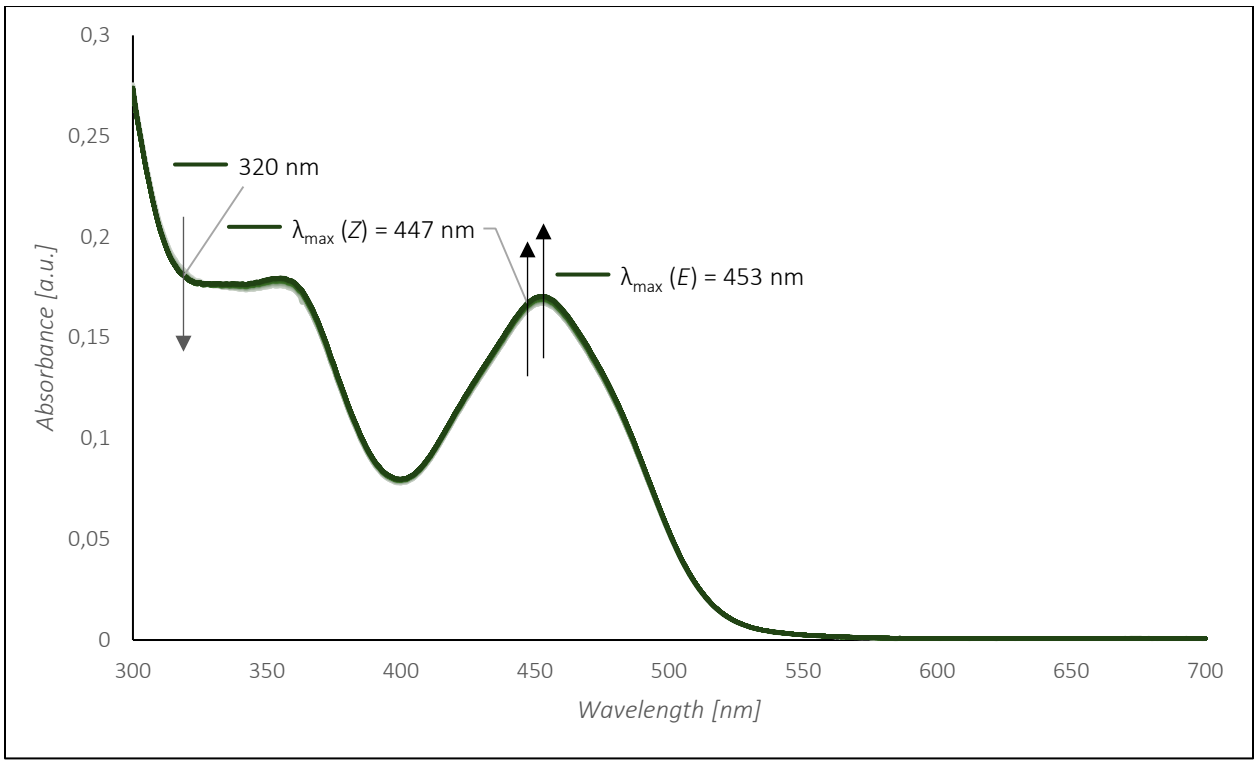

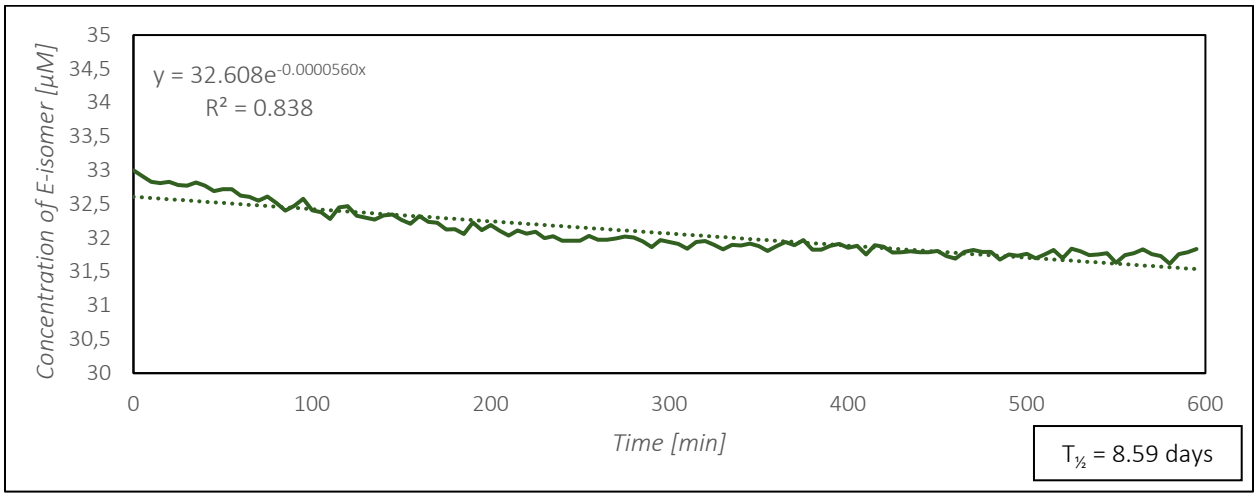

Note: Half-life was calculated using λ_{max} (*Z*) = 447 nm and 320 nm as representative for λ_{max} (*E*) = 453 nm.

HPLC conditions

Column:	ChiralPak AD-H column (5 μm, 250 x 4.6 mm)
Mobile Phase	90:10 *n*-hexane/iPrOH (isocratic, 1 mL/min)
Isosbestic Point	460 nm (in HPLC mobile Phase)
t_R(E)	11.88 min
t_R(Z)	9.95 min

Solution composition (%*E*-isomer)

Initial solution composition before irradiation: *E*-isomer (0.00%) / *Z*-isomer (100.00%)

Time	470 nm	Time	530 nm
5 min	85.60%	10 min	15.14%
10 min	86.14%	20 min	14.17%

Representative HPLC traces

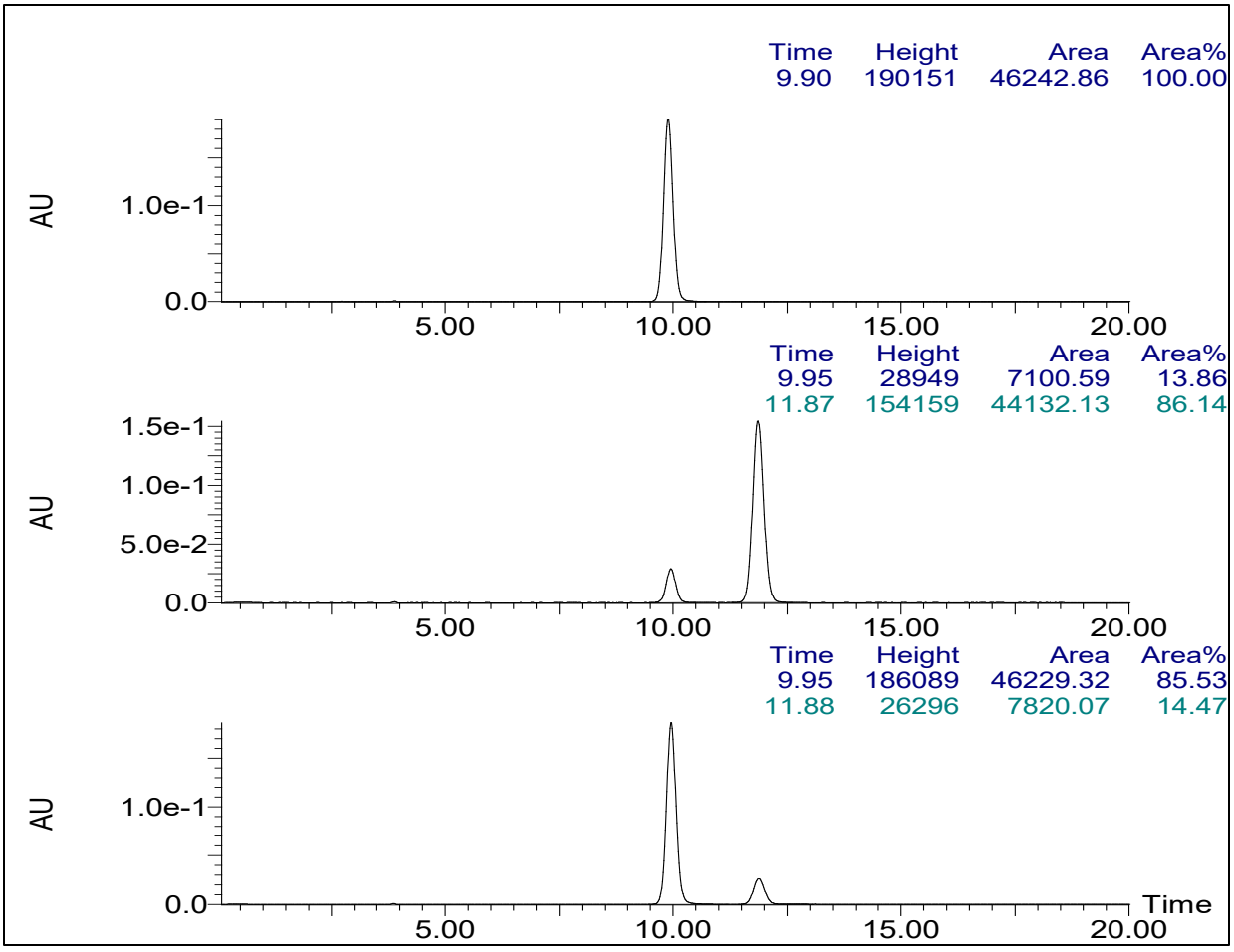

(*Z*)-2-(Naphthalen-2-ylmethylene)benzo[b]thiophen-3(2H)-one (11)

Prepared according to general procedure A.

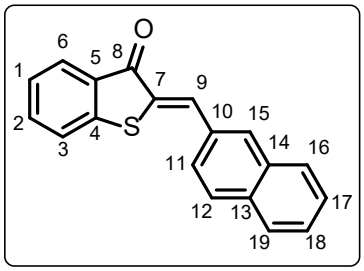

Hemithioindigo **6** (95.0 mg, 0.633 mmol, 1.0 equiv.), benzene (4.0 mL, 0.158 M), 2-naphthaldehyde (88.9 mg, 0.569 mmol, 0.90 equiv.). Stirred for 14 h under N_2 at 100°C. Upon cooling to room temperature precipitation occurred. Purified by DCVC (0% to 10% EtOAc in *n*-heptane with 1% increments) to afford the title compound (*Z*)-**11** (145 mg, 0.503 mmol, 88%) as an orange solid.

The data is in accordance with previously reported work.[150] No photophysical properties reported.

TLC: R_f = 0.70 (1:1 EtOAc/*n*-heptane)

LCMS (ESI) $[M+H]^+$ *m/z* calcd for $C_{19}H_{13}OS^+$: 289.0682 , *m/*z found: 288.97 $[M+H]^+$

R_t: 2.28 min (total run time: 2.6 min), purity >97%

^{1}H NMR (400 MHz, $CDCl_3$): δ 8.21 (s, 1H, **H-15**), 8.14 (s, 1H, **H-9**), 7.98 (d, *J* = 6.6 Hz, 1H, **H-6**), 7.96 – 7.91 (m, 2H), 7.89 – 7.84 (m, 1H), 7.81 (dd, *J* = 8.6, 1.8 Hz, 1H), 7.63 – 7.52 (m, 4H, **H-1**, **H-3**), 7.33 (td, *J* = 7.3, 1.0 Hz, 1H, **H-2**)

^{13}C NMR (101 MHz, $CDCl_3$): δ 188.8 (**C-8**), 146.3 (**C-5**), 135.4 (**C-1**), 134.0 (**C-10**/**C-14**), 133.9 (**C-9**), 133.4, 132.1 (**C-15**), 132.0, 130.7, 130.6, 129.0, 128.9, 127.9, 127.9, 127.3, 127.3, 127.0, 125.8 (**C-2**), 124.1

HRMS-ESI $[M+H]^+$ *m/z* calcd for $C_{19}H_{13}OS^+$: 289.0682 , *m/*z found: 289.0684 $[M+H]^+$ (ppm error: 0.726)

UV-Vis spectroscopy

HTI 2-naphthalene (**11**) (33 µM in DCM)

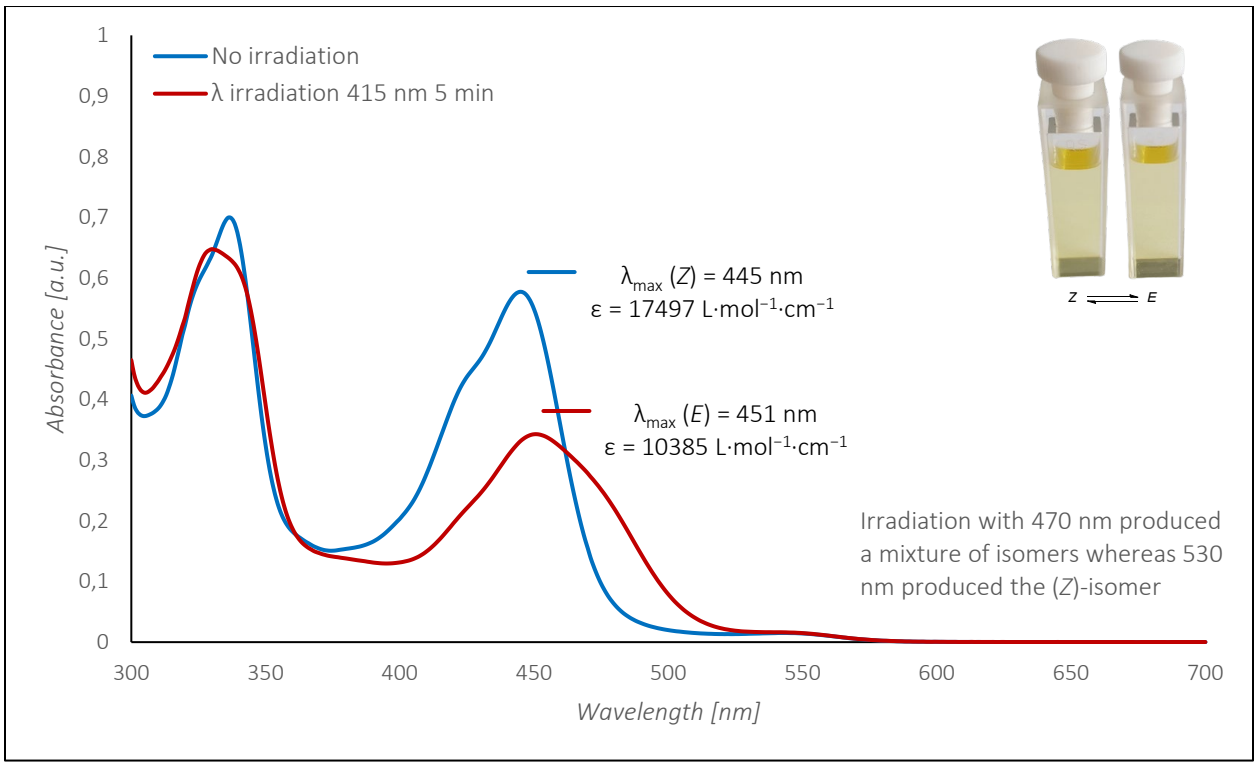

HTI 2-naphthalene (**11**) (33 µM in *n*-hexane/iPrOH 9:1)

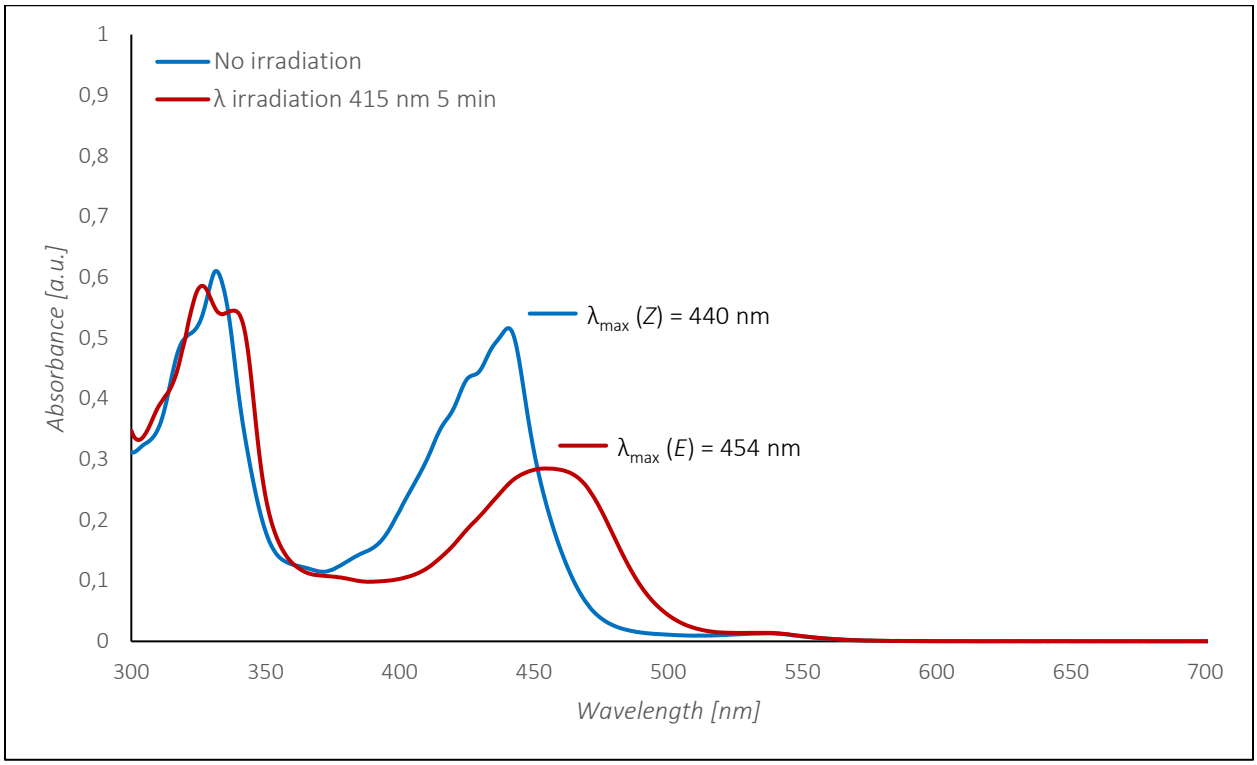

HTI 2-naphthalene (**11**) (33 μM in PhMe)

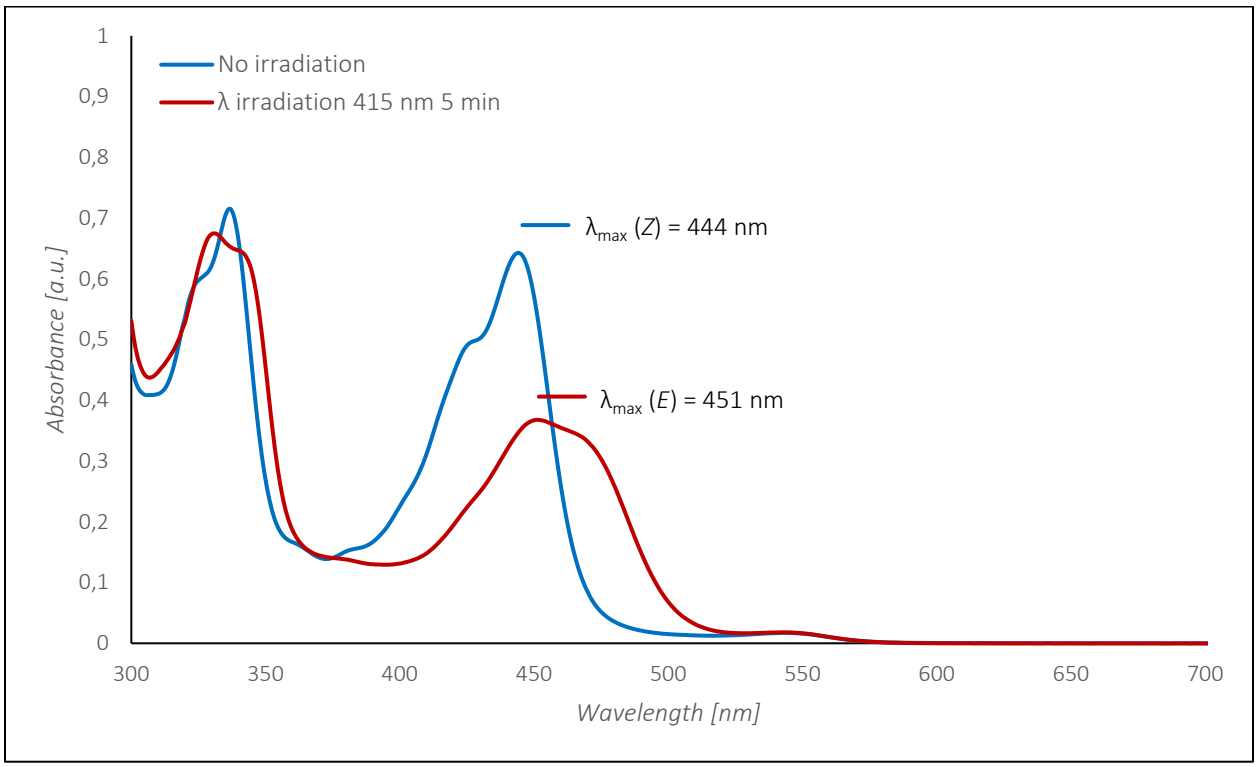

UV-Vis thermal relaxation spectroscopy

HTI 2-naphthalene (**11**) (33 μM in PhMe)

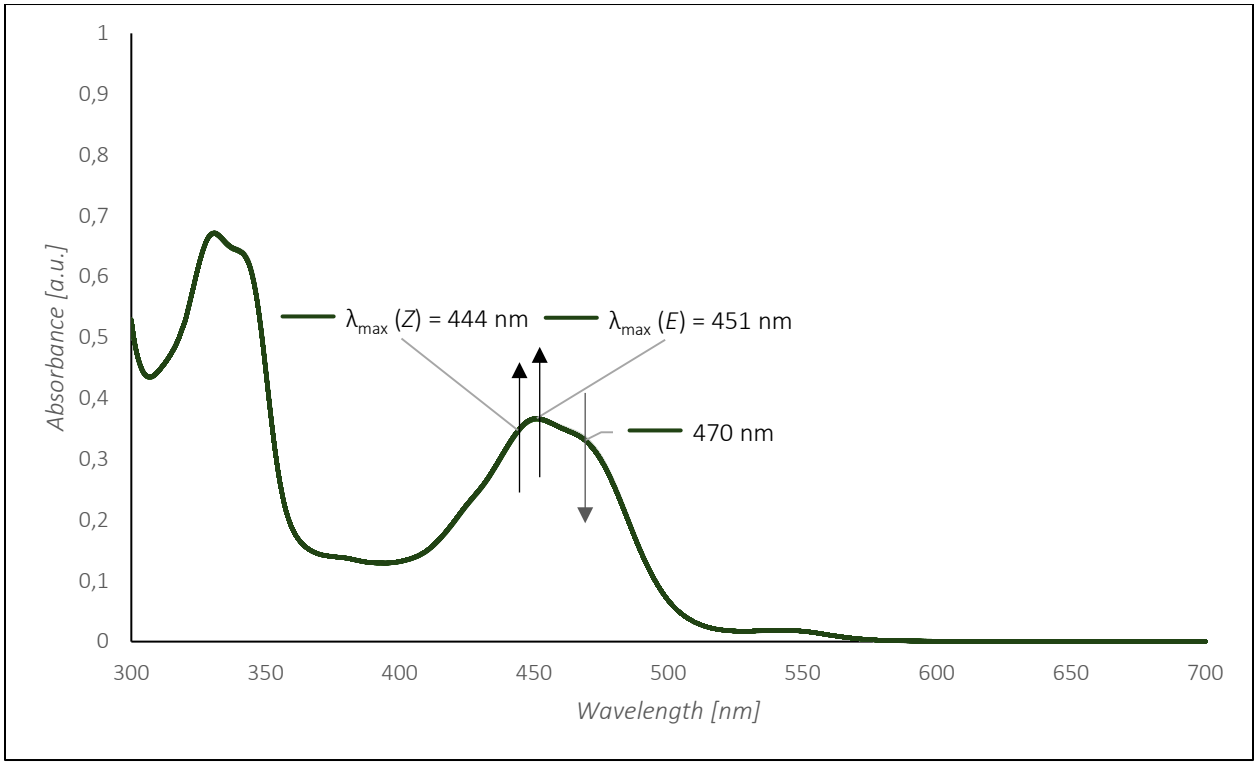

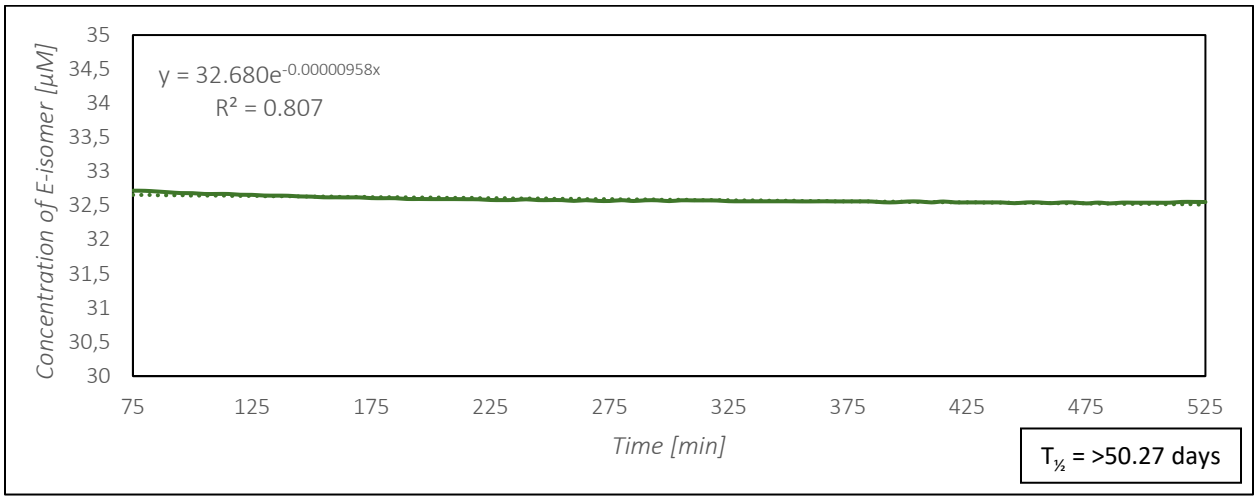

Note: Half-life was calculated using λ_{max} (*Z*) = 444 nm and 470 nm as representative for λ_{max} (*E*) = 451 nm.

HPLC conditions

Column:	ChiralPak AD-H column (5 μm, 250 x 4.6 mm)
Mobile Phase	90:10 *n*-hexane/iPrOH (isocratic, 1 mL/min)
Isosbestic Point	451 nm (in HPLC mobile Phase)
t_R(E)	12.42 min
t_R(Z)	11.38 min

Solution composition (%*E*-isomer)

Initial solution composition before irradiation: *E*-isomer (5.80%) / *Z*-isomer (94.20%)

Time	415 nm	530 nm
5 min	81.93	3.87
10 min	82.25	4.03

Representative HPLC traces

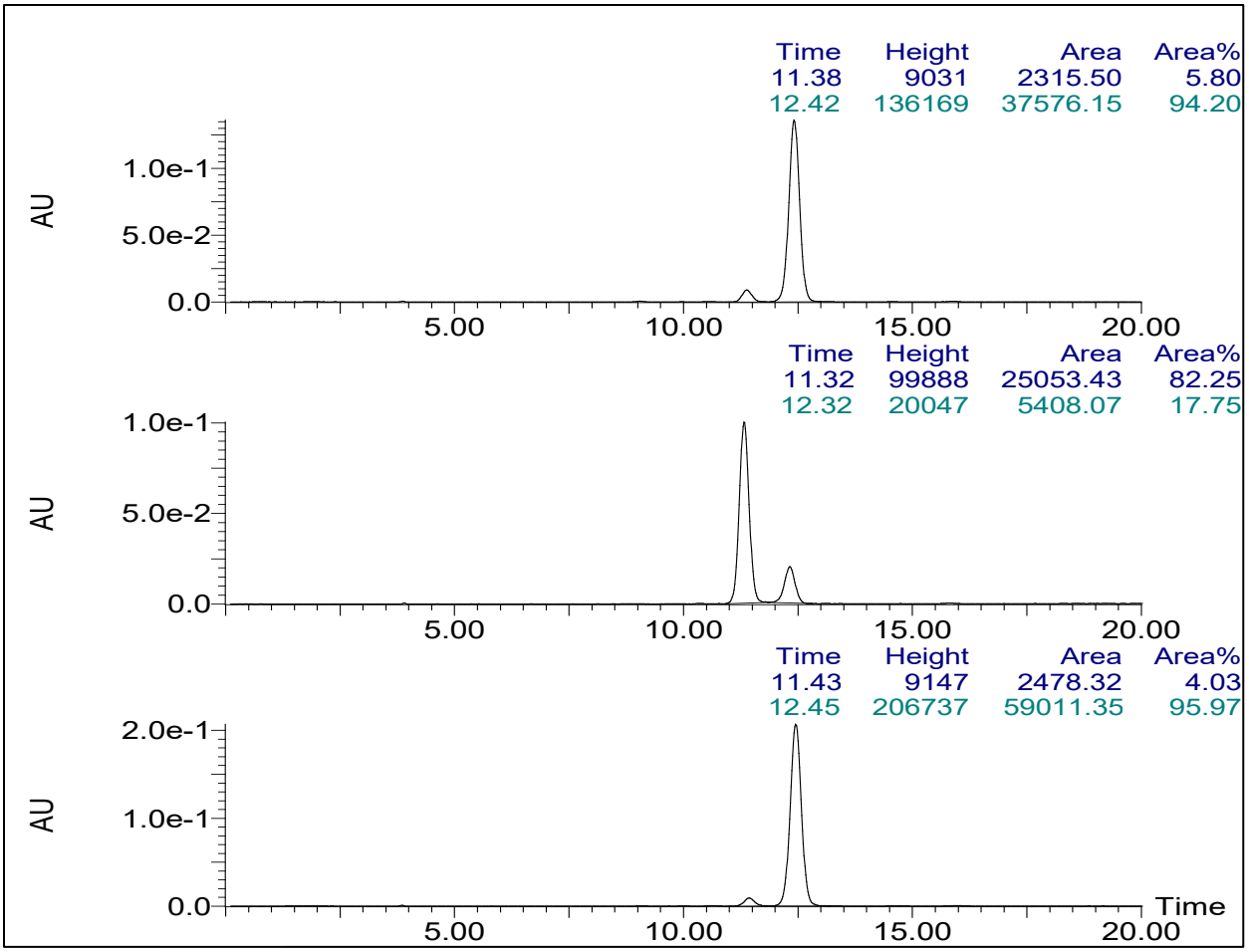

(*Z*)-2-Benzylidenenaphtho[2,1-b]thiophen-1(2H)-one (12)

Prepared according to general procedure A.

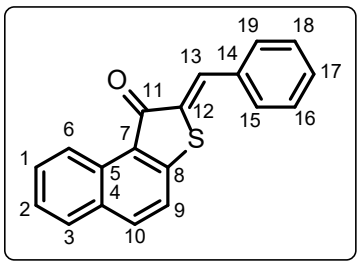

Hemithioindigo derivative **5** (81.2 mg, 0.405 mmol, 1.0 equiv.), benzene (4.0 mL, 0.101 M), benzaldehyde (0.36 mL, 0.354 mmol, 0.9 equiv.). Stirred for 3 h under N_2 at 100°C. Purified by DCVC (0% to 5% EtOAc in *n*-heptane with 0.5% increments) to afford the title compound (*Z*)-**12** (27 mg, 0.354 mmol, 26%) as a yellow orange solid.

TLC: R_f = 0.40 (1:1 EtOAc/*n*-heptane)

LCMS (ESI) $[M+H]^+$ *m/z* calcd for $C_{19}H_{13}OS^+$: 289.0682 , *m/*z found: 289.01 $[M+H]^+$

R_t: 3.55 min (total run time: 5.2 min), purity >99%

^{1}H NMR (400 MHz, DMSO-d_6): δ 9.25 (d, *J* = 8.4 Hz, 1H), 8.33 (d, *J* = 8.6 Hz, 1H), 8.10 (d, *J* = 8.1 Hz, 1H), 8.05 (s, 1H, **H-13**), 7.93 (d, *J* = 8.6 Hz, 1H), 7.88 (m, 1H, **H-15/19**), 7.86 (m, 1H, **H-15/19**), 7.83 – 7.77 (m, 1H), 7.69 – 7.50 (m, 4H)

^{13}C NMR (101 MHz, DMSO-d_6): δ 188.0 (**C-11**), 149.7, 136.9, 133.8 (**C-13**), 133.8, 131.5, 130.9 (**C-15/19**), 130.9 (**C-15/19**), 130.7, 130.4, 130.2, 129.9, 129.4 (**C-16/18**), 129.4 (**C-16/18**), 129.1, 126.6, 122.3, 122.2, 122.1

HRMS-ESI $[M+H]^+$ *m/z* calcd for $C_{19}H_{13}OS^+$: 289.0682 , *m/*z found: 289.0684 $[M+H]^+$ (ppm error: 0.726)

Note: The ^{13}C NMR peaks at 130.9 ppm and 129.4 ppm both correspond to 2 carbon signals each disclosed by 2D NMR.

UV-Vis spectroscopy

Phenyl HTI derivative (**12**) (33 µM in DCM)

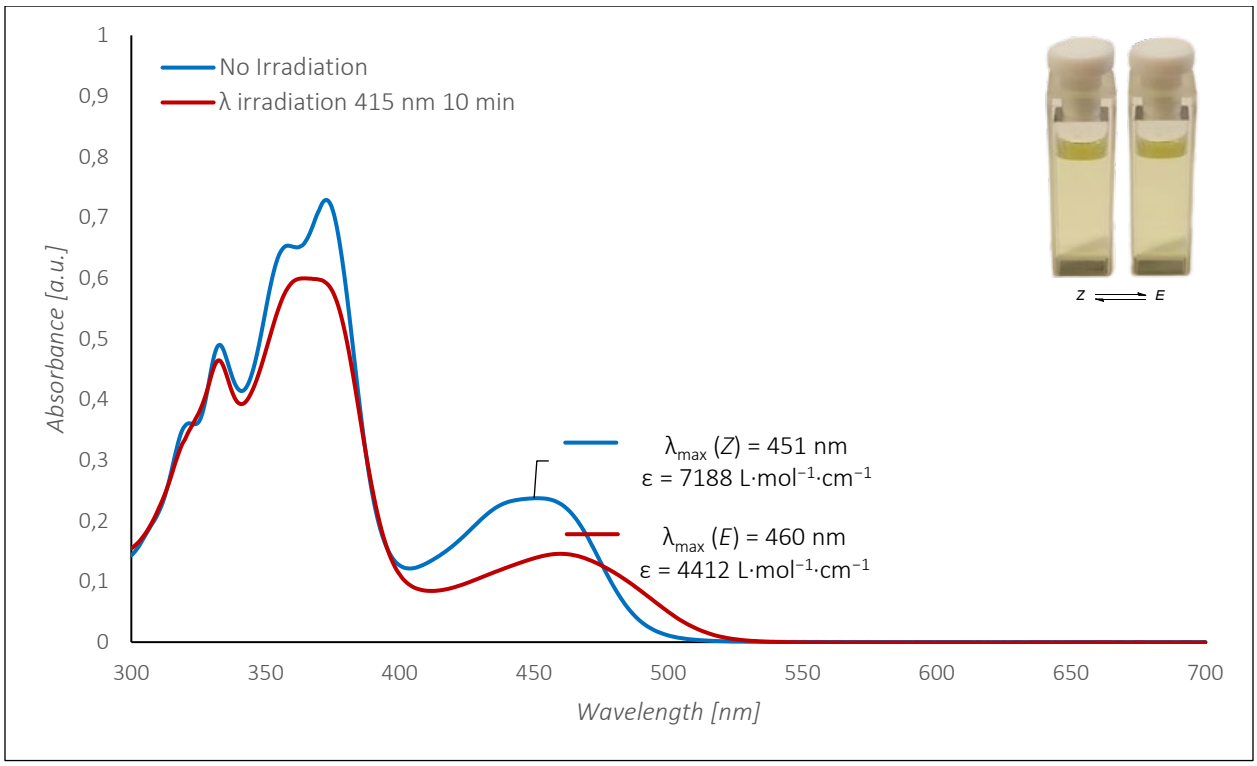

Phenyl HTI derivative (**12**) (33 µM in *n*-hexane/iPrOH 9:1)

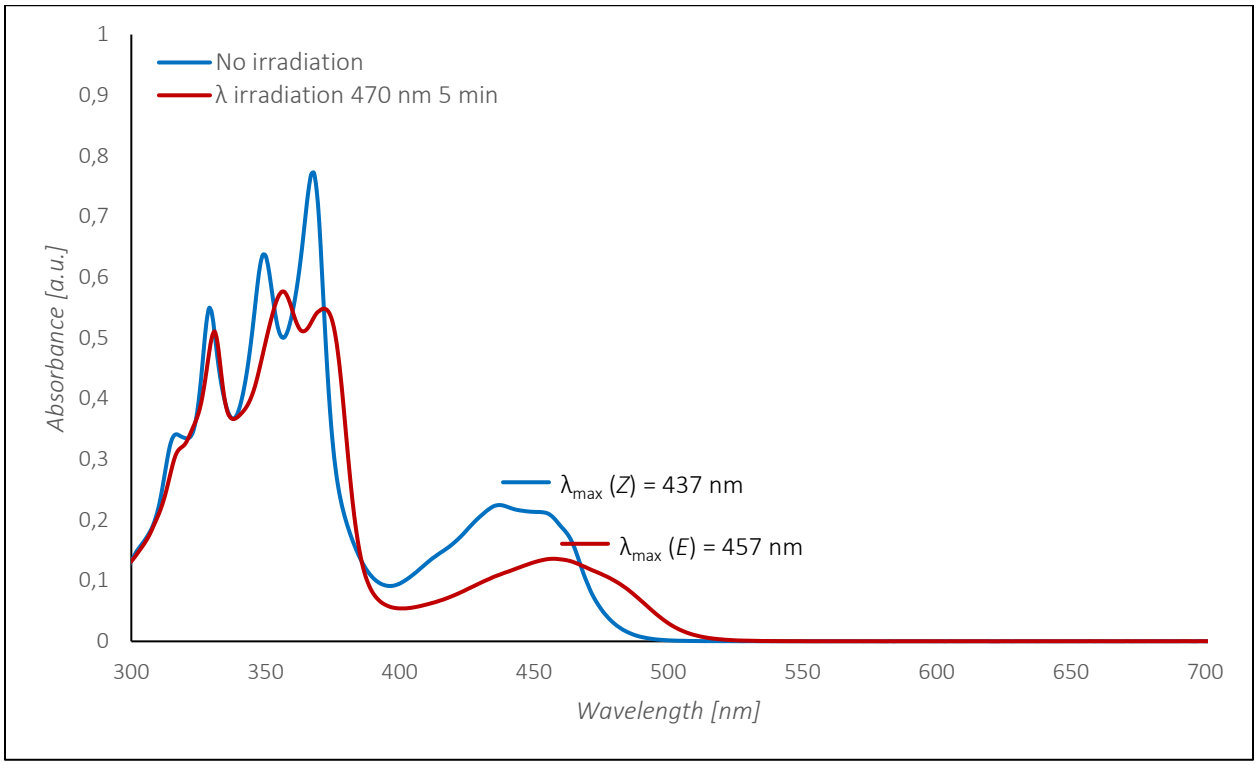

Phenyl HTI derivative (**12**) (33 μM in PhMe)

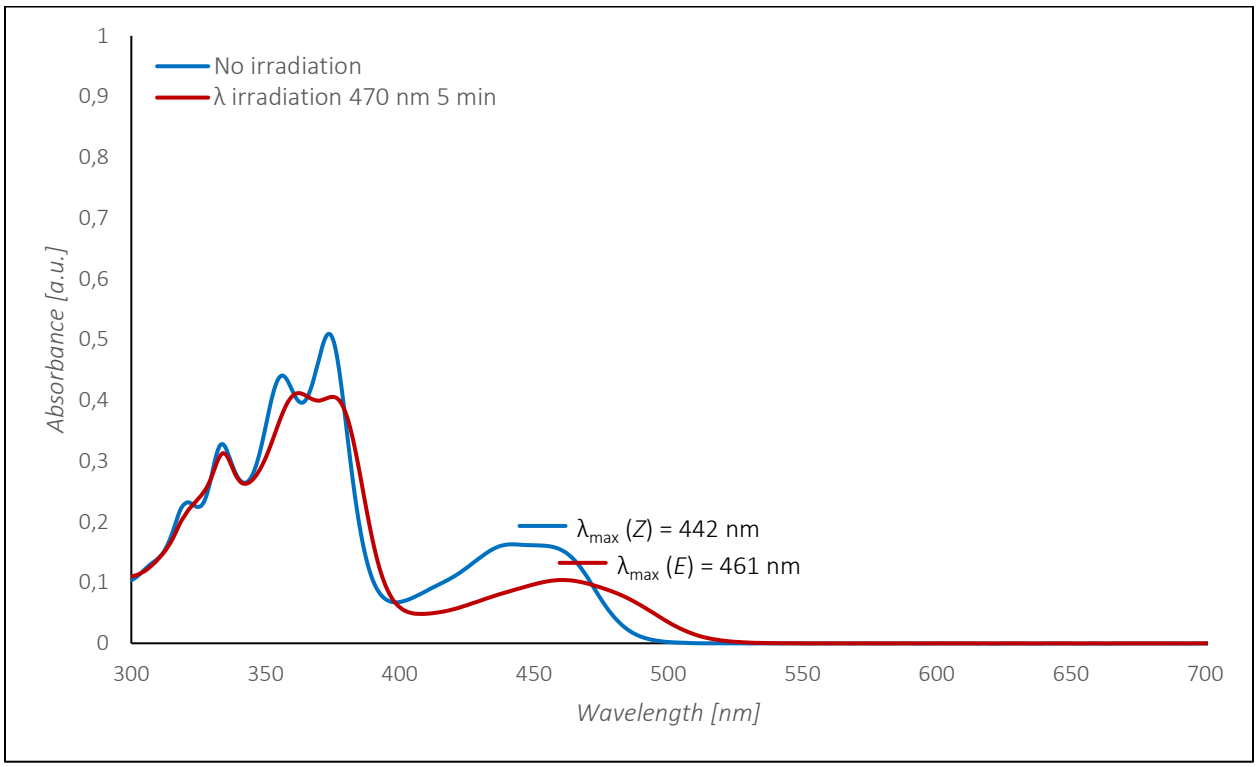

UV-Vis thermal relaxation spectroscopy

Phenyl HTI derivative (**12**) (33 μM in PhMe)

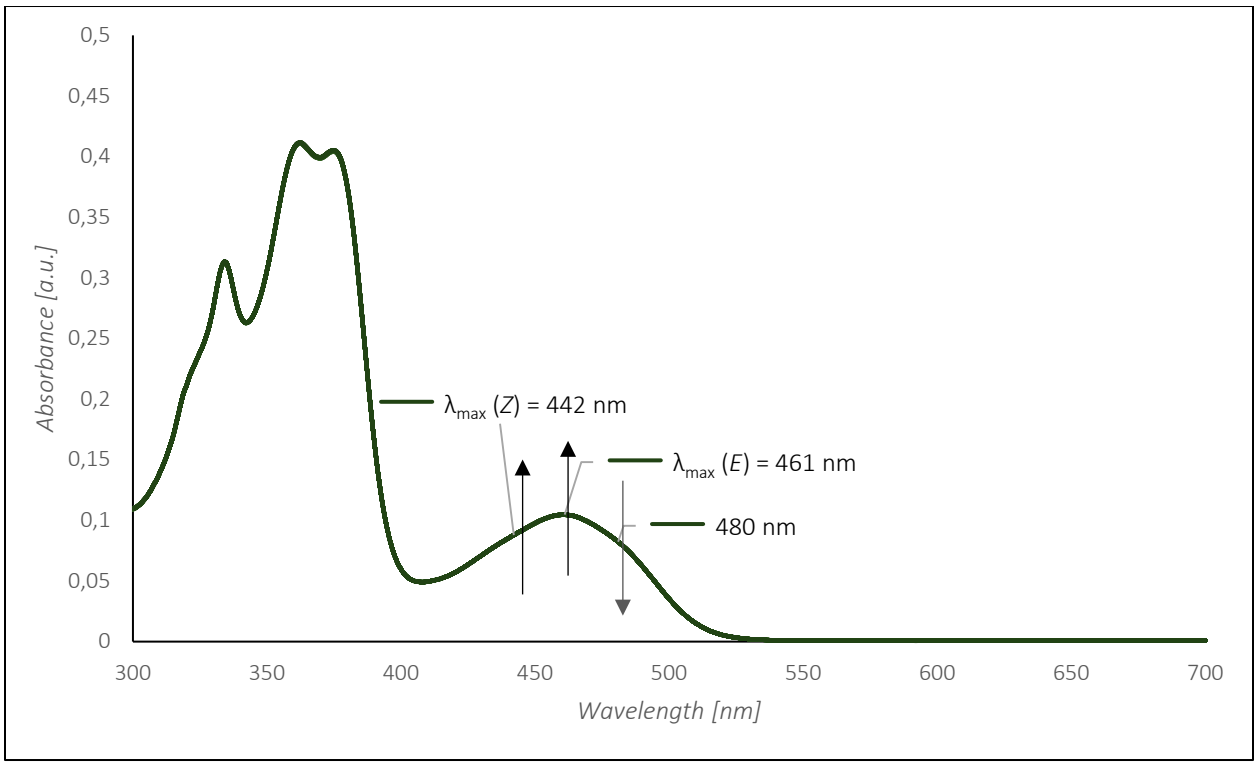

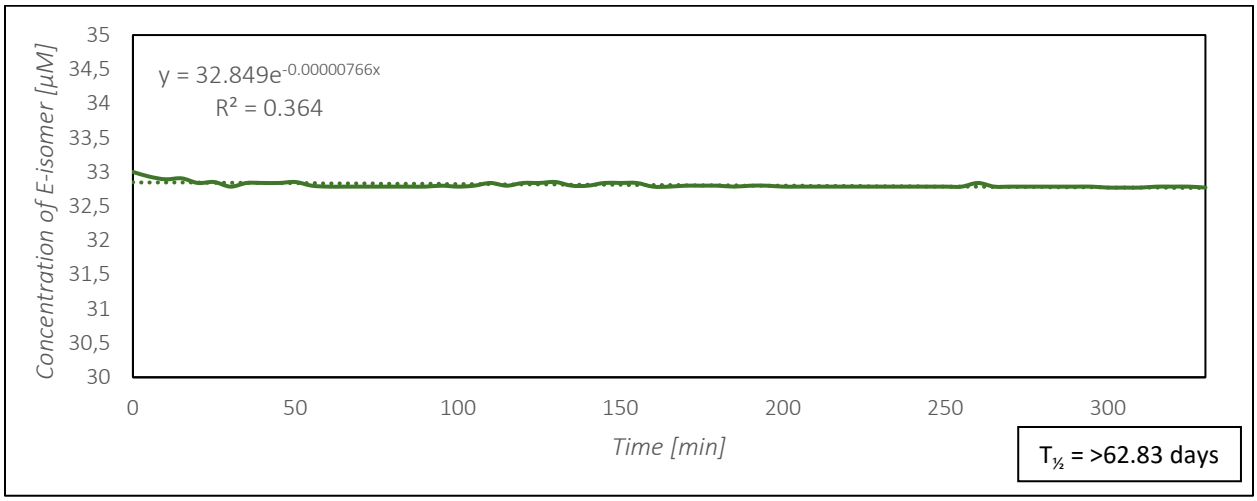

Note: Half-life was calculated using λ_{max} (*Z*) = 442 nm and 480 nm as representative for λ_{max} (*E*) = 461 nm.

HPLC conditions

Column:	ChiralPak AD-H column (5 μm, 250 x 4.6 mm)
Mobile Phase	90:10 *n*-hexane/iPrOH (isocratic, 1 mL/min)
Isosbestic Point	467 nm (in HPLC mobile Phase)
t_R(E)	8.05 min
t_R(Z)	9.37 min

Solution composition (%*E*-isomer)

Initial solution composition before irradiation: *E*-isomer (0.00%) / *Z*-isomer (100.00%)

Time	470 nm	530 nm
10 min	59.77	12.17
20 min	75.00	11.28
30 min	77.13	11.31

Note: The sample was irradiated in DCM following a direct injection. Representative HPLC traces.

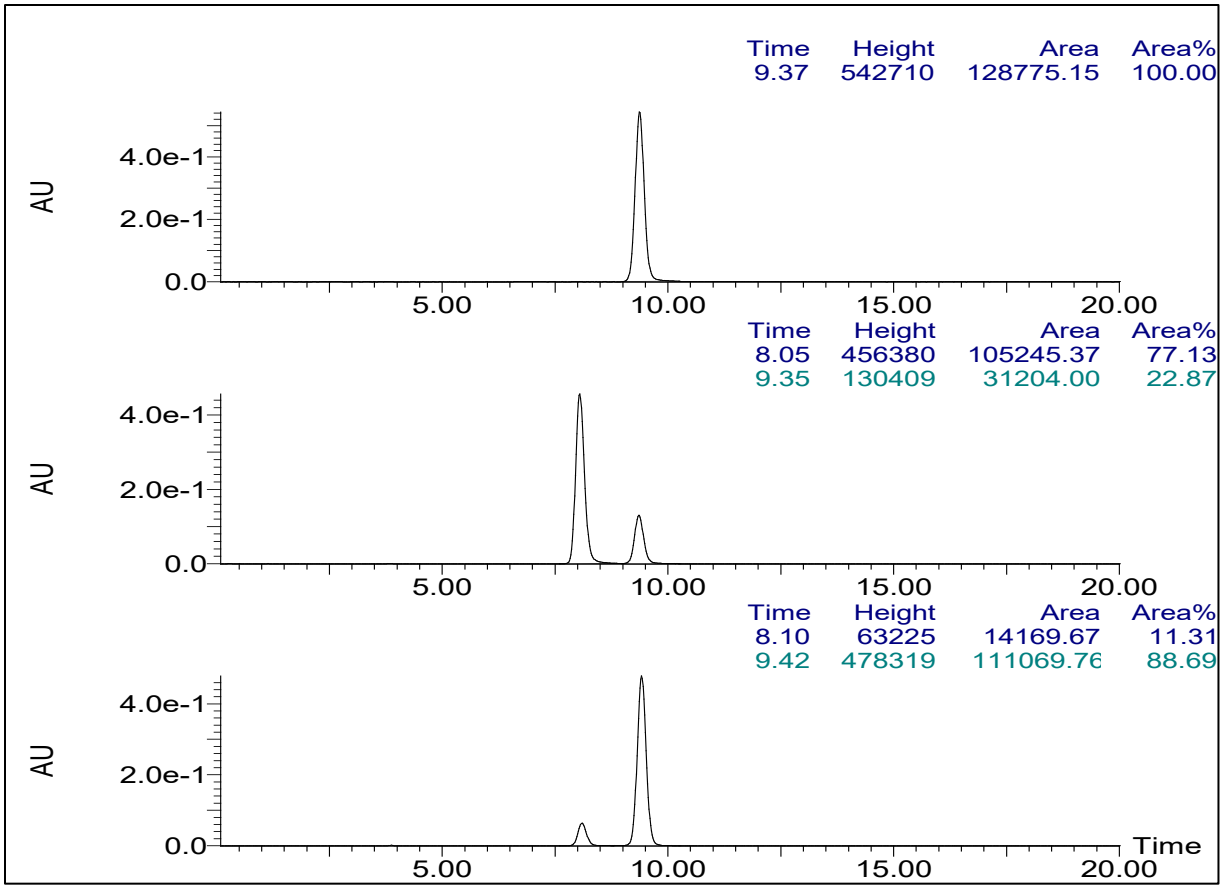

(*Z*)-2-(Naphthalen-2-ylmethylene)naphtho[2,1-b]thiophen-1(2H)-one (13)

Prepared according to general procedure **A.**

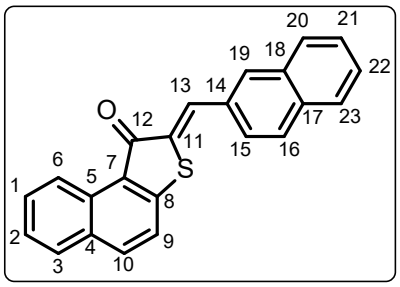

Hemithioindigo derivative **5** (83.1 mg, 0.415 mmol, 1.0 equiv.), benzene (4.0 mL, 0.104 M), 2-naphthaldehyde (63.8 mg, 0.408 mmol, 1.0 equiv.). Stirred for 2.5 h under N_2 at 100°C. Compound was judged sufficiently pure after work-up. Afforded the title compound (*Z*)-**13** (70 mg, 0.207 mmol, 51%) as an orange-brown solid.

TLC: R_f = 0.57 (1:1 EtOAc/*n*-heptane)

LCMS (ESI) $[M+H]^+$ *m/z* calcd for $C_{23}H_{15}OS^+$: 339.0838 , *m/*z found: N/A $[M+H]^+$

R_t: 1.62 min (84%) + 2.17 min (16%) (total run time: 2.6 min)

^{1}H NMR (400 MHz, DMSO-d_6): δ 9.26 (dd, *J* = 8.1, 0.9 Hz, 1H), 8.44 (m, 1H), 8.32 (d, *J* = 8.6 Hz, 1H), 8.18 (s, 1H, **H-13**), 8.09 (m, 3H), 8.02 – 7.99 (m, 1H), 7.95 (m, 1H), 7.93 (m, 1H), 7.80 (ddd, *J* = 8.4, 6.9, 1.3 Hz, 1H), 7.68 – 7.61 (m, 3H)

^{13}C NMR (101 MHz, DMSO-d_6): δ 188.0 (**C-12**), 149.7, 137.0, 133.9 (**C-13**), 133.5, 132.9, 132.0, 131.6, 131.4, 130.5, 130.0, 129.1, 129.0, 128.8, 128.2, 127.8, 127.2, 126.7, 126.6, 122.4, 122.3, 122.1

HRMS-ESI $[M+H]^+$ *m/z* calcd for $C_{23}H_{15}OS^+$: 339.0838 , *m/*z found: 339.0837 $[M+H]^+$ (ppm error: -0.295)

Note: There is one quaternary carbon signal missing from the ^{13}C NMR spectrum. Performing 2D NMR did not disclose the missing peak.

UV-Vis spectroscopy

2-Naphthyl HTI derivative (**13**) (33 µM in DCM)

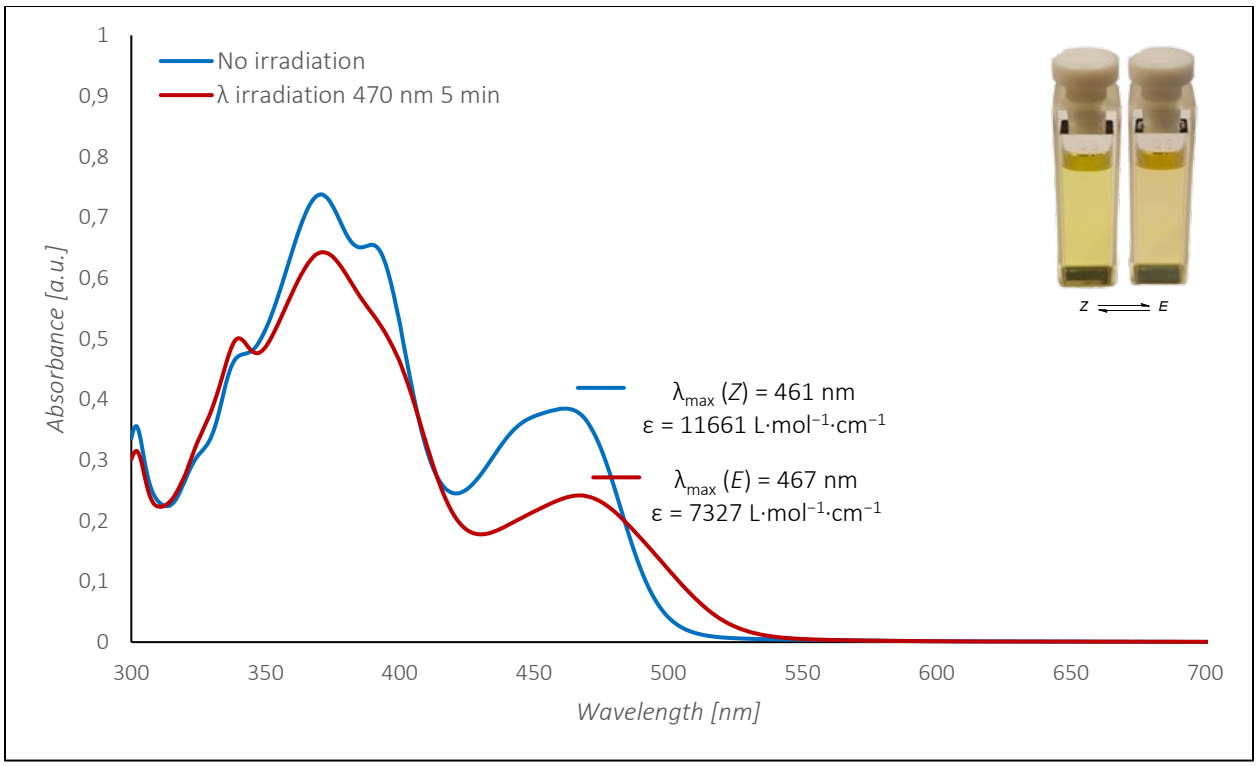

2-Naphthyl HTI derivative (**13**) (33 µM in *n*-hexane/iPrOH 9:1)

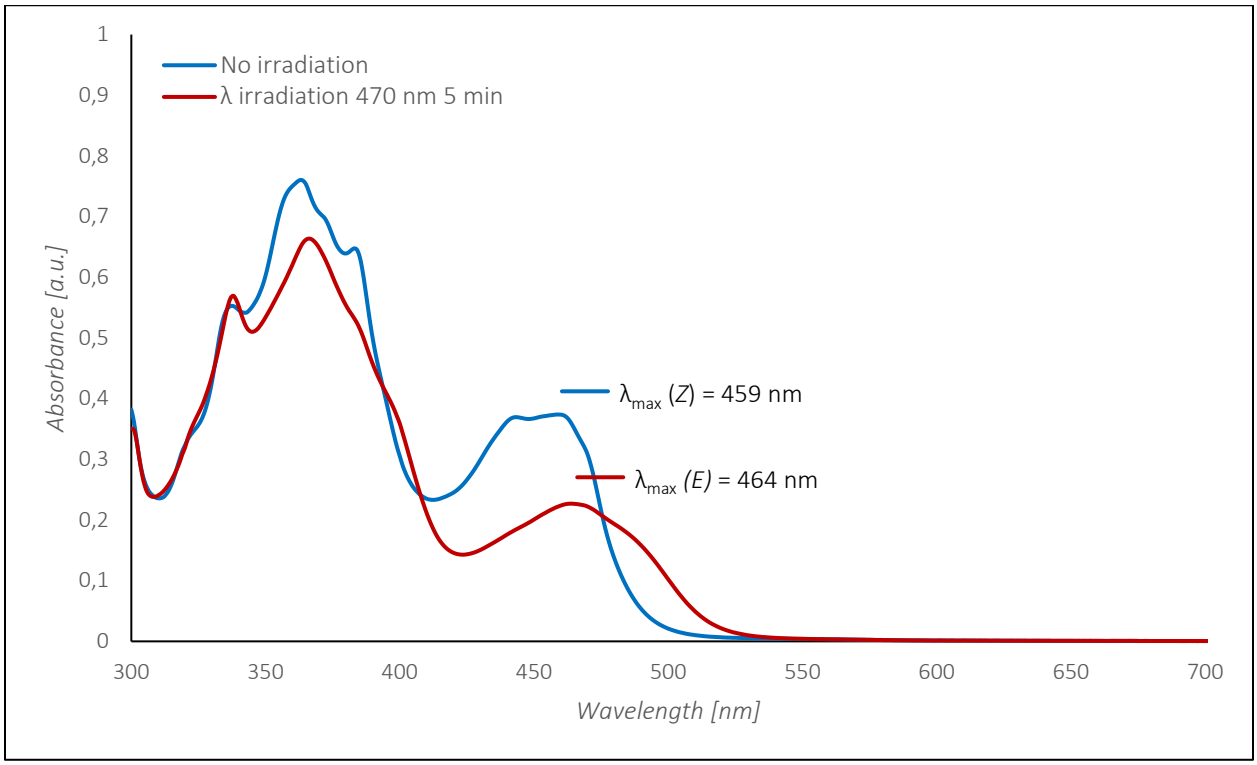

2-Naphthyl HTI derivative (**13**) (33 μM in PhMe)

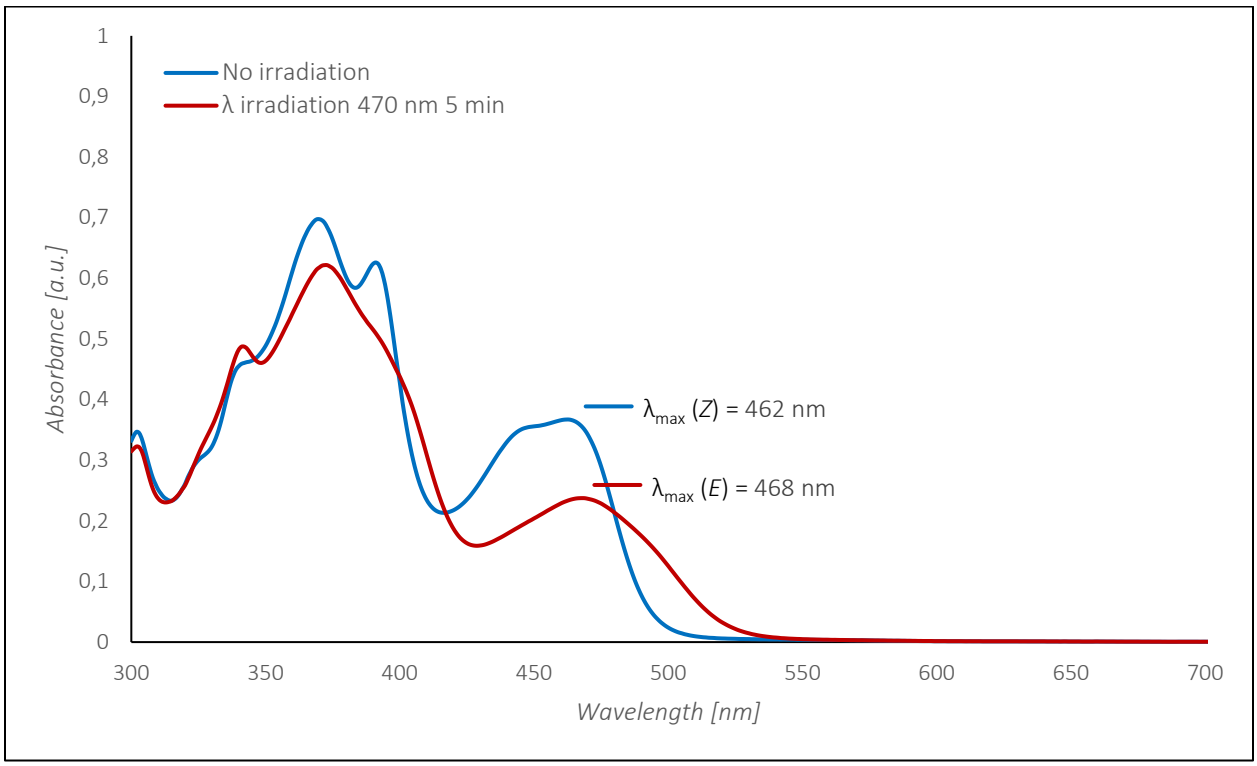

UV-Vis thermal relaxation spectroscopy

2-Naphthyl HTI derivative (**13**) (33 μM in PhMe)

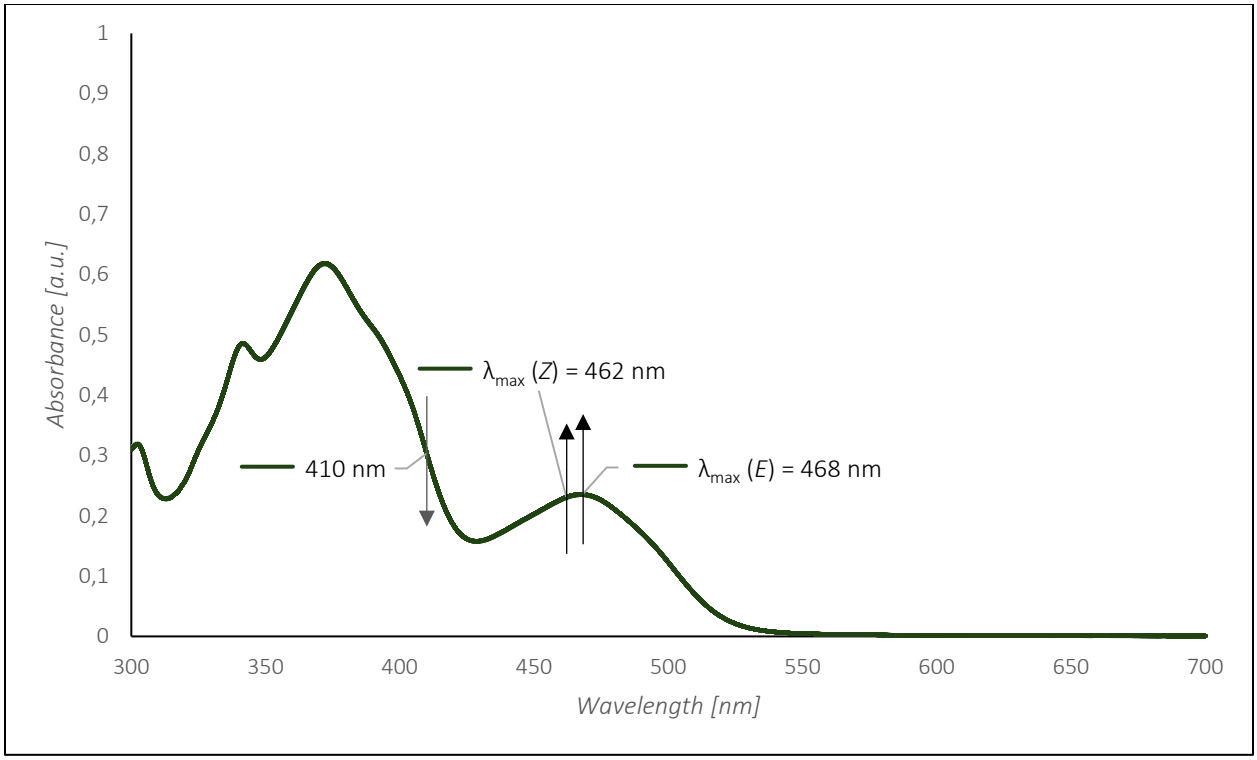

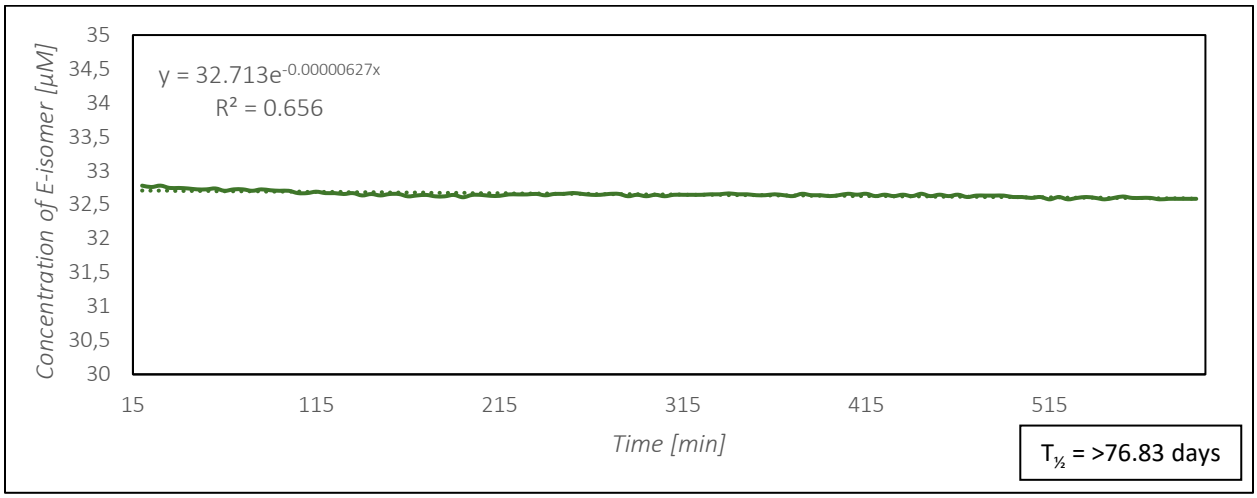

Note: Half-life was calculated using λ_{max} (*Z*) = 462 nm and 410 nm as representative for λ_{max} (*E*) = 468 nm.

HPLC conditions

Column:	ChiralPak AD-H column (5 μm, 250 x 4.6 mm)
Mobile Phase	90:10 *n*-hexane/iPrOH (isocratic, 1 mL/min)
Isosbestic Point	475 nm (in HPLC mobile Phase)
t_R(E)	15.32 min
t_R(Z)	12.90 min

Solution composition (%*E*-isomer)

Initial solution composition before irradiation: *E*-isomer (0.78%) / *Z*-isomer (99.22%)

Time	470 nm	530 nm
5 min	74.17	14.58
10 min	75.09	13.41

Note: The sample (1 mg/mL) was irradiated in DCM following a direct injection. Representative HPLC traces.

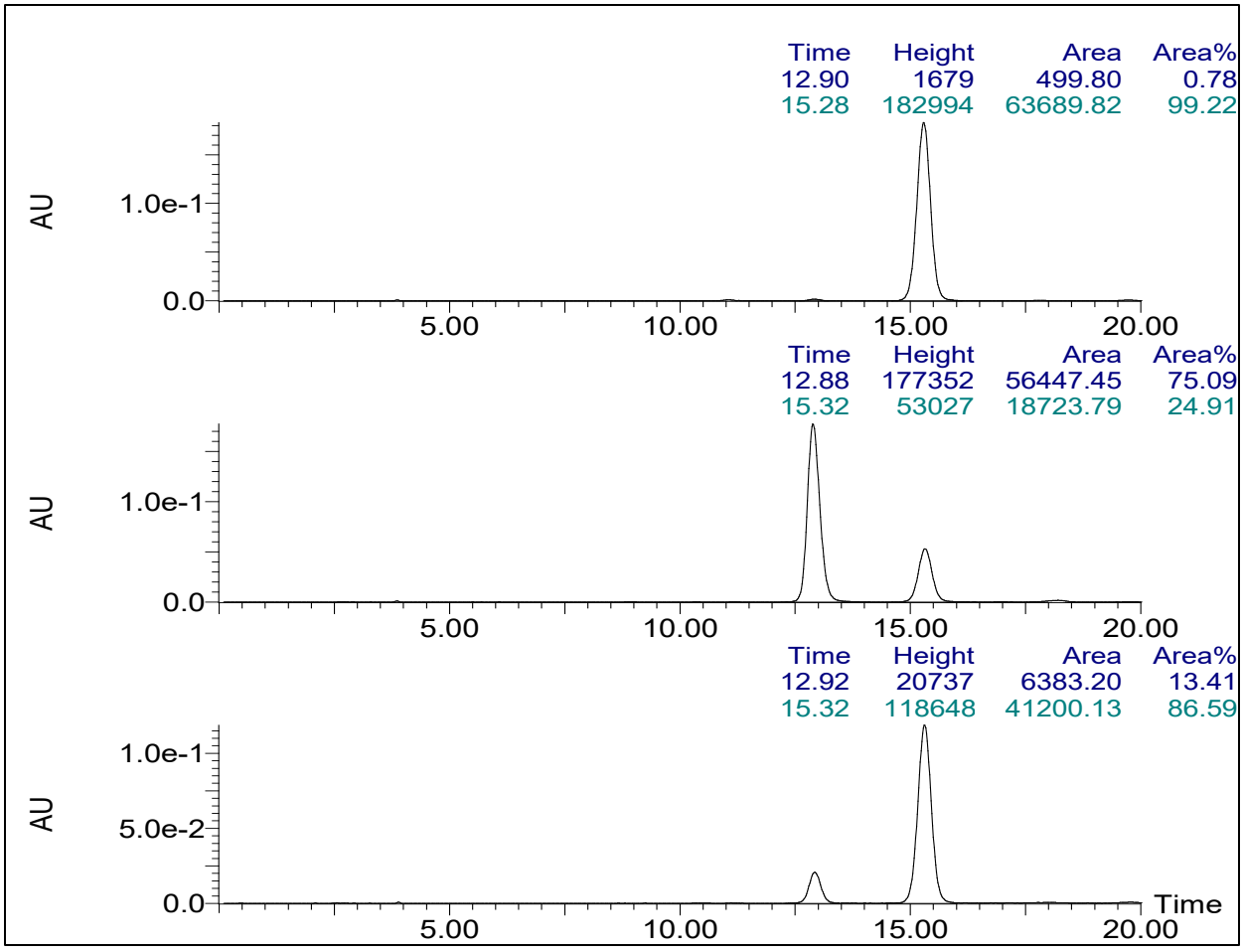

(*Z*)-2-((1H-Pyrrol-2-yl)methylene)benzo[b]thiophen-3(2H)-one (14)

Prepared according to general procedure A.

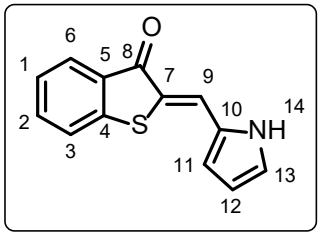

Hemithioindigo **6** (87.0 mg, 0.582 mmol, 1.0 equiv.), EtOH (2.0 mL, 0.291 M), 1H-pyrrole-2-carbaldehyde (56.0 mg, 0.593 mmol, 1.0 equiv.). The solution was purged with N_2 for 10 min before piperidine was added. Stirred for 22 h under Ar at 40°C. Purified by DCVC (0% to 50% EtOAc in *n*-heptane with 5% increments) to afford the title compound (*Z*)-**14** (70.0 mg, 0.308 mmol, 53%) as an orange solid.

The data is in accordance with previously reported work.[136]

TLC: R_f = 0.41 (2:3 EtOAc/*n*-heptane)

LCMS (ESI) $[M+H]^+$ *m/z* calcd for $C_{13}H_{10}NOS^+$: 228.0478, *m/z* found: 228.45 $[M+H]^+$

R_t: 1.69 min (total run time: 2.6 min), purity >98%

^{1}H NMR (800 MHz, DMSO-d_6): δ 11.84 (s, 1H, **H-14**), 7.87 (s, 1H, **H-9**), 7.82 – 7.80 (m, 1H, **H-6**), 7.77 – 7.74 (m, 1H, **H-3**), 7.68 (ddd, *J* = 8.2, 7.1, 1.4 Hz, 1H, **H-1**), 7.37 (m, 1H, **H-2**), 7.28 (td, *J* = 2.6, 1.2 Hz, 1H, **H-13**), 6.79 – 6.76 (m, 1H, **H-11**), 6.42 (dt, *J* = 4.2, 2.3 Hz, 1H, **H-12**)

^{13}C NMR (201 MHz, DMSO-d_6): δ 186.8 (**C-8**), 144.4 (**C-5**), 135.2 (**C-1**), 131.0 (**C-4**), 128.2 (**C-10**), 126.1 (**C-6**), 125.9 (**C-2**), 125.7 (**C-13**), 124.6 (**C-3**), 123.6 (**C-9**), 122.9 (**C-7**), 115.3 (**C-11**), 112.6 (**C-12**)

HRMS-ESI $[M+H]^+$ *m/z* calcd for $C_{13}H_{10}NOS^+$: 228.0478 , *m/z* found: 228.0483 $[M+H]^+$ (ppm error: 2.19)

(*E*)-**14**:

^{1}H NMR (800 MHz, DMSO-d_6): δ 13.31 (s, 1H, **H-14**), 7.90 (ddd, *J* = 7.8, 1.3, 0.7 Hz, 1H, **H-6**), 7.76 (tt, *J* = 3.6, 0.8 Hz, 1H, **H-3**), 7.68 (ddd, *J* = 8.1, 7.0, 1.3 Hz, 2H, **H-1**), 7.64 (s, 1H, **H-9**), 7.45 – 7.43 (m, 1H, **H-13**), 7.39 (ddd, *J* = 8.0, 7.0, 1.0 Hz, 1H, **H-2**), 6.93 (dt, *J* = 3.6, 1.7 Hz, 1H, **H-11**), 6.45 (dt, *J* = 3.7, 2.3 Hz, 1H, **H-12**)

^{13}C NMR (201 MHz, DMSO-d_6): δ 184.7 (**C-8**), 145.1 (**C-5**), 134.4 (**C-1**), 132.6 (**C-4**), 130.5 (**C-10**), 130.0 (**C-9**), 127.0 (**C-13**), 126.2 (**C-6**), 125.0 (**C-2**), 124.1 (**C-3**), 122.0 (**C-11**), 121.4 (**C-7**), 112.8 (**C-12**)

Note: A 1:2 (*Z*/*E*)-ratio was observed for (*E*)-**14** by ^{1}H NMR.

UV-Vis spectroscopy

HTI pyrrole (**14**) (33 µM in DCM)

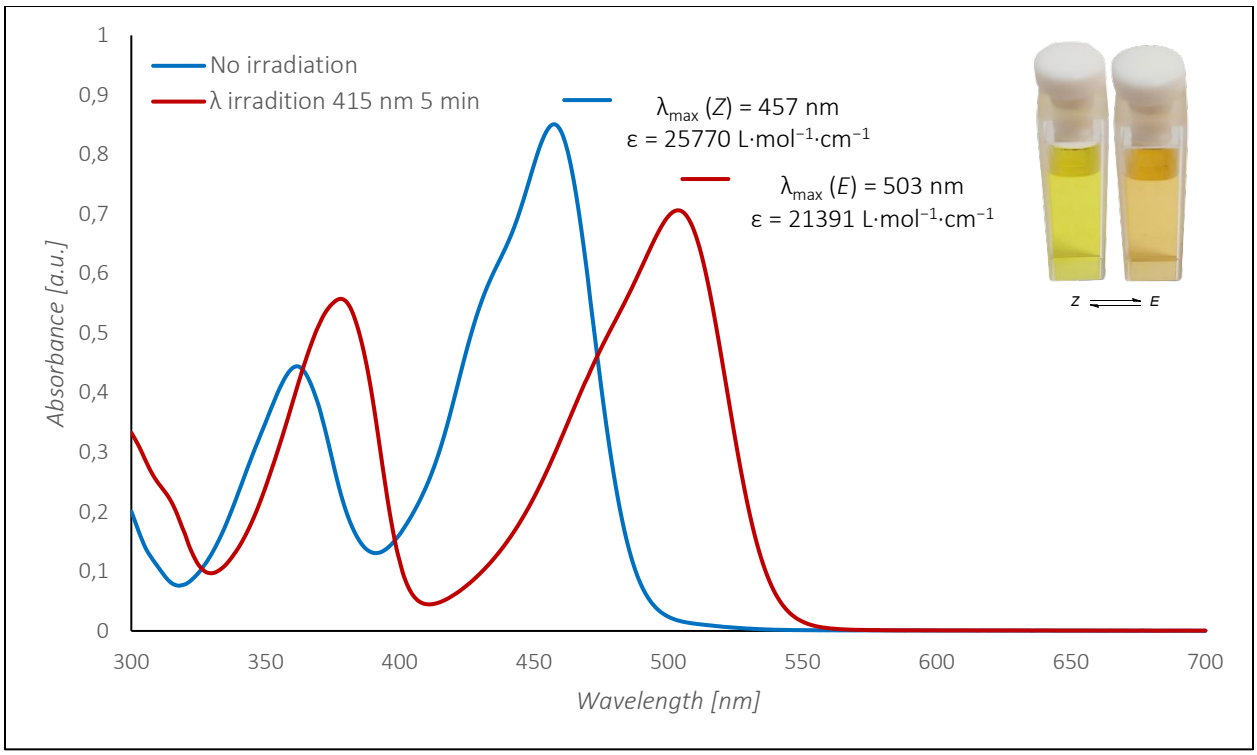

HTI pyrrole (**14**) (33 µM in *n*-hexane/iPrOH 1:1)

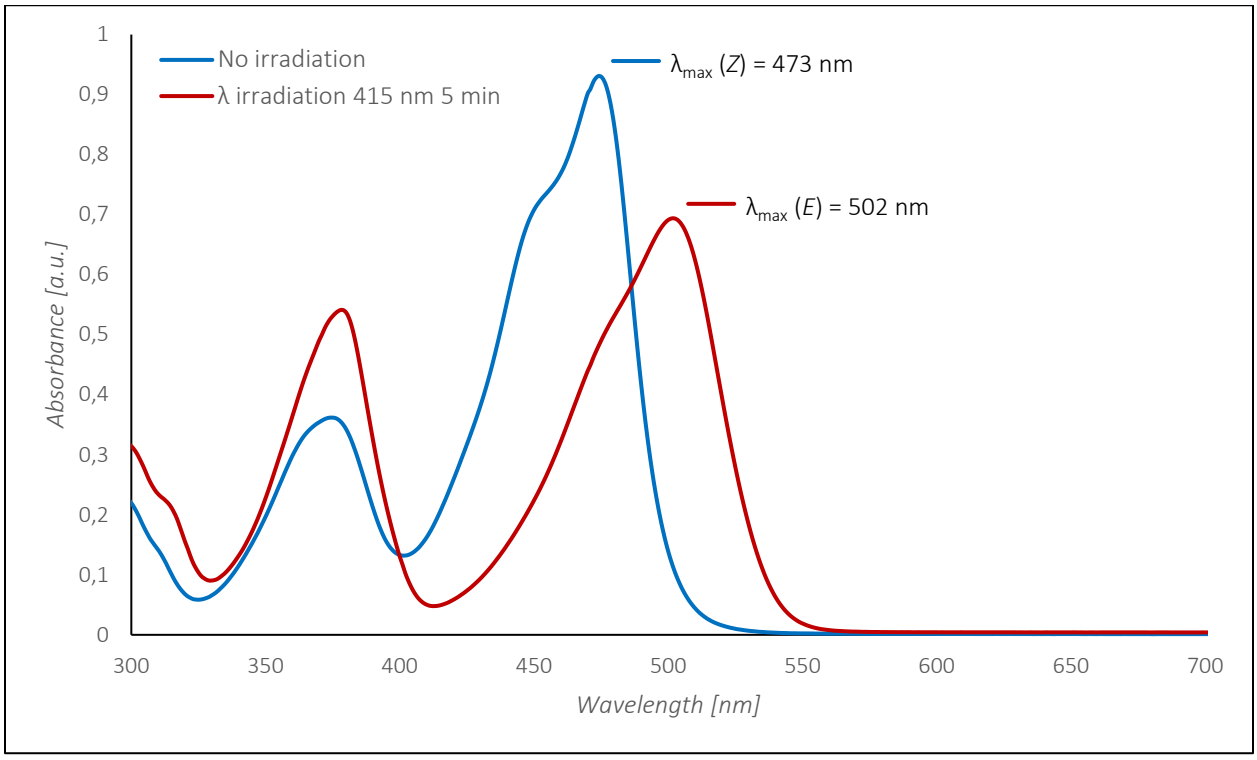

HTI pyrrole (**14**) (33 μM in *n*-hexane/iPrOH 9:1)

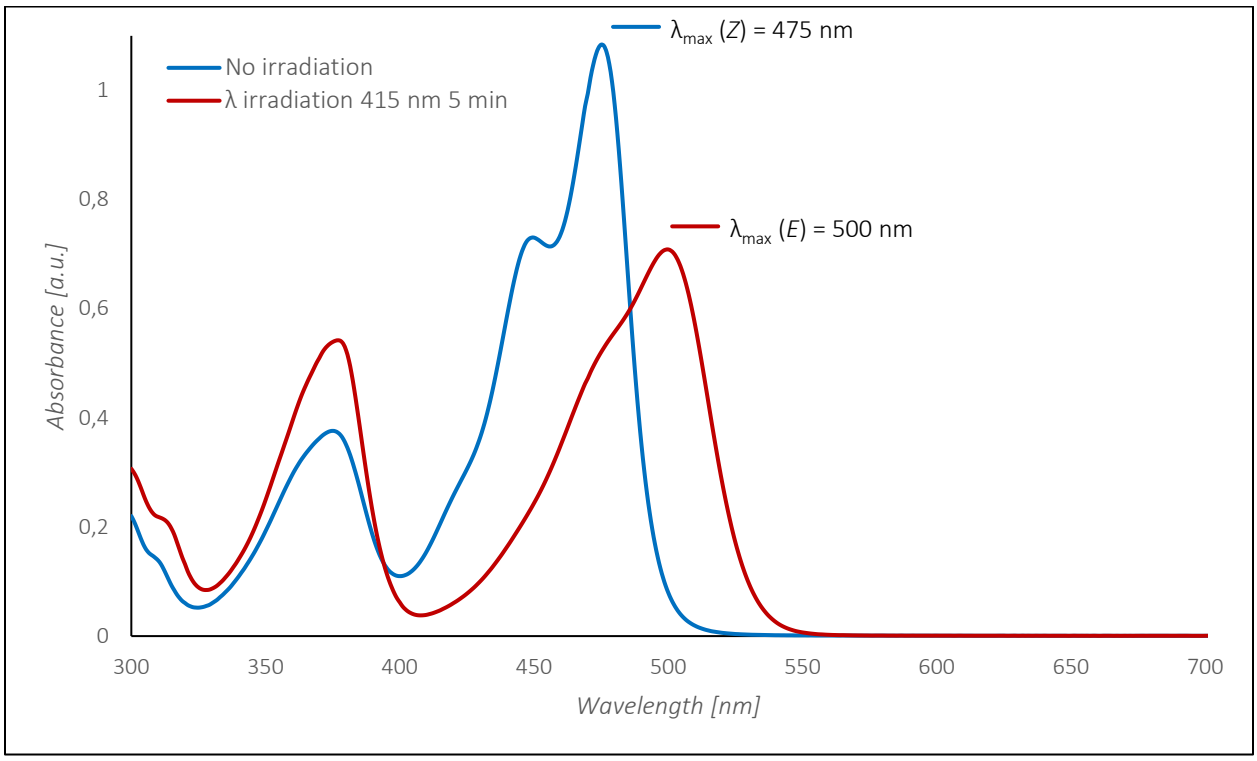

HTI pyrrole (**14**) (33 μM in PhMe)

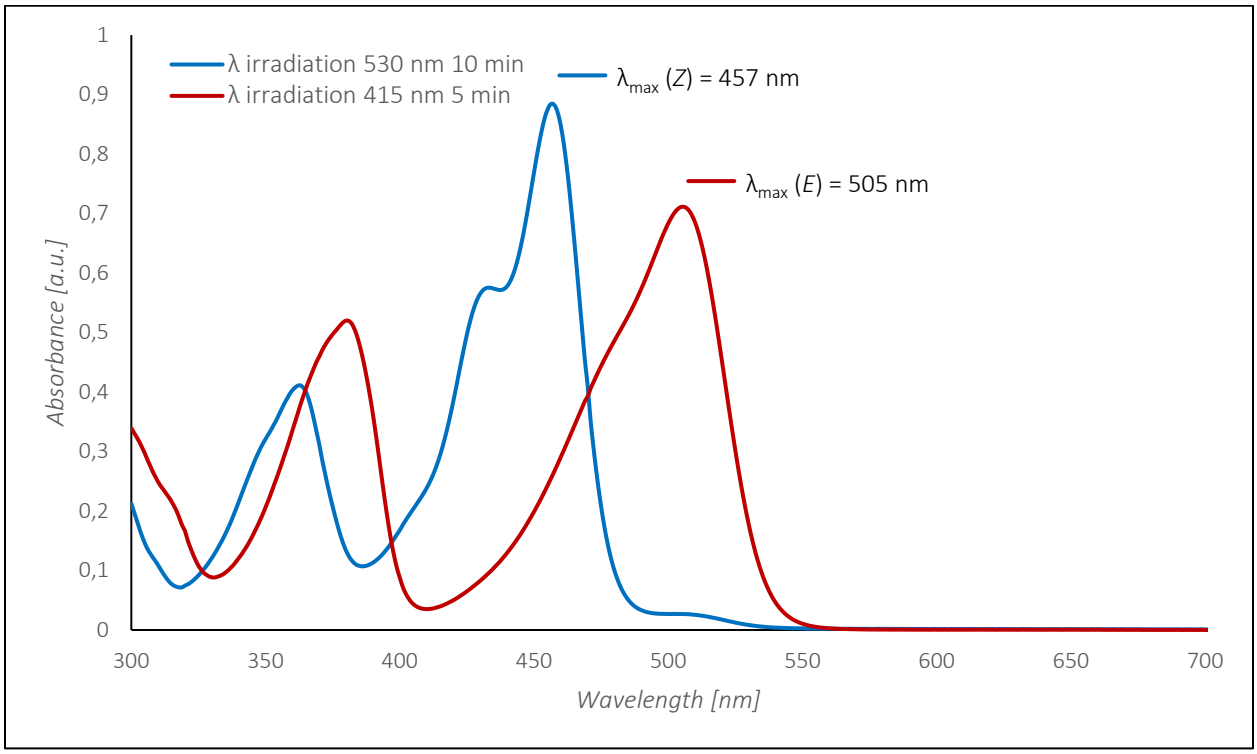

Fluorescence spectroscopy

HTI pyrrole (**14**) (33 µM in DCM)

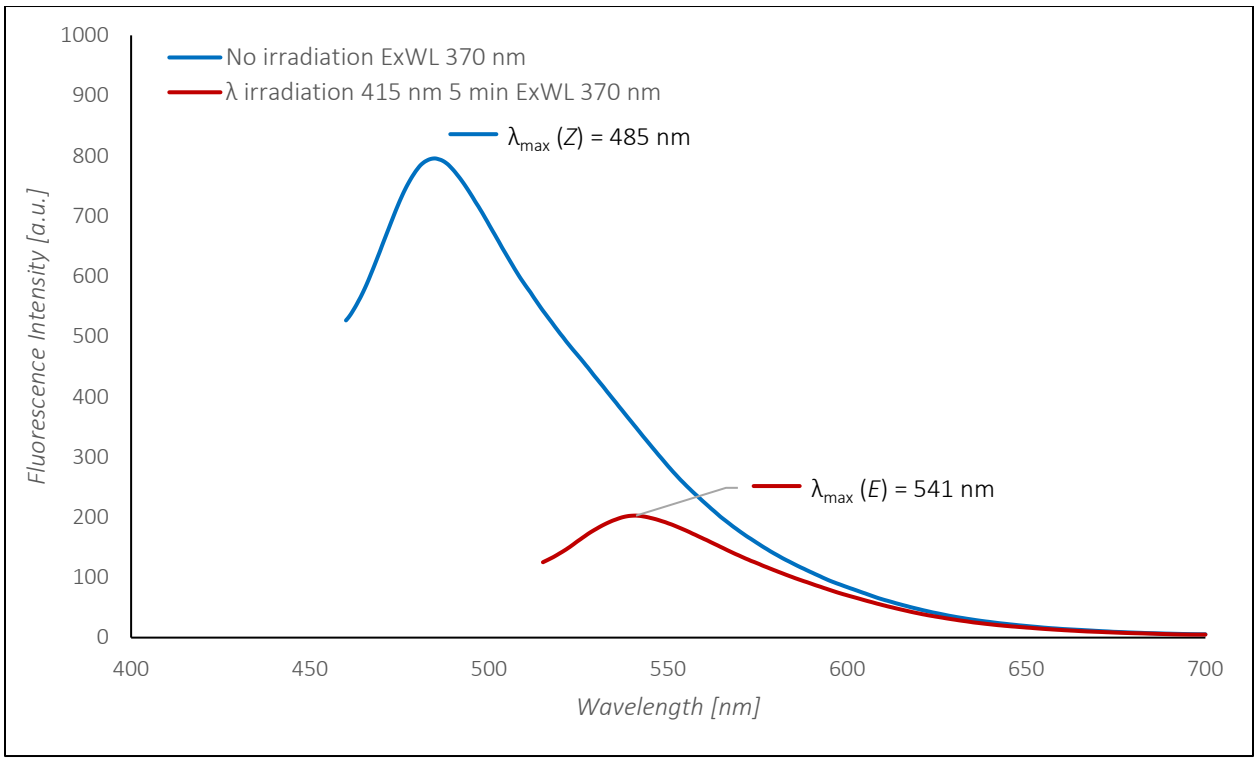

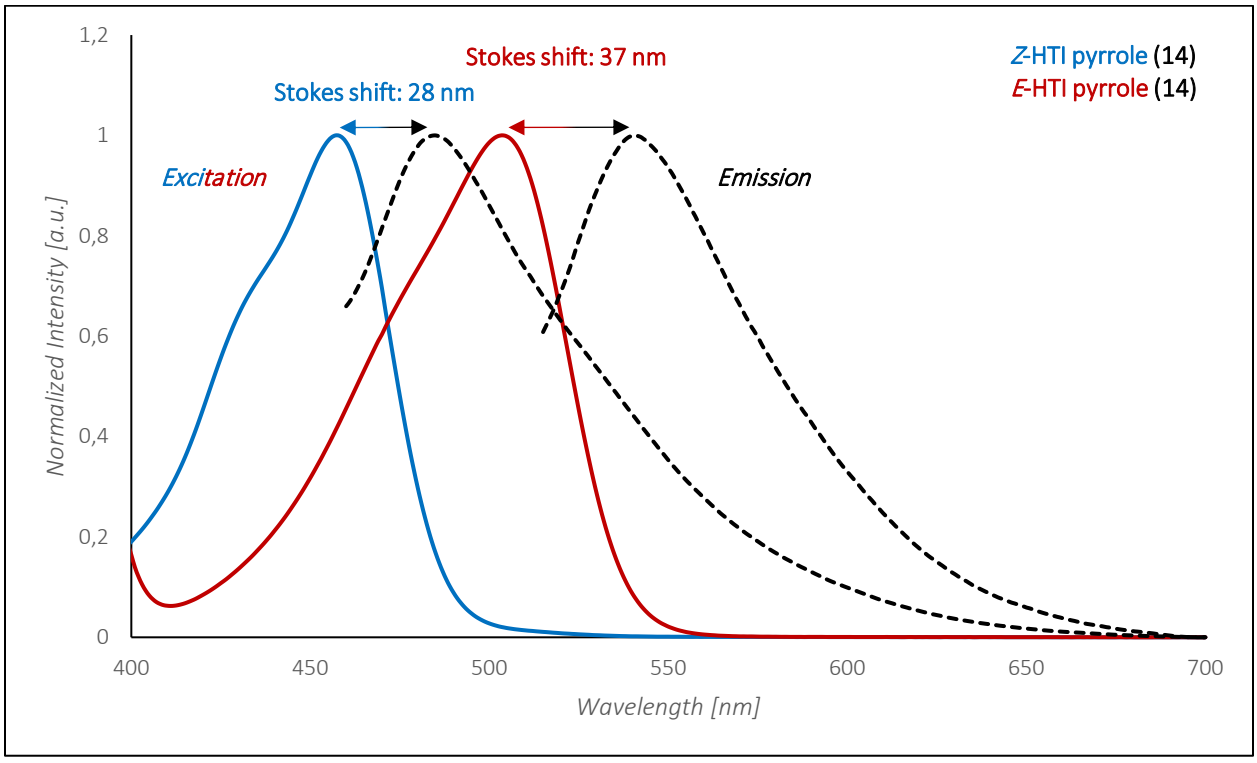

UV-Vis thermal relaxation spectroscopy

HTI pyrrole (**14**) (33 μM in PhMe)

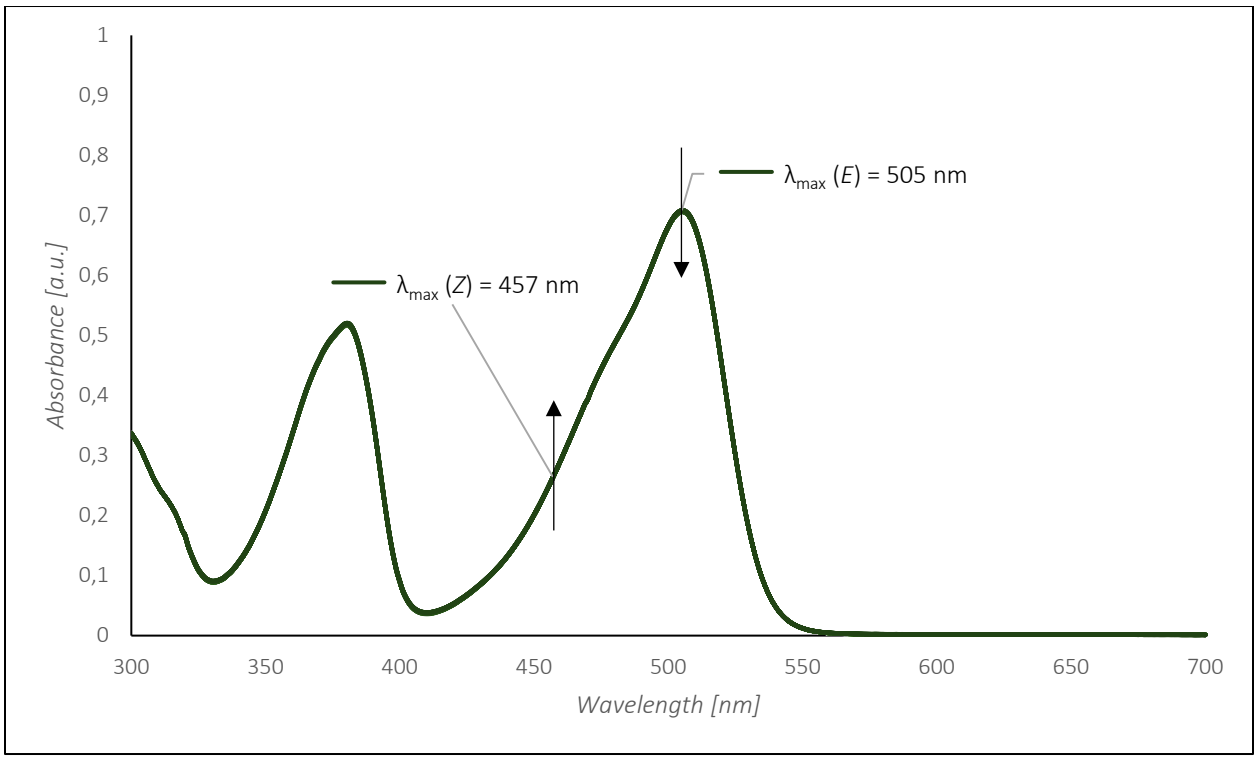

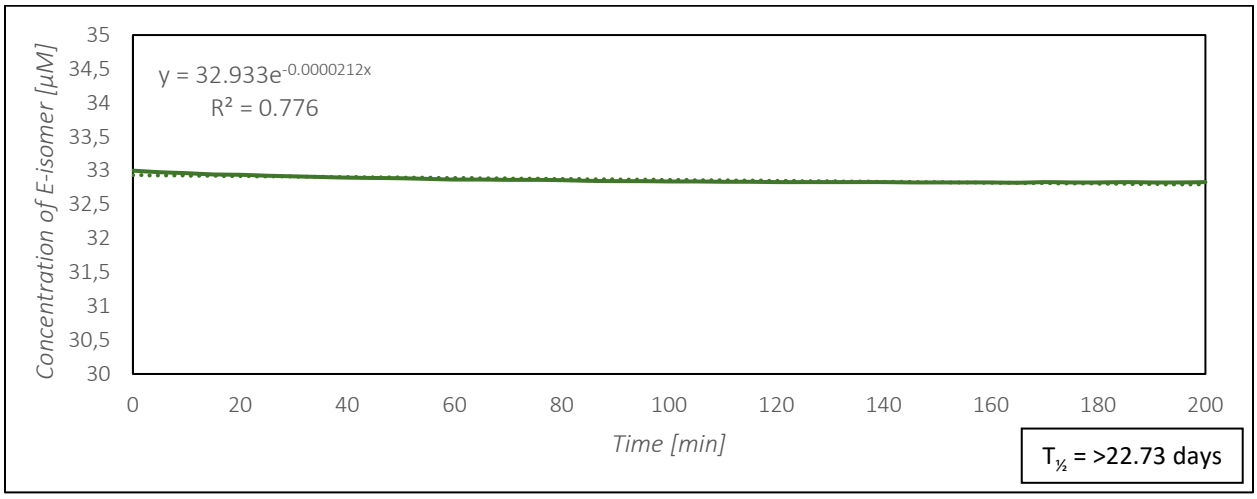

HPLC conditions

Column:	ChiralPak AD-H column (5 μm, 250 x 4.6 mm)
Mobile Phase	90:10 *n*-hexane/iPrOH (isocratic, 1 mL/min)
Isosbestic Point	486 nm (in HPLC mobile Phase)
t_R(E)	7.37 min
t_R(Z)	12.38 min

Solution composition (%*E*-isomer)

Initial solution composition before irradiation: *E*-isomer (0.86%) / *Z*-isomer (99.14%)

Time	415 nm	530 nm
10 min	88.04	2.54
20 min	95.93	3.75

Representative HPLC traces

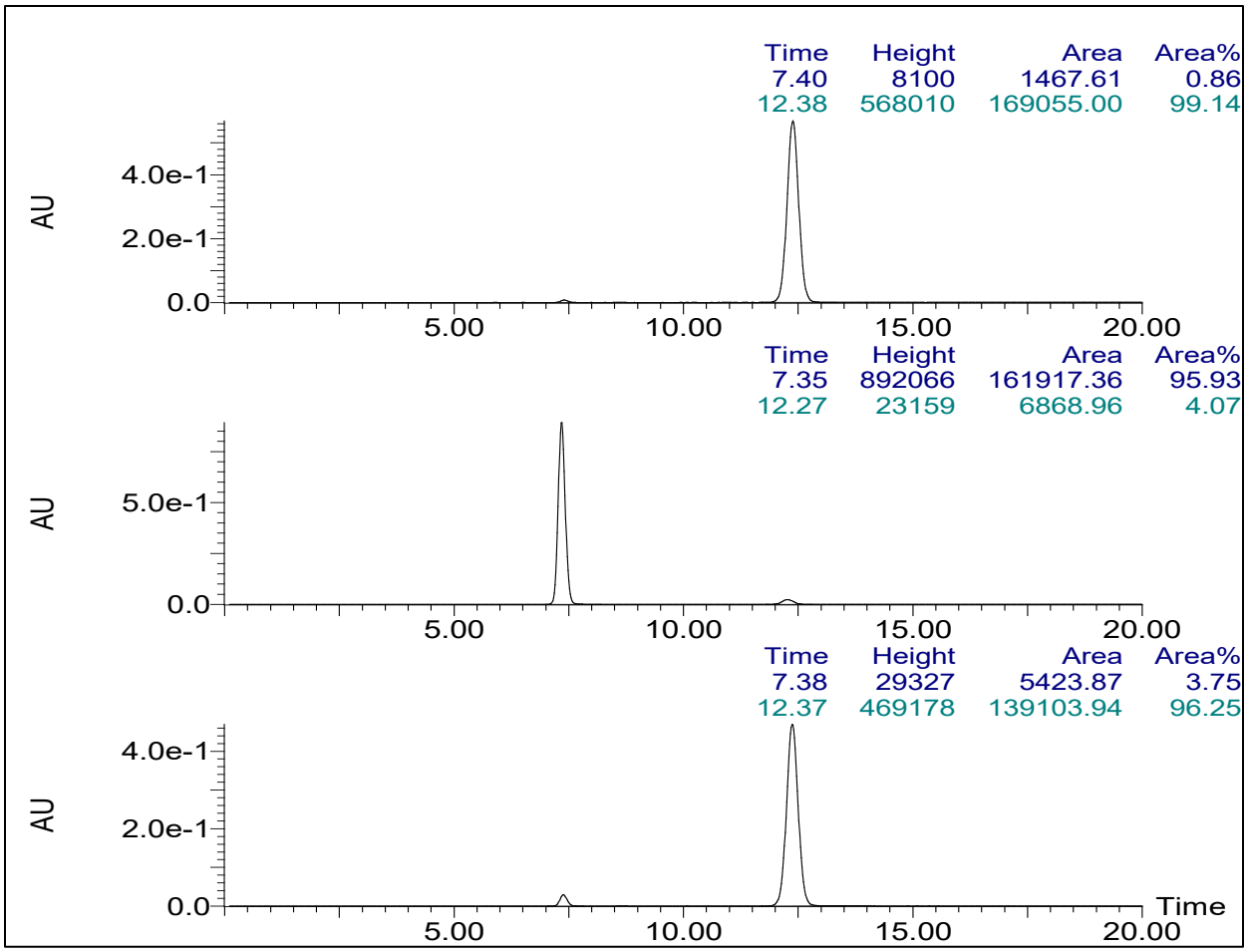

(*Z*)-2-((1H-Indol-2-yl)methylene)benzo[b]thiophen-3(2H)-one (15)

Prepared according to general procedure A.

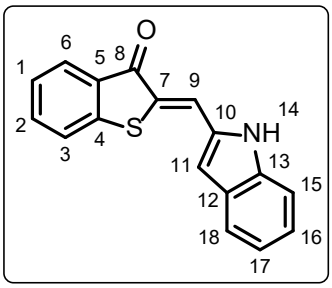

Hemithioindigo **6** (89.0 mg, 0.594 mmol, 1.0 equiv.), benzene (2.0 mL, 0.297 M), indole-2-carbaldehyde (73.0 mg, 0.504 mmol, 0.85 equiv.). The solution was purged with N_2 for 10 min before piperidine was added. Stirred for 17 h under Ar at 40°C. Purified by DCVC (0% to 100% EtOAc in *n*-heptane with 5% increments) to afford the title compound (*Z*)-**15** (116 mg, 0.419 mmol, 83%) as a bordeaux red solid.

TLC: R_f = 0.24 (1:3 EtOAc/*n*-heptane)

LCMS (ESI) $[M+H]^+$ *m/z* calcd for $C_{17}H_{12}NOS^+$: 278.0634, *m/z* found: 278.50 $[M+H]^+$

R_t: 2.09 min (total run time: 2.6 min), purity >98%

^{1}H NMR (800 MHz, DMSO-d_6): δ 11.75 (s, 1H, **H-14**), 7.95 (m, 1H, **H-9**), 7.87 (ddd, *J* = 7.6, 1.3, 0.6 Hz, 1H, **H-6**), 7.82 (d, *J* = 7.8 Hz, 1H, **H-3**), 7.74 (ddd, *J* = 8.0, 7.2, 1.3 Hz, 1H, **H-1**), 7.71 (dd, *J* = 8.0, 1.0 Hz, 1H, **H-18**), 7.46 (dd, *J* = 8.2, 1.0 Hz, 1H, **H-15**), 7.42 (td, *J* = 7.4, 0.9 Hz, 1H, **H-2**), 7.25 (ddd, *J* = 8.1, 6.9, 1.1 Hz, 1H, **H-17**), 7.09 (ddd, *J* = 7.9, 6.9, 1.0 Hz, 1H, **H-16**), 7.07 (m, 1H, **H-11**)

^{13}C NMR (201 MHz, DMSO-d_6): δ 187.0 (**C-8**), 144.5 (**C-5**), 137.9 (**C-12**), 135.9 (**C-1**), 133.1 (**C-10**), 130.3 (**C-4**), 128.7 (**C-7**), 128.6 (**C-13**), 126.5 (**C-6**), 126.3 (**C-2**), 124.7 (**C-3**), 124.7 (**C-17**), 122.9 (**C-9**), 121.6 (**C-18**), 120.5 (**C-16**), 112.0 (**C-15**), 107.4 (**C-11**)

HRMS-ESI $[M+H]^+$ *m/z* calcd for $C_{17}H_{12}NOS^+$: 278.0634 , *m/z* found: 278.0636 $[M+H]^+$ (ppm error: 0.719)

(*E*)-**15**:

^{1}H NMR (400 MHz, DMSO-d_6): δ 12.56 (s, 1H, **H-14**), 7.93 (m, 1H), 7.81 (m, 1H), 7.77 (m, 1H), 7.73 (ddd, *J* = 8.1, 6.2, 1.3 Hz, 1H), 7.70 – 7.67 (m, 2H), 7.42 (m, 1H), 7.32 (ddd, *J* = 8.2, 6.9, 1.1 Hz, 1H), 7.20 (m, 1H), 7.11 (ddd, *J* = 8.1, 7.0, 0.9 Hz, 1H)

Note: A sample of (*Z*)-**15** was irradiated in an LCMS vial in DCM following a solvent exchange to DMSO-d_6. A 1:4 (*Z*/*E*)-ratio was observed for (*E*)-**15** by ^{1}H NMR.

Photoisomerization of an NMR sample performed directly in DMSO-d_6 did not produce the desired (*E*)-isomer in greater than *Z*/*E* 9:1, likely impeded by the viscous properties of DMSO. Switching directly in CD_2Cl_2 afforded clean (*E*)-isomer, however with a loss in ^{1}H NMR spectrum quality.

UV-Vis spectroscopy

HTI indole (**15**) (33 µM in DCM)

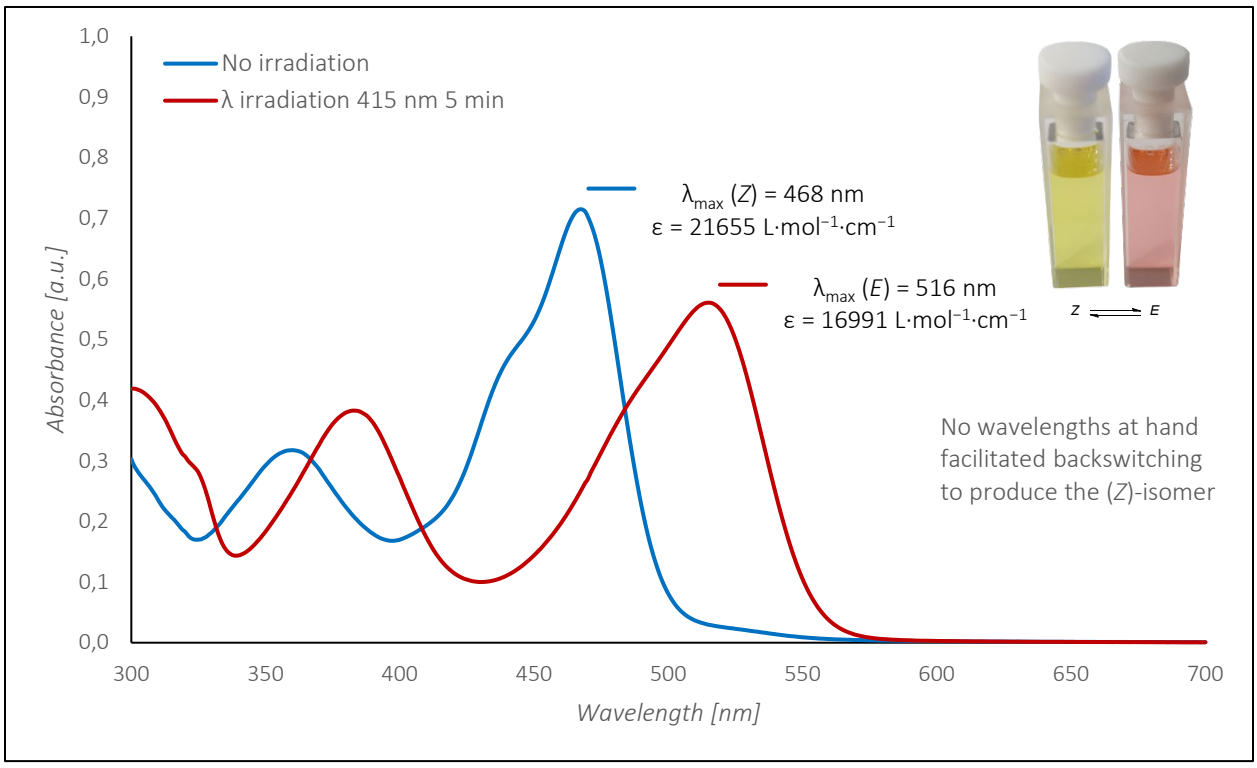

HTI indole (**15**) (33 µM in *n*-hexane/iPrOH 9:1)

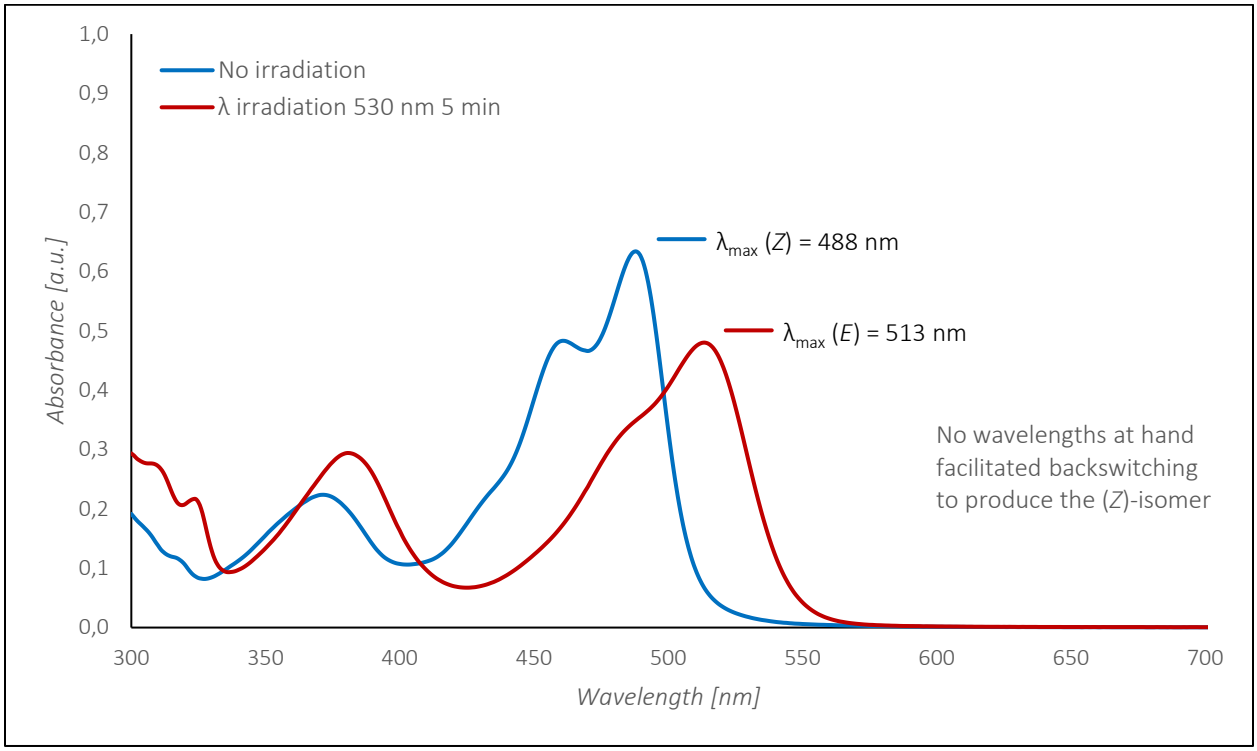

HTI indole (**15**) (33 μM in iPrOH)

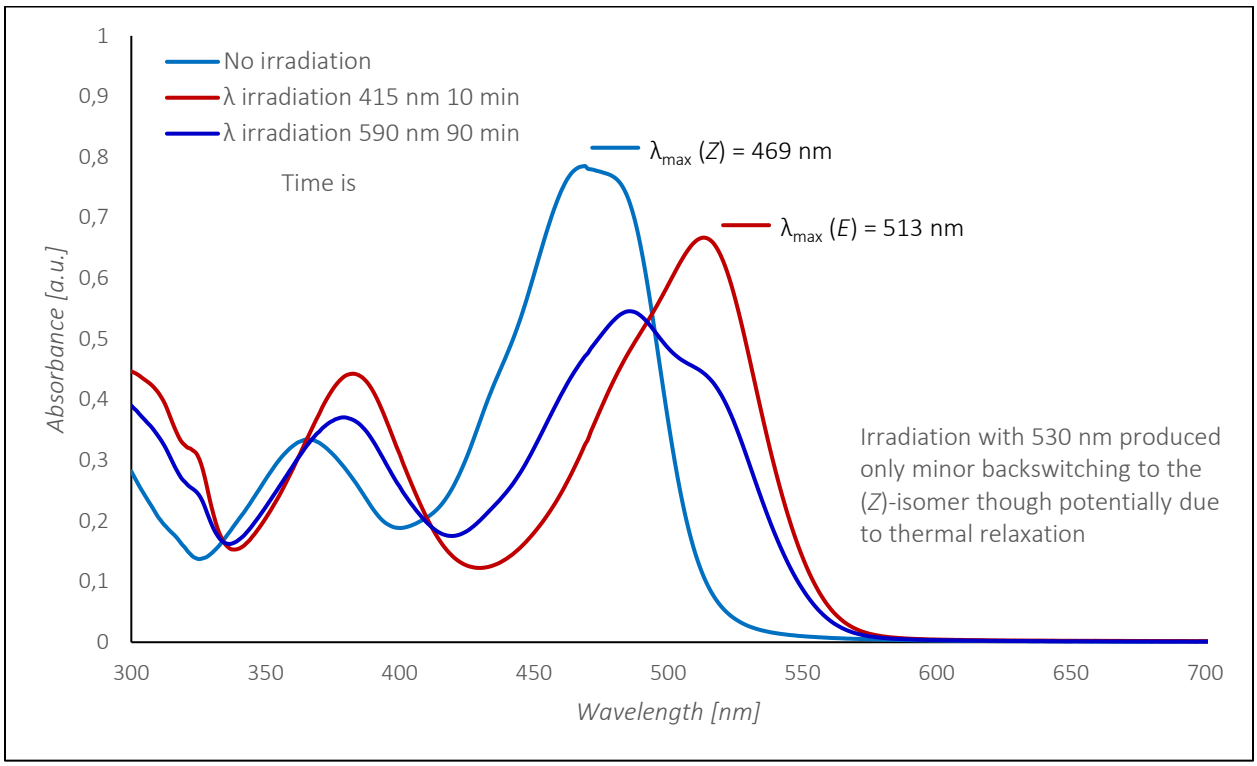

HTI indole (**15**) (33 μM in THF)

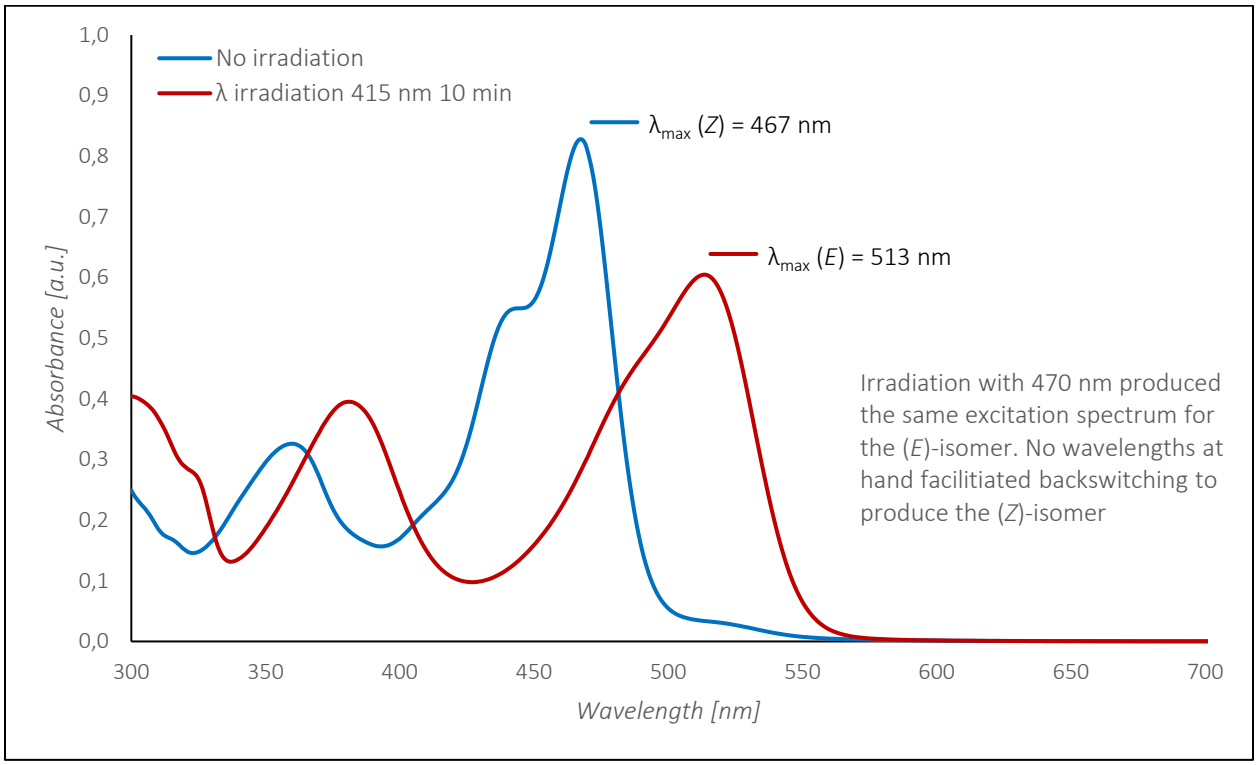

HTI indole (**15**) (33 μM in PhMe)

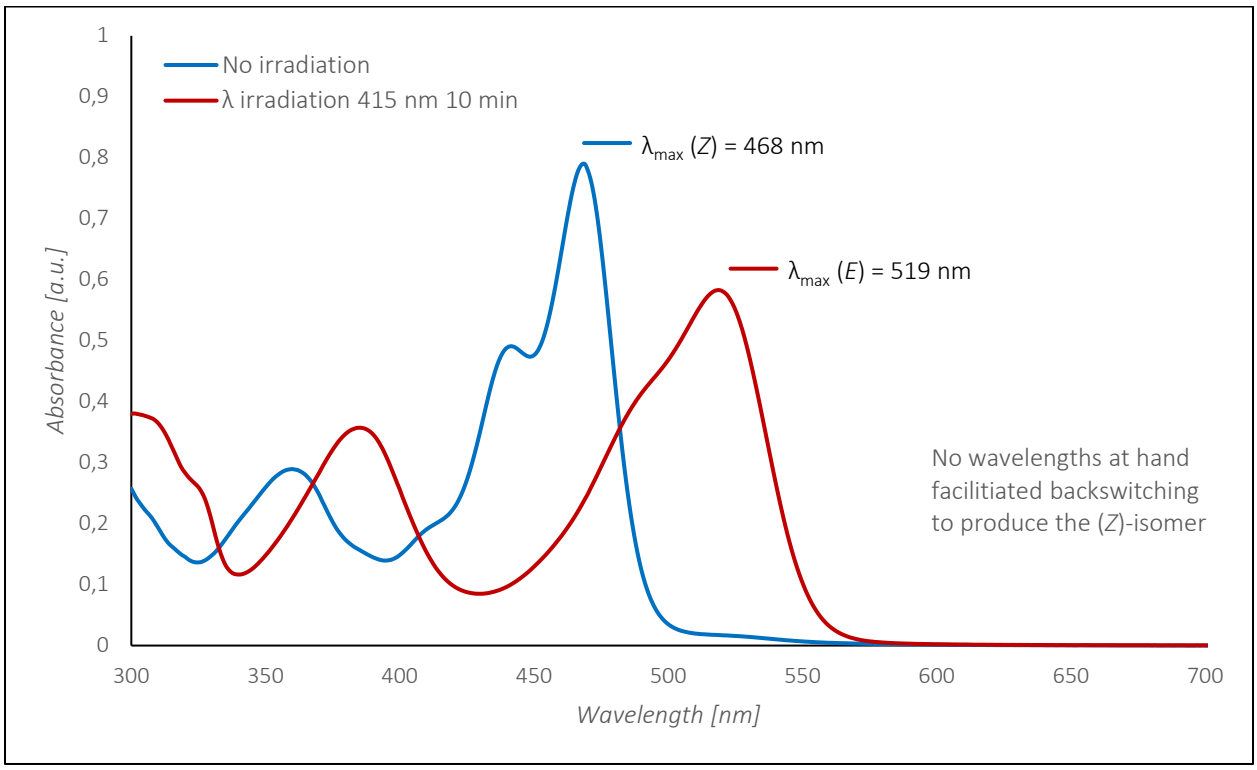

HTI indole (**15**) (33 μM in DMSO)

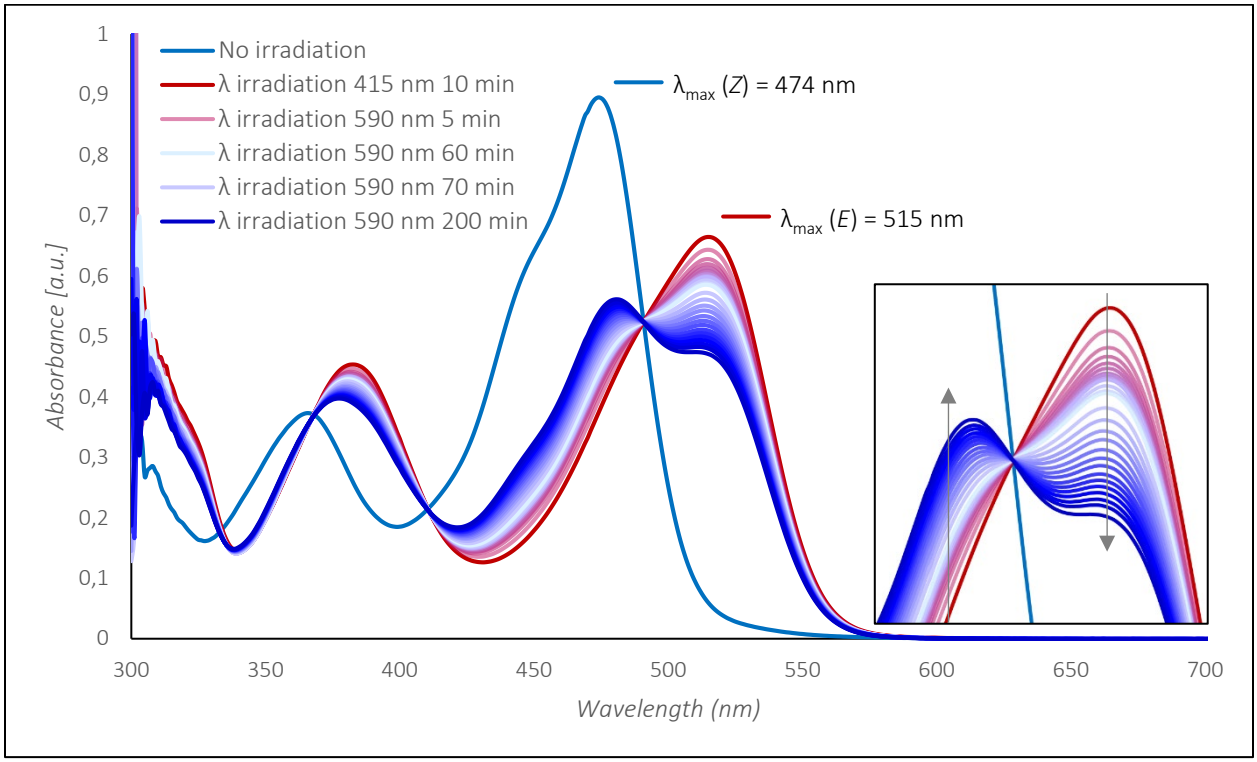

Fluorescence spectroscopy

HTI indole (**15**) (33 μM in DCM)

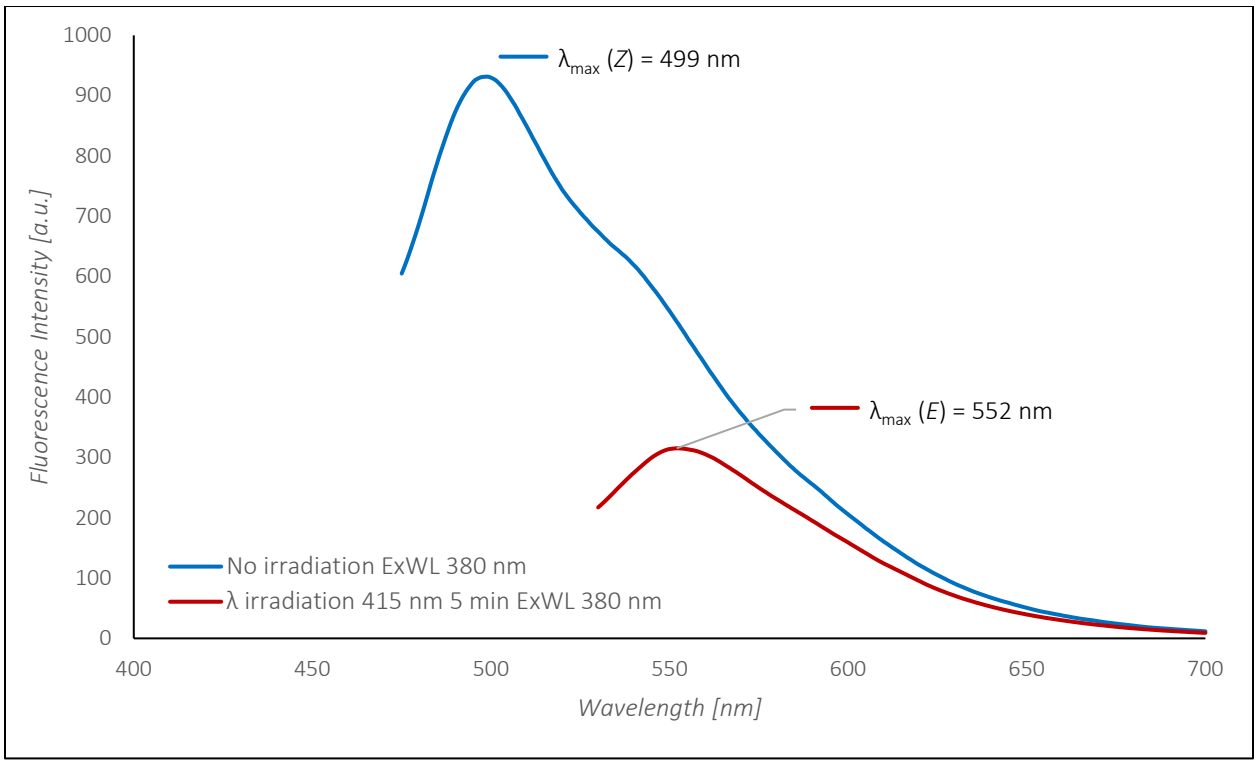

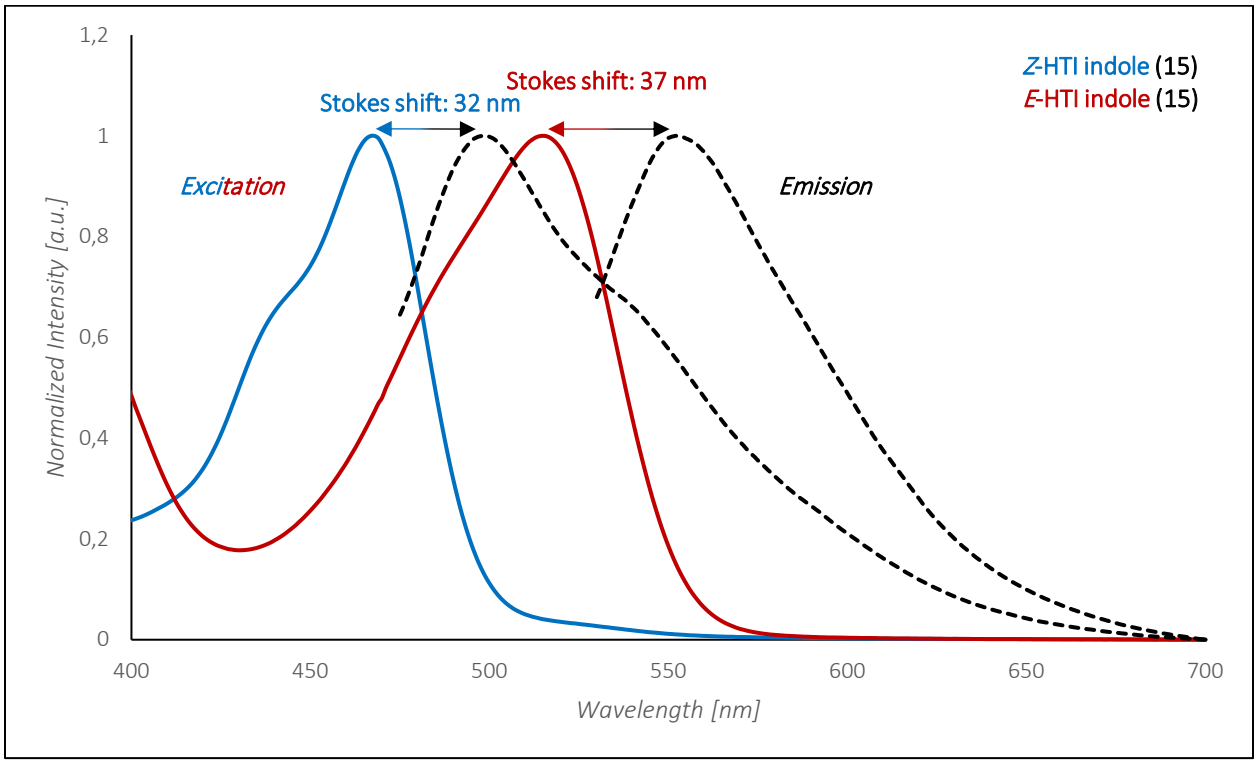

UV-Vis thermal relaxation spectroscopy

HTI indole (**15**) (33 μM in DMSO)

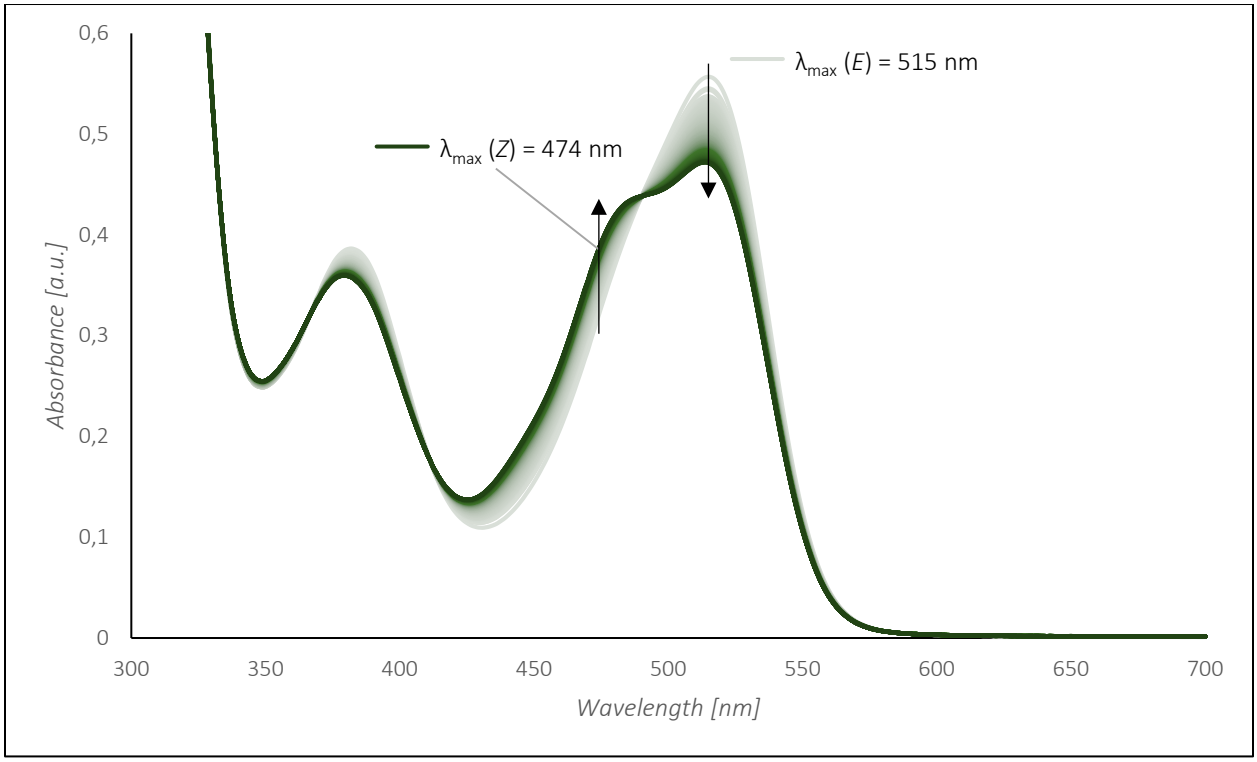

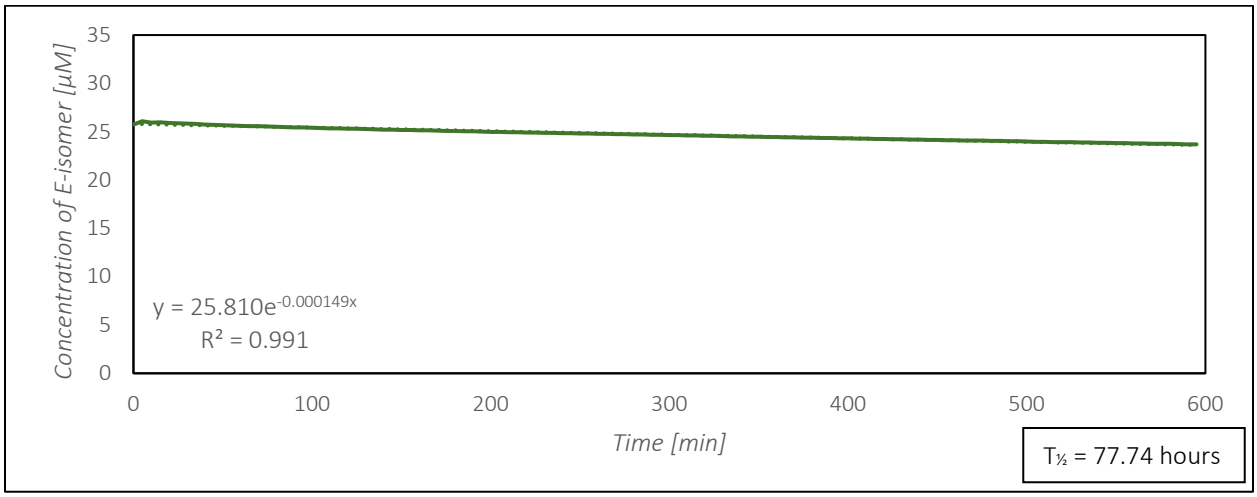

HTI indole (**15**) (33 μM in PhMe)

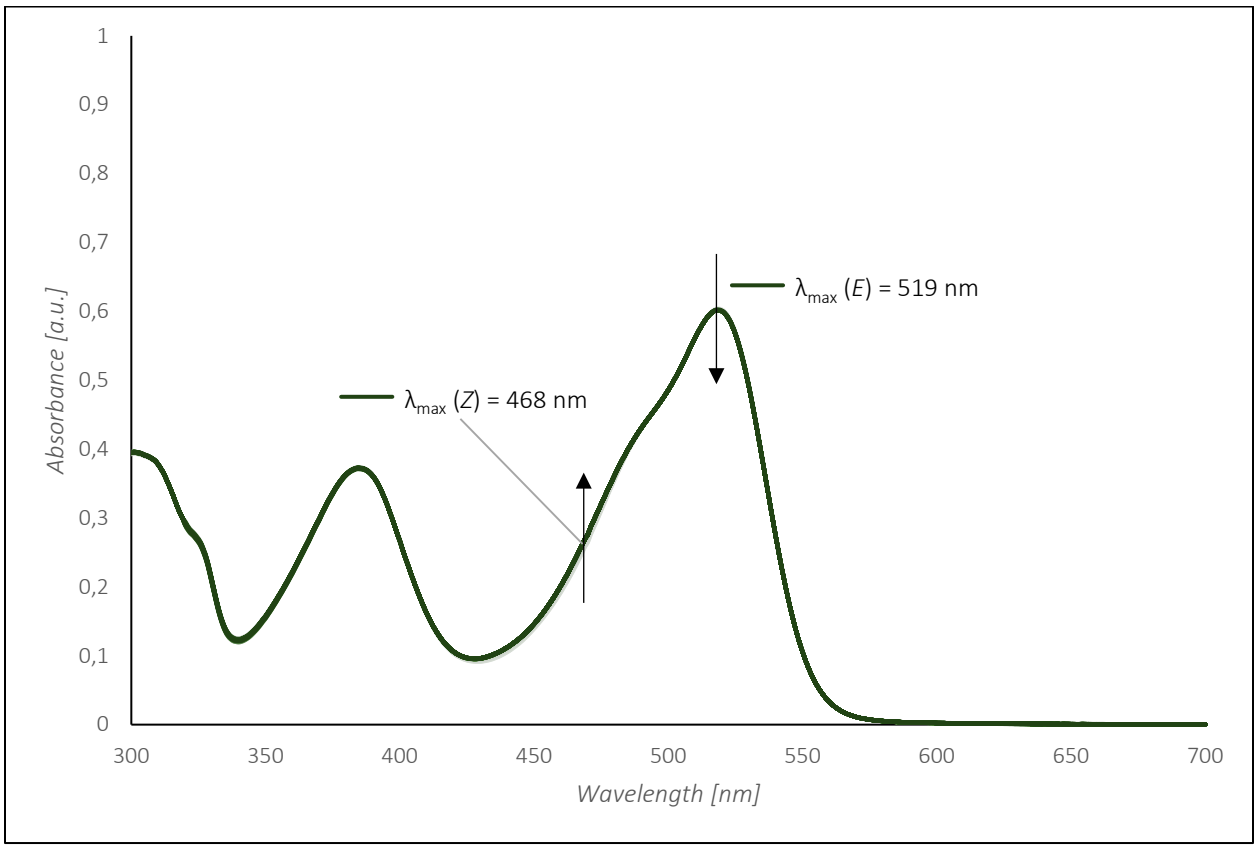

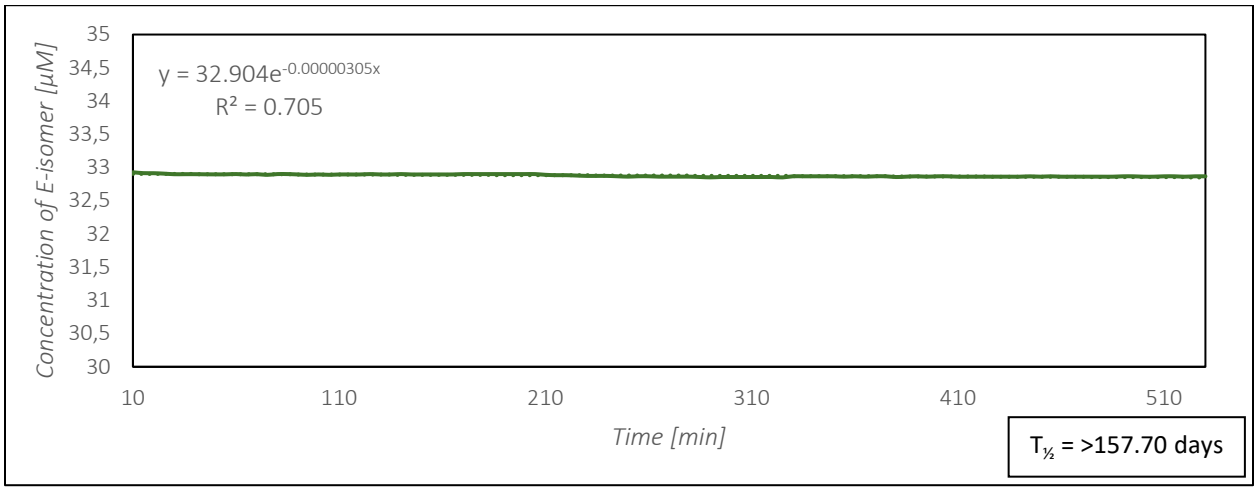

HPLC conditions

Column:	ChiralPak AD-H column (5 μm, 250 x 4.6 mm)
Mobile Phase	90:10 *n*-hexane/iPrOH (isocratic, 1 mL/min)
Isosbestic Point	498 nm (in HPLC mobile Phase)
t_R(E)	8.82 min
t_R(Z)	17.05 min

Solution composition (%*E*-isomer)

Initial solution composition before irradiation: *E*-isomer (2.60%) / *Z*-isomer (97.40%)

Time	415 nm	530 nm
10 min	98.43	94.79
20 min	99.21	96.16

Representative HPLC traces

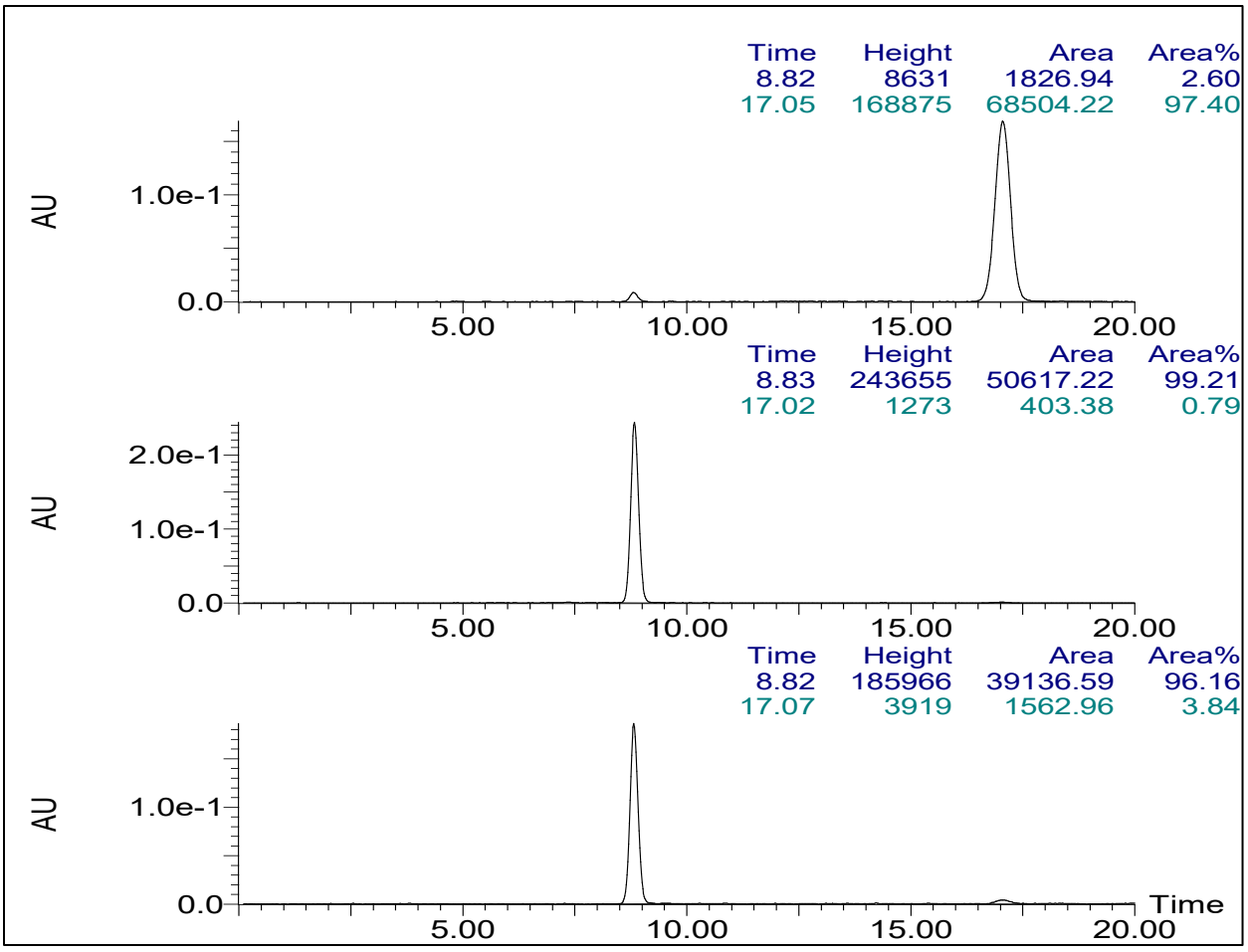

HPLC conditions

Column:	ChiralPak AD-H column (5 μm, 250 x 4.6 mm)
Mobile Phase	90:10 *n*-hexane/iPrOH (isocratic, 1 mL/min)
Isosbestic Point	498 nm (in HPLC mobile Phase)
t_R(E)	8.37-8.65 min
t_R(Z)	14.6-15.75 min

Solution composition (%*E*-isomer)

Initial solution composition before irradiation: *E*-isomer (1.64%) / *Z*-isomer (98.36%)

Time	415 nm	590 nm
10 min	97.88	86.74
20 min	-	80.82
30 min	-	70.83
40 min	-	63.14

Note: Sample prepared (0.66 mg/mL), filtered, irradiated in and measured directly from iPrOH.

Representative HPLC traces

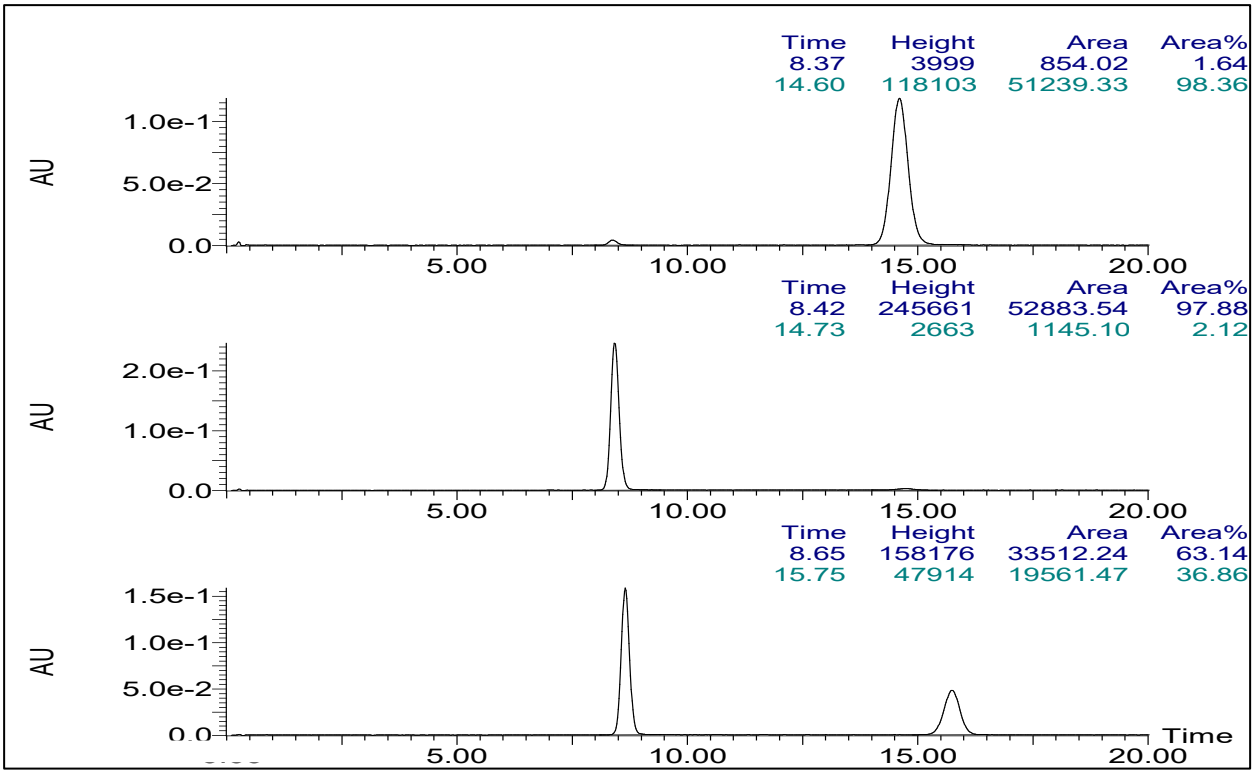

^{1}H NMR thermal relaxation spectroscopy

HTI indole (**15**) (CD_2Cl_2)

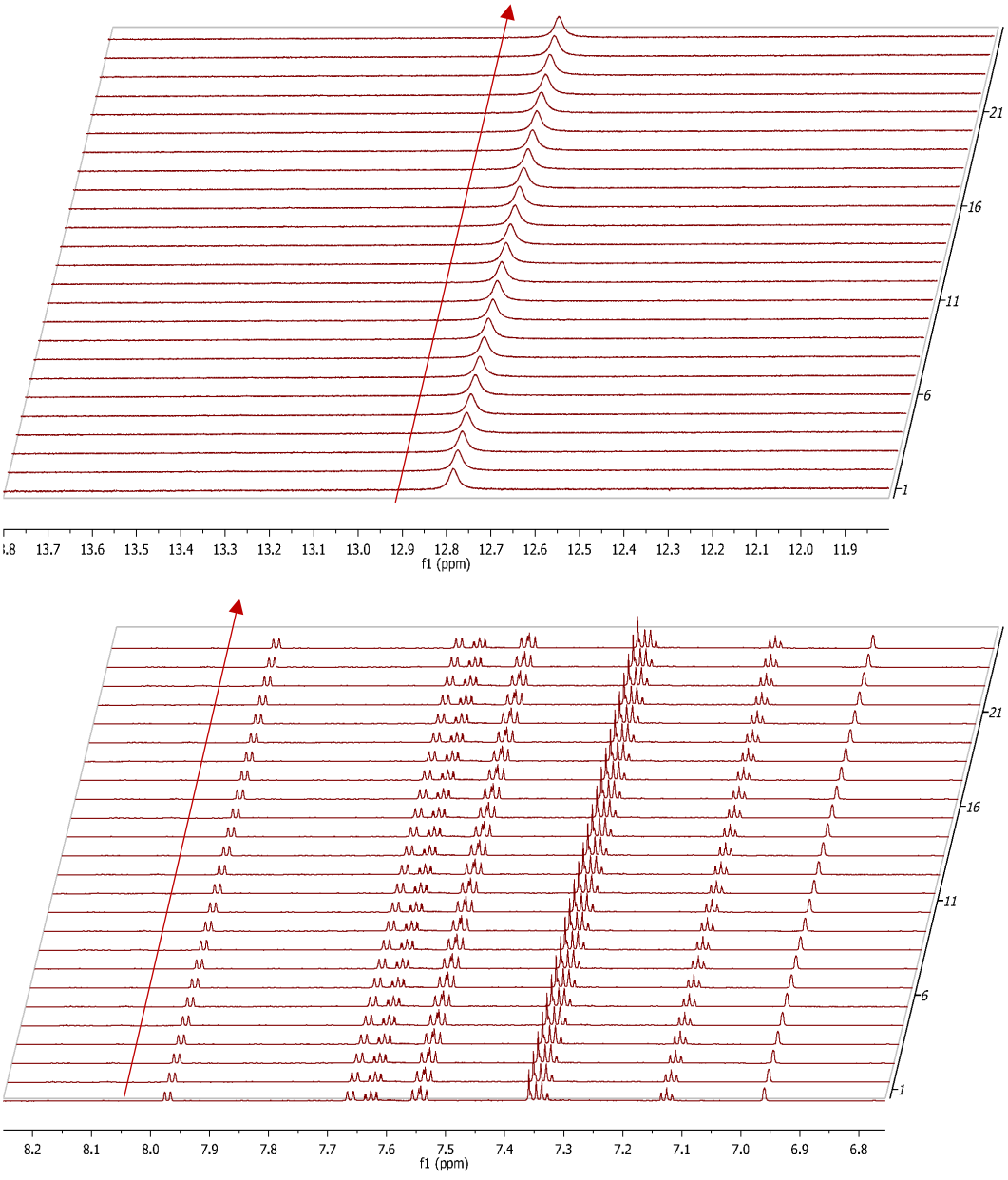

Note: Indole-NH of the (*E*)-**15** at 12.78 ppm plotted vs. time (relaxation).

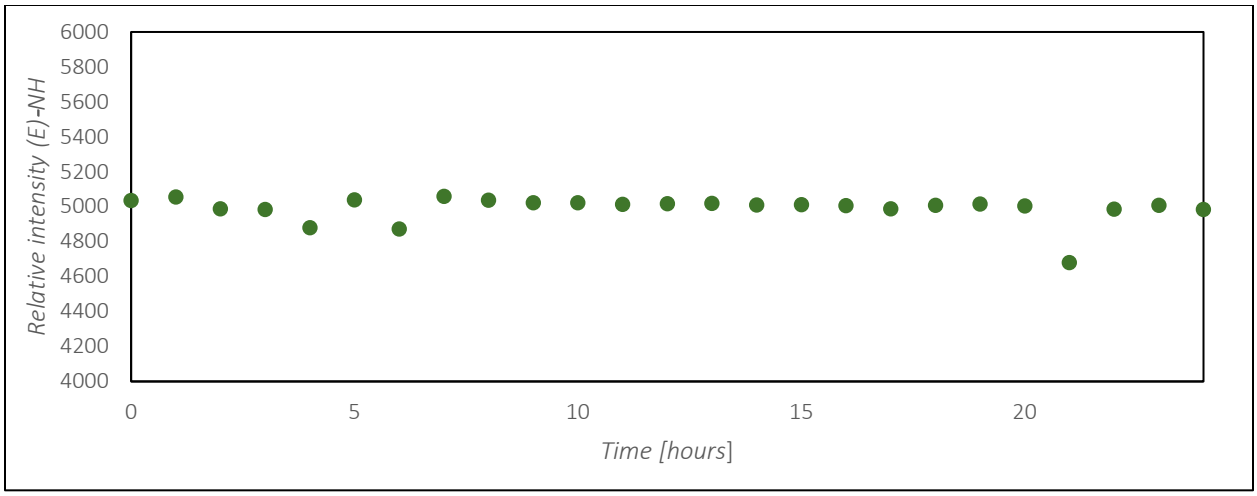

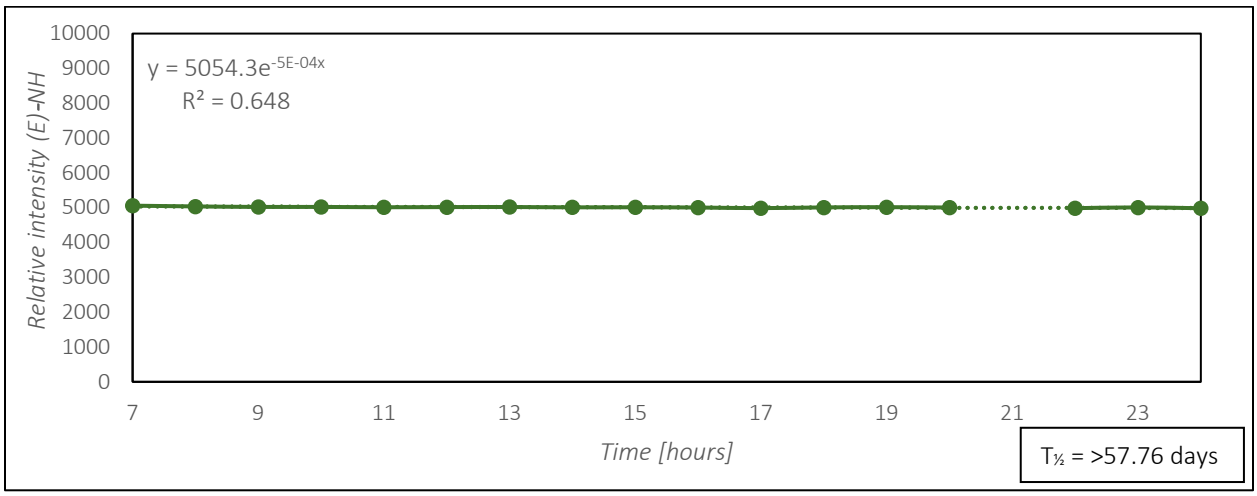

(*Z*)-**15**:

^{1}H NMR (800 MHz, CD_2Cl_2): δ 8.61 (s, 1H), 7.93 (s, 1H), 7.91 (m, 1H), 7.70 (dq, *J* = 8.0, 1.0 Hz, 1H), 7.63 (m, 1H), 7.59 (dt, *J* = 7.8, 0.9 Hz, 1H), 7.46 (dq, *J* = 8.2, 0.9 Hz, 1H), 7.35 (ddd, *J* = 7.9, 7.1, 1.0 Hz, 1H), 7.31 (ddd, *J* = 8.1, 6.9, 1.1 Hz, 1H), 7.16 (ddd, *J* = 7.9, 7.0, 1.0 Hz, 1H), 7.12 (m, 1H)

(*E*)-**15**:

^{1}H NMR (800 MHz, CD_2Cl_2): δ 12.78 (s, 1H), 7.97 (ddd, *J* = 7.8, 1.3, 0.7 Hz, 1H), 7.66 (dq, *J* = 8.1, 1.0 Hz, 1H), 7.63 (ddd, *J* = 8.3, 7.1, 1.3 Hz, 1H), 7.55 (m, 1H), 7.54 (dt, *J* = 7.9, 0.9 Hz, 1H), 7.36 (s, 1H), 7.35 (m, 1H), 7.33 (m, 1H), 7.13 (ddd, *J* = 7.9, 6.8, 0.9 Hz, 1H), 7.96 (m, 1H)

(*Z*)-2-((1H-Pyrrol-2-yl)methylene)naphtho[2,1-b]thiophen-1(2H)-one (16)

Prepared according to general procedure B.

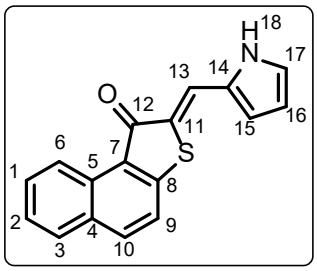

Hemithioindigo derivative **5** (93.5 mg, 0.467 mmol, 1.0 equiv.), PhMe (2.0 mL, 0.234 M) and pyrrole-2-carbaldehyde (44.4 mg, 0.467 mmol, 1.0 equiv.). Stirred for 3 h under Ar at 40°C. Afforded the title compound (*Z*)-**16** (107 mg, 0.385 mmol, 82%) as an orange solid.

TLC: R_f = 0.61 (1:1 EtOAc/*n*-heptane)

LCMS (ESI) $[M+H]^+$ *m/z* calcd for $C_{17}H_{12}NOS^+$: 278.0634, *m/z* found: 278.27 $[M+H]^+$

R_t: 2.10 min (total run time: 2.6 min), purity >99%

^{1}H NMR (800 MHz, DMSO-d_6): δ 11.90 (s, 1H, **H-18**), 9.29 (d, *J* = 8.3 Hz, 1H, **H-6**), 8.23 (d, *J* = 8.6 Hz, 1H, **H-10**), 8.05 (d, *J* = 8.1 Hz, 1H, **H-3**), 7.95 (s, 1H, **H-13**), 7.87 (d, *J* = 8.6 Hz, 1H, **H-9**), 7.74 (t, *J* = 7.6 Hz, 1H, **H-1**), 7.60 (t, *J* = 7.4 Hz, 1H, **H-2**), 7.31 (s, 1H, **H-15**), 6.84 (s, 1H, **H-17**), 6.45 (s, 1H, **H-16**)

^{13}C NMR (201 MHz, DMSO-d_6): δ 187.3 (**C-12**), 148.0 (**C-8**), 135.7 (**C-10**), 131.4 (**C-4/5**), 130.5 (**C-4/5**), 129.4 (**C-1**), 128.8 (**C-3**), 128.1 (**C-14**), 126.2 (**C-2**), 125.7 (**C-15**), 124.2 (**C-13**), 123.4 (**C-7/11**), 123.4 (**C-7/11**), 122.3 (**C-9**), 122.1 (**C-6**), 115.1 (**C-17**), 112.6 (**C-16**)

HRMS-ESI $[M+H]^+$ *m/z* calcd for $C_{17}H_{12}NOS^+$: 278.0634, *m/z* found: 278.0635 $[M+H]^+$ (ppm error: 0.360)

Melting point: 245-250°C (decomposes)

UV-Vis spectroscopy

2-Pyrrole HTI derivative (**16**) (33 µM in DCM)

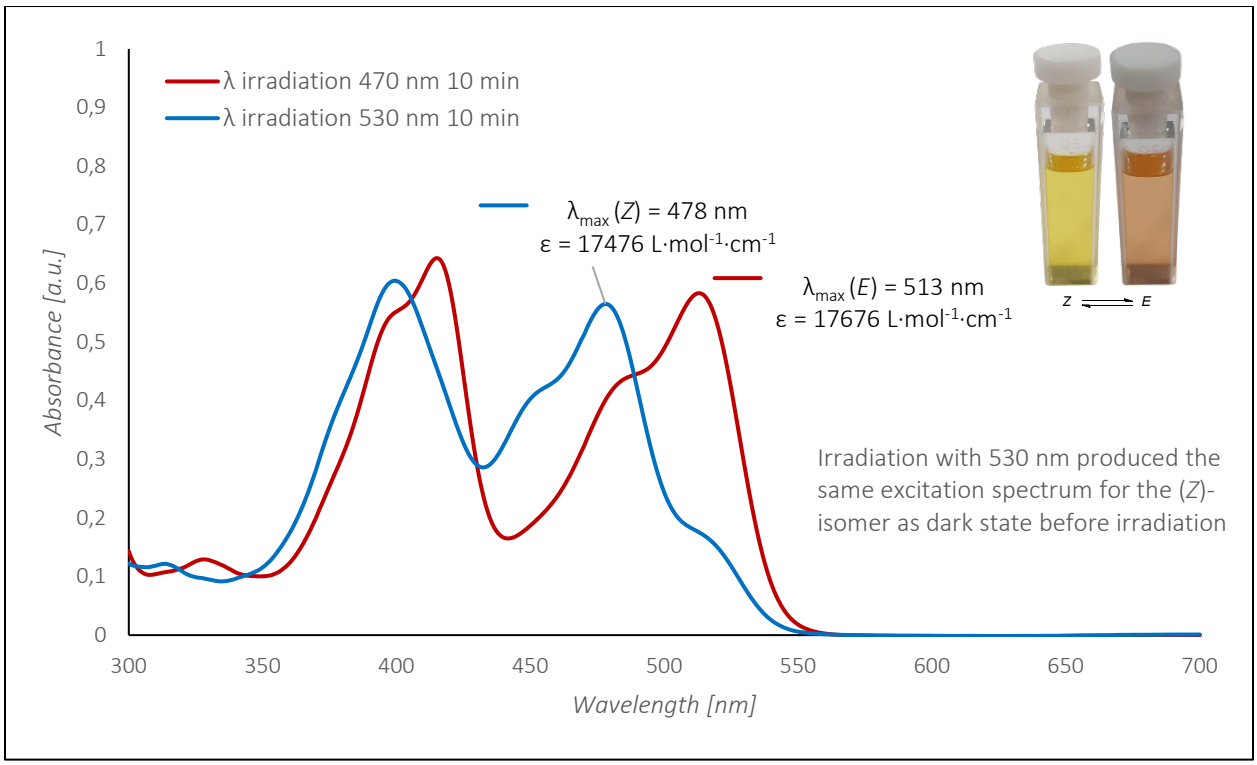

2-Pyrrole HTI derivative (**16**) (33 µM in *n*-hexane/iPrOH 9:1)

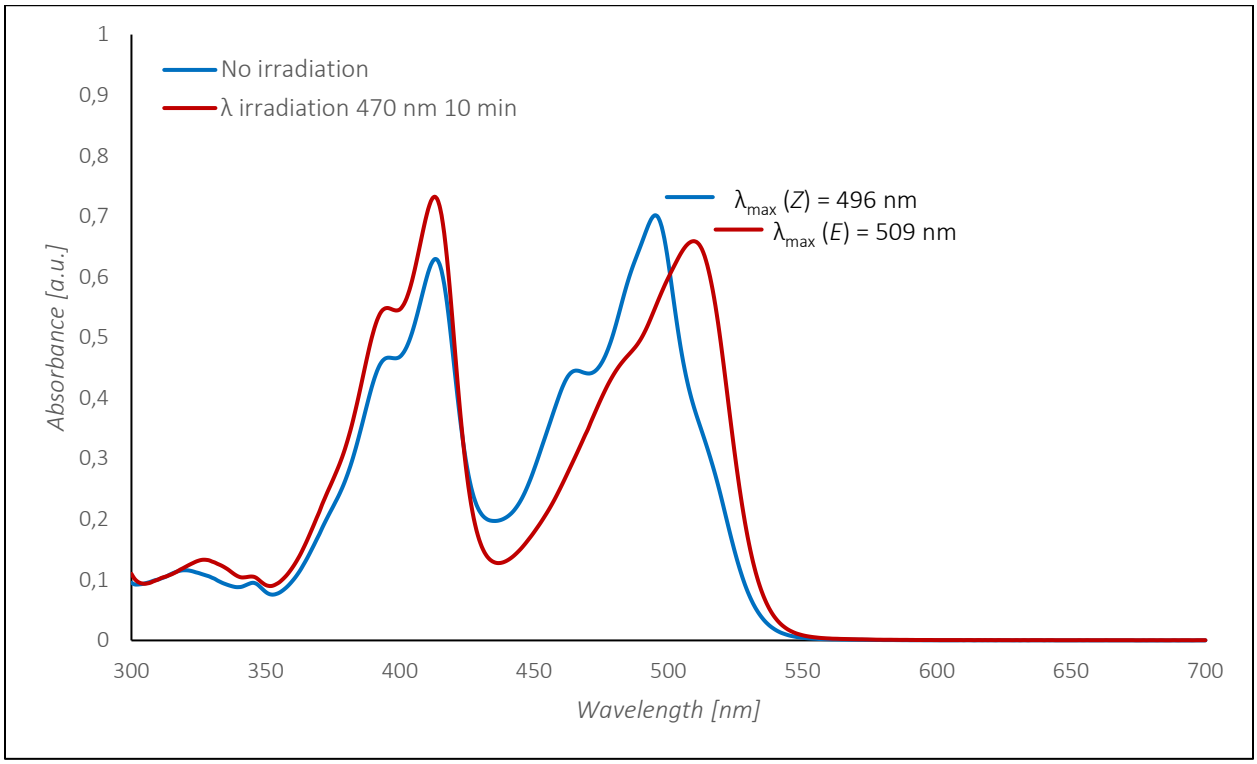

2-Pyrrole HTI derivative (**16**) (33 μM in PhMe)

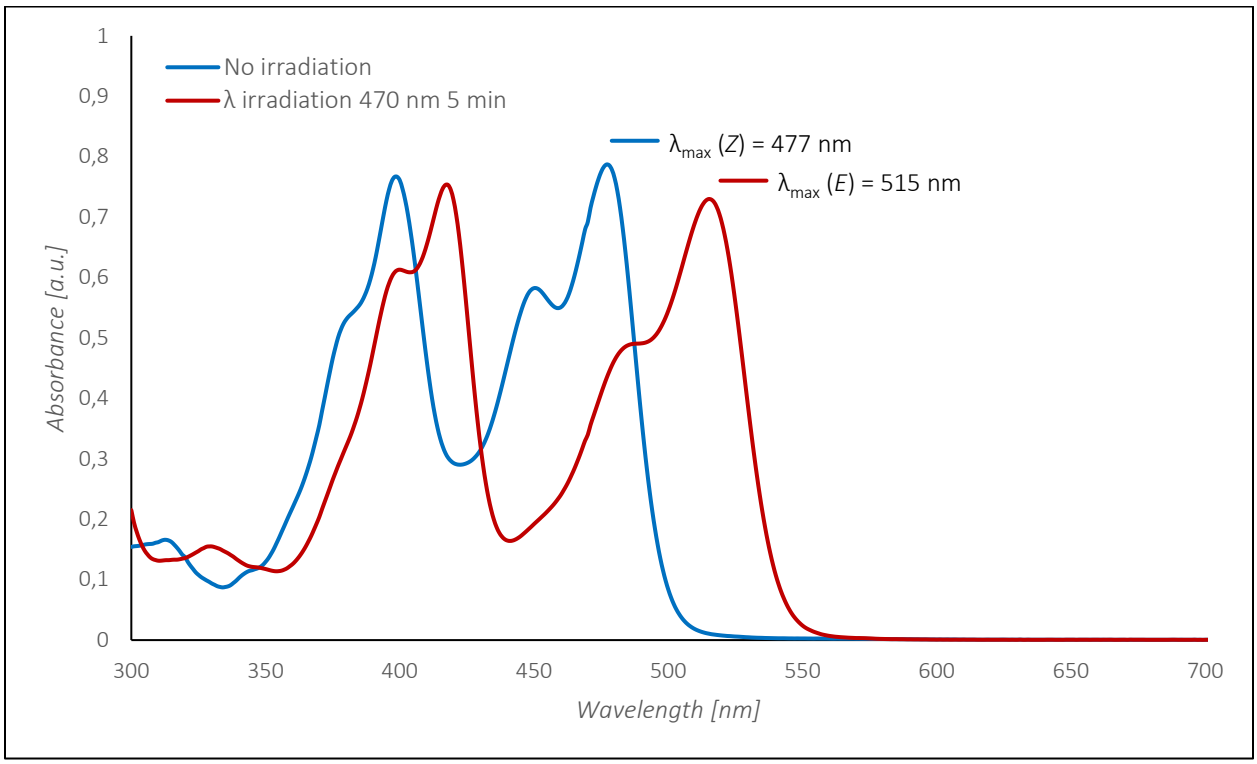

Fluorescence spectroscopy

2-Pyrrole HTI derivative (**16**) (33 μM in DCM)

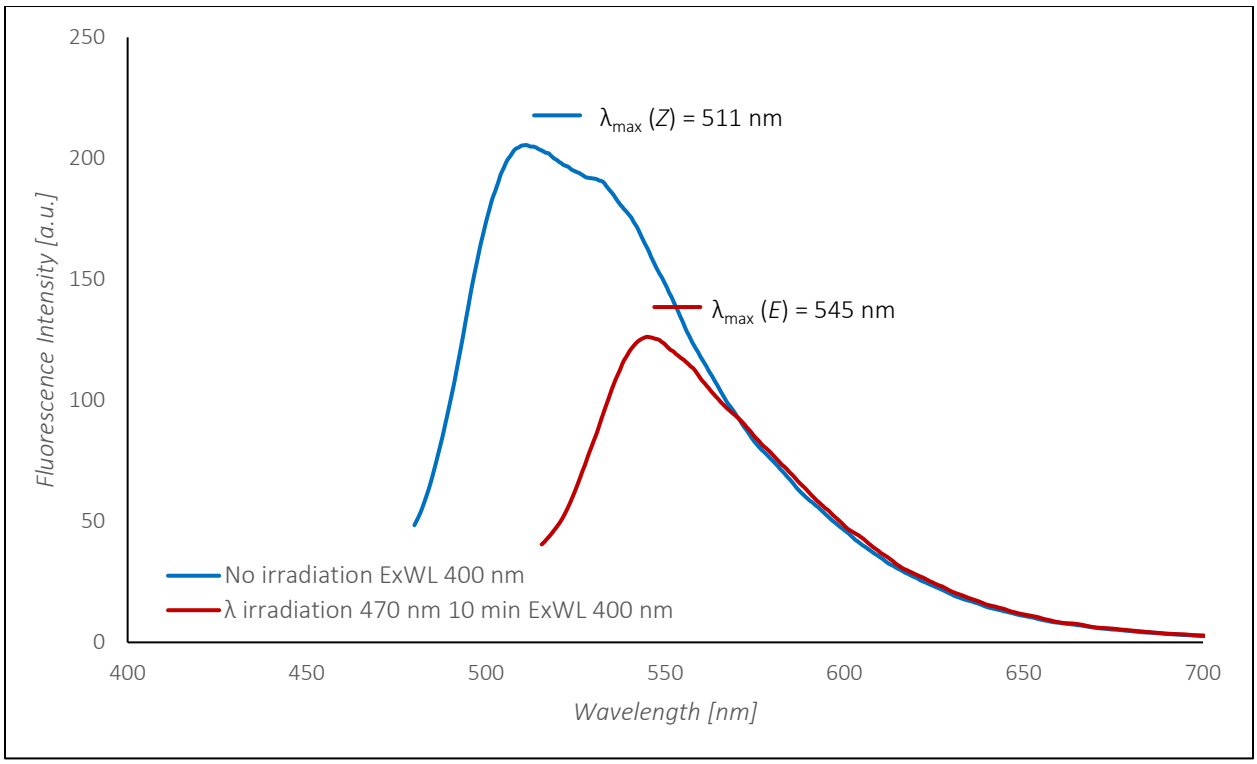

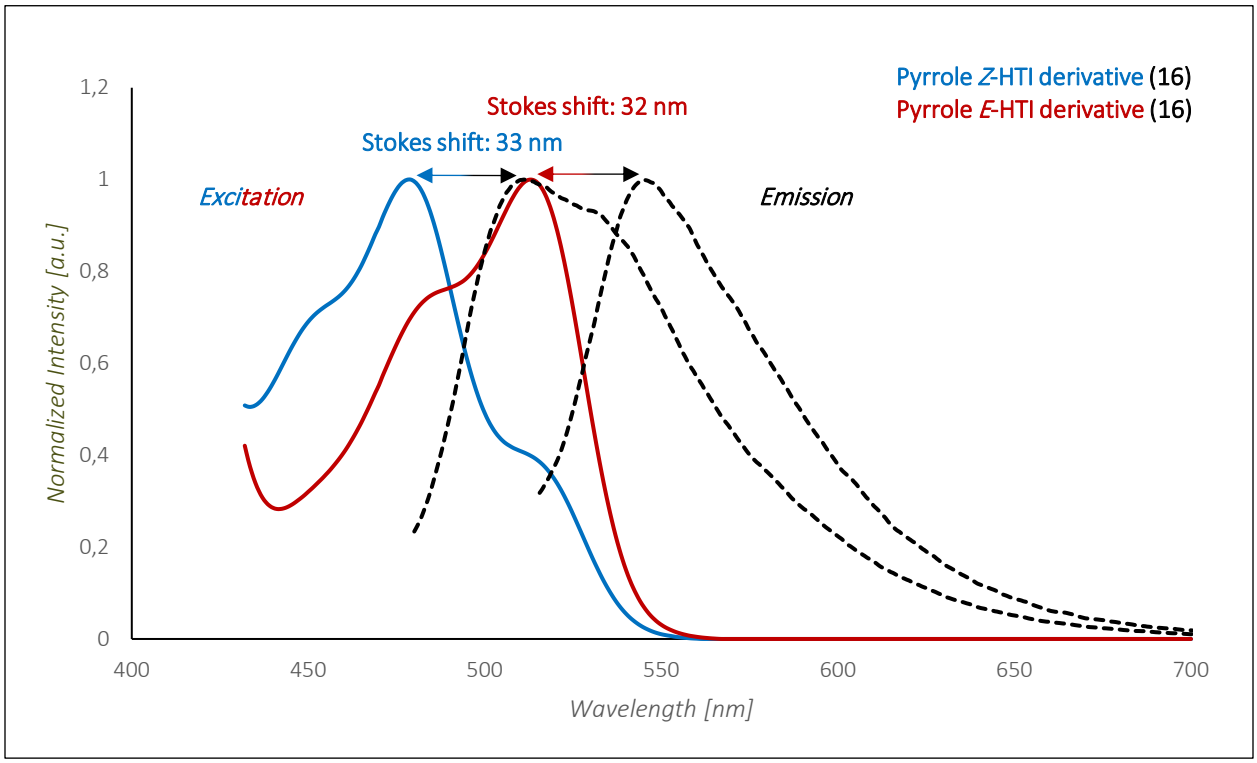

UV-Vis thermal relaxation spectroscopy

2-Pyrrole HTI derivative (**16**) (33 μM in DCM)

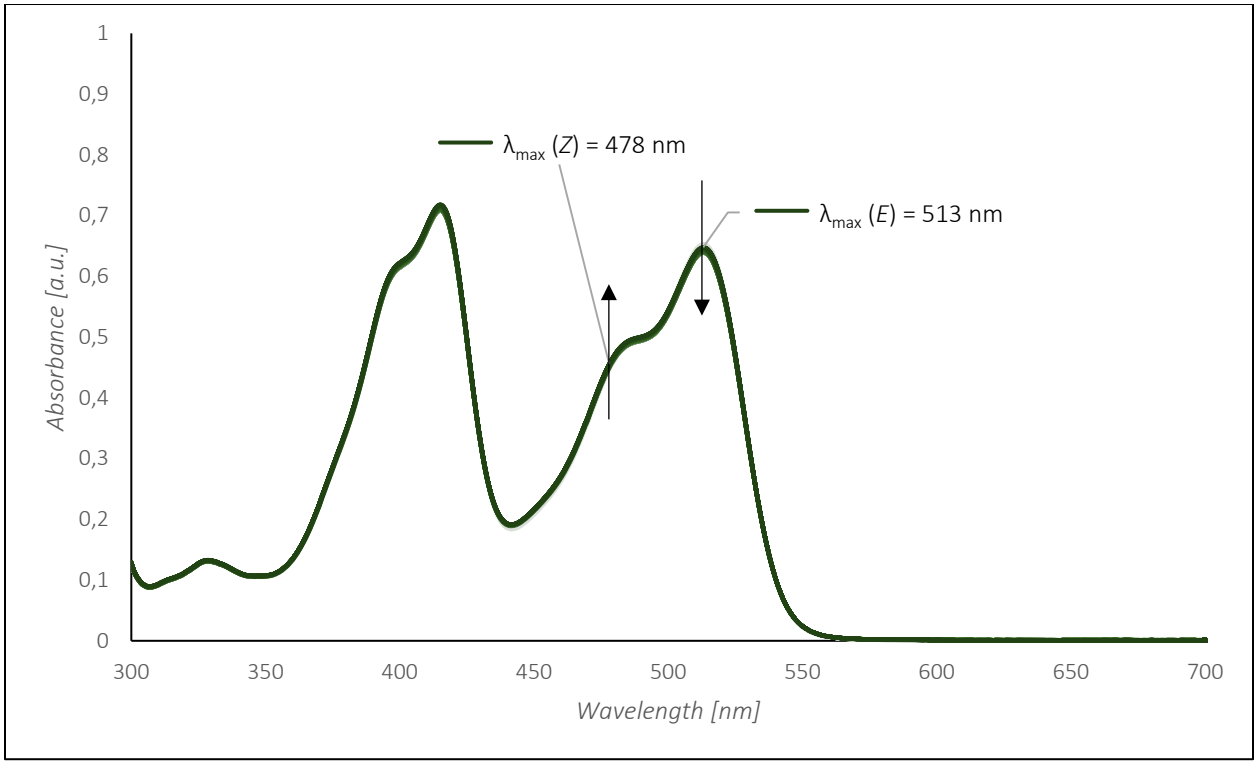

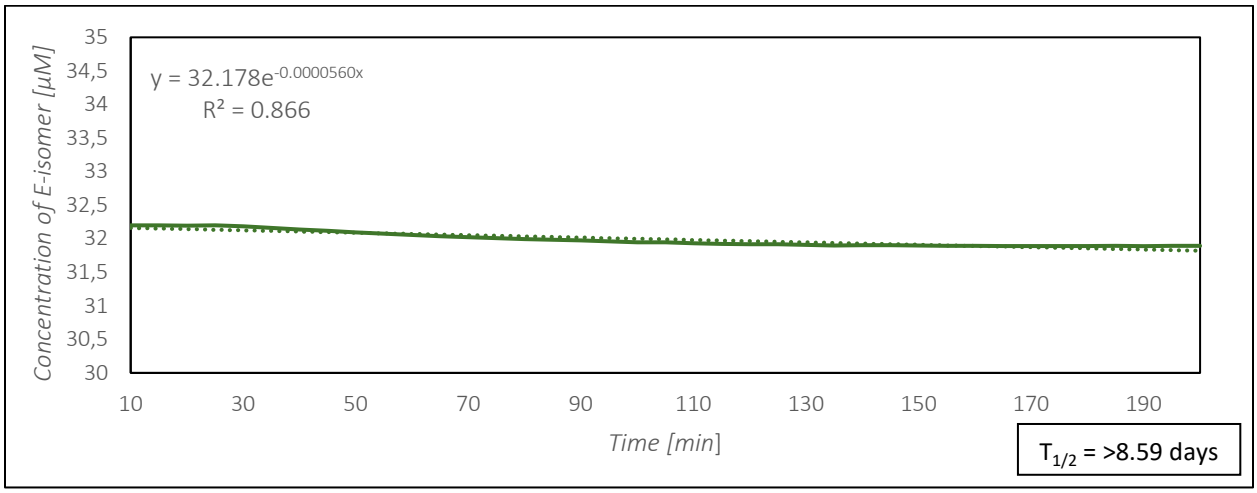

2-Pyrrole HTI derivative (**16**) (33 μM in PhMe)

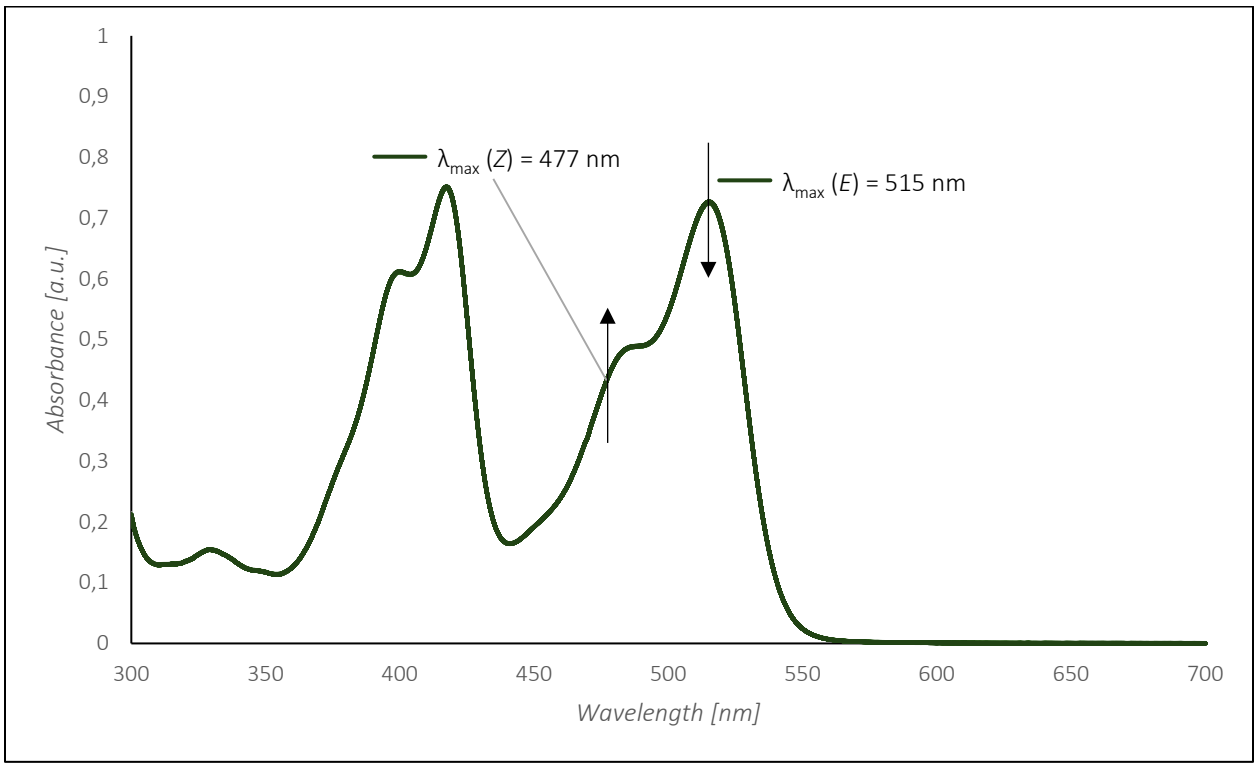

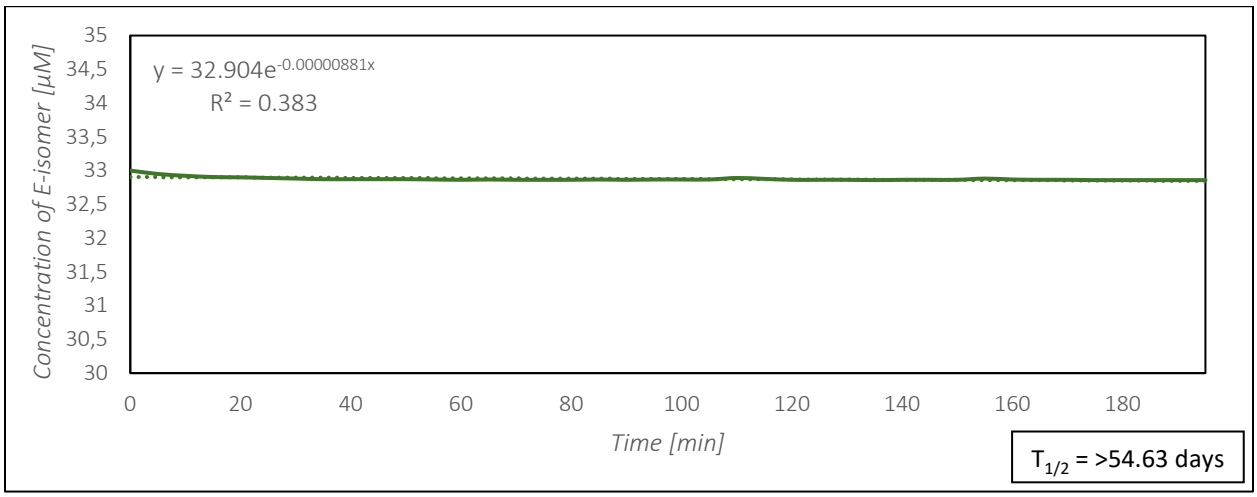

HPLC conditions

Column:	ChiralPak AD-H column (5 μm, 250 x 4.6 mm)
Mobile Phase	90:10 *n*-hexane/iPrOH (isocratic, 1 mL/min)
Isosbestic Point	502 nm (in HPLC mobile Phase)
t_R(E)	7.63 min
t_R(Z)	11.52 min

Solution composition (%*E*-isomer)

Initial solution composition before irradiation: *E*-isomer (0.48%) / *Z*-isomer (99.52%)

Time	470 nm	Time	530 nm
10 min	86.86	10 min	60.03
20 min	87.61	30 min	27.92
-	-	50 min	26.10

Note: The sample (1 mg/mL) was irradiated in DCM following a direct injection.

Representative HPLC traces

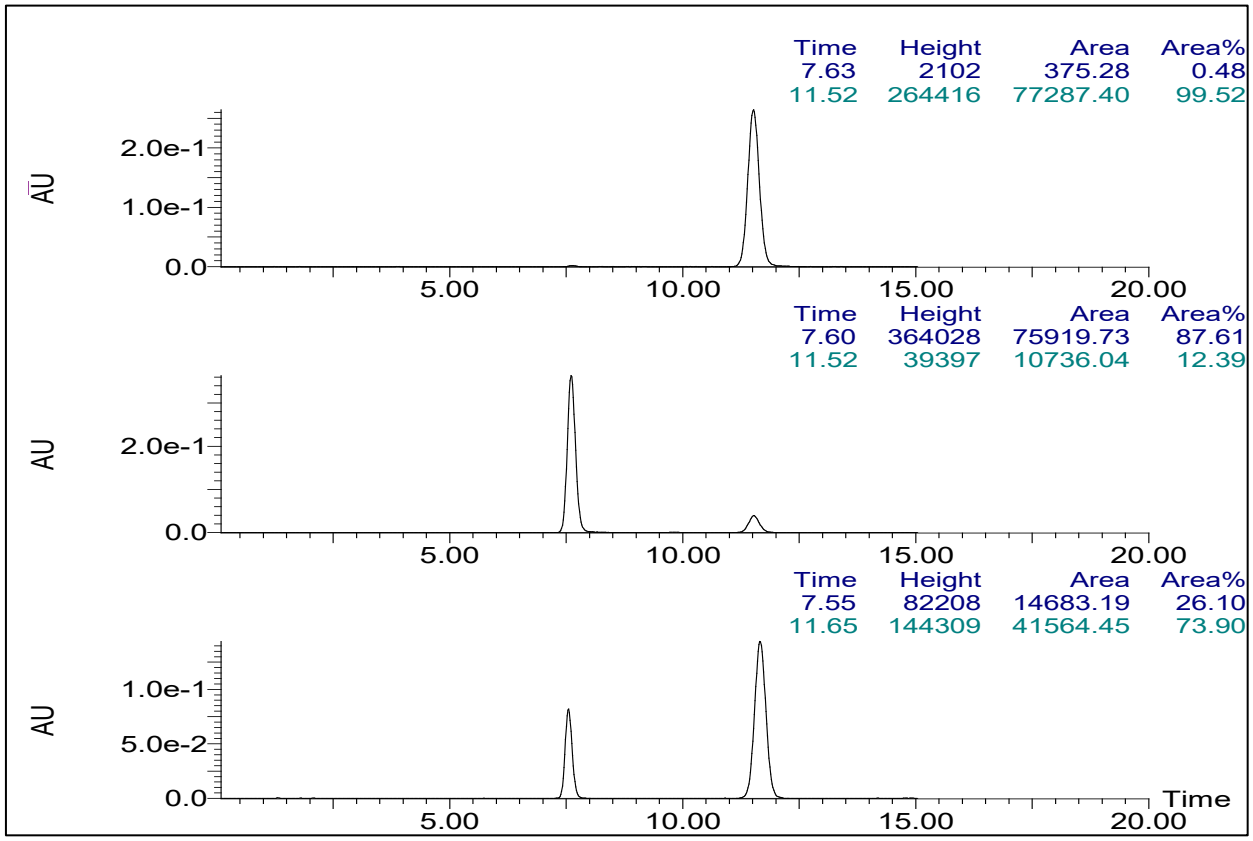

(*Z*)-2-((1H-Indol-2-yl)methylene)naphtho[2,1-b]thiophen-1(2H)-one (17)

Prepared according to general procedure B.

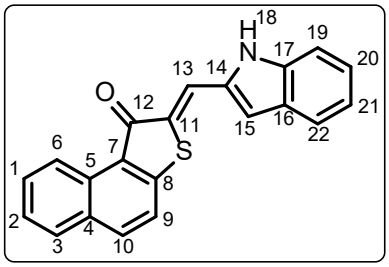

Hemithioindigo derivative **5** (101 mg, 0.505 mmol, 1.0 equiv.), PhMe (2.0 mL, 0.253 M) and indole-2-carbaldehyde (66.6 mg, 0.468 mmol, 0.93 equiv.). Stirred for 3 h under Ar at 40°C. Afforded the title compound (*Z*)-**17** (86.6 mg, 0.265 mmol, 57%) as a red solid.

TLC: R_f = 0.78 (1:1 EtOAc/*n*-heptane + 1% TEA)

LCMS (ESI) $[M+H]^+$ *m/z* calcd for $C_{21}H_{14}NOS^+$: 328.0791, *m/z* found: 328.01 $[M+H]^+$

R_t: 3.41-4.28 min broad peak (total run time: 5.2 min), purity >N/A

^{1}H NMR (800 MHz, DMSO-d_6): δ 11.81 (s, 1H, **H-18**), 9.26 (d, *J* = 8.3 Hz, 1H, **H-6**), 8.30 (d, *J* = 8.5 Hz, 1H, **H-10**), 8.08 (d, *J* = 8.0 Hz, 1H, **H-3**), 8.03 (s, 1H, **H-13**), 7.92 (d, *J* = 8.5 Hz, 1H, **H-9**), 7.78 (ddd, *J* = 8.3, 6.8, 1.3 Hz, 1H, **H-1**), 7.72 (d, *J* = 7.9 Hz, 1H, **H-22**), 7.63 (ddd, *J* = 8.0, 6.8, 1.2 Hz, 1H, **H-2**), 7.48 (d, *J* = 8.1 Hz, 1H, **H-19**), 7.26 (ddd, *J* = 8.0, 6.7, 1.1 Hz, 1H, **H-20**), 7.14 (s, 1H, **H-15**), 7.10 (t, *J* = 7.4 Hz, 1H, **H-21**)

^{13}C NMR (151 MHz, DMSO-d_6): δ 187.5 (**C-12**), 148.6 (**C-8**), 137.9 (**C-16**), 136.6 (**C-10**), 133.0 (**C-14**), 131.5 (**C-4/5**), 130.5 (**C-4/5**), 129.8 (**C-1**), 129.1 (**C-11**), 129.0 (**C-3**), 128.6 (**C-17**), 126.5 (**C-2**), 124.6 (**C-20**), 123.7 (**C-13**), 122.9 (**C-7**), 122.3 (**C-9**), 122.1 (**C-6**), 121.6 (**C-22**), 120.5 (**C-21**), 111.9 (**C-19**), 107.4 (**C-15**)

^{1}H NMR (800 MHz, C_4H_8O): 11.03 (s, 1H, **H-18**), 9.66 (d, *J* = 8.4 Hz, 1H, **H-6**), 8.40 (d, *J* = 8.5 Hz, 1H), 8.26 (s, 1H, **H-13**), 8.21 (d, *J* = 8.0 Hz, 1H), 7.97 (d, *J* = 8.5 Hz, 1H), 7.94 (t, *J* = 7.6 Hz, 1H), 7.92 (d, *J* = 8.0 Hz, 1H), 7.80 (t, *J* = 7.4 Hz, 1H), 7.67 (d, *J* = 8.1 Hz, 1H), 7.47 (t, *J* = 7.5 Hz, 1H), 7.40 (d, *J* = 2.1 Hz, 1H), 7.33 (t, *J* = 7.4 Hz, 1H)

HRMS-ESI $[M+H]^+$ *m/z* calcd for $C_{21}H_{14}NOS^+$: 328.0791, *m/z* found: 328.0789 $[M+H]^+$ (ppm error: -0.610)

Melting point: 287-289°C

(*E*)-**17**:

^{1}H NMR (800 MHz, DMSO-d_6): δ 12.84 (s, 1H, **H-18**), 9.48 (d, *J* = 7.8 Hz, 1H), 8.28 (d, *J* = 8.5 Hz, 1H), 8.10 – 8.07 (m, 1H), 7.94 (t, 1H), 7.88 (d, *J* = 8.5 Hz, 1H), 7.81 (ddd, *J* = 8.3, 6.8, 1.3 Hz, 1H), 7.79 – 7.75 (m, 1H), 7.74 – 7.71 (m, 1H), 7.66 – 7.61 (m, 1H), 7.36 (ddd, *J* = 8.1, 6.8, 1.1 Hz, 1H), 7.28 – 7.25 (m, 1H), 7.15 – 7.12 (m, 1H)

^{1}H NMR (800 MHz, C_4H_8O): δ 13.41 (s, 1H, **H-18**), 9.83 (d, *J* = 8.3 Hz, 1H, **H-6**), 8.37 (d, *J* = 8.5 Hz, 1H), 8.21 (d, *J* = 8.0 Hz, 1H), 7.99 (t, *J* = 7.7 Hz, 1H), 7.92 – 7.87 (m, 4H), 7.82 (t, *J* = 7.4 Hz, 1H), 7.58 (t, *J* = 7.6 Hz, 1H), 7.34 (t, *J* = 7.4 Hz, 1H), 7.32 – 7.29 (m, 1H)

Note: A 1.5:1 (*Z*/*E*)-ratio was observed for (*E*)-**17** in DMSO, whereas THF afforded clean (*E*)-**17** by ^{1}H NMR.

UV-Vis spectroscopy

2-Indole HTI derivative (**17**) (33 µM in DCM)

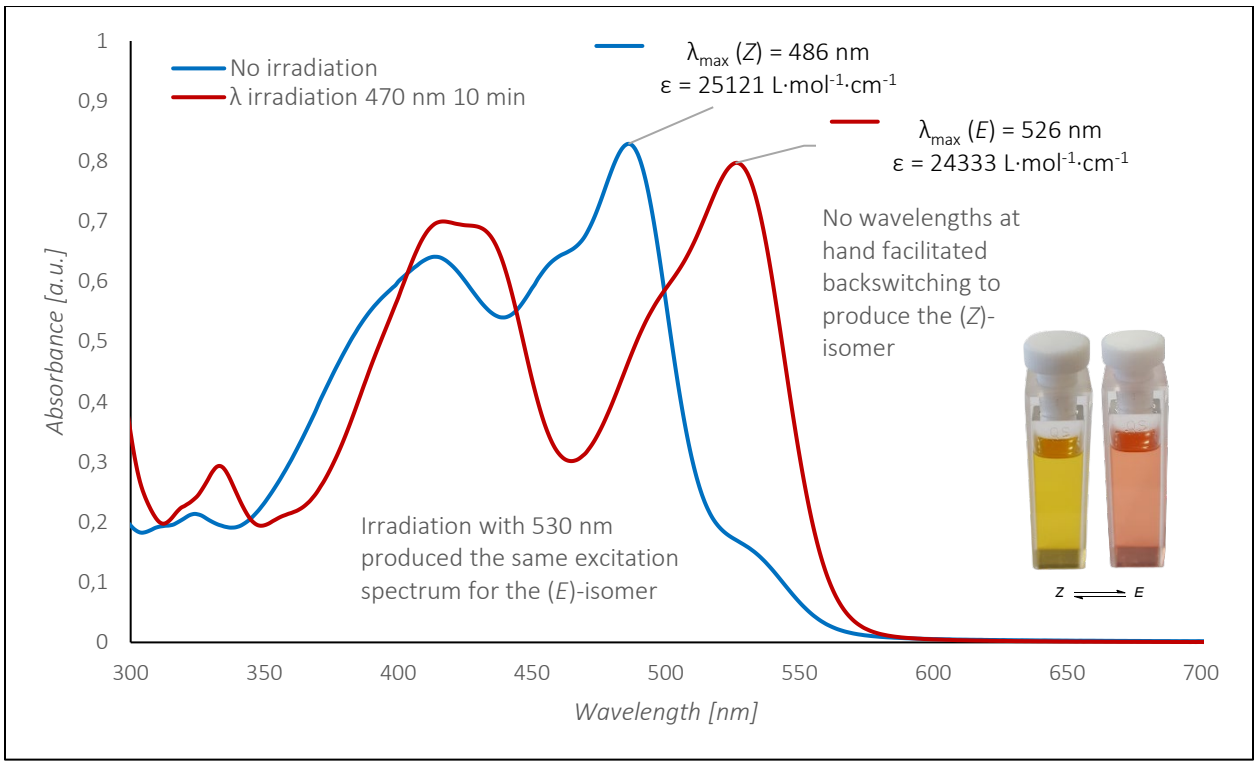

2-Indole HTI derivative (**17**) (33 µM in *n*-hexane/iPrOH 9:1)

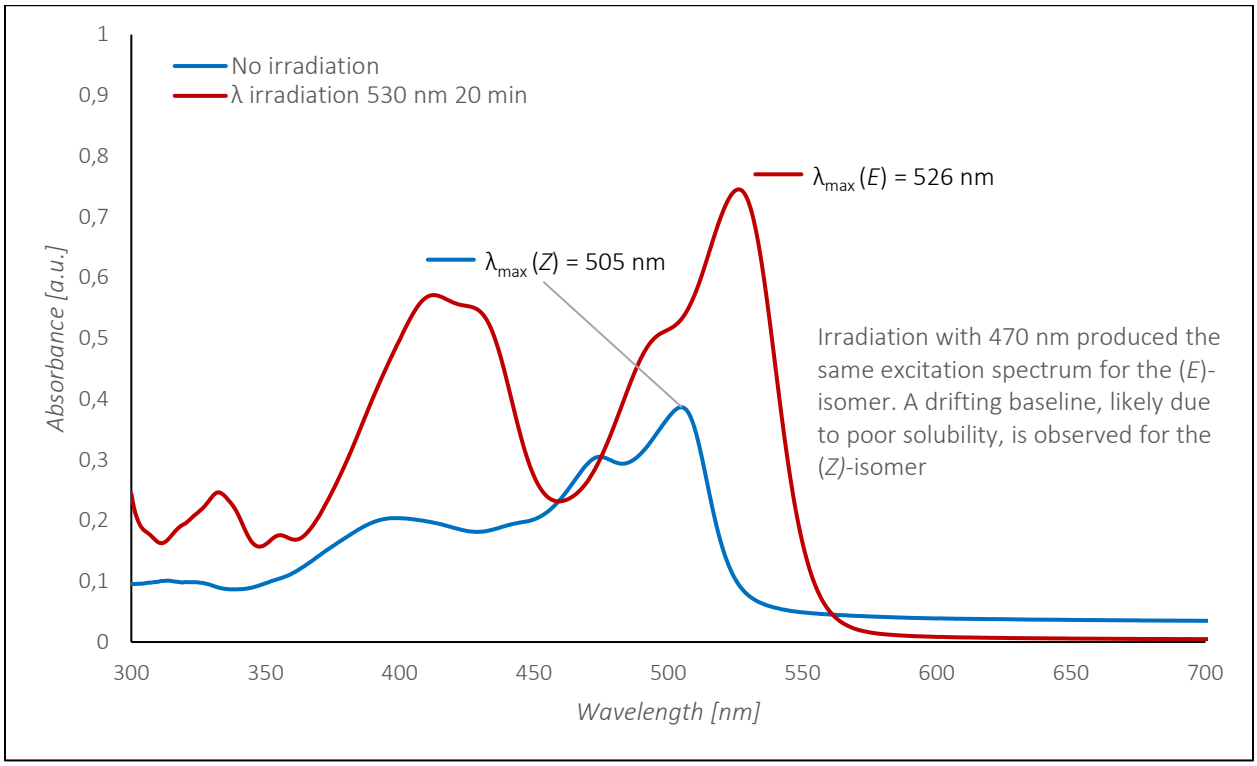

2-Indole HTI derivative (**17**) (33 µM in iPrOH)

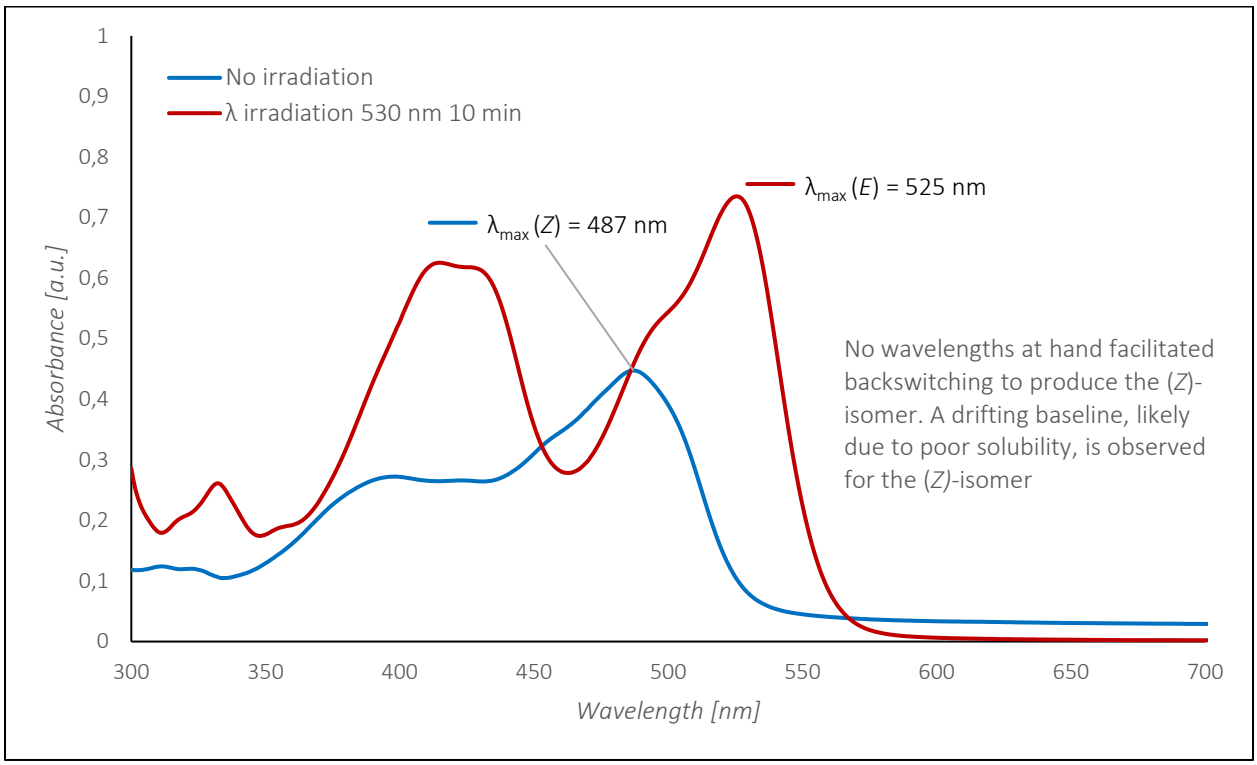

2-Indole HTI derivative (**17**) (33 µM in THF)

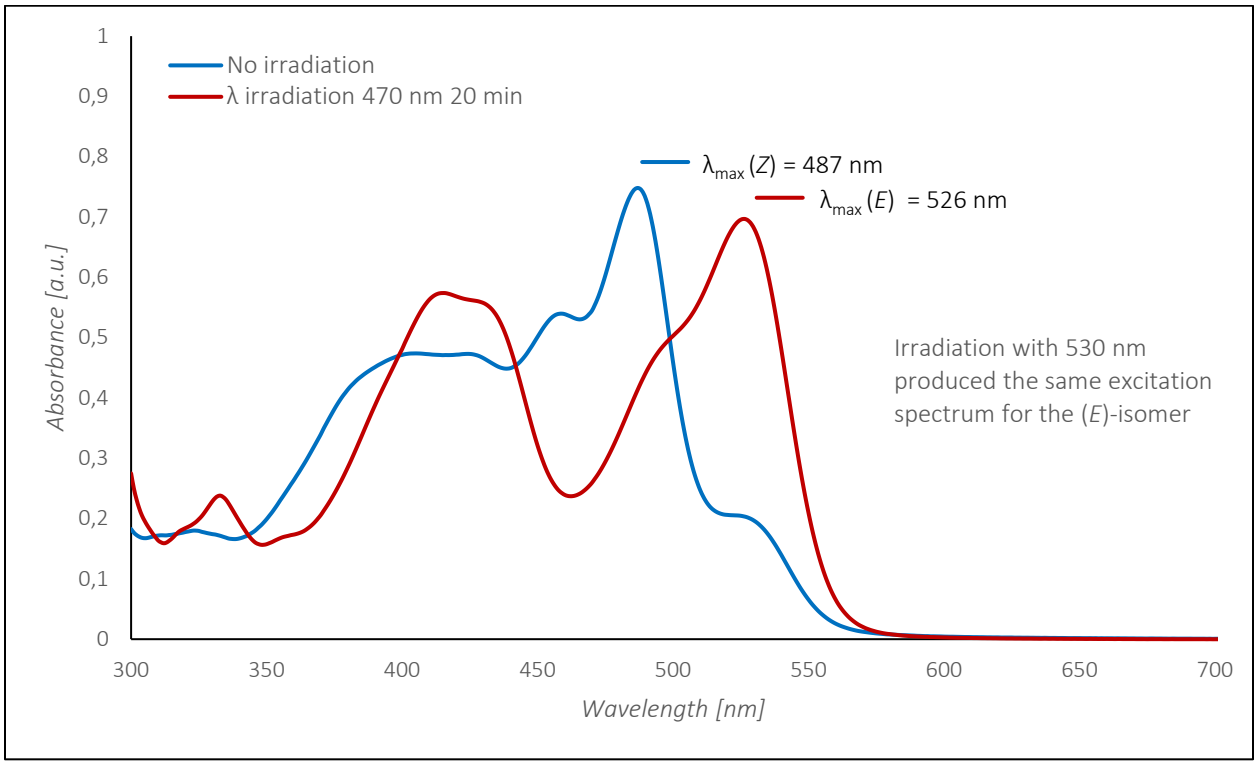

2-Indole HTI derivative (**17**) (33 µM in PhMe)

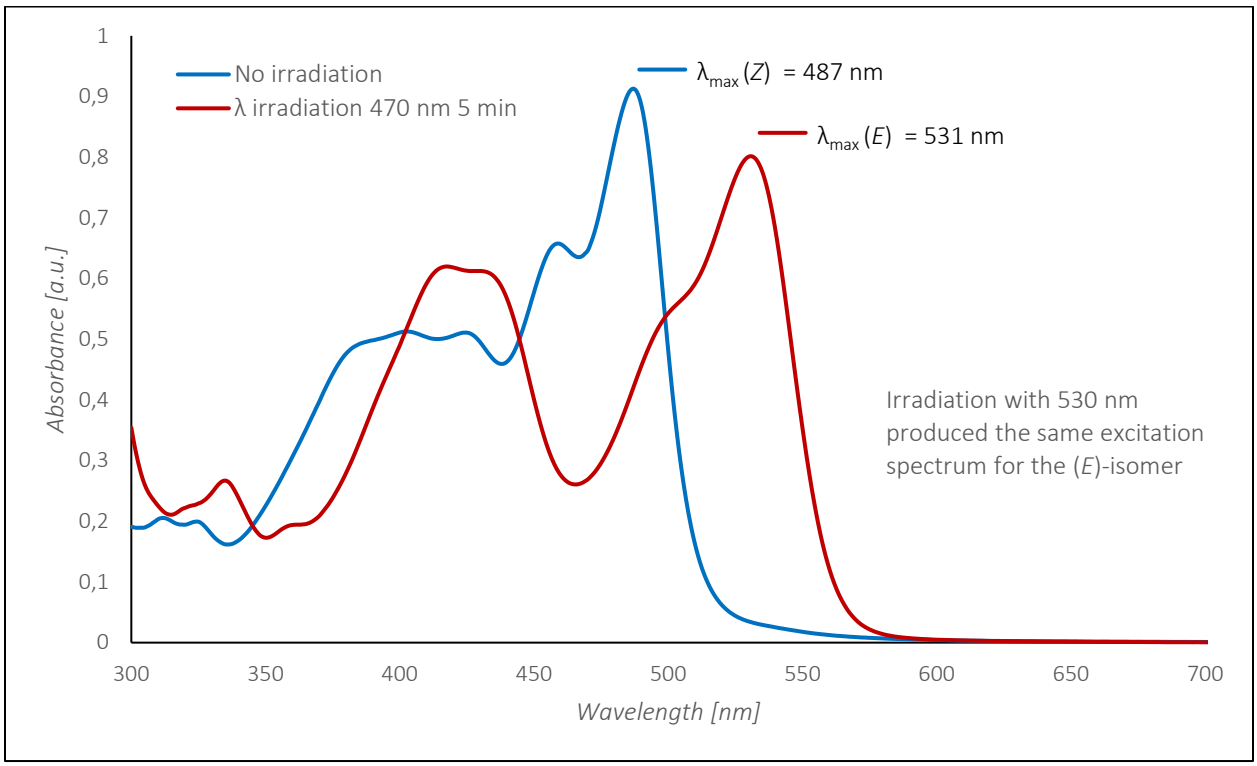

2-Indole HTI derivative (**17**) (33 µM in DMSO)

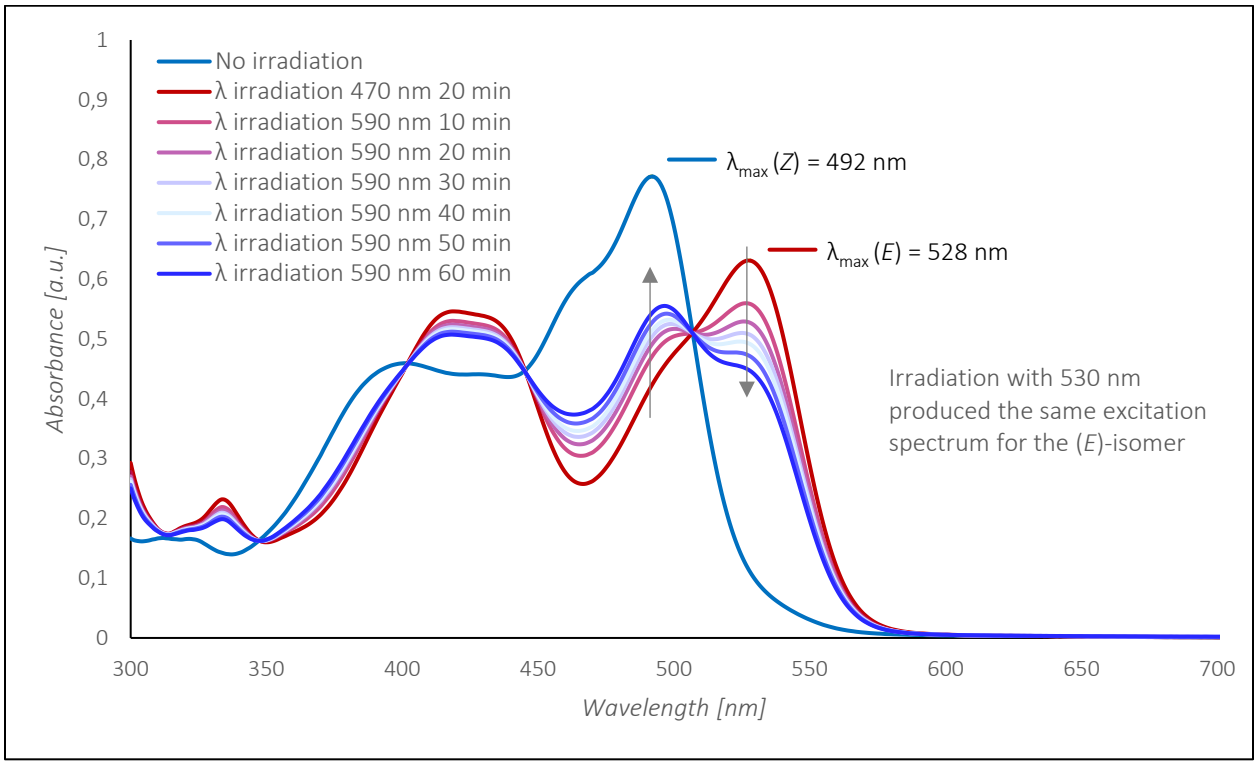

Fluorescence spectroscopy

2-Indole HTI derivative (**17**) (33 μM in DCM)

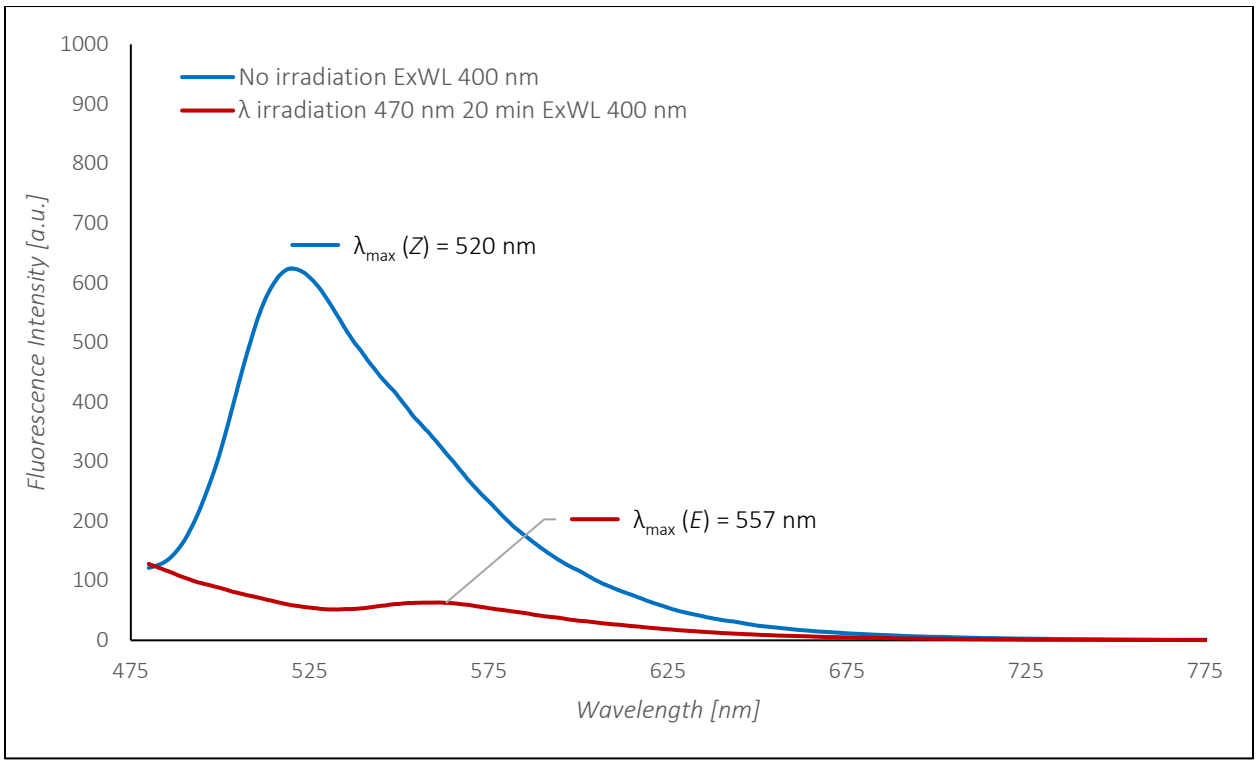

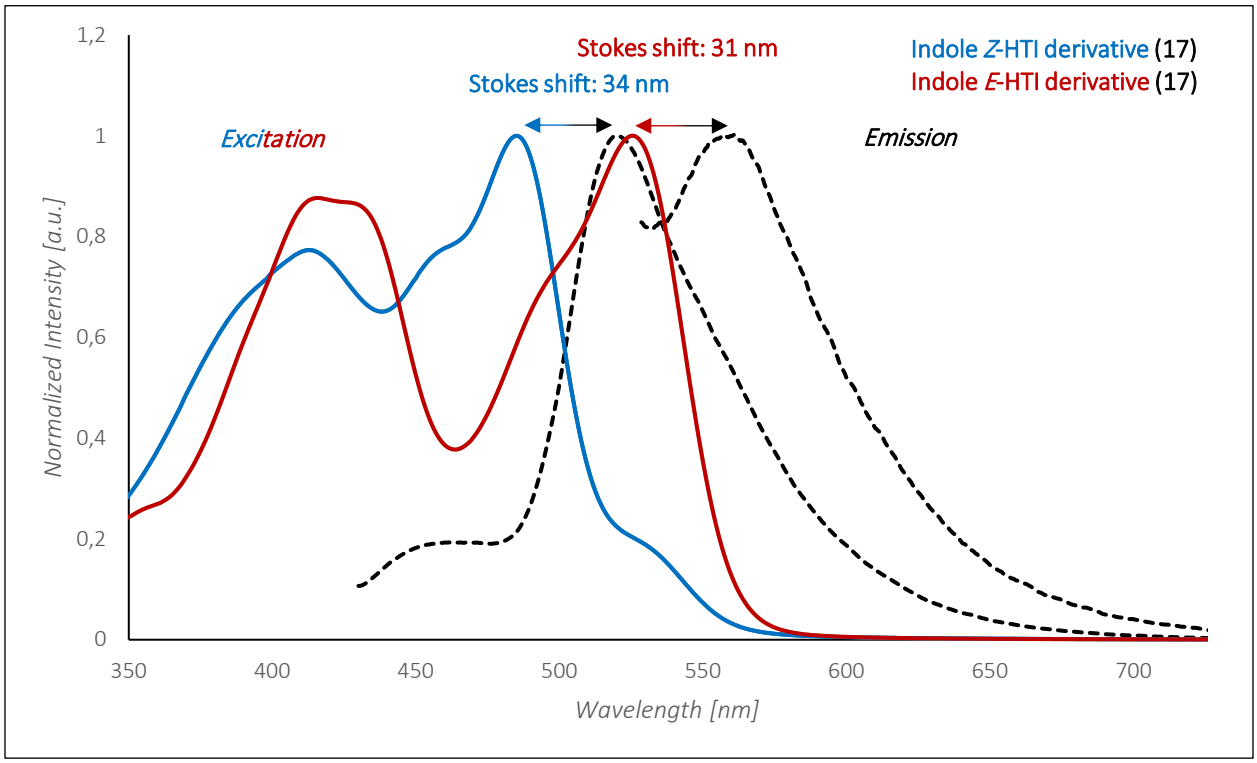

UV-Vis thermal relaxation spectroscopy

2-Indole HTI derivative (**17**) (33 μM in DMSO)

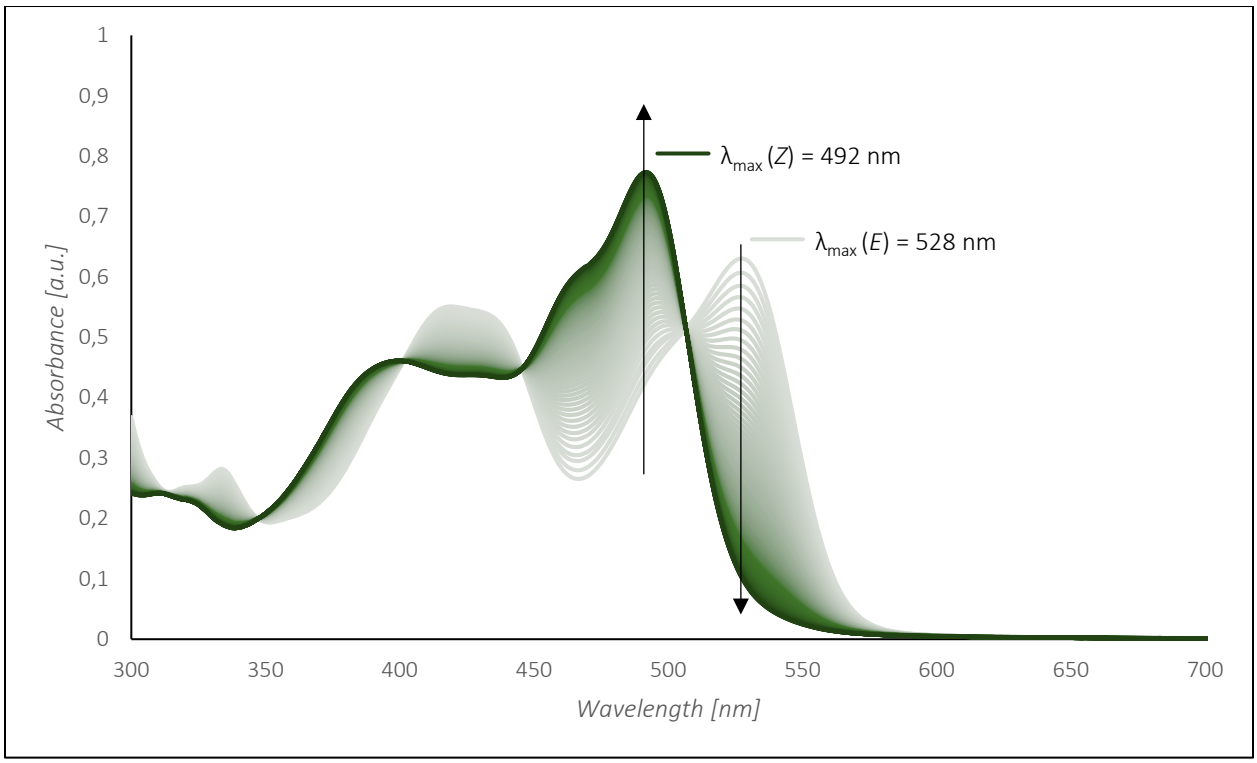

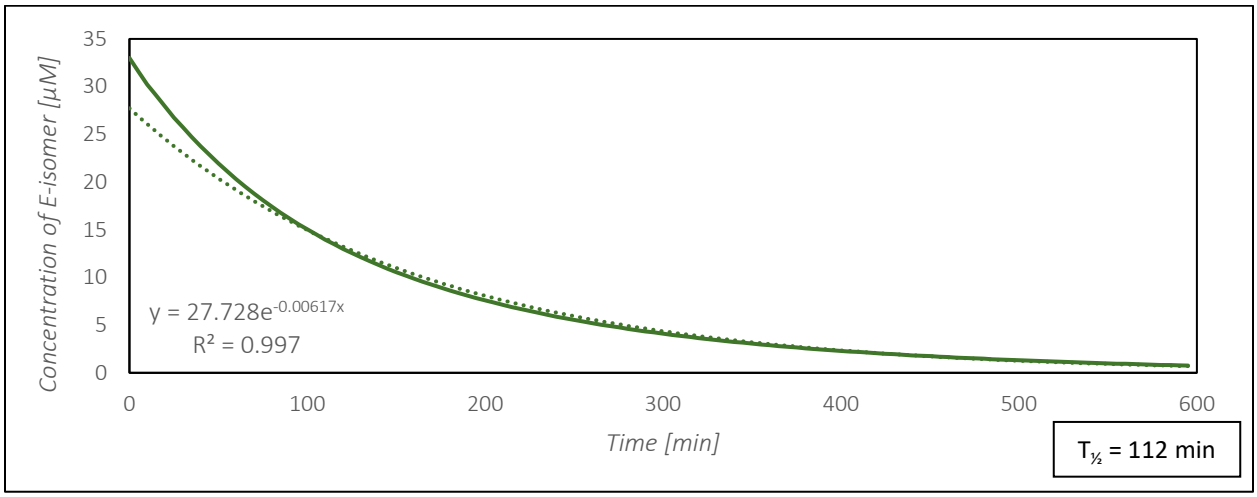

2-Indole HTI derivative (**17**) (33 μM in PhMe)

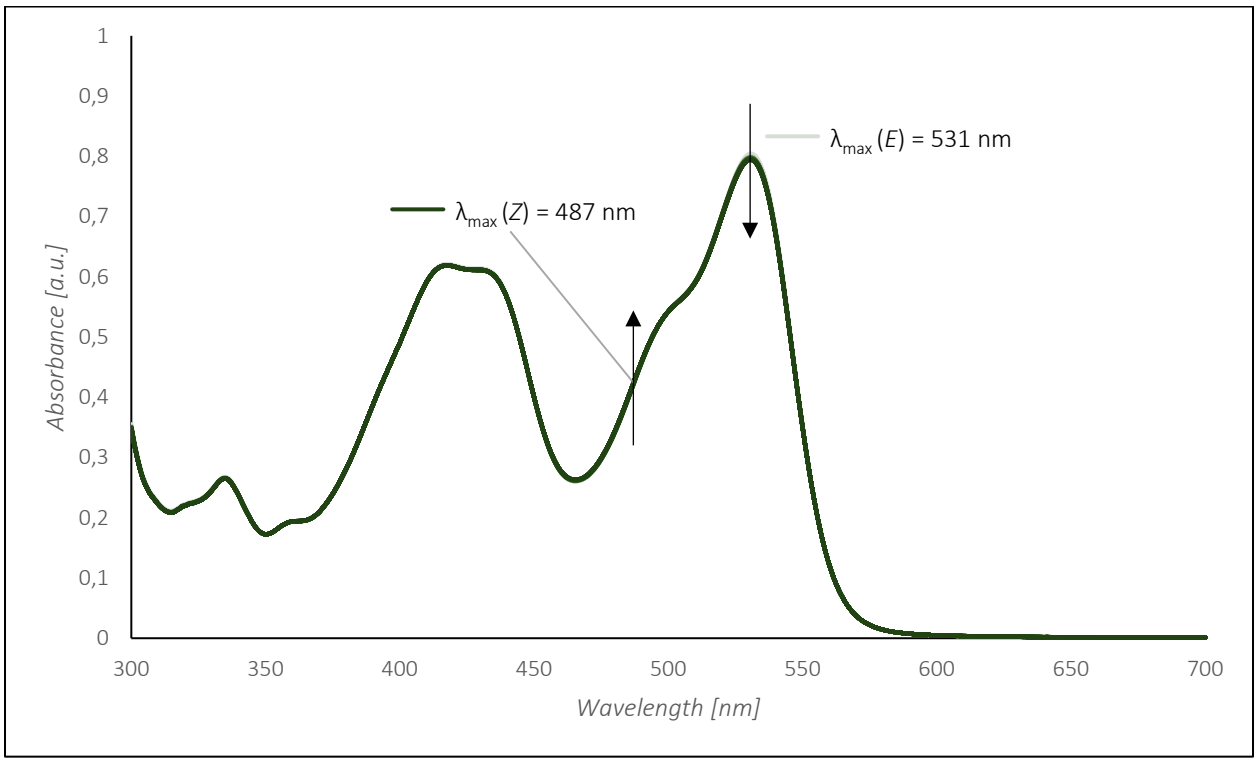

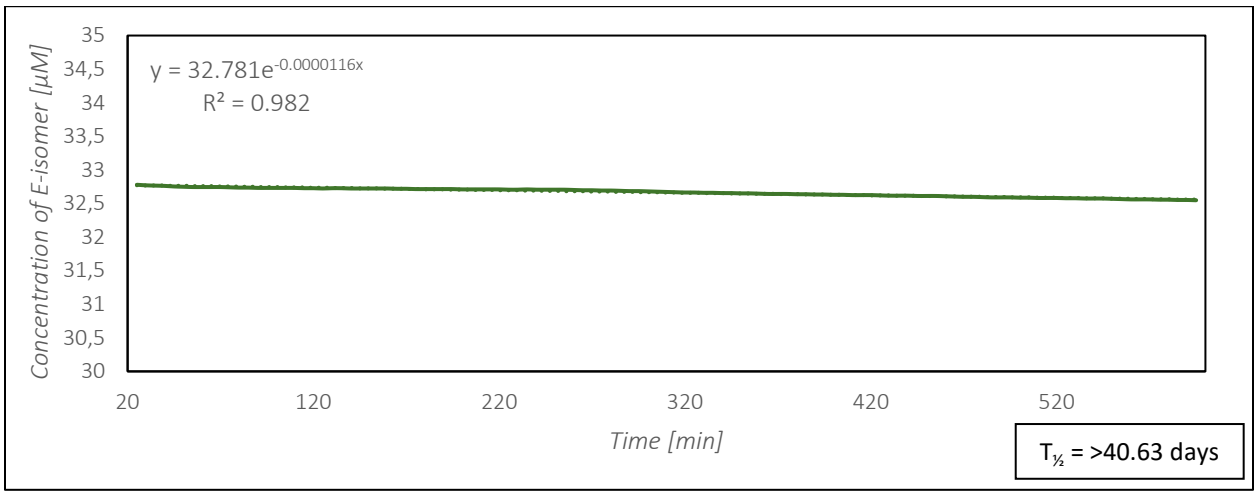

(*Z*)-2-(1H,1'H-[2,2'-Bipyrrol]-5-ylmethylene)benzo[b]thiophen-3(2H)-one (18)

Prepared according to general procedure B.

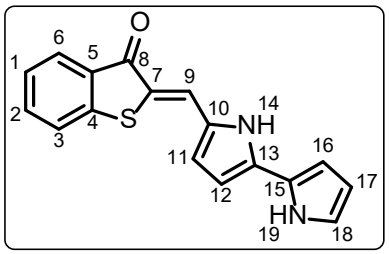

Hemithioindigo **6** (53 mg, 0.353 mmol, 1.0 equiv.), PhMe (2.0 mL, 0.176 M) and bipyrrole-5-carbaldehyde **9** (46.0 mg, 0.287 mmol, 0.81 equiv.). Stirred for 2.5 h under Ar at 100°C. Afforded the title compound (*Z*)-**18** (31.7 mg, 0.108 mmol, 38%) as a dark purple solid.

TLC: R_f = 0.52 (1:1 EtOAc/*n*-heptane + 1% TEA)

LCMS (ESI) $[M+H]^+$ *m/z* calcd for $C_{21}H_{14}NOS^+$: 328.0791, *m/z* found: 328.01 $[M+H]^+$

R_t: 3.41-4.28 min broad peak (total run time: 5.2 min)

^{1}H NMR (800 MHz, DMSO-d_6): δ 11.88 (s, 1H, **H-14/19**), 11.35 (s, 1H, **H-14/19**), 7.85 (s, 1H, **H-9**), 7.80 (d, *J* = 7.7 Hz, 1H, **H-6**), 7.76 (d, *J* = 7.9 Hz, 1H, **H-3**), 7.66 (t, *J* = 7.5 Hz, 1H, **H-2**), 7.37 (t, *J* = 7.4 Hz, 1H, **H-1**), 6.90 (d, *J* = 2.5 Hz, 1H, **H-18**), 6.84 (d, *J* = 4.2 Hz, 1H, **H-11**), 6.72 (d, *J* = 4.4 Hz, 1H, **H-12**), 6.53 (s, 1H, **H-16**), 6.15 (q, *J* = 2.8 Hz, 1H, **H-17**)

^{13}C NMR (201 MHz, DMSO-d_6): δ 185.8 (**C-8**), 143.8 (**C-5**), 134.5 (**C-2**), 133.3 (**C-13**), 131.4 (**C-4**), 127.9 (**C-10**), 125.7 (**C-6**), 125.6 (**C-1**), 124.4 (**C-3**), 123.8 (**C-15**), 122.7 (**C-9**), 121.4 (**C-7**), 119.9 (**C-16/18**), 117.4 (**C-11**), 109.3 (**C-17**), 108.8 (**C-12**), 106.1 (**C-16/18**)

HRMS-ESI $[M+H]^+$ *m/z* calcd for $C_{17}H_{13}N_2OS^+$: 293.0743, *m/z* found: 293.0744 $[M+H]^+$ (ppm error: 0.341)

Melting point: 273-275°C (decomposes)

UV-Vis spectroscopy

Bipyrrole HTI (**18**) (33 µM in DCM)

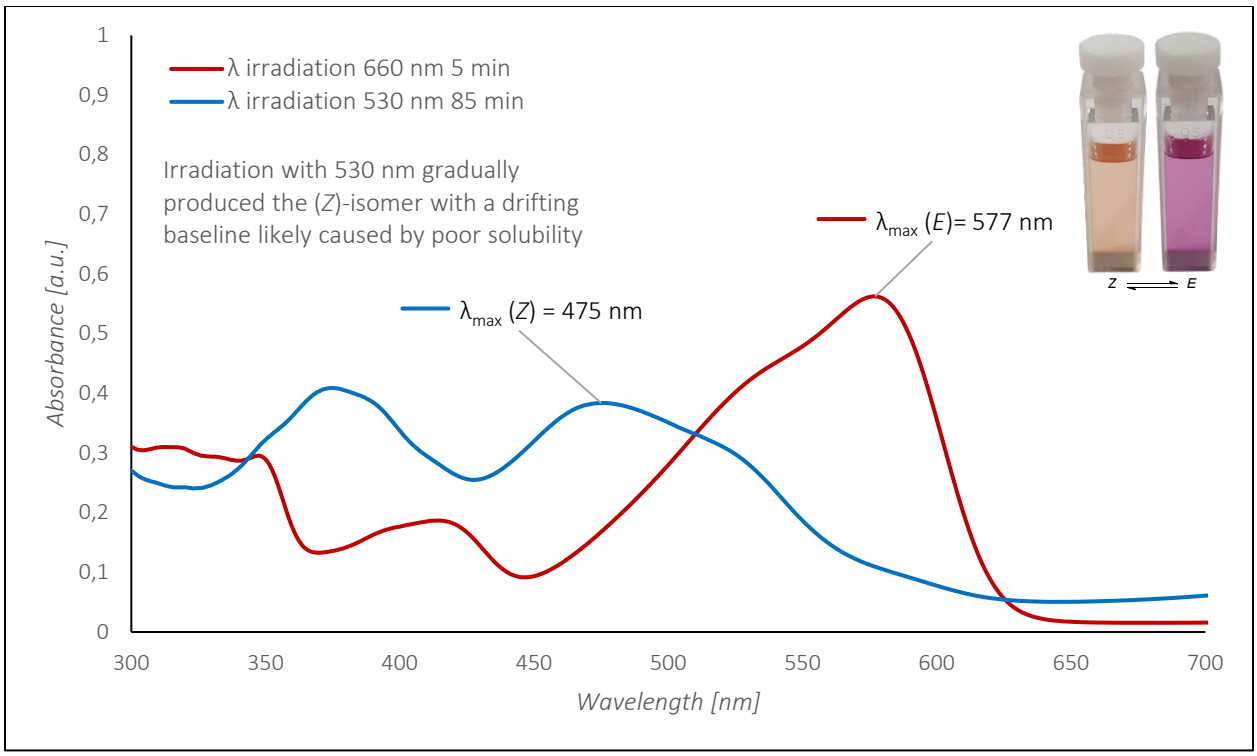

Bipyrrole HTI (**18**) (33 µM in *n*-hexane/iPrOH 9:1)

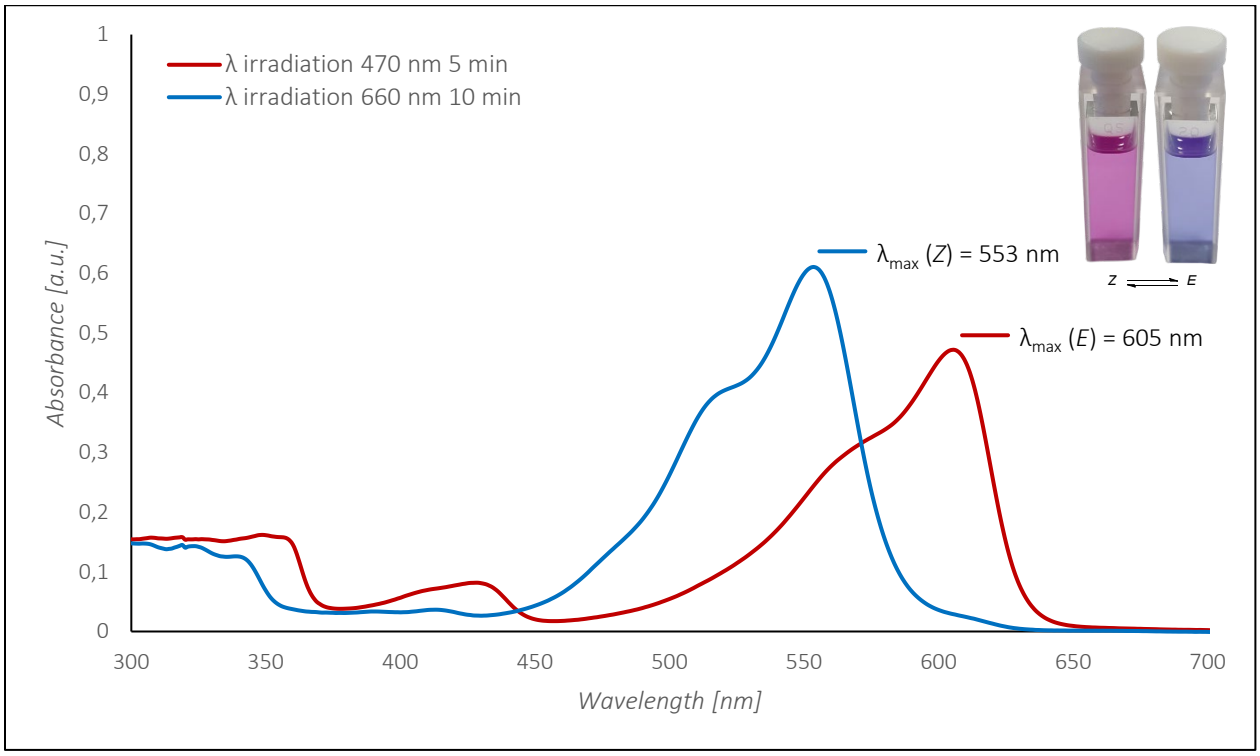

Bipyrrole HTI (**18**) (33 µM in iPrOH)

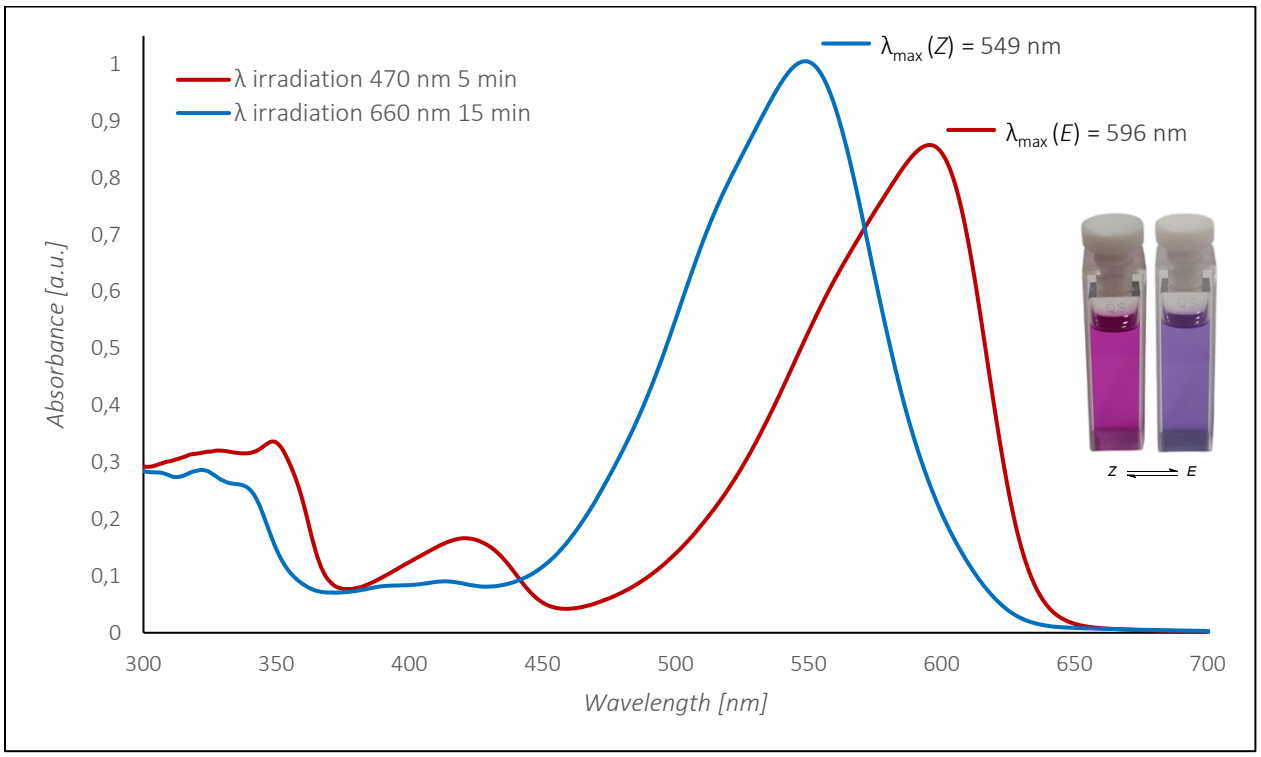

Bipyrrole HTI (**18**) (33 µM in THF)

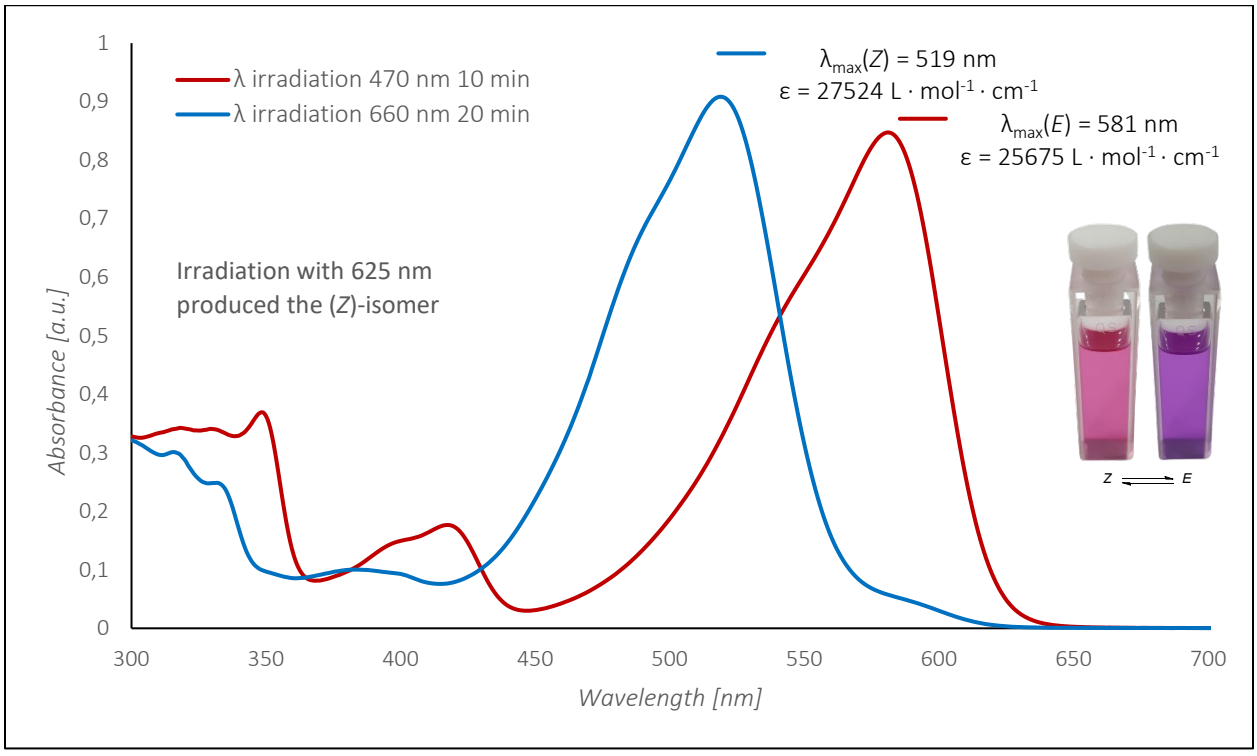

Bipyrrole HTI (**18**) (33 μM in PhMe)

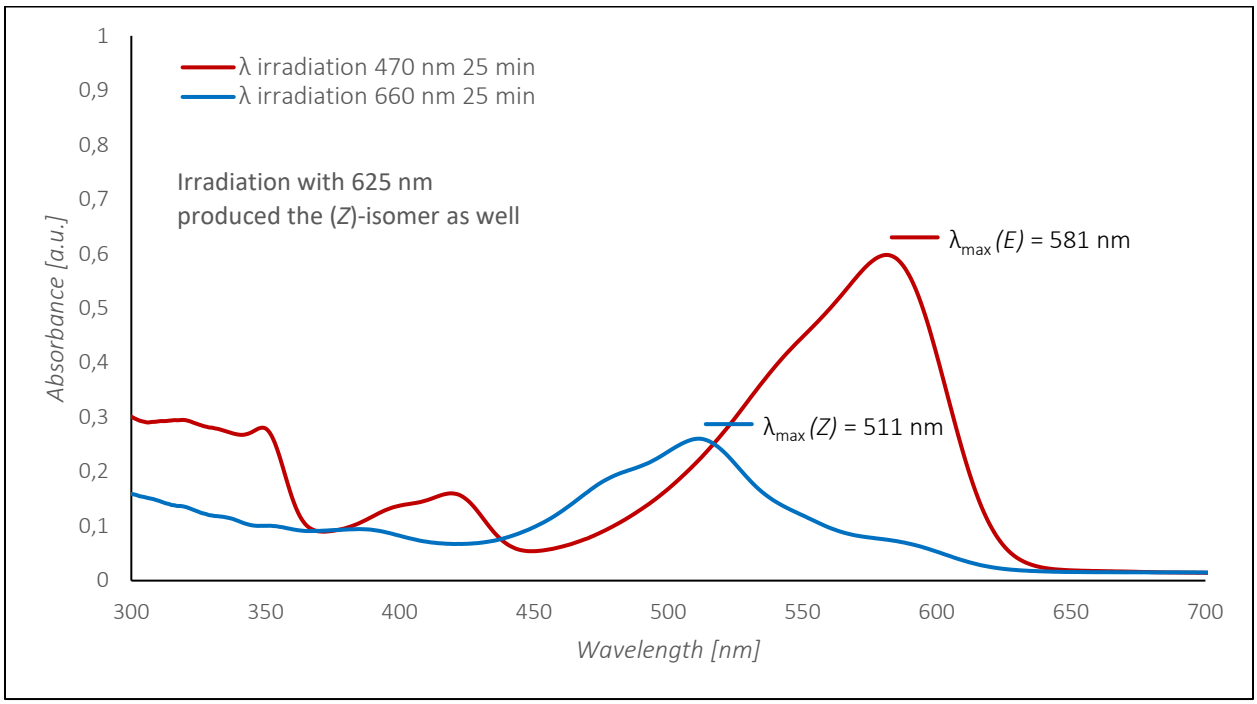

Bipyrrole HTI (**18**) (33 μM in DMSO)

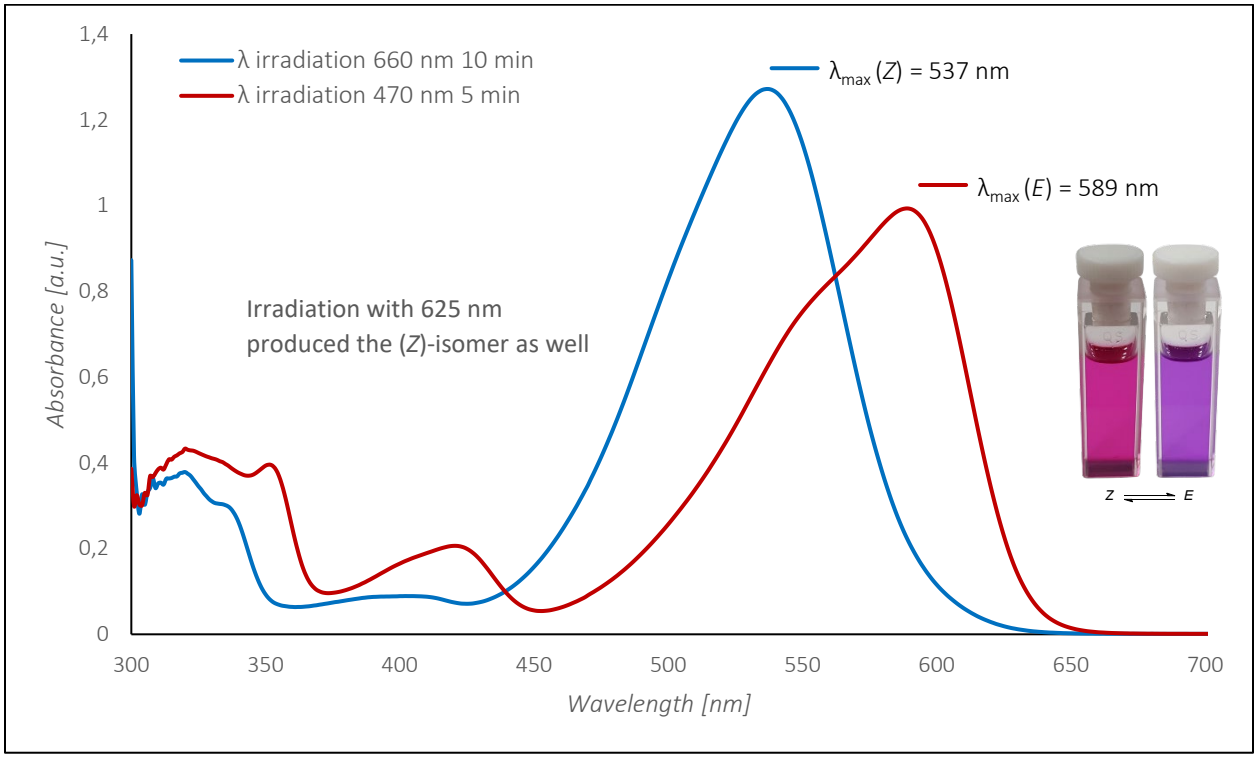

Bipyrrole HTI (**18**) (33 µM in acetone)

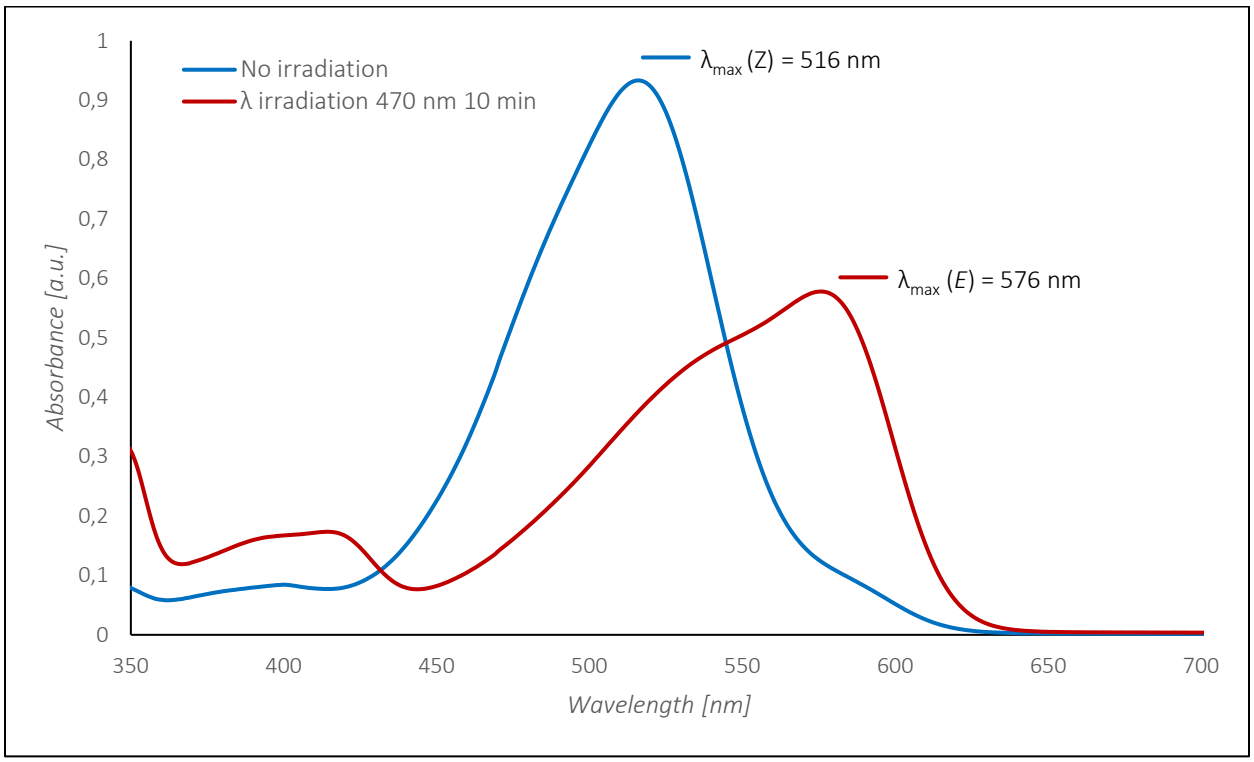

UV-Vis thermal relaxation spectroscopy

Bipyrrole HTI (**18**) (33 µM in THF)

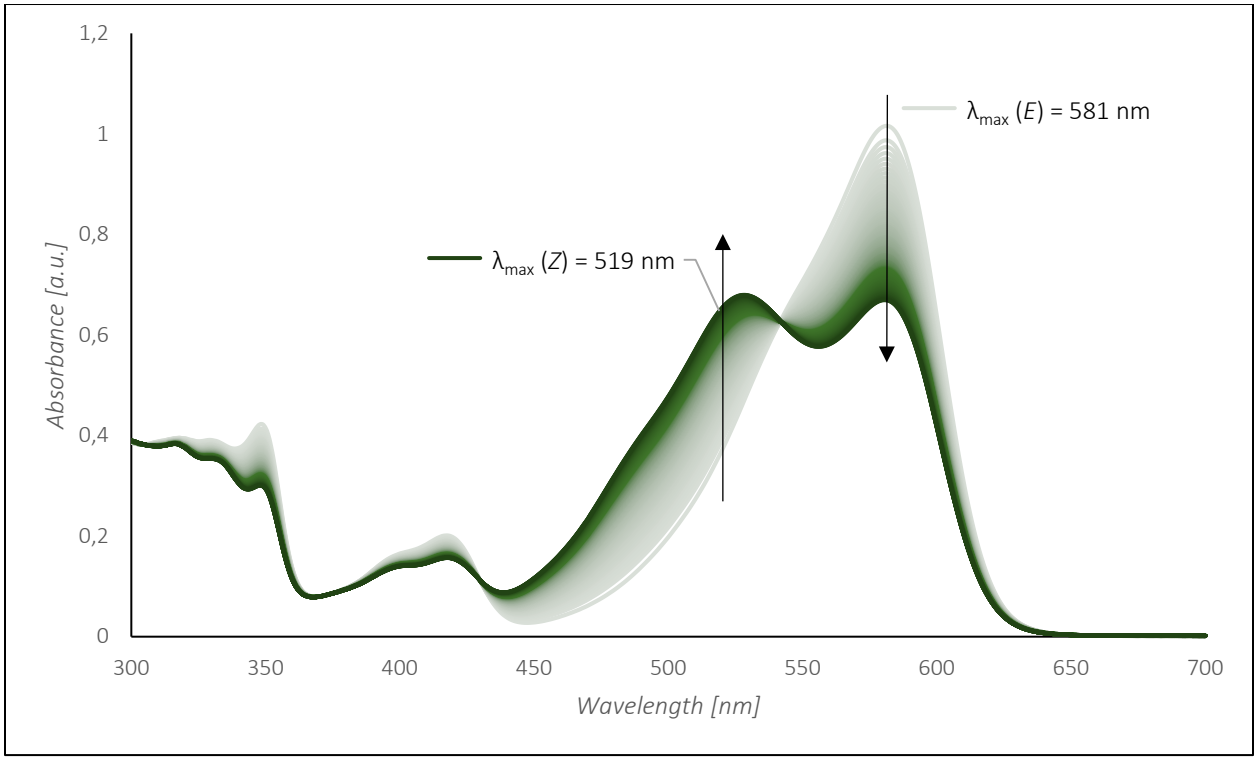

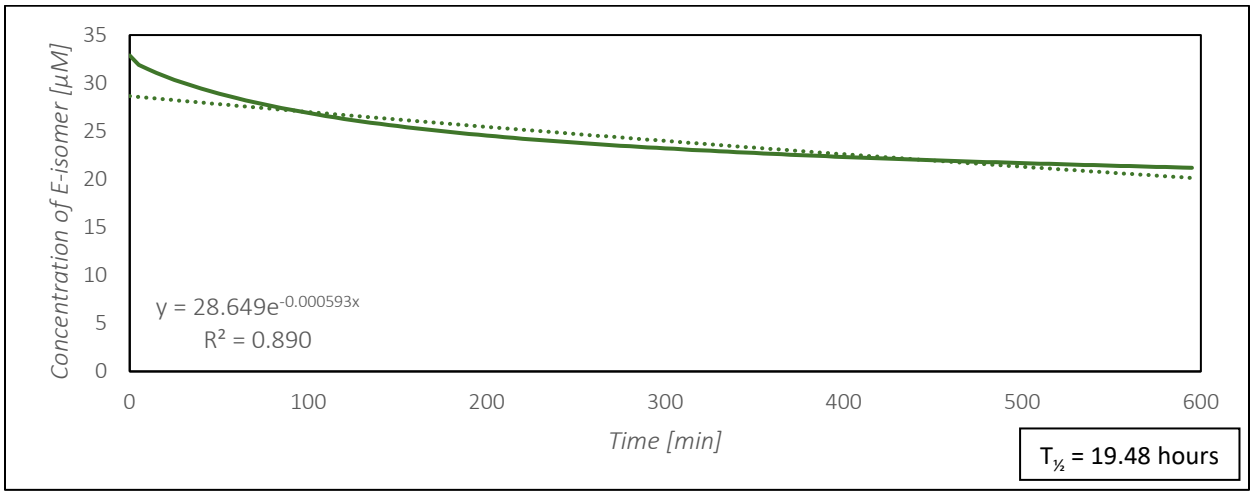

Bipyrrole HTI (**18**) (33 μM in PhMe)

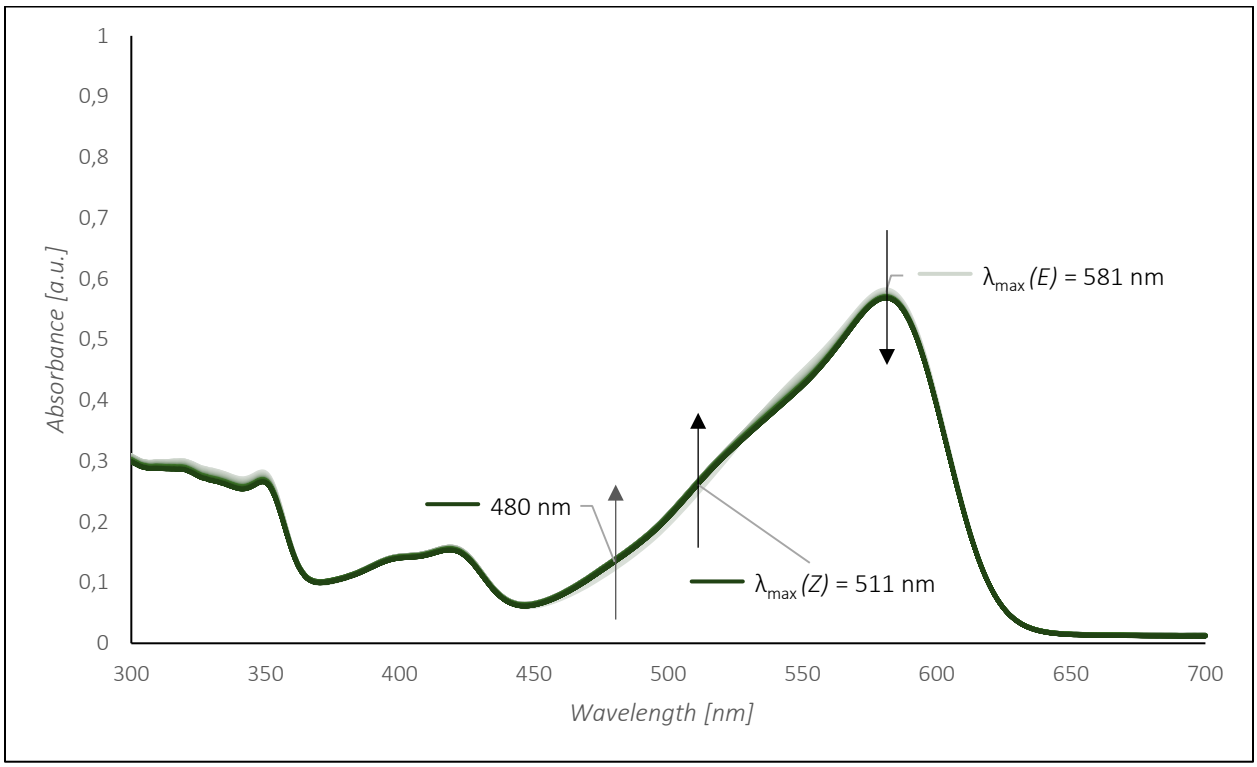

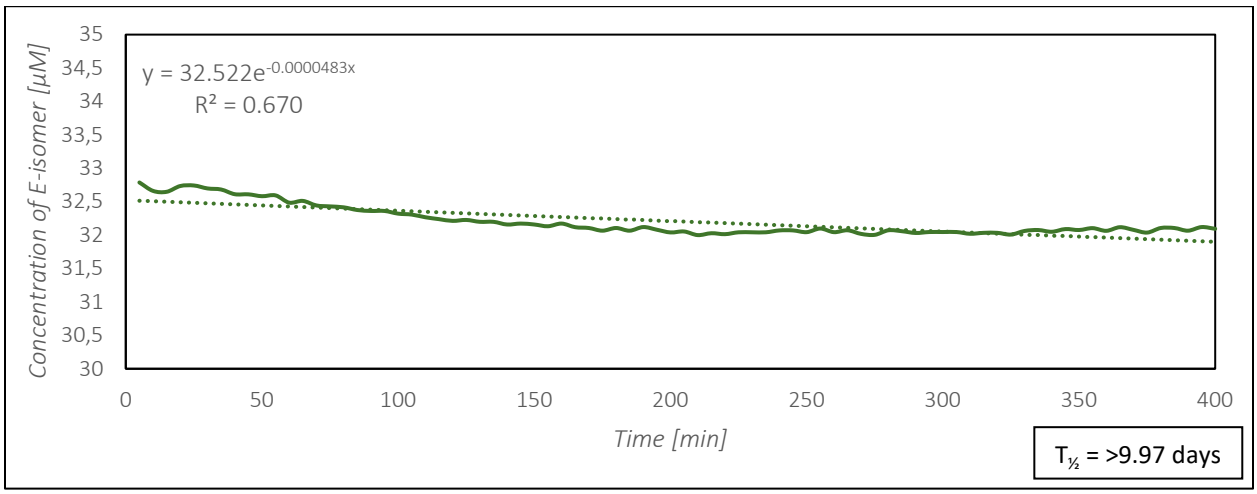

Note: Half-life was calculated using 480 nm as representative for λ_{max} (*Z*) = 511 nm and λ_{max} (*E*) = 581 nm.

UV-Vis photobleaching spectroscopy

Bipyrrole HTI (**18**) (33 μM in THF)

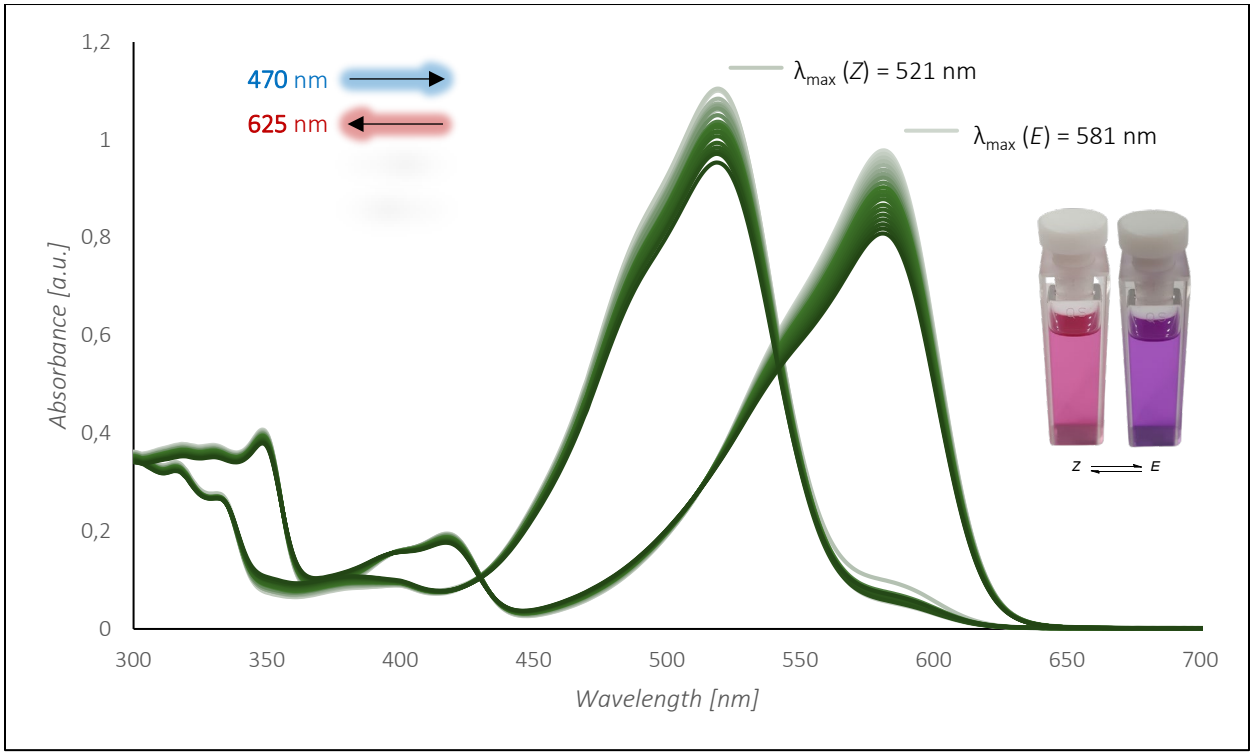

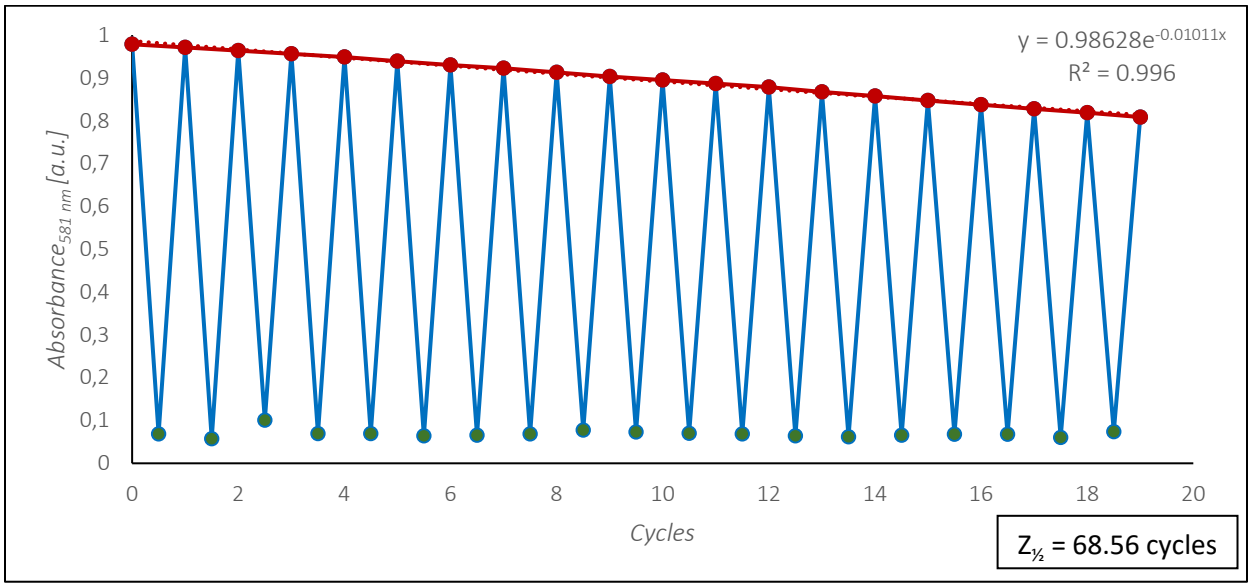

Note: Red marker is after irradiation with 625 nm (1 Amp) for 3 minutes, whereas blue marker is after irradiation with 470 nm (1 Amp) for 2 minutes.

5 Appendix

Nuclear magnetic resonance spectroscopy

^{1}H NMR, ^{13}C NMR

(2-Naphthylthio)acetic acid (3)

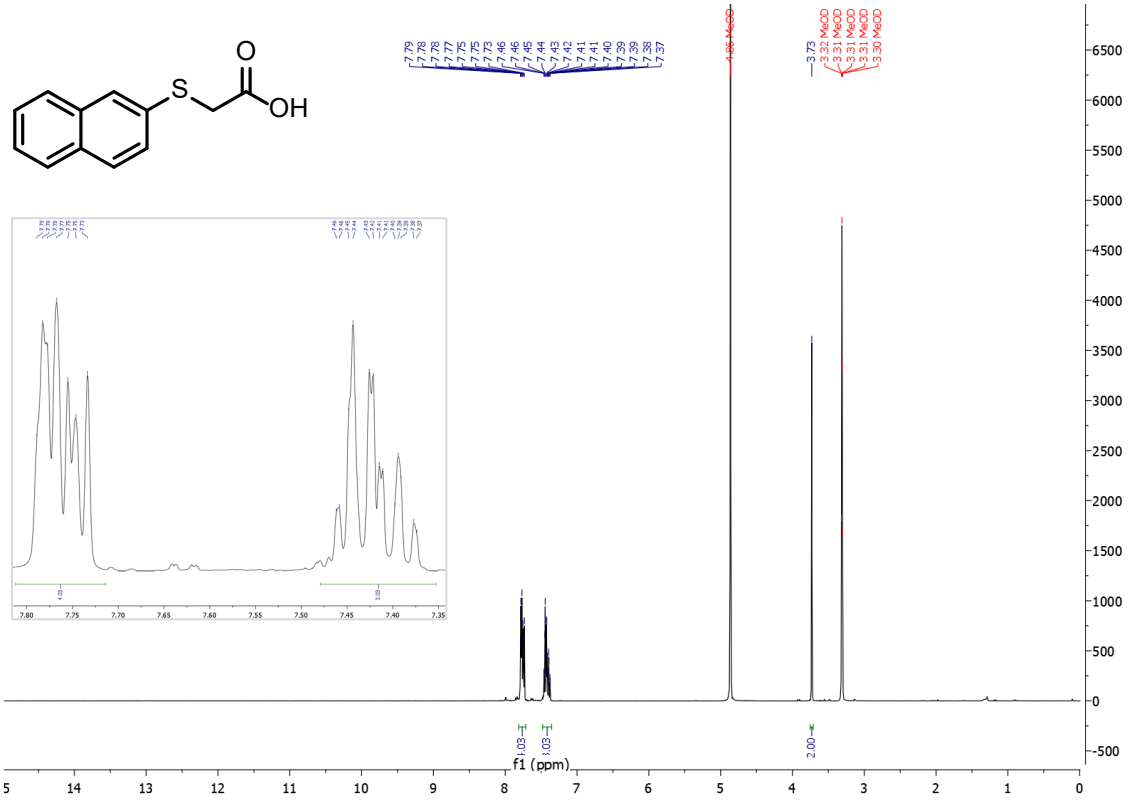

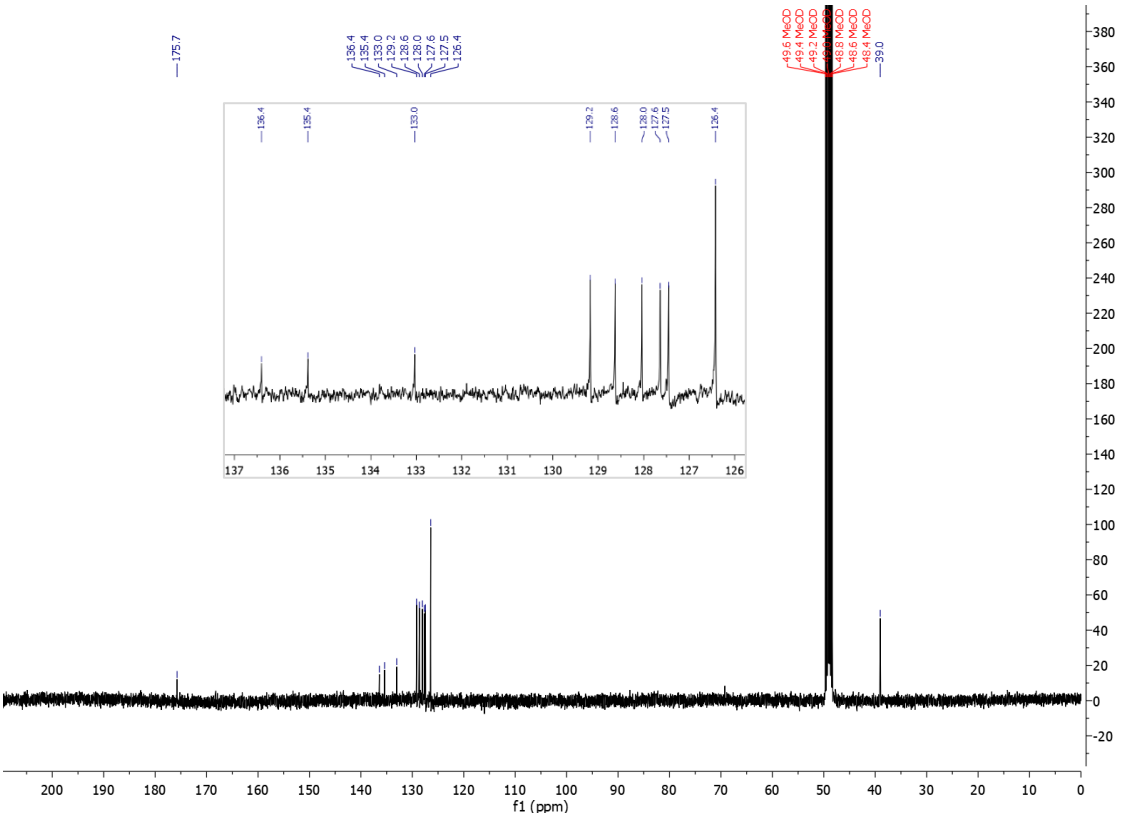

Naphtho[2,1-b]thiophen-1(2H)-one (5)

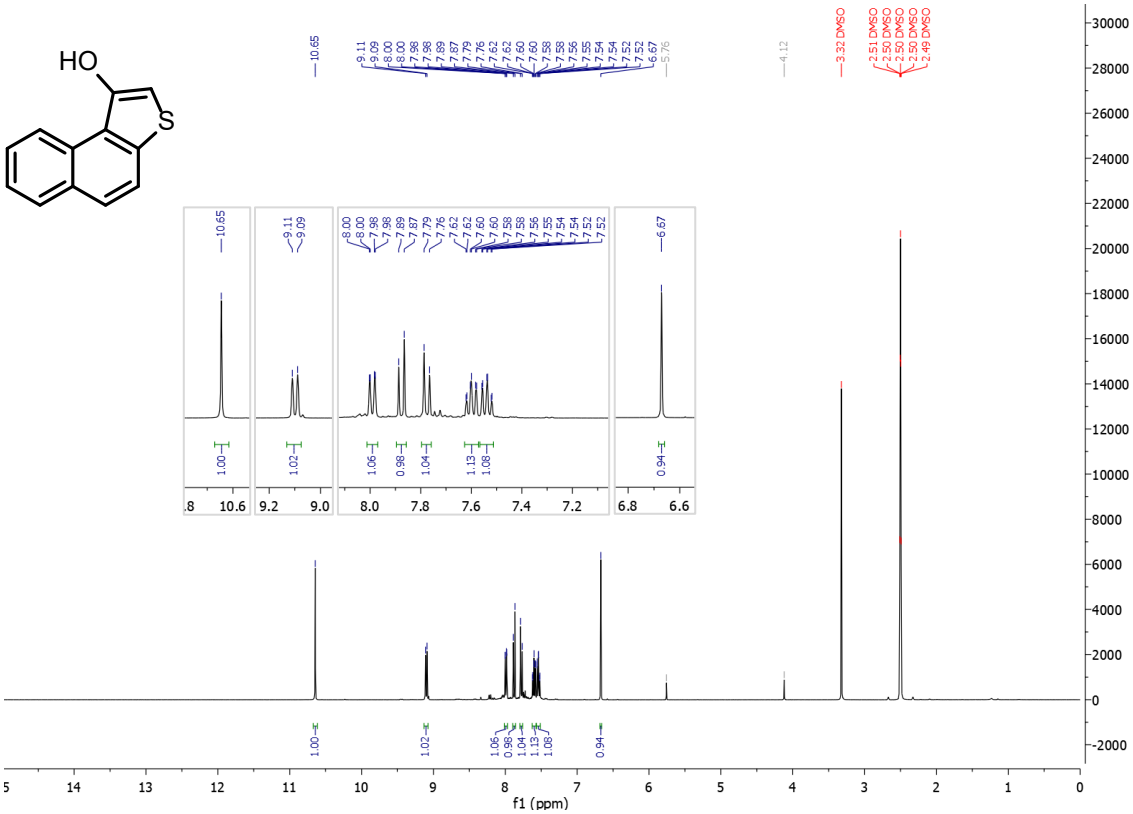

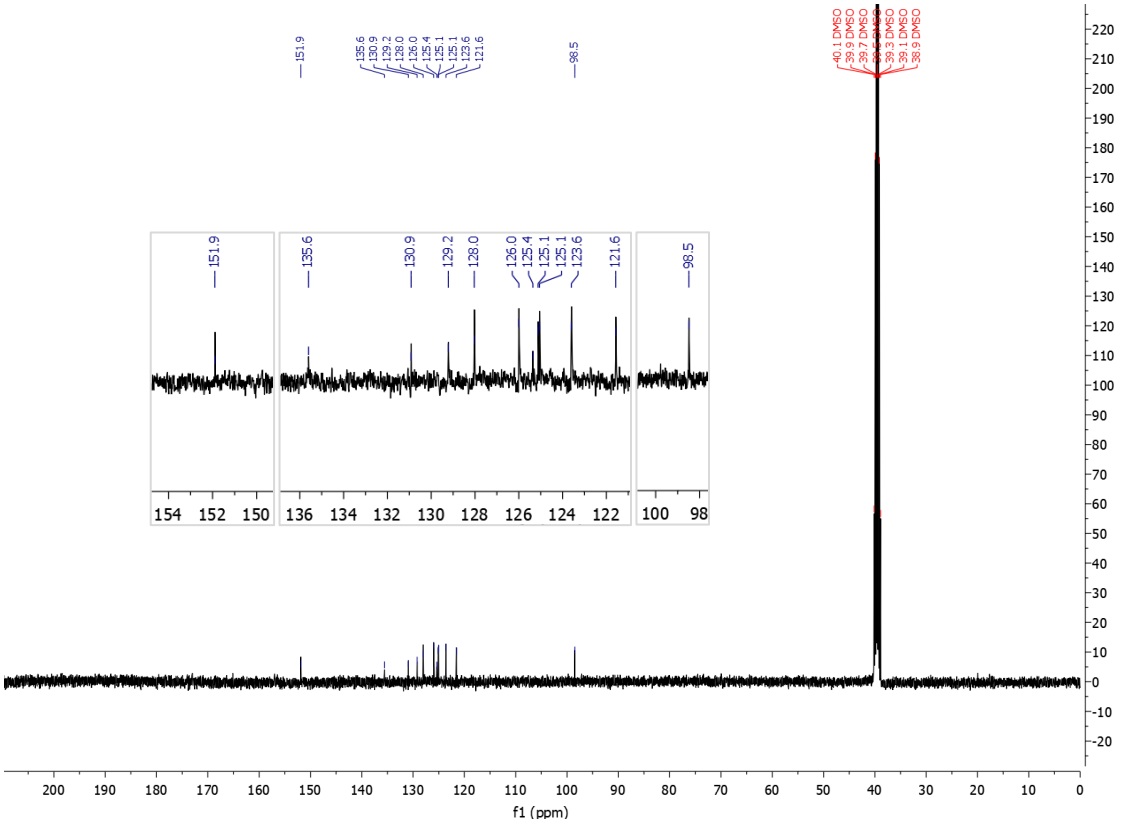

(*Z*)-2-(Naphthalen-1-ylmethylene)benzo[b]thiophen-3(2H)-one (10)

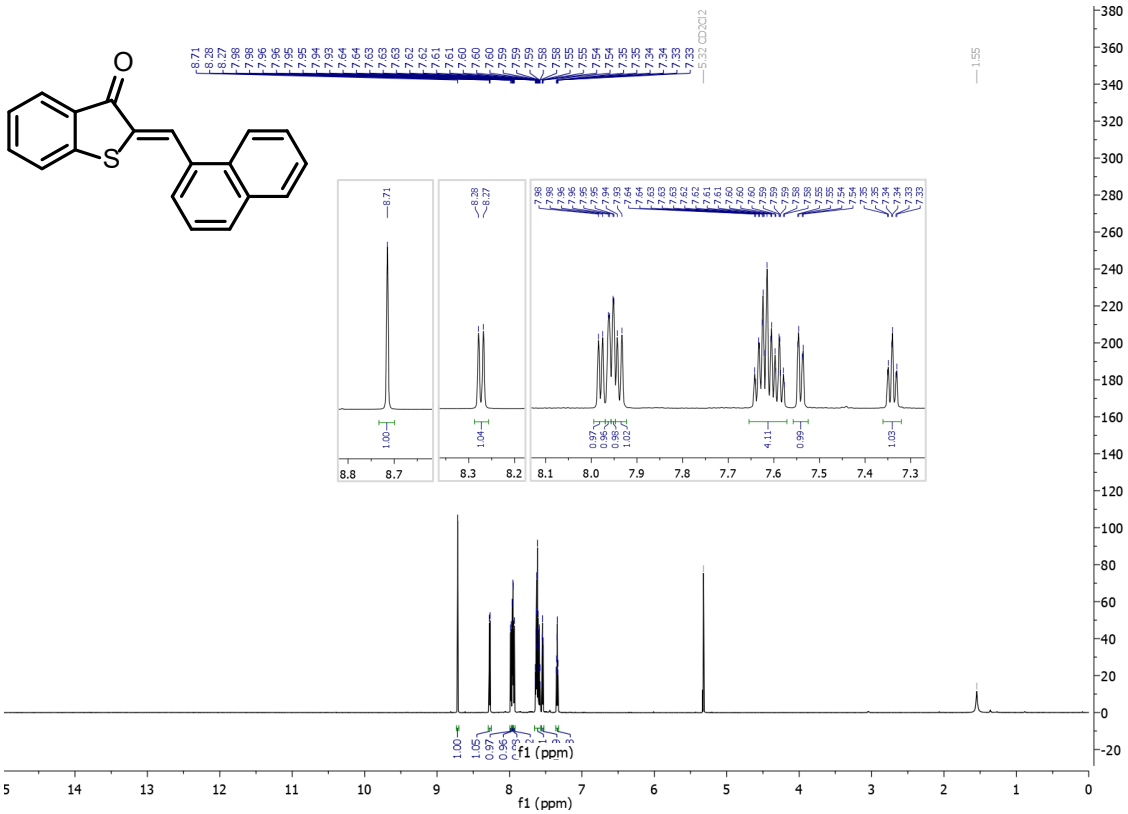

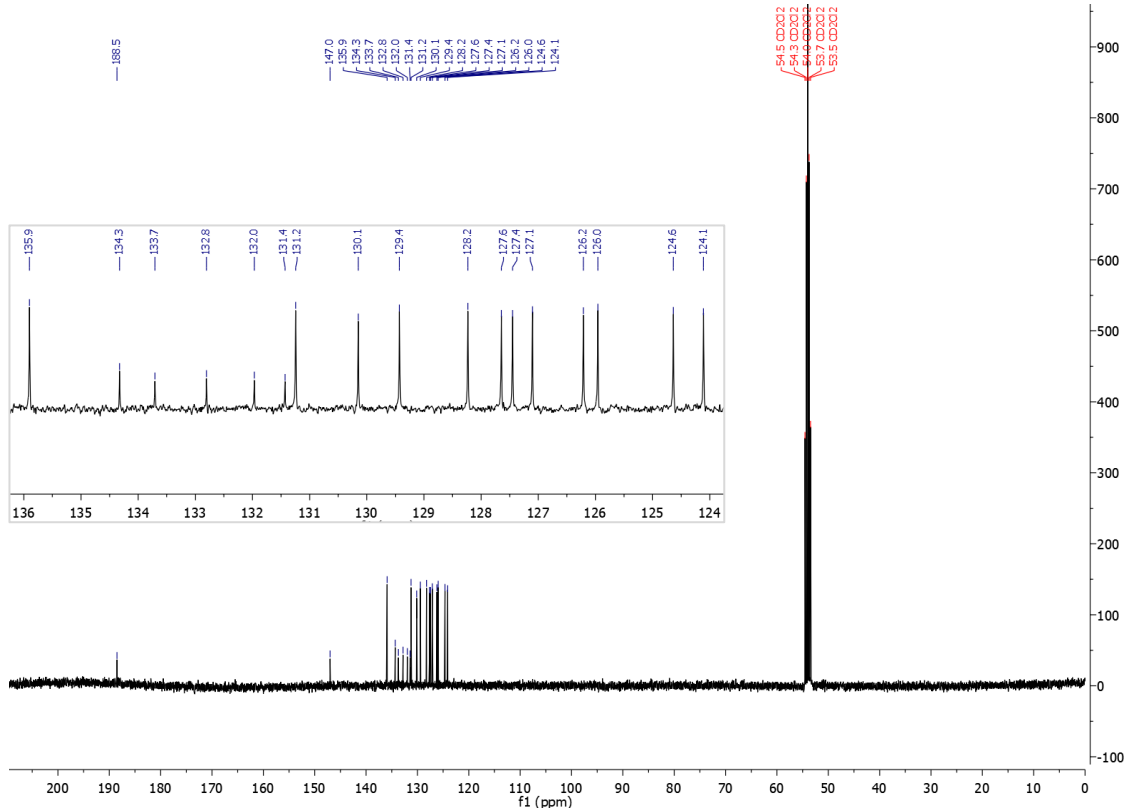

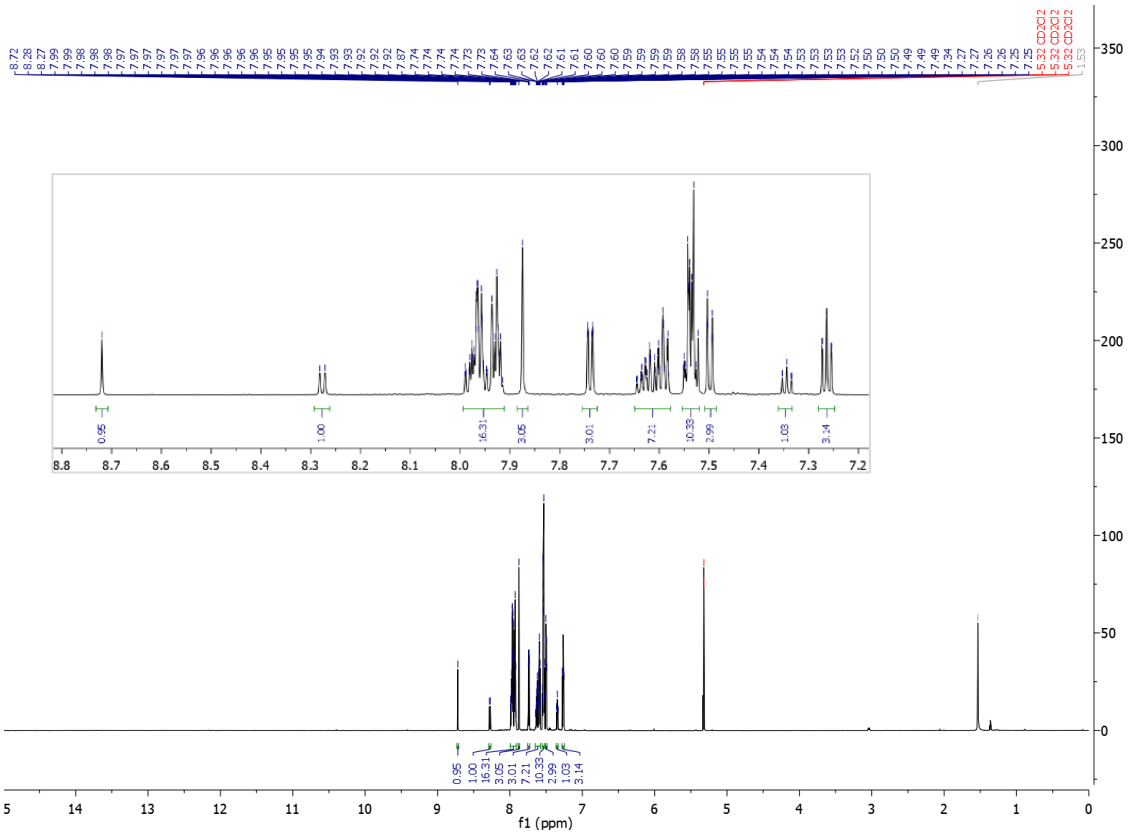

Note: Compound (**10**) in 1:3 (*Z*/*E*)

(*Z*)-2-(Naphthalen-2-ylmethylene)benzo[b]thiophen-3(2H)-one (11)

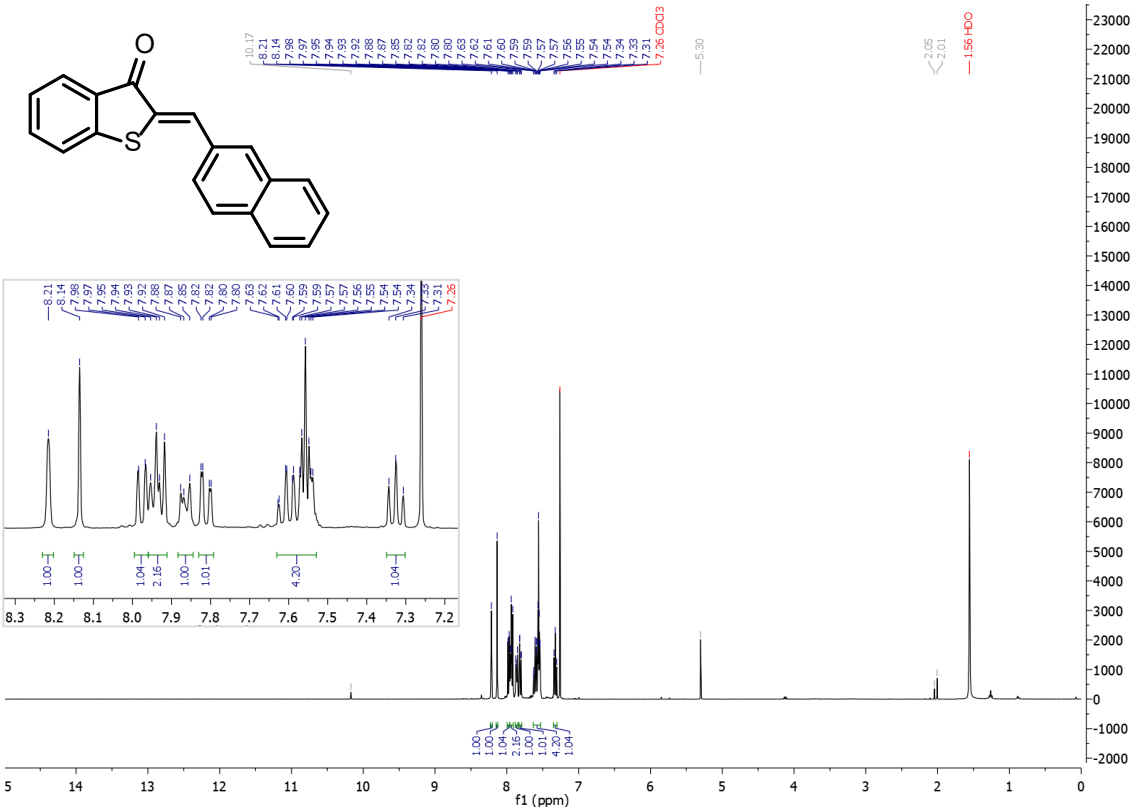

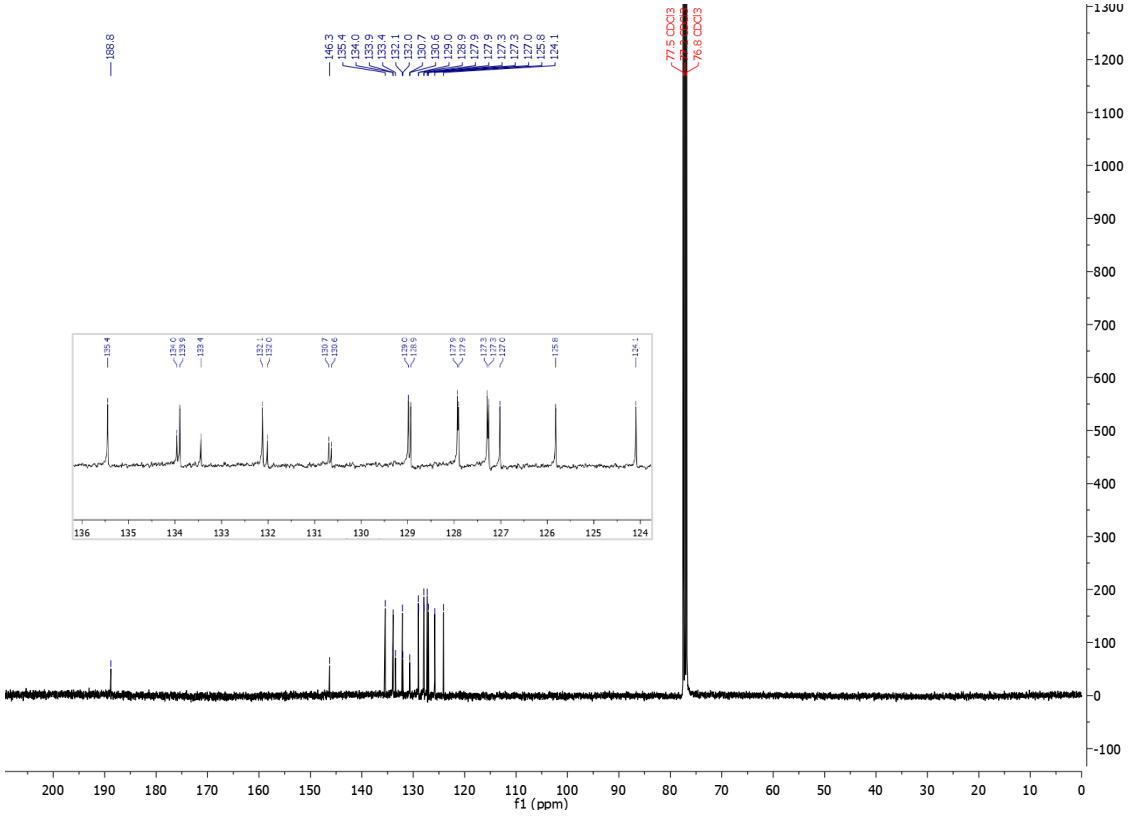

(*Z*)-2-benzylidenenaphtho[2,1-b]thiophen-1(2H)-one (12)

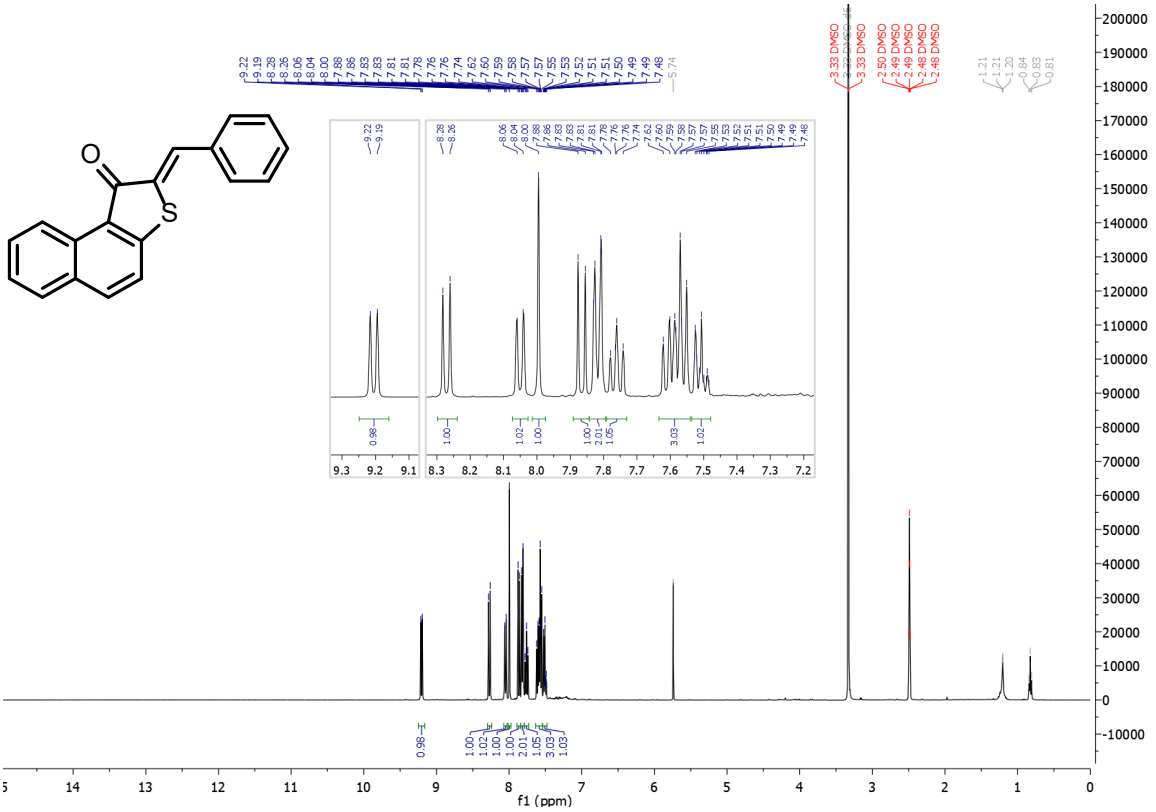

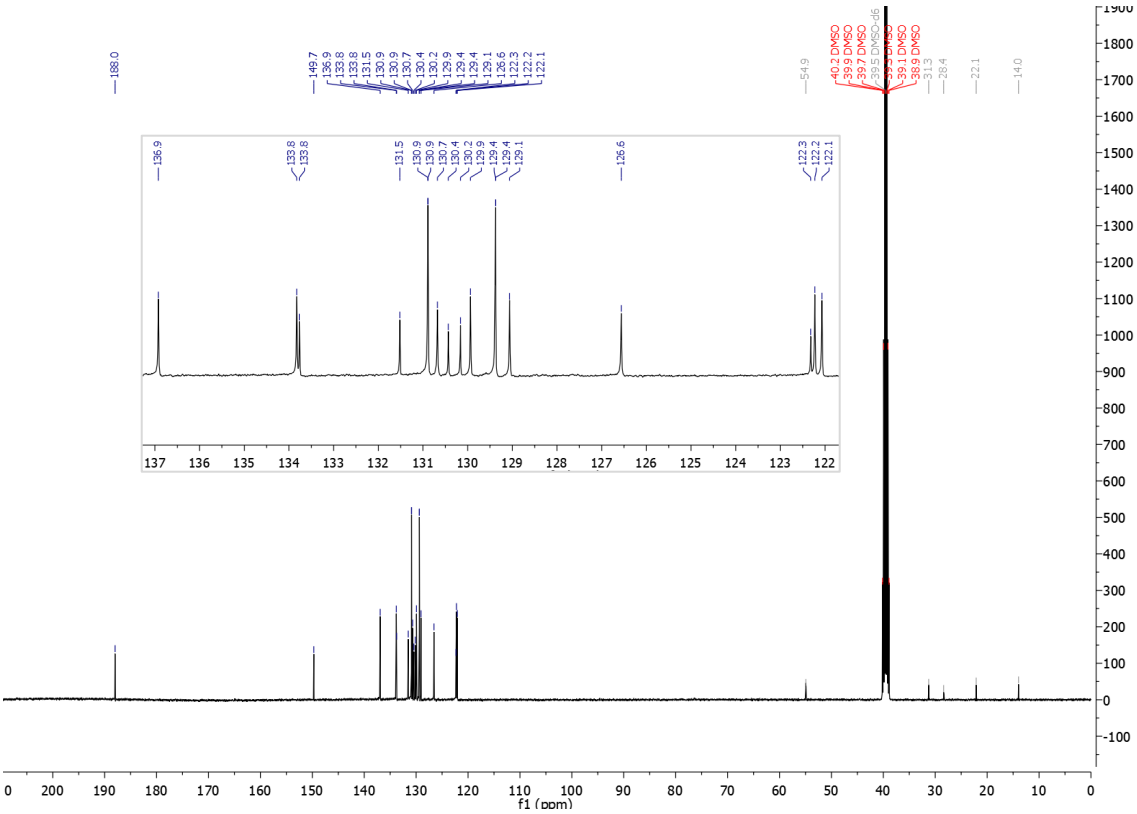

(*Z*)-2-(naphthalen-2-ylmethylene)naphtho[2,1-b]thiophen-1(2H)-one (13)

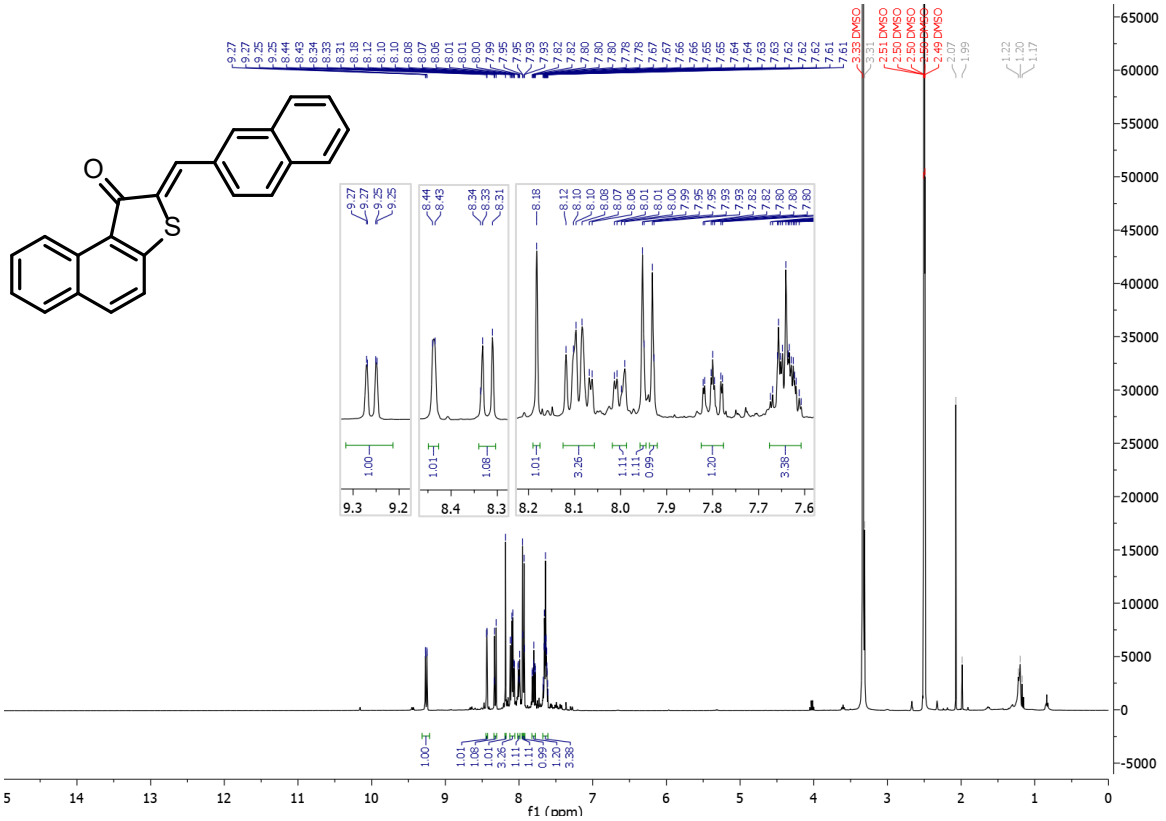

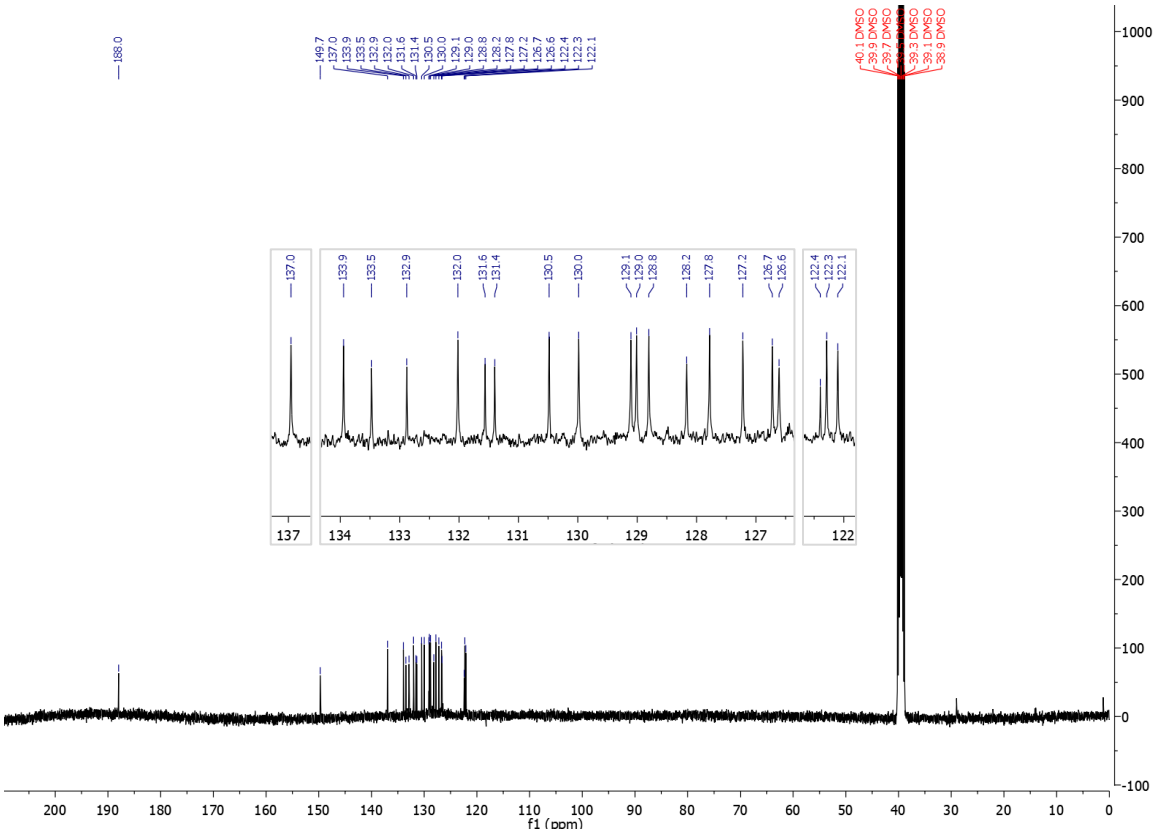

(*Z*)-2-((1H-Pyrrol-2-yl)methylene)benzo[b]thiophen-3(2H)-one (14)

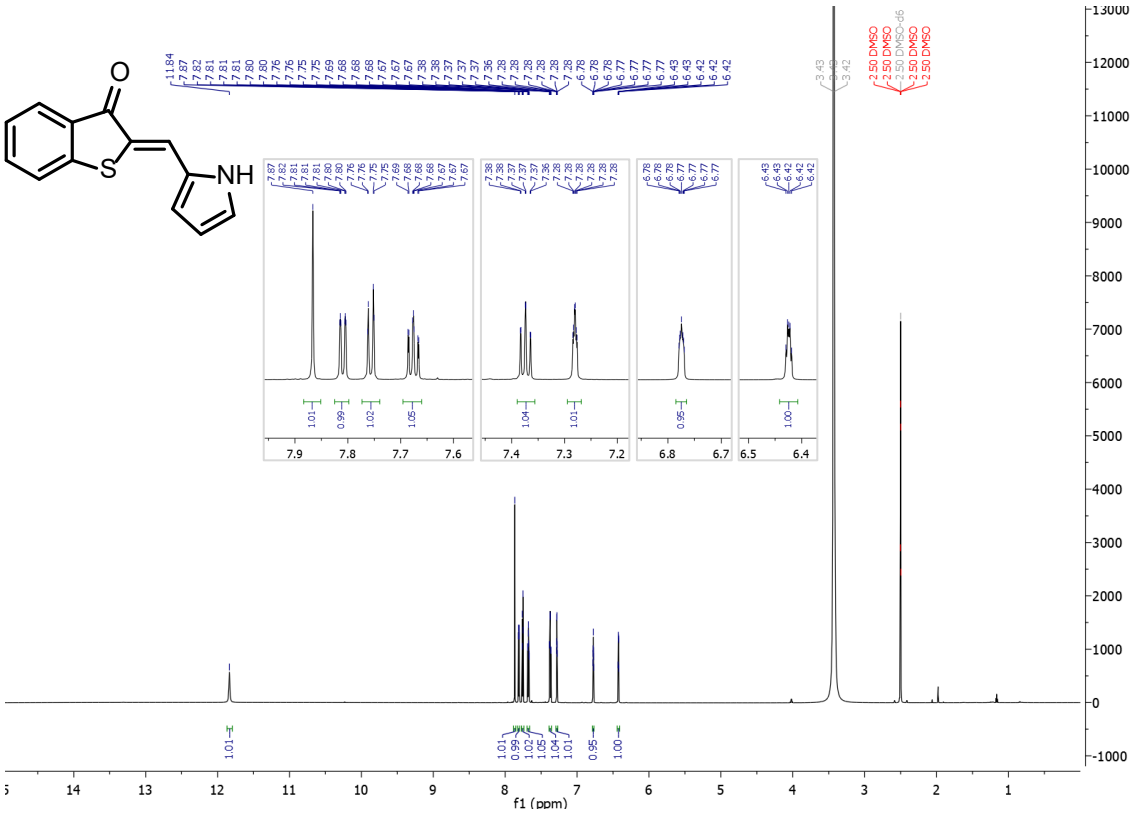

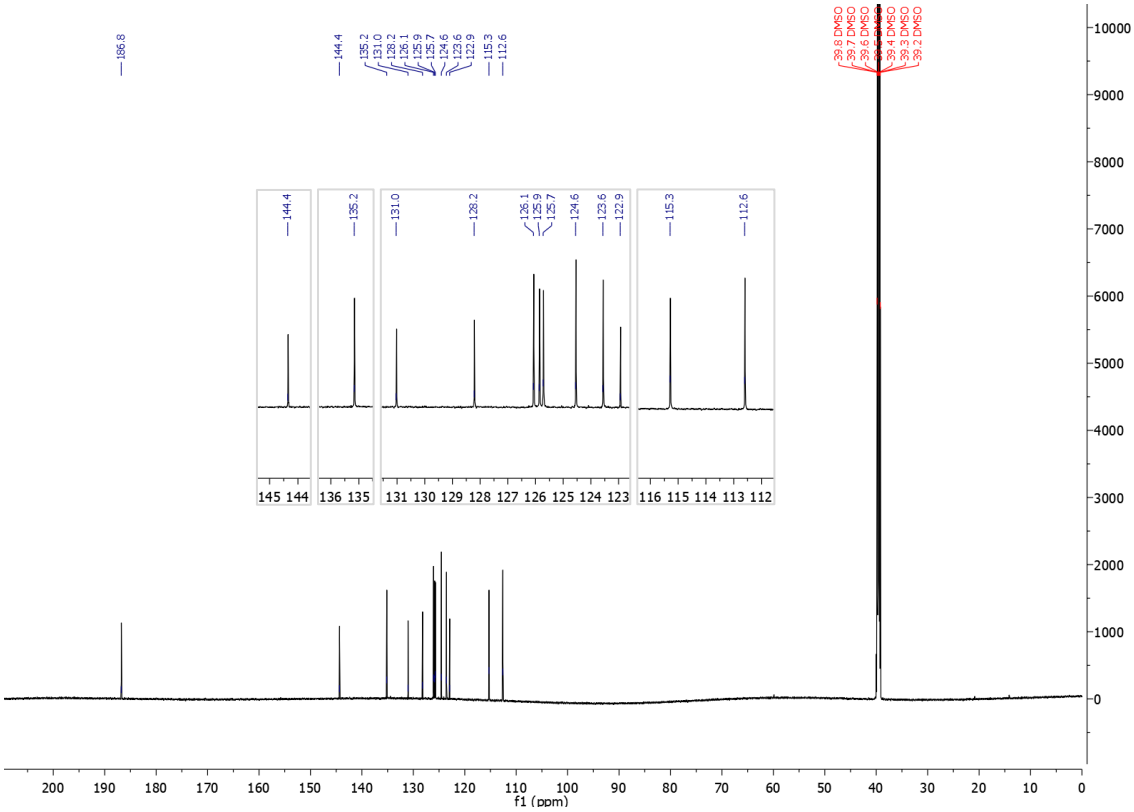

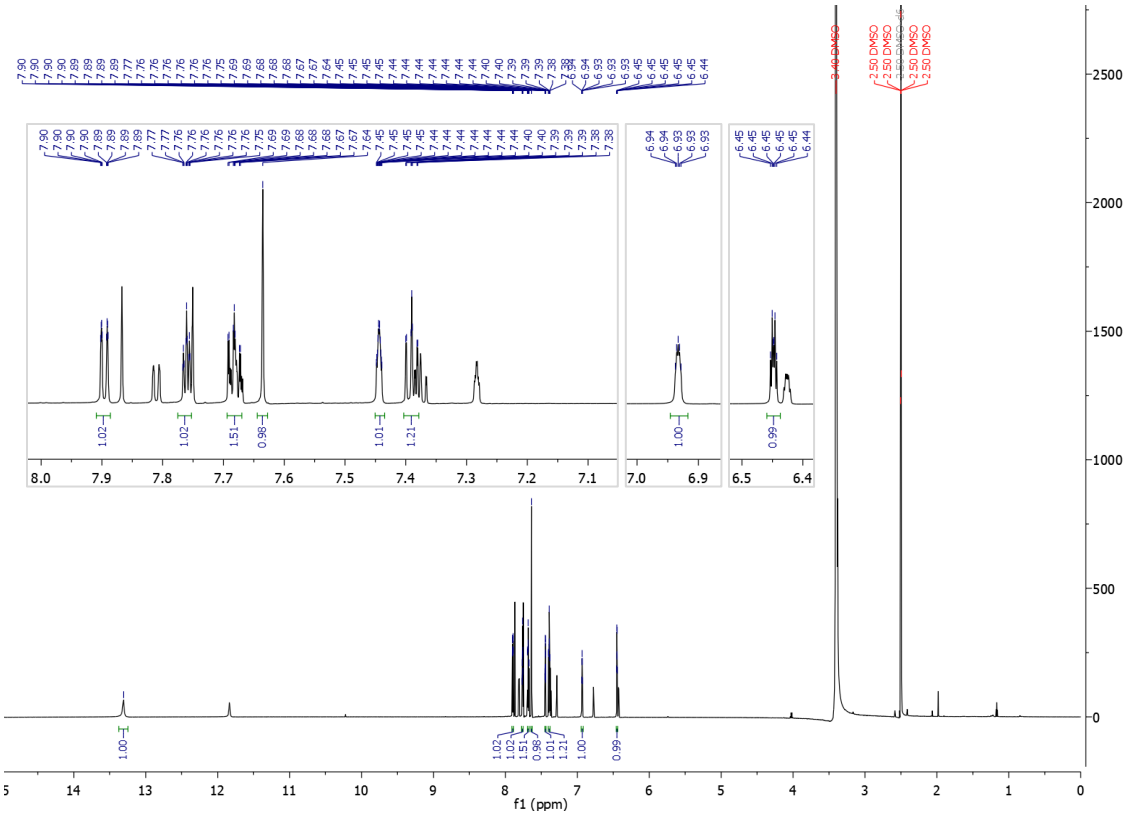

Note: Compound (**14**) in 1:2 (*Z*/*E*)

(*Z*)-2-((1H-Indol-2-yl)methylene)benzo[b]thiophen-3(2H)-one (15)

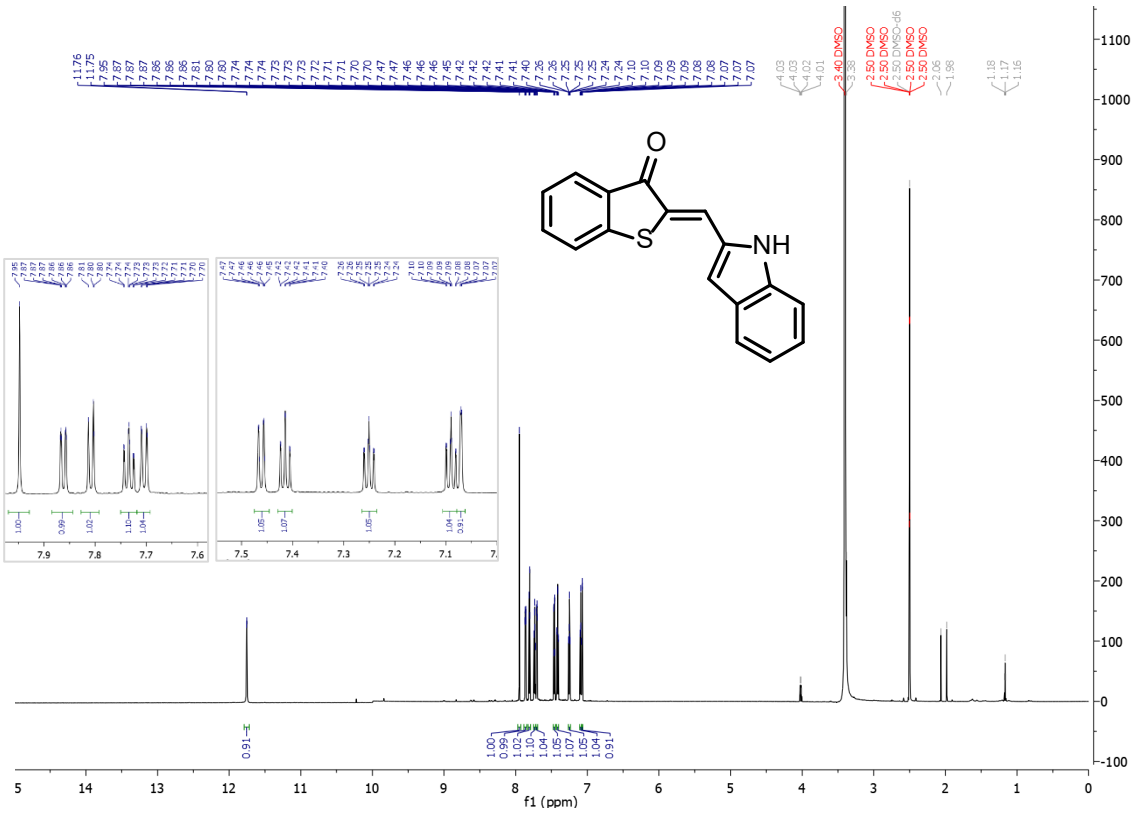

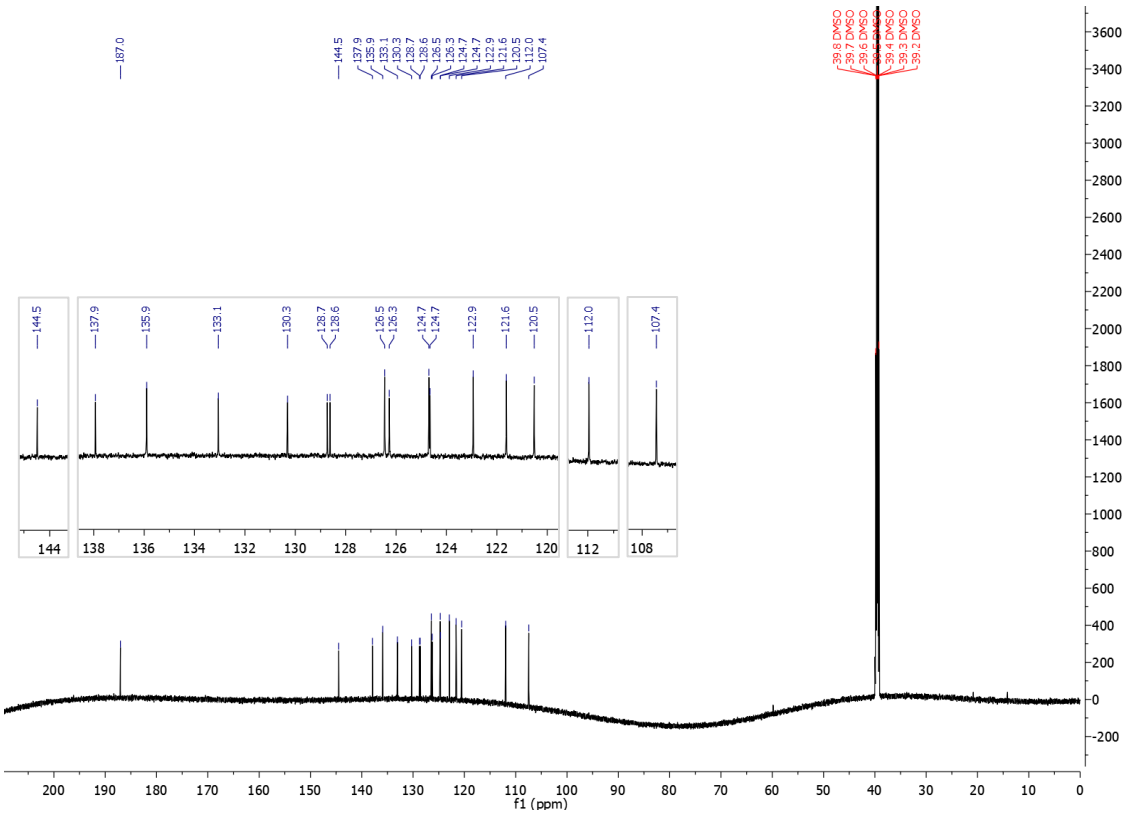

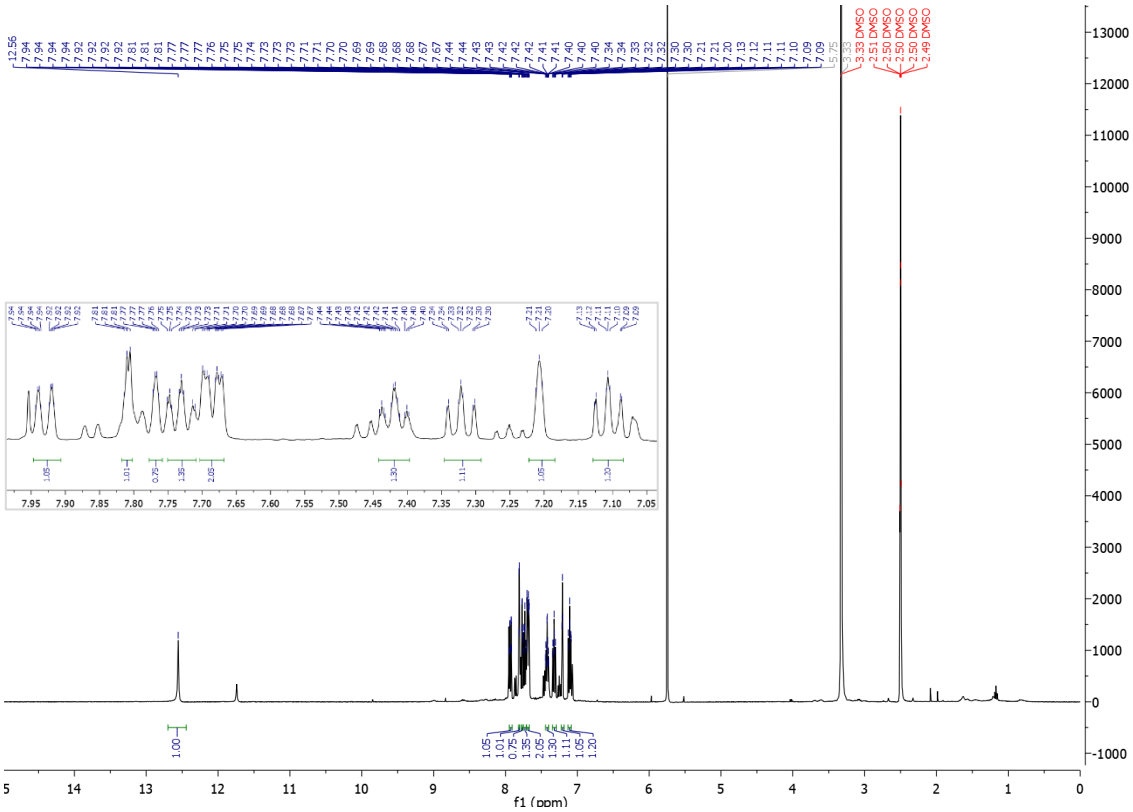

Note: Compound (**15**) in 1:4 (*Z*/*E*)

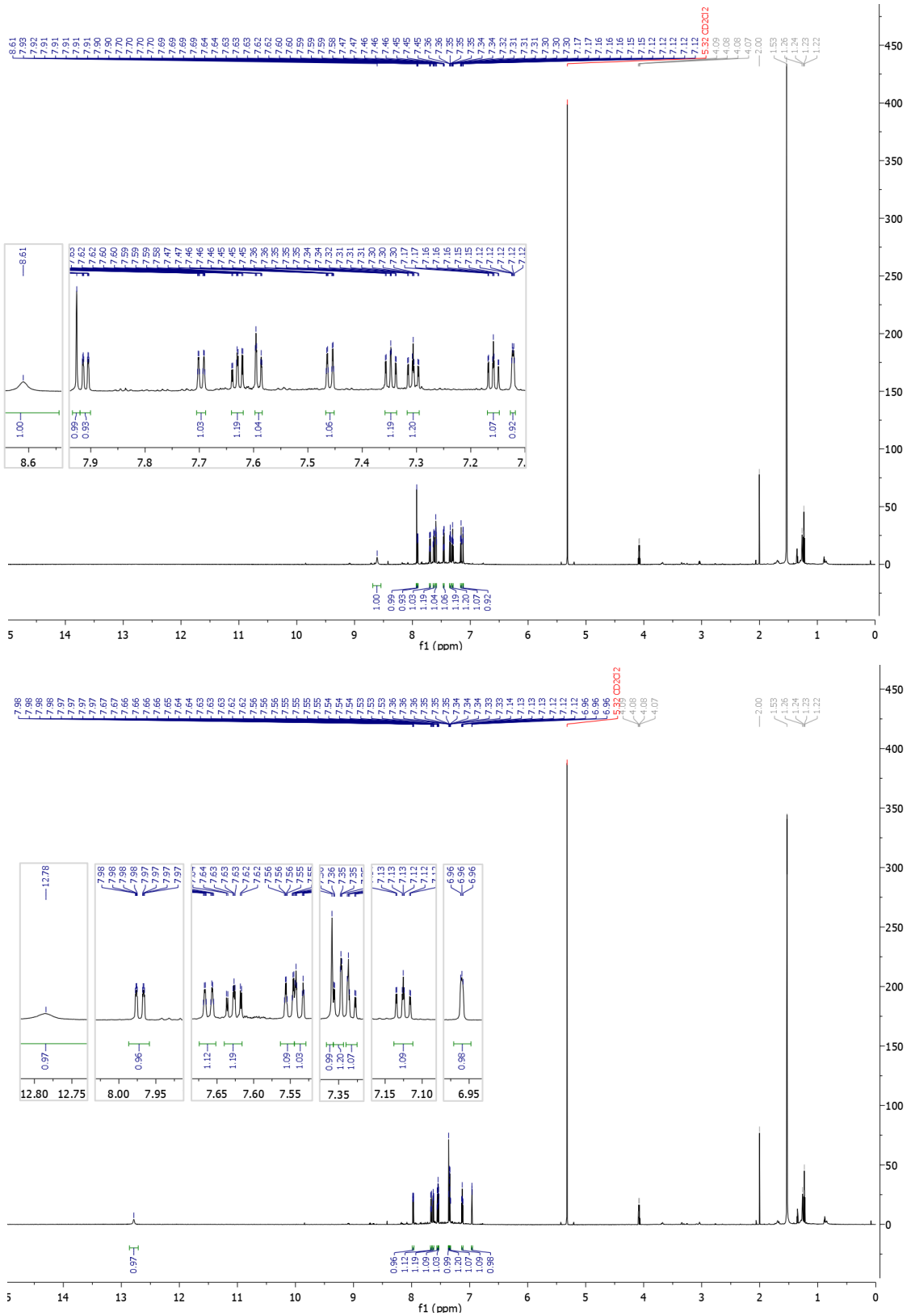

Note: Compound (**15**) in >99 (*E*)-isomer used for ^{1}H NMR thermal relaxation spectroscopy

(*Z*)-2-((1H-pyrrol-2-yl)methylene)naphtho[2,1-b]thiophen-1(2H)-one (16)

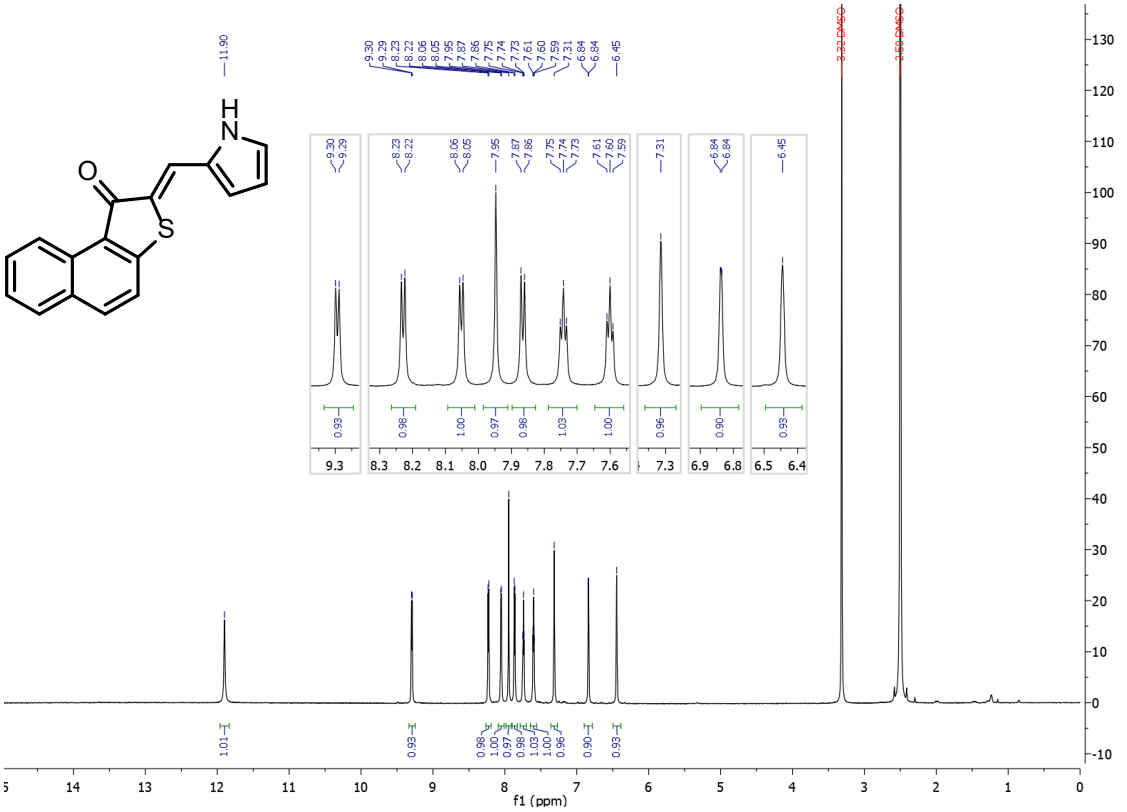

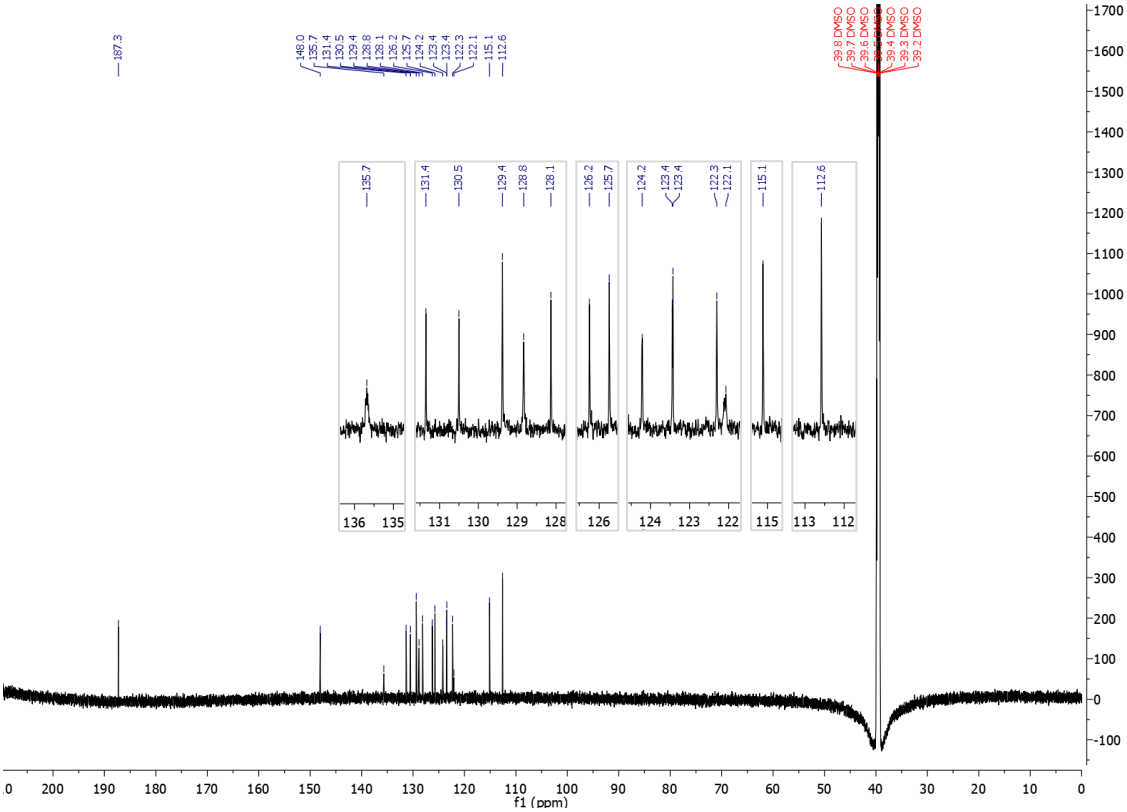

(*Z*)-2-((1H-indol-2-yl)methylene)naphtho[2,1-b]thiophen-1(2H)-one (17)

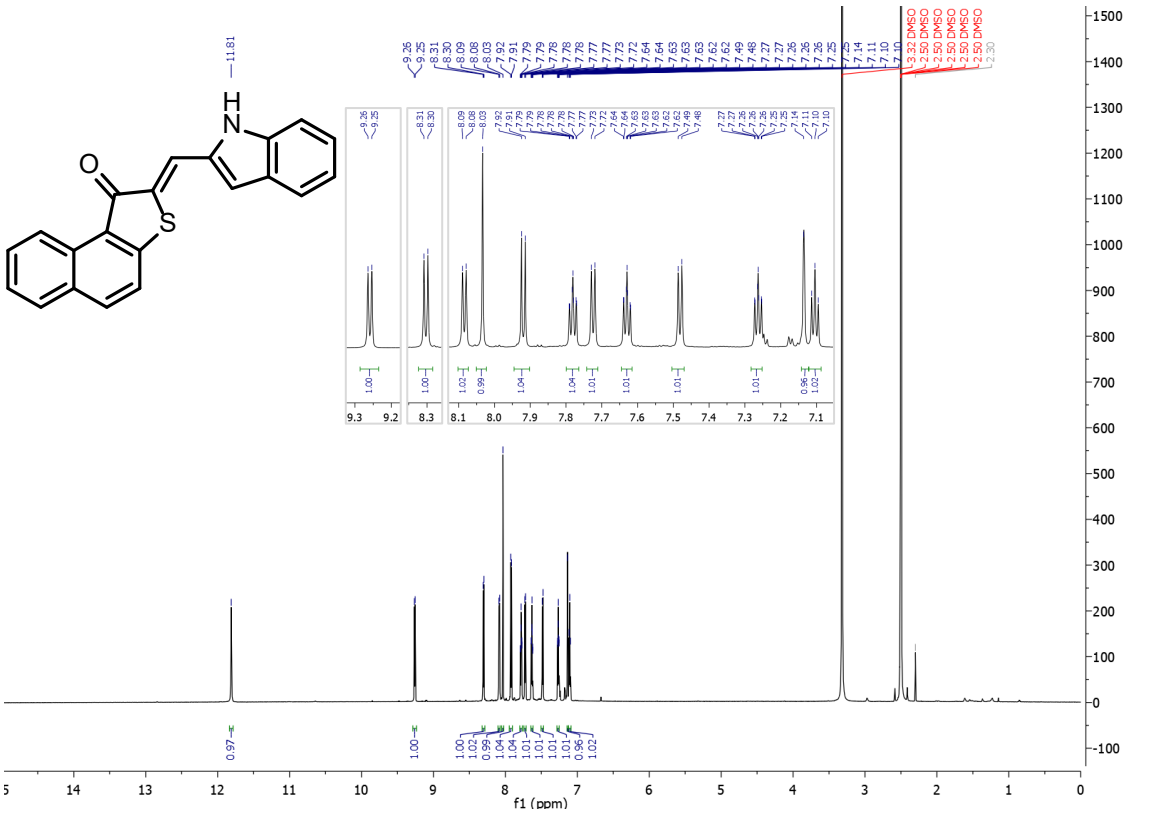

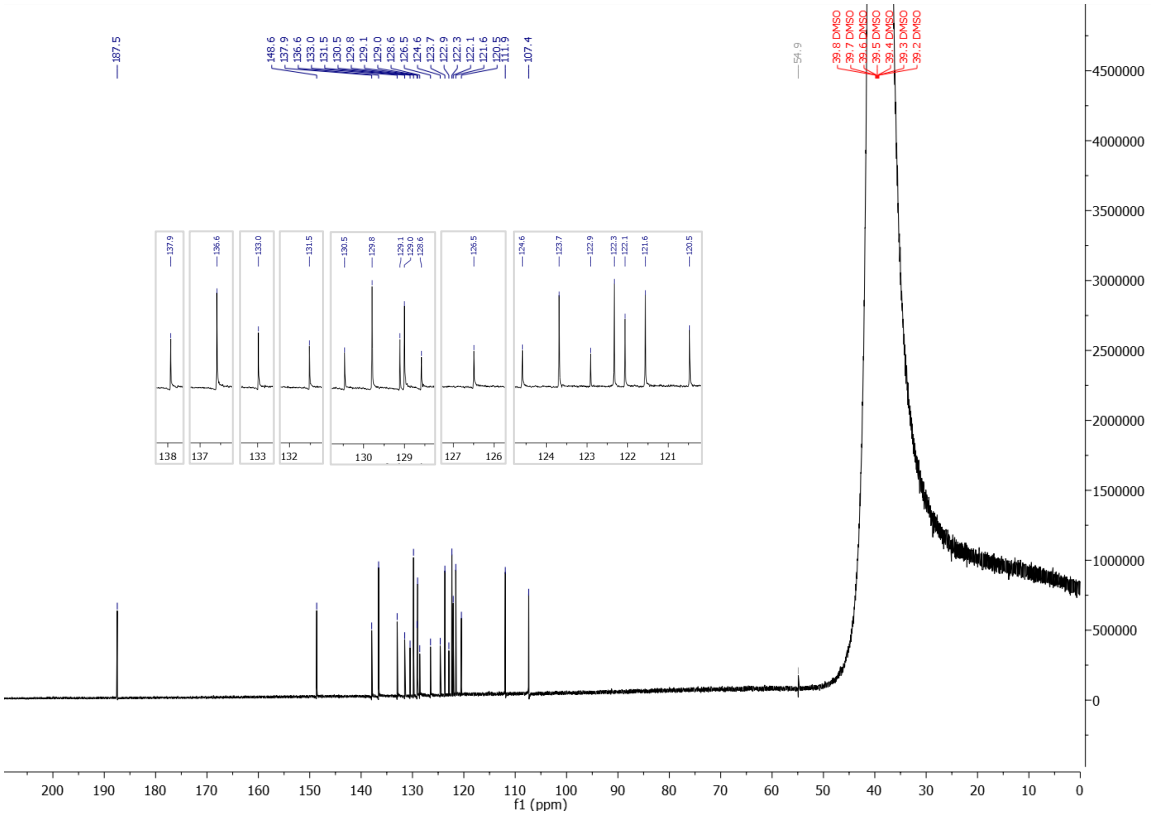

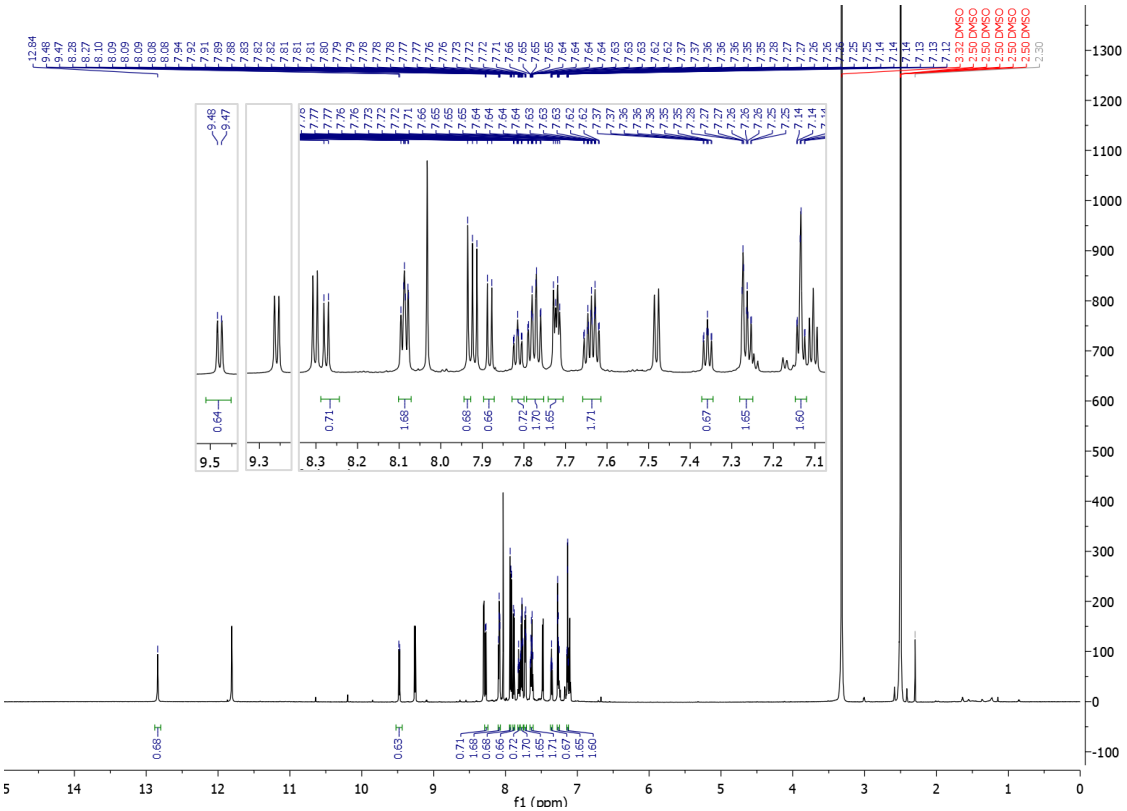

Note: Compound (**17**) in 1.5:1 (*Z*/*E*)

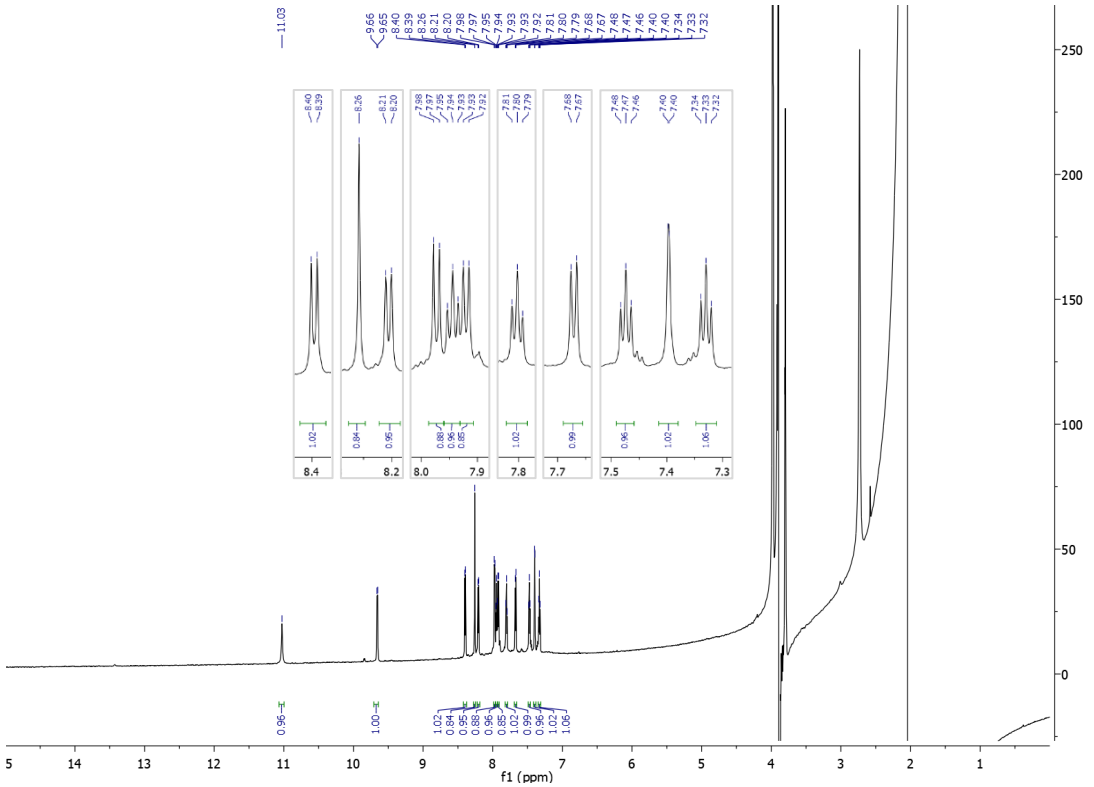

Note: Compound (*Z*-**17**) with double solvent suppression of the THF proton signals

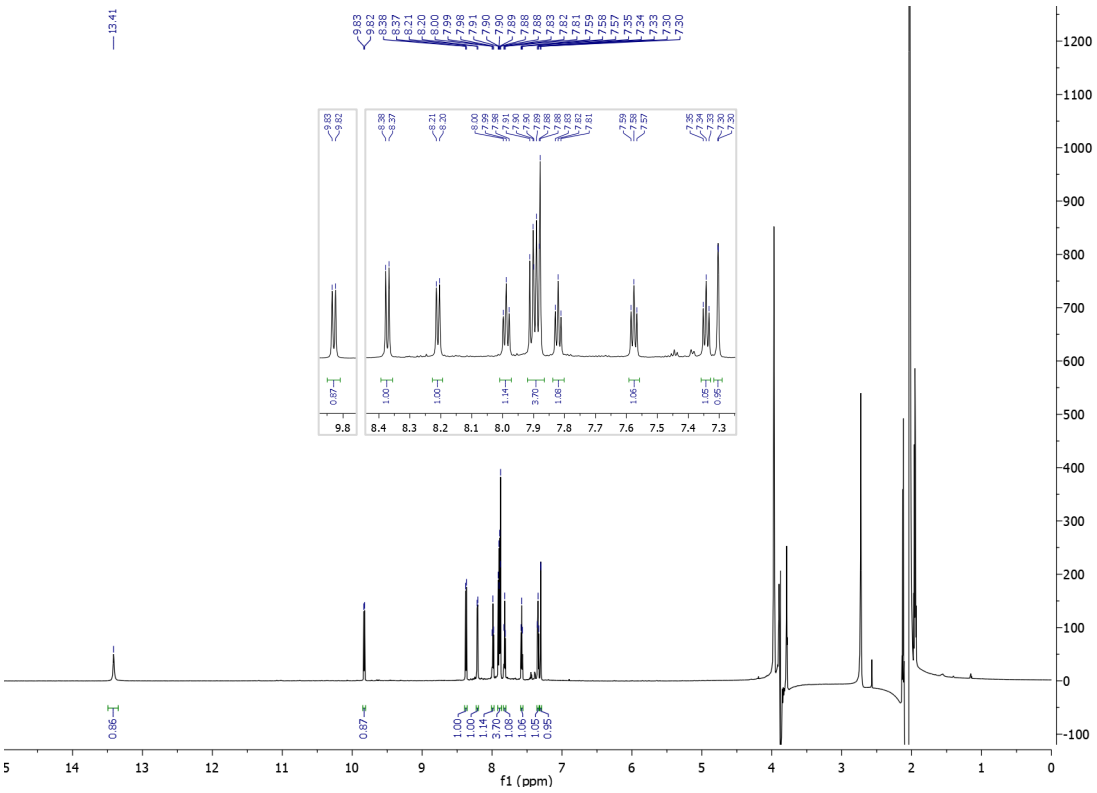

Note: Compound (*E*-**17**) with double solvent suppression of the THF proton signals

(*Z*)-2-(1H,1'H-[2,2'-bipyrrol]-5-ylmethylene)benzo[b]thiophen-3(2H)-one (18)

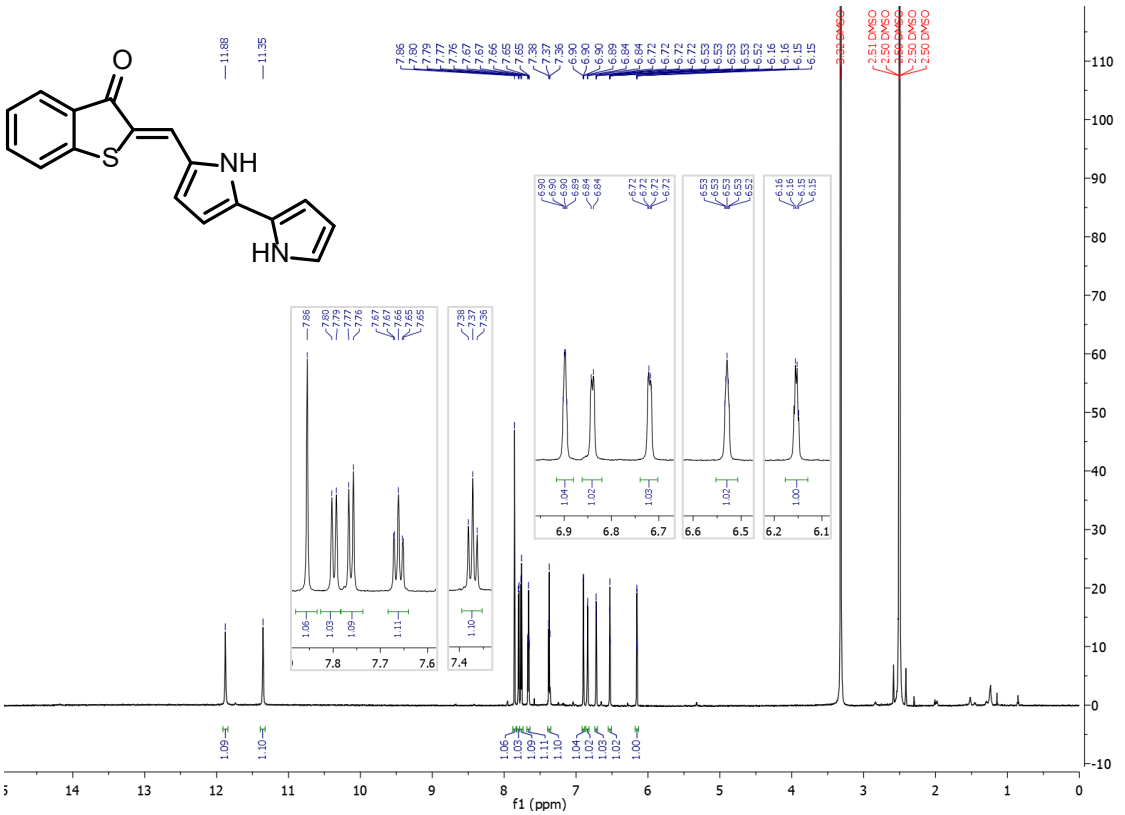

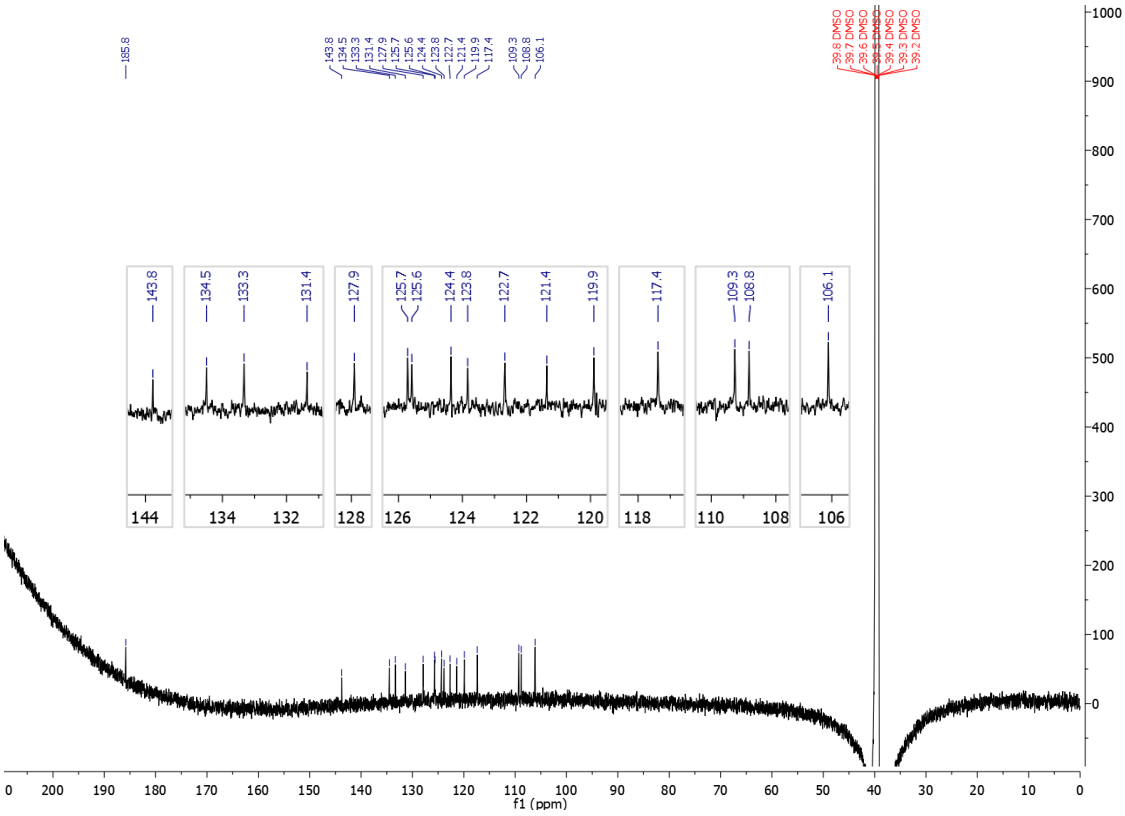

4. MICROREACTORS COUPLED WITH ELECTRO- & PHOTOCHEMISTRY

The way organic synthesis is currently carried out has not changed significantly in the last five decades. While other disciplines have embraced automation to increase productivity and enhance the discovery process, organic synthesis is still mostly carried out in round-bottomed flasks by individual chemists with a very limited throughput. Therefore, new technologies are in demand that seeks to improve the state of synthetic chemistry in a research laboratory. Flow chemistry is a relatively new technology, which has emerged and received a remarkable amount of attention in the past two decades. It offers attractive opportunities for enhanced process control and couples exceptionally well with electro- and photochemistry, which are inherently green processes. Flow chemistry is typically performed with microreactors possessing small inner diameter length scales. However, current drawbacks include that the microfluidic equipment and process setup are too costly for the occasional user.[151] Recent advances in 3D printing, however, addresses this by allowing reactor design to be fast, convenient and cheap.

4.1 FLOW CHEMISTRY

Flow chemistry involves the use of channels or tubing to conduct a reaction in a continuous stream rather than in a flask (**Figure 4.1**).[151] The fluids are driven by applying a pressure gradient between the in- and outlet of the reactor using either syringe or peristaltic pumps. A few important parameters change when going from the familiar batch setup to flow conditions. Among these is the reaction stoichiometry, which is controlled by the reagent concentrations and flow rate of the inlet streams, in contrast to the reagent concentrations and volumetric ratio for batch conditions. Furthermore, due to the defined reactor volume, the reaction time is described as the residence time of the solution within the confines of the reactor controlled by the overall flowrate, while for batch chemistry it is defined as the time period in which the reaction is held at a given set of conditions.

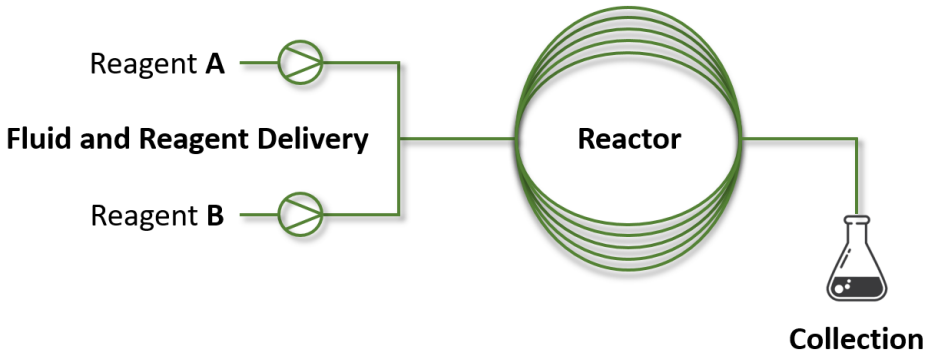

Figure 4.1. *Illustration of a simple continuous flow diagram of two pumps introducing reagent A and B into a reactor with subsequent collection at the end of the channel.*

Continuous flow chemistry is advantageous in many aspects to the traditional batch chemical setup that uses a flask, due to the continuous nature, but also the small reactor volume (Table 4.1). Flow is perfectly suited for exothermic (runaway) reactions as the substantial increase in surface area to volume ratio provides excellent heat transfer characteristics. Additionally, the small reaction channels entails that the primary mixing mechanism moves from convection to diffusion resulting in enhanced mass transfer, and hence, homogenous conditions can be established in milliseconds. The enclosed system with little to no headspace allows reaction pressures that are orders of magnitude higher than operational possible with flasks, microwave vials or pressure tubes. Furthermore, reactions can be conducted with temperatures above the boiling point of the solvents with narrow temperature profiles. Hence, reaction times are often significantly reduced down to minutes or even seconds.[152–154] From a safety point of view, flow chemistry offers safe handling of hazardous and toxic intermediates, partly due to the enclosed system, but also as a consequence of the small volumetric quantity, which batch chemistry evidently struggles to find good solutions for.[155,156] In addition, the conversion to product is translated to a function of time, and with fast reaction kinetics combined with a continuous removal of product from the reactor zone, byproduct formation is often significantly reduced, which leads to an overall increase in reaction quality. The enhanced process control further ensures an improved control of the stereochemical outcome, chemical yield and results in increased reproducibility.[157–159] The ability to scale up reactions is conveniently executed by simply increasing the run time of the process, which not only ensures the reaction conditions remain the same, but also mitigates the potential dangers that follow working with larger volumes and moles of reactants. An alternative is the numbering-up strategy with more channels in parallel mode. Lastly, reaction telescoping is neatly arranged through serial coupling of reactors that can perform different tasks, which may conveniently be controlled through automation with real-time in- or on-line analysis that provides information about reaction performance with feedback loops requiring only minimal human interaction.[157,160–162]

By scaling down flow chemistry to the microfluidic regimen, the advantages and disadvantages of flow compared to batch chemistry are further enhanced. These include very rapid steady-state conditions with almost near-instantaneous heat transfer and mixing, in addition to handling of minuscule amount of volumes, which thereby reduces the amount of sample required.

Table 4.1. *Overview of advantageous properties adapting batch to continuous flow conditions.*

Pros of Continuous Flow Chemistry

Process Control	Safety	Smaller Footprint	
Product Quality/Efficiency		In-line Downstream Processing	
Scale up	Reproducibility	Telescoping	Automation
Mass & Heat Transfer		Electro- & Photochemistry	
Extreme Conditions		Literature Procedures	
Operational Stability (Precipitation → Fouling)			
Time-Consuming & Costly Development			

However, flow chemistry cannot be applied to solve every challenge in organic synthesis. Batch reactors exert a better operational stability as reactions involving insoluble reagents or precipitation of product may be inadequate for flow, due to fouling and clogging of the system (Table 4.1). Furthermore, developing a flow process can be time-consuming and costly, which is why a balance between convenience and achieving the overall goal needs to be considered. Although reproducibility sometimes proves difficult, the majority of reported chemical reaction procedures in the literature are for batch chemistry. Therefore, if the reaction is safe in batch and reported at an acceptable level with respect to yield, scale and reaction time, it is favoured to reproduce the conventional reaction conditions instead of trying to convert it to flow conditions.[151]

4.2 MICROFLUIDIC FLOW REACTORS

Technological advances have made chemical laboratories in hand-held systems possible developed on silicon or polymer chips. These lab-on-a-chip (LOC) systems, or microfluidic reactors, typically possess narrow channels in the µm range and permits easy handling of volumes down to picoliters. It is important to remember that the attenuation of light even at low mM concentrations does not effectively allow transmittance past an inner diameter of 0.5 mm. [151] Hence, the small channel dimensions of a photochemical microreactor is advantageous in contrast to a batch reactor. For electrochemical applications, the microreactor facilitates lowered cell resistance, which also entails a decreased evolution of heat, due to the small length scale in contrast to batch reactors. Bulk electrolysis in non-aqueous solvent requires supporting electrolytes to facilitate charge transfers and drive electrochemistry, while microreactors often eliminate the need for electrolytes altogether.[163] A further elaboration of this can be found in the subsequent section, which briefly describes electrochemistry in flow. The continuous nature benefits both of the mentioned processes as the product is swiftly removed from the reactor zone preventing its decomposition or further transformation that leads to byproducts formation. Several open-source and commercial reactors for carrying out photochemistry or electrochemistry in flow exist as both of these processes benefit tremendously from the small length scale presented by microfluidic flow reactors (Figure 4.2).

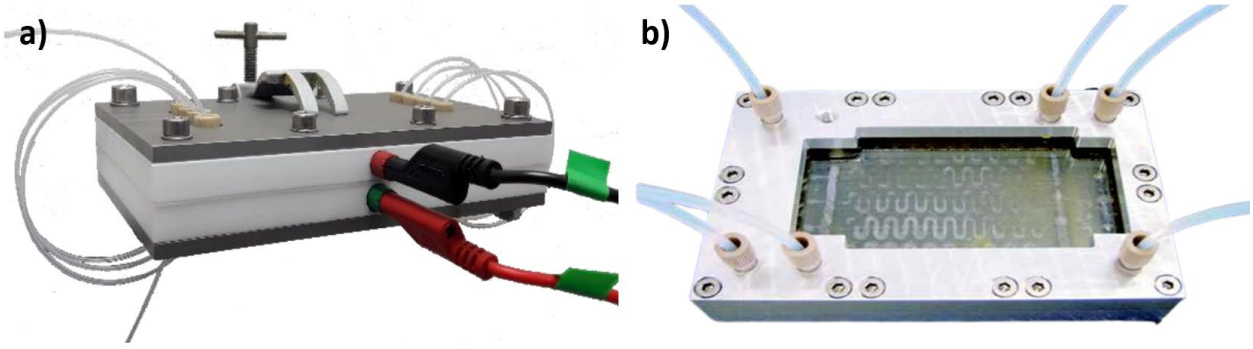

Figure 4.2. Examples of microfluidic flow reactors. a) Machined parallel (8-channel) electrochemical reactor. Adapted from T. Nöel et al.[164] *b) Mikroglass® chemtech GmbH commercial machined photochemical reactor. Adapted from Mikroglass chemtech GmbH product catalogue.*

4.2.1 ELECTROCHEMISTRY IN FLOW

To better grasp and appreciate the field of electrochemistry, a brief introduction follows. Electrochemistry is the branch of chemistry, which relates to electrochemical processes (electrons transfers) initiated or accompanied by the passage of an electric current. In organic synthesis, it typically involves oxidation-reduction (redox) reactions that occur at the interface of a metallic electron conducting electrode and an ionic solution. Accordingly, molecules are reduced at the negative cathode and oxidized at the positive anode electrode in the electrolytic cell when a current is applied. While still regarded as a very specialized field requiring expensive equipment and a lot of expertise, it has seen a steady increase in interest in the past decade, especially owing to the mild reaction conditions and high chemoselectivity offered by the method.[165,166] In addition, it provides a sustainable method to replace the use of stoichiometric amounts of oxidants and reducing agents for organic transformations, thus resulting in less environmental impact.[167]

The molecular diffusion distance:

$$d = \sqrt{2Dt} \quad (1)$$

The Ohmic drop:

$$\Delta U = IR_{drop} = I\frac{1}{A_e}\frac{d}{\kappa} \quad (2)$$

Joule's 1st law:

$$P \sim R_{drop} I^2 \quad (3)$$

The reduced length scale in microfluidic flow reactors couples extremely well with electrochemistry. In electrochemical microreactors, mass transport is largely dominated by diffusion. Small molecules in liquid (diffusivity D = 10^{-5} cm^2 s^{-1}) can diffuse 50 µm in 1 s, while it takes 1 day for it to diffuse 1.3 cm (eq. 1). Hence, the smaller the reactor channels, the faster the electro-chemical reactions, due to the shorter diffusion path to the electrodes.[168] In contrast, batch reactors cannot rely on diffusion as the interelectrode gaps are large, thus intense stirring is required to assist mass transfer from the bulk to the electrode surface.[167] Furthermore, laminar flow is a fluid behaviour only accomplished with microfluidics, and describes when the fluid is flowing in parallel lamellae. Mixing between the individual segments with this flow regime is thus governed exclusively by diffusion.[167] This phenomenon can be exploited to selectively direct the substrate of interest (from the specific inlet stream) over either the cathode or the anode electrode to enable selective electrochemical transformations. The relative distance between the two electrodes is of further importance, due to the so-called ohmic drop (R_{drop}), or voltage drop (ΔU) (eq. 2).[167] When the electric current (I) travels through the liquid phase between the electrodes it encounters a resistance. Naturally, this resistance increases with a larger interelectrode distance (d), but decreases with higher conductivity of the solution (κ) or a larger electrode surface (A_e). Microfluidic length scales therefore favours electrochemical reactions, while for batch conditions, the solution to mitigate the ohmic drop is often to add more electrolytes, but this complicates the purification and increases the cost of running the reaction. In addition, as Nernst diffusion layers (10-500 µm) overlap in microreactors allowing the anodic to be coupled with the cathodic electrode processes, electrolytes can at times be completely removed.[167] The last important phenomenon to pay attention to is Joule heating, the heating up of the solution, which occurs as a consequence of the electric current travelling through it. Joule's first law describes that the power of heat (P) depends on the magnitude of the current and the ohmic drop (eq. 3). It is therefore safe to assume that microreactors are advantageous to batch reactors with little heat generation combined with the otherwise rapid heat exchange.

A drawback of most electrochemical flow reactors is that they cannot be adjusted to accommodate different electrodes in a modular sense, and each set of electrodes requires a de novo construction of an electrochemical reactor.[163,169] This is particularly problematic if one seeks to screen a large variety of conditions rapidly. Additionally, not many studies report the coupling of an electrochemical process to an additional transformation in flow.

The Nöel research group (2018) reported an elegant electrochemical microreactor with a numbering up strategy consisting of 8 channels in parallel (**Figure 4.2a**).[164] The electrodes can be changed by disassembling the body. However, the modular design was crafted in a mechanical workshop. The Wirth research group (2017) reported an electrochemical microreactor, which comprised a fluorinated ethylene propylene (FEP) spacer with channels to do flow cut into the spacer (**Figure 4.3**).[170] The neat design was conveniently 3D printed using vat photopolymerization technology. However, the design cannot be described as modular. The Lam research group (2019), in collaboration with the Hilton research group, combined efforts to design and fabricate a simple 3D printed electrochemical microreactor using material extrusion technology, which had enclosed electrodes inserted via a pause-and-dump method upon printing (**Figure 4.4**).[163] This great open-source reactor allows access for others to conduct electrochemistry in flow. However, the reactor design is not modular to accommodate different electrodes. Furthermore, neither of the mentioned microreactors are multifunctional with the possibility for a rapid change to do photochemistry.

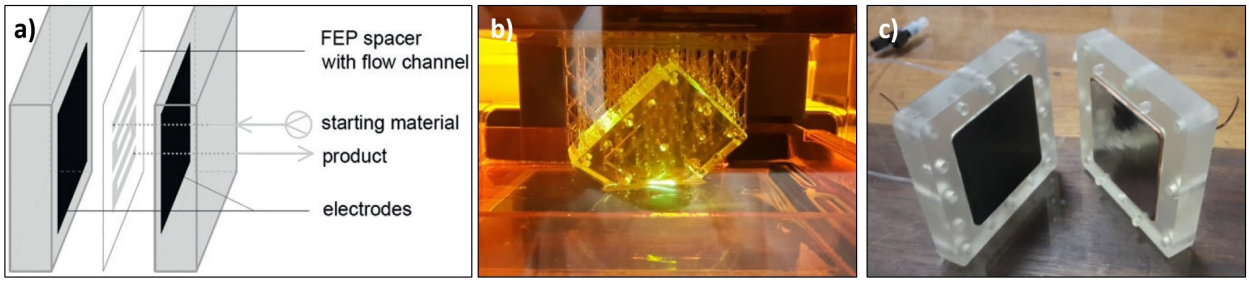

Figure 4.3. *Electrochemical flow reactor fabricated with stereolithography (SLA) 3D printing technique. a) Schematic diagram. b) 3D printing of half the reactor. c) Electrode insert. Adapted from A. A. Folgueiras-Amador et al.*[170]

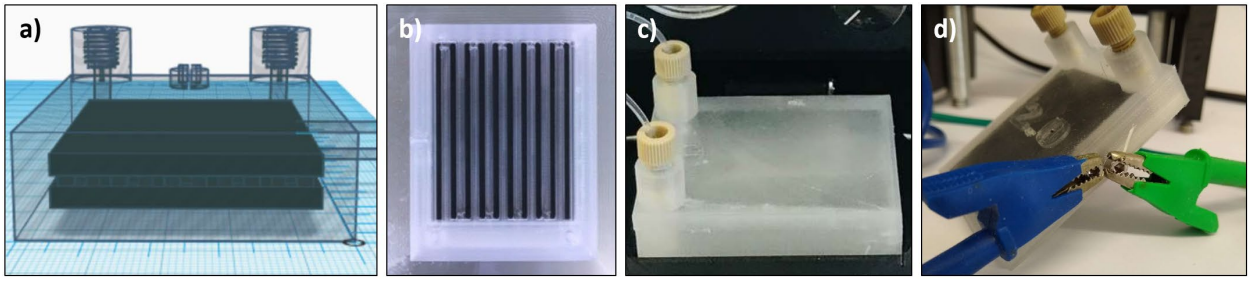

Figure 4.4. *Electrochemical flow reactor fabricated with fused deposition modelling (FDM) 3D printing technique. a) Schematic diagram. b) Top view of the printed channels on top of the first electrode. c-d) Attachment of metal pins to either the commercial Electrasyn 2.0 or Kelvin clips to close the circuit and drive electrochemistry in flow. Adapted from C. G. W. Melis et al.*[163]

4.3 ADDITIVE MANUFACTURING TECHNOLOGIES

Three-dimensional (3D) printing, more formally known as additive manufacturing (AM), where material is selectively placed in a layer-by-layer fashion has received increased attention in both the industry and in the academia in recent years, where it has been applied in the rapid fabrication of customizable objects and equipment with complex unique architectural structures from low-cost inert printable materials. Innovative 3D printing techniques contribute considerably to the Do-It-Yourself (D.I.Y.) movement with emphasis on open-source design principles for conducting scientific research, and provides an expanded access to otherwise expensive and highly specialized equipment with resolutions down to microscales. It is a rapidly growing research area with progressive technological advancements that sees to bring down the cost and increase the scope in a wealth of fields from small biomedical applications[171,172] to the construction of entire homes.[173]

A multitude of 3D printing techniques have already been developed including material extrusion, material jetting, binder jetting, selective laser sintering and vat polymerization.[171] However, as these are out of scope for this short introduction, emphasis will be on the two most commonly employed techniques, namely stereolithography (SLA) and fused deposition modelling (FDM). The latter constitute the fabrication method of choice for the studies reported in this thesis.

4.3.1 PROCESS STEPS PRIOR TO 3D PRINTING

In common for all 3D printing techniques is the initial process step using a computer-aided design (CAD) software to make a three-dimensional digital model (3D file). Alternatively, the object in question can be scanned with the help of a magnetic resonance imaging (MRI) scanner or 3D-scanner to reverse engineer a digital model. Subsequently, the digital model is converted into coordinates that is readable for the 3D printer. A typical format is the Standard Tessellation Language (STL) file that use polygons, most often triangles, to describe the surface geometry of the 3D digital model. This simplifies the complex model into a decipherable code for the printer. The STL file is then sliced using a slicing programme, which generates the many individual layers the printer will use to construct the object, to give a G-code file that send the commands to the printer. Concurrently, various settings can be adjusted, which includes adding support material, printing temperatures, print speed, fan speed for cooling, exposure time, fill pattern in walls, thickness and so on. The full list of settings available to the user is quite substantial and provides a lot of option for correcting failed prints or do a last bit of polishing to obtain a better surface quality, which can be crucial for an application in microscale. With the G-code in hand, printing can commence.

4.3.2 VAT PHOTOPOLYMERIZATION 3D PRINTING TECHNOLOGY

Stereolithography (SLA) is a vat photopolymerization-based technology, and was the first developed and commercialized 3D printing technique (**Figure 4.5**). It uses a vat of liquid photopolymer resin that is cured by light radiation in a specific geometric pattern dictated by the G-code to construct the 3D model layer-

by-layer. The polymerized structure anchored to a build platform is progressively dragged away from the light source to expose more resin to be cured for the next individual layer.

Both a bottom-up and top-down version of this technique exist referring to the direction of the movement of the build platform. The main advantage of the bottom-up method is that it requires only the bottom surface of the vat to be covered with resin in addition to what makes up the model, and is thus very material economic. However, peeling the cured layer off the bottom surface of the vat after each successive curing, may result in a failed print where the anchor attachment (the first layer) gets loose, due to the strong interaction with the bottom surface. This is particularly problematic for layers with large surface areas. Non-specific light scattering limits the resolution of this technique to about 20-30 microns in commercially available printers, however, the recent developed two-photon polymerization (2PP) techniques have achieved resolutions down to impressive 0.1 µm.[174,175] The SLA printing process often requires post-curing, post processing, and sacrificial support structures. In addition, the number of available printing materials are limited. Embedding physical objects inside the printed object is easily handled and recent studies have even demonstrated the incorporation of active pharmaceuticals in the resin to be effective.[171]

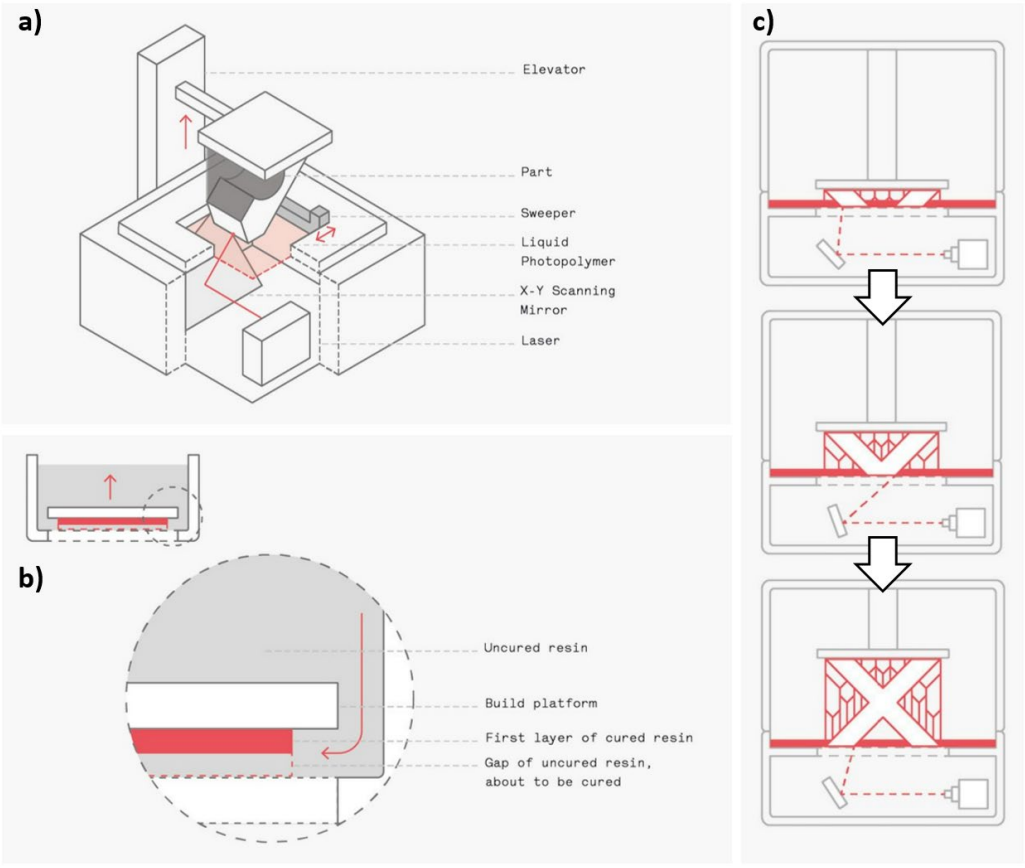

***Figure 4.5**. Illustration of stereolithography (SLA) 3D printing technique. a) In this example is shown a bottom-up SLA 3D printer. b) The build platform moves up to expose new resin that can be cured for the next layer. c) Side view of the printing process of an object. Adapted from B. Redwood et al.*[176]

4.3.3 MATERIAL EXTRUSION 3D PRINTING TECHNOLOGY

Fused deposition modelling (FDM) is a material extrusion-based technology, and is the most commonly encountered technique, primarily due to its lower cost and simple operation (**Figure 4.6**). A thermoplastic filament is continuously fed through a heated extrusion nozzle, and then deposited onto the print bed layer-by-layer to build the object as dictated by the G-code. As the molten filament cools, the layers fuse together through layer adhesion (isotropy). It is often a combination of both the nozzle and the platform (print bed) moving in the x, y and z directions that guide the deposition of the thermoplastic to its precise location on the platform.

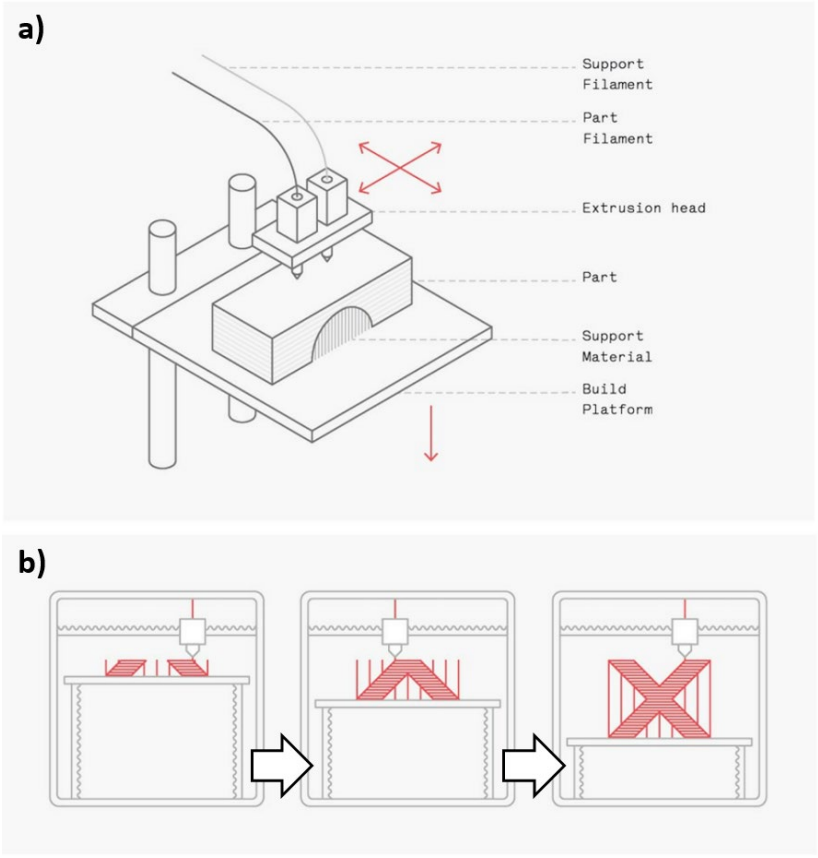

Figure 4.6. *Illustration of fused deposition modelling (FDM) 3D printing technique. a) In this example, the nozzle extruder moves in the X-Y plane and the build platform in the Z plane; b) Side view of the printing process of an object. Adapted from B. Redwood et al.*[176]

FDM printing is limited to thermoplastic filaments, but incorporation of co-materials to give the printed object exotic properties have been developed and include among other biodegradable, conductive, luminescence, magnetic and colour changing properties. Furthermore, 3D printed biomaterials have been developed to generate complex tissues and organs suitable for transplantation.[177] Polylactic acid (PLA) and polyethylene terephthalate glycol (PETG) are by far the preferred thermoplastics for most print jobs as they are cheap, have decent to good mechanical strength and comprise some of the easiest to succeed with

printing materials, thus giving a low entry barrier to the field. However, the chemical resistance is not excellent, thus other thermoplastics such as polypropylene (PP) or acrylonitrile butadiene styrene (ABS) must be considered, but the printing difficulty increases. The main reason being that they do not handle the tension or stress from the process of cooling down very well, which can lead to deformation, shrinkage or warping of the model. To mitigate these effects, both the nozzle and the print bed temperatures can be adjusted through the slicing settings. Sometimes a lengthy trial-and-error process. As such, the first couple of layers need to be near-perfect to not end up with a so-called spaghetti print. Hence, a small defect in the surface of any of the first layers, often resulting from material build-up on the nozzle, which is dropped during printing, can cause a havoc when the nozzle attempts to extrude material onto the defected layer and is either blocked or starts stringing. As these problems primarily persist in the first couple of layers, fan cooling is often completely removed, print bed temperature increased and the first couple of layers closely monitored. Post processing with FDM printing is often very minimal and consist of removing excess support plastic (if used) by hand or sanding down the surface for a smooth surface. FDM 3D printers are less accurate than SLA 3D printers, typically in the range of 50 microns. However, high-end hybrid printers achieve resolutions down to 10 microns,[178] but they are not very affordable.

Fully open-source 3D printed microfluidic flow equipment is available from different sources and includes both pumps, mixers, droplet-generators, reactors for various operations, phase-separators for work-up, small-scale purification systems encompassing silica columns and spectroscopic flow cells for analysis etc.[179–186] A few illustrative examples are included in **Figure 4.7**. The D.I.Y. movement hones the philosophy 'if you can imagine it, you can print it'. Commercial alternative equipment can cost up to several thousand euros, however, possessing a 3D printer might cut the expenses to only a fraction, while allowing freedom to customize or adapt the designs as to ones needs.

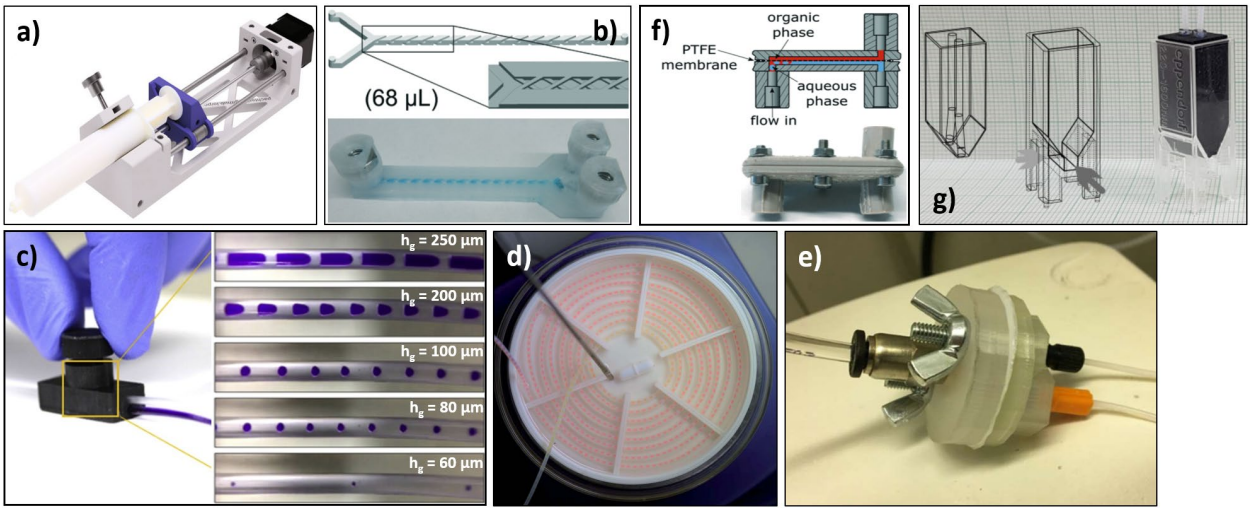

Figure 4.7. *Selected examples from the literature on additive manufactured open-source flow equipment. a) 'Poseidon' single-piston syringe pump. b) Y-shaped mixer. c) Droplet-generator. d) Tube reactor for oil bath compatibility. e) Backpressure regulator. f) Aqueous phase separator. g) Flow-through cuvette insert. Adapted from references.*[179–181,187–189]

4.4 PROJECT OUTLINE

Continuous flow chemistry with microreactors is advantageous in many aspects to conventional batch chemistry that uses a round-bottomed flask setup as process control and safety is significantly enhanced. In particular, electro- and photochemistry that are inherently green processes benefit tremendously from the reduced length scales presented by microfluidics. However, current microfluidic flow equipment is expensive and does not allow for rapid screening of various electrodes with modular capabilities to facilitate photochemistry using the same reactor. Recent advances in 3D printing may offer the solution as it allows the reactor design to be fast, convenient, customizable and most importantly cheap. Furthermore, it only requires sharing a file with the community for others to copy and start using the reactor, which increases the general access to microfluidic flow equipment.

Therefore, to address the current lack of access to cheap and modular flow equipment, the aim is to design and manufacture such a microreactor using 3D printing technologies (**Figure 4.8**). The reactor should be modular with facile exchange of electrodes to perform electrochemistry, and encompass the possibility to change the electrode for an optical material that facilitates the transmittance of light to carry out photochemistry in flow.

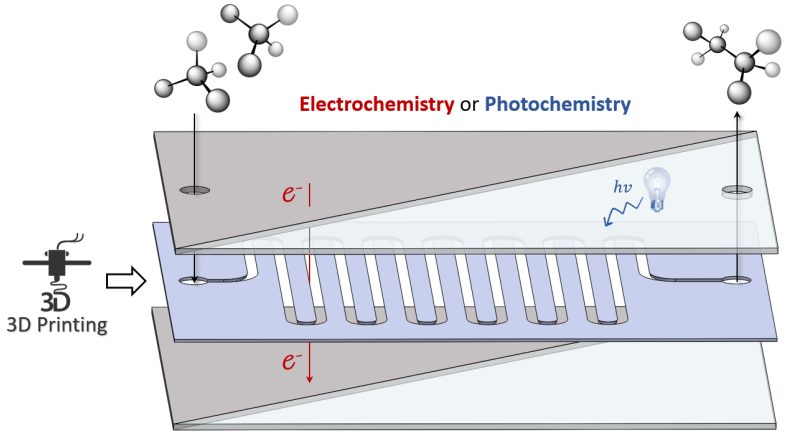

Figure 4.8. *3D printed modular microreactor to enable electro- or photochemical transformations in flow.*

The need for a low-cost, rapidly manufacturable microfluidic reactor in our research group arose during a project investigating photochemical [2+2] cycloadditions in flow. These were carried out in a microfluidic photoreactor fabricated with a silicon micro processing technology (**Figure 4.9d**).[190] This required extensive expertise and access to specialized equipment in the manufacturing process, and did not offer us the design flexibility we were after. However, while investigating the reactions comprising various excitable olefins with linear-, carbocyclic- and heterocyclic coupling partners photosensitized by thioxanthone to generate a small cyclobutane-containing fragment library (**Figure 4.9a-b**), an unexpected result was obtained (**Figure 4.9c**).[190] The reaction of citraconic anhydride (**8**) with 2,3-dimethylbut-2-ene (**9**) produced a complex mixture of products. Isolation of the major component in the mixture afforded just enough material to detect a mysterious compound, which did not make much sense from the reaction scheme. Repeating the experiment in flow led to the same result. It is therefore of interest to isolate this compound in greater yields in order to characterize it.

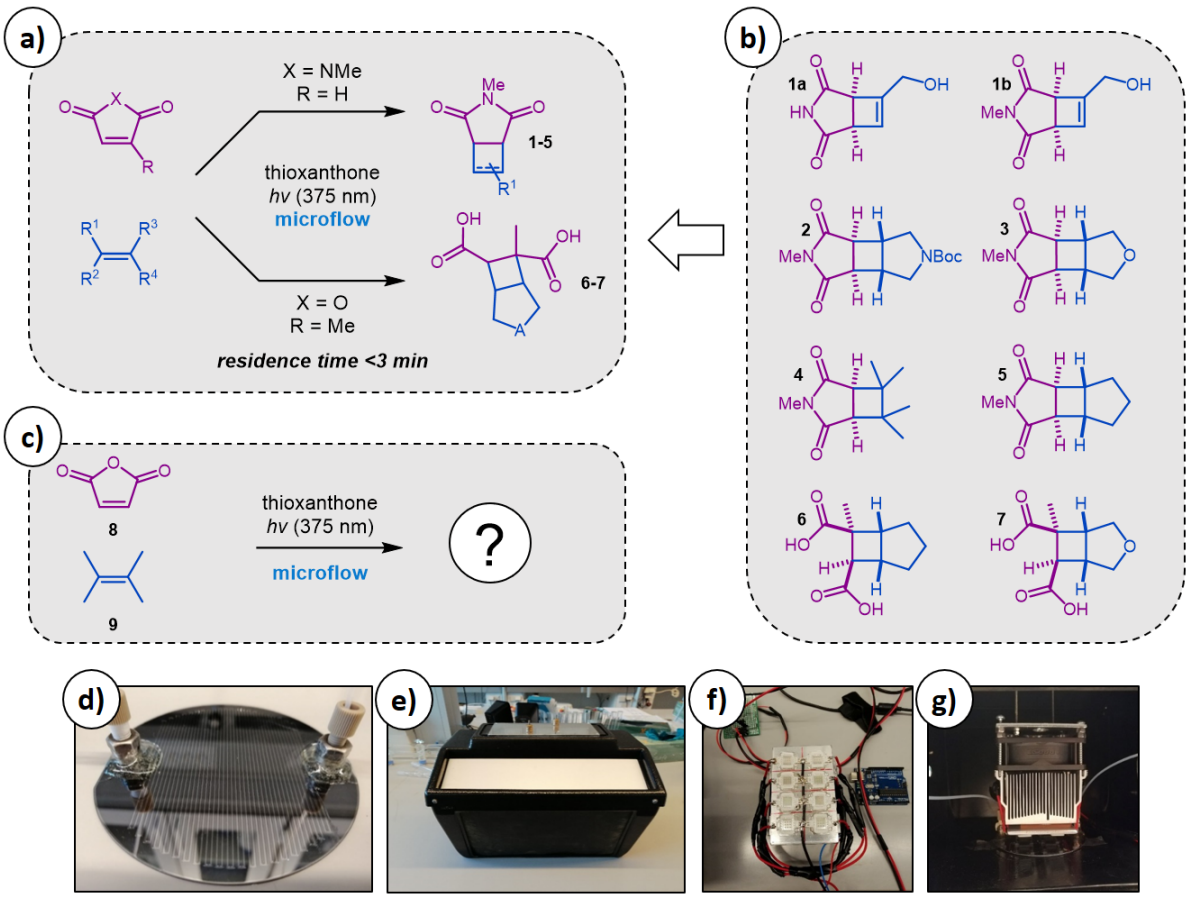

Figure 4.9. Photochemical [2+2] cycloaddition reactions conducted in the Laraia research group. a) Schematic overview of reactions. b) Synthesis of a small cyclobutane-containing fragment library c) Unexpected reaction between citraconic anhydride (8) and 2,3-dimethylbut-2-ene (9). d) Completed reactor with tubing attachment. e) Modified UV chamber f) 375 nm 80 W LED light source. g) Set-up during reaction. Adapted from M. Bargum et al. [190]

4.5 PHOTOCHEMICAL CYCLOADDITION WITH CITRACONIC ANHYDRIDE

Initial efforts aimed to reproduce the reaction conditions of the photochemical [2+2] cycloaddition in flow employing the same silicon chip-based microreactor and equipment (**Figure 4.9d-g**). However, as the fabricated UV-A (375 nm) light-source fitted inside the repurposed TLC chamber was defect due to a loose soldering connection, it was decided for convenience to translate the reaction into batch conditions. Part of the work has been published.[190]

A Thorlabs (365 nm) LED fitted with a collimator and adjusted to maximum output was used to illuminate the reaction solution in a round-bottomed flask. Isolation of the major component in the complex mixture did not yield the theoretically expected cyclobutane **11**, but instead a dihydrooxepin-2(3H)-one (ketal) structure **15**. This side-product is supported by experimental analyses (see section 4.8 in the Experimental).

A tentative reaction mechanism to access the dihydrooxepin-2(3H)-one **15** is given in **Scheme 4.1**. While a standard photochemical [2+2] cycloaddition reaction follows the pink pathway to cyclobutane **11**, an alternative pathway could be that the biradical intermediate **10** undergoes a homolytic bond cleavage to form the carboxylate biradical species **12**. Recombination of radicals to produce ketene **13**, sets up a photochemical [1,3]-sigmatropic rearrangement to deliver the dione **14**. This can hydrolyse upon purification to produce the final ketal **15** with a dihydrooxepin-2(3H)-one core structure. Interestingly, if the less substituted and thereby less stable secondary biradical of **10** was formed, it would produce the dihydrooxepin-2(3H)-one structure with the methyl group of the citraconic anhydride positioned *β* to the ketal functional group following the same suggested mechanism. However, as no heteronuclear multiple bond correlation (HMBC) was observed between the protons of this methyl and the carbons of adjacent methyl groups, the connectivity of the atoms can be assumed to correspond to the reported structure of **15**. Hence, either this alternative biradical is not formed, or it is too unstable with poor cyclization quantum yields and rapidly undergoes fragmentation to the starting materials.

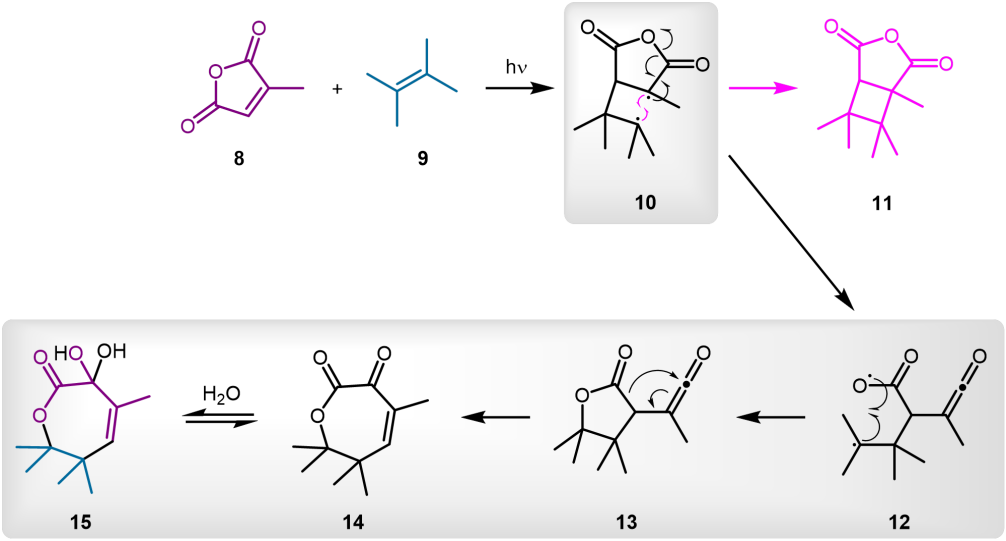

Scheme 4.1. *Tentative reaction mechanism for the synthesis of dihydrooxepin-2(3H)-one* ***15***

This study demonstrates the first reported method to obtain the dihydrooxepin-2(3H)-one scaffold accessed through a photochemical cycloaddition of citraconic anhydride and 2,3-dimethylbut-2-ene with thioxanthone as the photosensitizer. Although yields were not great (15%), it could serve as an interesting starting point with the aim of accessing this scaffold reliably and in higher yields through method development. Disclosure or confirmation of the reaction mechanism possibly through designed trapping experiments of the produced radicals could suit as an initial investigation to better tailor subsequent reaction optimization.

4.6 ADDITIVE MANUFACTURING OF PHOTO- & ELECTROCHEMICAL FLOW MICROREACTORS

There are certain requirements necessary for the performance of a flow system. First and foremost, materials in contact with any fluids or reagents, need to exert chemical compatibility to not deteriorate or deform upon use. This applies to both the tubing that connects the different parts of the flow system in addition to the reactor itself and other relevant components. Polytetrafluoroethylene (PTFE) tubing is an inert material used to ensure excellent chemical compatibility, while polypropylene (PP) is the material of choice for reactor printing, due to a combination of chemical resistance, flexibility and a lowered melting temperature, hence no special extruder hot-end is required for printing. The drawbacks of PP as will be evident from the discussion detailing the printing process of the reactor includes heavy warping and issues with adherence to the bed (build platform). Furthermore, the reliability of the system should be high to prevent a reduced performance as a consequence of its continuous use. Accordingly, less reactors need to be printed saving both time and material. Lastly, the channel characteristics need to be considered in the initial design phase as it will impact the hydrodynamic resistance together with the efficiency of electro- and photochemical transformations.

4.6.1 DESIGN, FABRICATION & TESTING

The initial electrochemical reactor was designed to encompass electrodes to sandwich and enclose the channels from the top and bottom (**Figure 4.10**). The streams of three inlets combine in a T-like mixer that leads into the reactor zone with channels of squared cross section (1.5 x 1.5 mm), and exits through a single outlet. Two squared spaces and four holes are incorporated at a different level than the pockets for the electrodes to facilitate squeezing the entire system together with stiff sealing plates and possibly O-rings. In this context, the central part of the sealing plates should be removed to allow wires for the circuit to connect with the electrodes. Space for an O-ring around the middle point of both electrodes was thought to produce a better sealing and add mechanical stability to the system. FDM 3D printing afforded the millireactor in PLA, however, the large overhang of channels proved problematic as support material was needed to keep it from collapsing while printing. This resulted in a print with a very rough bottom surface from the support material that had melted together with the thermoplastic of the reactor, and thus did not meet the expectations required for a non-leaking system.

Attempts to solve the overhang led to the flat millireactor design of version 2 (**Figure 4.11**) that makes use of the same squared channels from the first version. The design facilitates either electrodes or glass plates to enclose the flow reactor for a multifunctional purpose. The flat design removes the overhangs, and solves the printing issue of the first reactor design. FDM 3D printing produced the multifunctional millireactor in PP. However, the leak test failed as the solution creeped out of areas where the inlet and outlet connected to the reactor. To mitigate this, a small overhang of material was incorporated into the design of version 3 to enclose the channels at the edges that connect to the inlet and outlet (**Figure 4.11**). This appeared to solve the issues with leakage near the edges of the reactor, but the central part still wetted the entire aluminium sealing (test) plate (**Figure 4.12**).

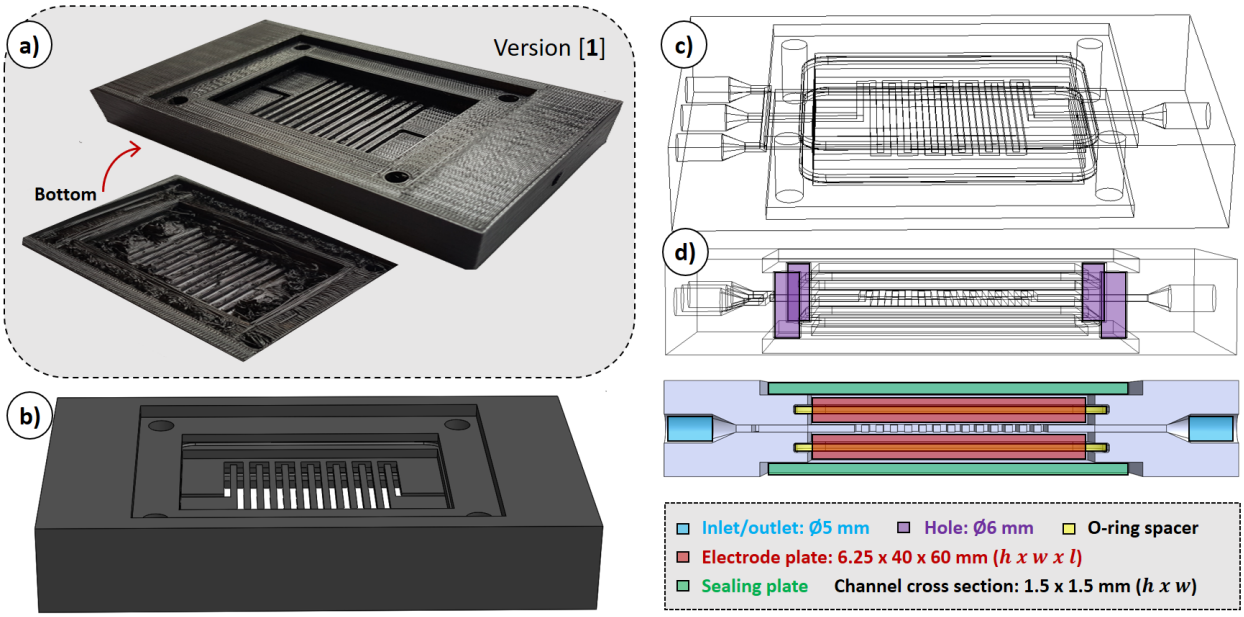

Figure 4.10. Design and manufacturing of a modular electrochemical millireactor in PLA (test print). The model has a horizontal plane of symmetry. a) FDM 3D printed model with an insert of the bottom face. b-c) CAD models top-side view and d) side view.

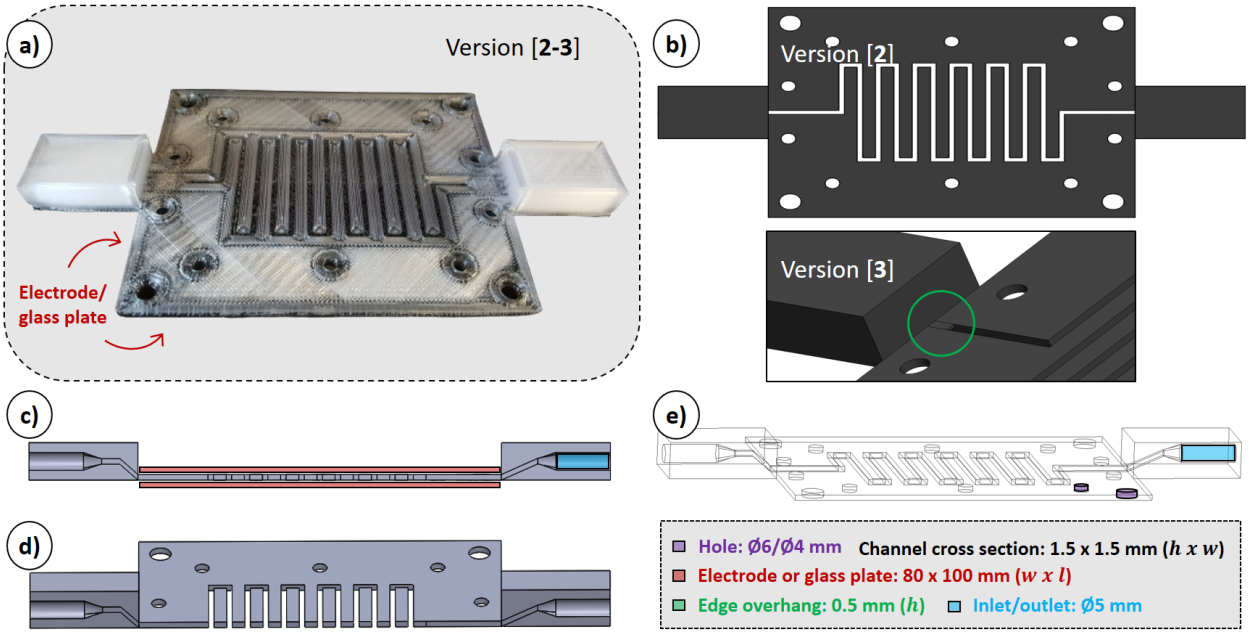

Figure 4.11. Design and manufacturing of a multifunctional photo- and electrochemical millireactor in PP. a) FDM 3D printed model. b) CAD models of version [2] top view (top) and version [3] top-side view (bottom). Edge overhang (green). c) CAD models side view, d) top-side view with cutaway through a vertical plane and e) top side-view.

A new multifunctional microreactor was designed (version 4) that employed the same reactor dimensions of version 3, albeit the channels now have a rectangular cross section (0.5 x 1.5 mm), while the inlet and outlet are relocated to sit on the same face of the reactor (**Figure 4.13**). The decreased channel height is beneficial not only for photo- and electrochemical transformations, but may also allow the flexible reactor printed in PP to be squeezed more tightly to prevent leakage. Similarly, two central holes were incorporated to support a more even pressure, since leakage from the central part of the reactor was a concern. A snake mixer was integrated in the beginning of the reactor to ensure solution homogeneity and

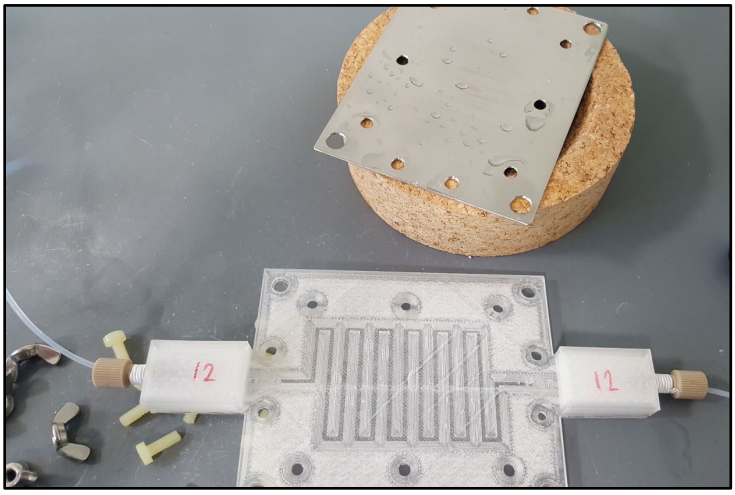

Figure 4.12. *Leak test of the multifunctional millireactor version [3] with a printed (closed) bottom and open top. The aluminium plate was custom drilled. Sealing with PTFE screws and aluminium wing nuts.*

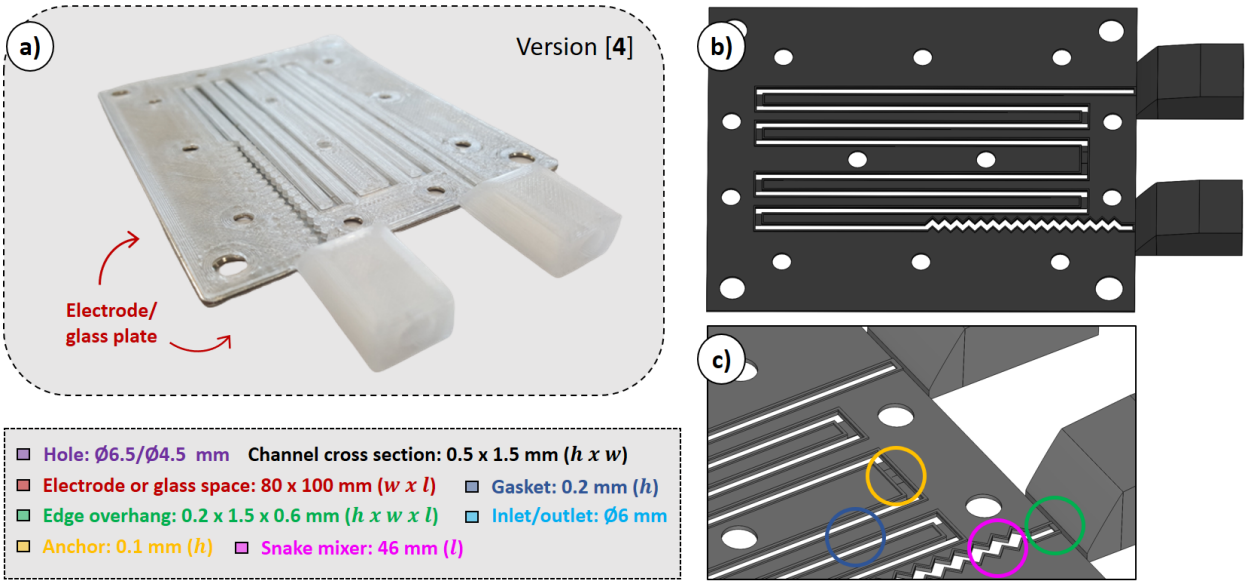

Figure 4.13. *Design and manufacturing of a multifunctional photo- and electrochemical microreactor in PP. a) FDM 3D printed model. CAD models b) top view and c) zoom-in top-side view.*

faster steady state. The same method of 3D printing (FDM) was used to generate a model fit for testing. Numerous printing related issues were encountered in the process (**Figure 4.14**), but the most devastating was print warping, where the reactor (object) detach from the print bed. This is especially profound near the edges or corners of an object. Stress and tension leading to thermal contraction (shrinkage) in the cooling process together with the characteristics that PP does not like to stick to anything but itself gives warping, which cascades into a whole lot of other issues. Preventive measures to give better print qualities included a homemade cardboard box around the 3D printer to mitigate fluctuations in temperature around the object, PP tape on the bed, which is a must for printing with PP, and helper-disks to protect the corners from detaching (**Figure 4.14**). To prevent warping of the printed channels, design optimizations led to the integration of small (100 µm height) anchors (**Figure 4.13**). This solved warping of the channels, however, none of the mentioned efforts solved the actual leakage. Alternative methods, like printing a thin gasket (200 µm height) around the edge of the channels or placing a thin FEP film (**Figure 4.15**) in between the reactor and the aluminium sealing plate also failed to provide a working solution. With countless print settings tested without success, the reactor was abandoned.

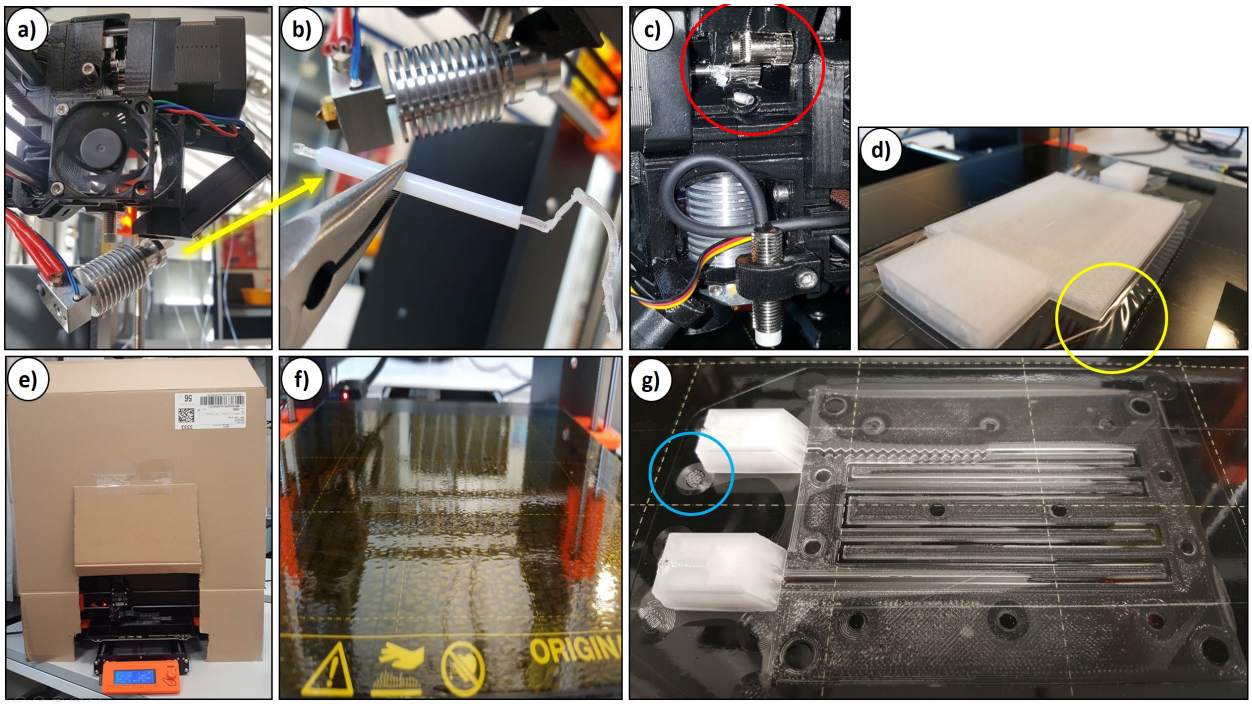

Figure 4.14. *Commonly encountered 3D printing issues using polypropylene material and suggested preventive measures. a-b) Jammed filament inside the PTFE tube of the extruder head (yellow arrow). Only solution is either a cold pull method or disassemble the extruder. c) Drive gear has grinded the filament leaving the gear teeth full of material (red) and thus unable to grab and direct the filament. The solution is to clean the teeth and adjust the screw for the drive gear. Otherwise adjust print settings. d) Warping is pulling the object and tape (yellow) away from the bed. Possible preventive measures exist, e) Home-made enclosure to increase the temperature and prevent temperature fluctuations, f) Polypropylene tape on the bed to increase adhesion of the object, and g) Helper-disks (blue) incorporated to protect corners.*

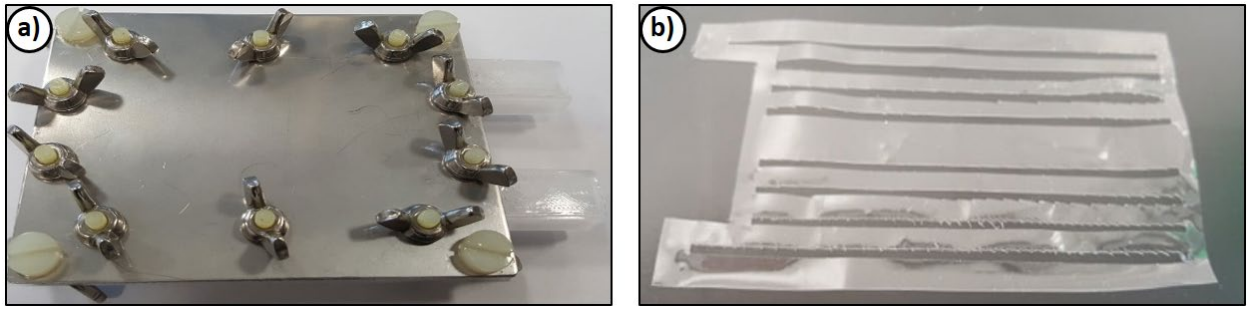

Figure 4.15. *Multifunctional microreactor version [4] flipped (bottom side) view. a) Leak test with attached custom made aluminium plates using PTFE screws and aluminium wing nuts (version without the two central holes). b) FEP film cut to fit channels.*

In search for a different approach, and inspired by an enclosed electroreactor (**Figure 4.4**),[163] another microreactor was designed (version 5) that incorporated space for a glass disk to be embedded into the circular disk reactor while printing (**Figure 4.16**). The placement of the inlet and outlet was modified to a vertical position in the process, while the design of the channels was kept similar to previous reactor versions. The anticipation was that sealing would improve as the deposition of filament could fuse into and fill out potential gaps. However, FDM 3D printing of PP directly on top of glass led to severe warping, which makes perfect sense in hindsight. Completion of a successful print was only realised through constant monitoring and intervention to fix deposition mistakes. Furthermore, the glass disk had to be pressed down

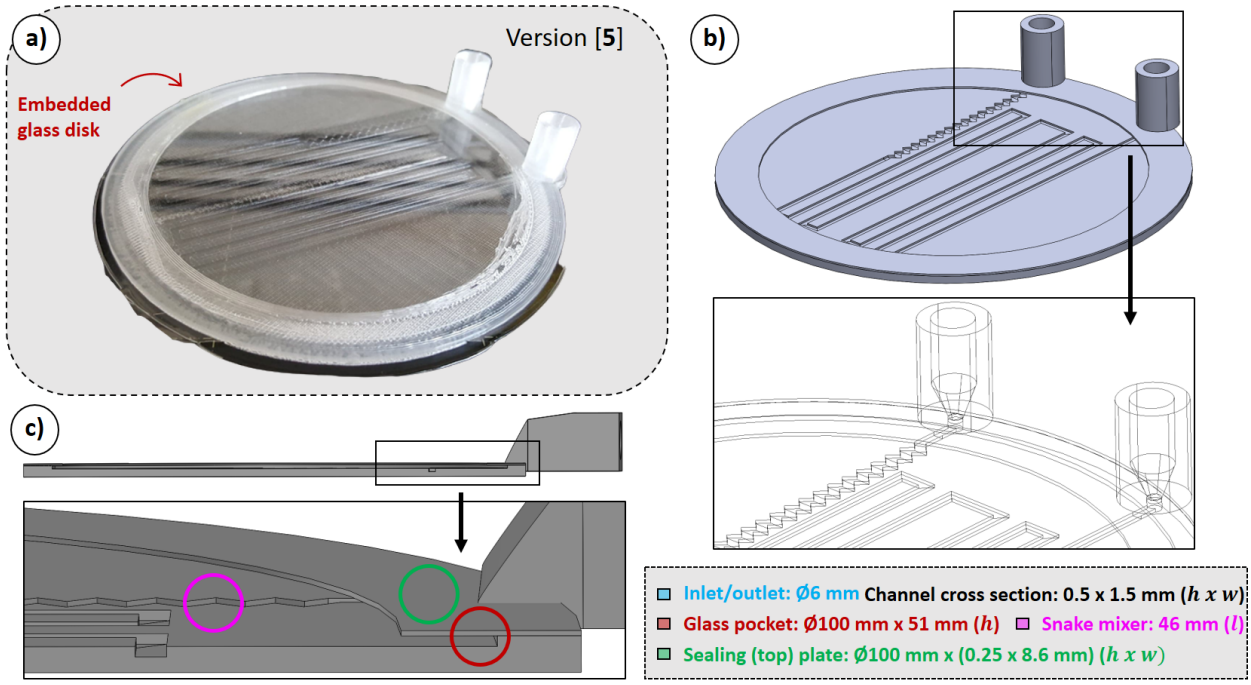

Figure 4.16. *Design and manufacturing of photochemical microreactor in PP. a) FDM 3D printed model. CAD models b) top-side view and zoom-in, c) side view and zoom-in of a previous prototype with a horizontal placement of the inlet and outlet.*

into the reactor while printing the sealing layer. The reactor did not pass the following leak test, likely due to the eminent warping of the print. Even with two clamps pinning down the photoreactor and applying a substantial squeeze to the entire system the issue remained unsolved (Figure 4.17).

Figure 4.17. Leak test of photochemical microreactor version [5] at 0.5 mL/min, while two clamps apply a pressure.

Driven by curiosity while interested in obtaining a functional reactor to finally commence on electrochemistry in flow, the convenient option was to copy and use a reported working reactor from the literature. Hence, the fully enclosed electroreactor with embedded graphite electrodes was reproduced for less than 10 euros (Figure 4.18).[163] However, internal leakages were observed through the 3D printed PP reactor where both the top and bottom of the electrodes were wetted in addition to solution coming out of the side pinholes where the current will connect. Various print settings were adjusted in attempts to obtain a non-leaking reactor. These included bed and nozzle temperatures, print size to counter shrinkage, fan speeds to mitigate warping in the cooling process, supports in the form of brims and rafts, retraction length and speed to prevent oozing, flow rate of the melted filament besides a whole range of settings only pertaining to slicing gaps, walls, infills and how they all combine and overlap with each other. Furthermore, a CAD model of the design was made to allow customizations on the fly as the original reactor is reported in the literature with non-editable files. No changes to the reactor dimensions solved the internal leakage of the system. Having communicated with the authors, apparently they observe leakages as well, but accept it as reactions are not impacted. One successful non-leaking reactor was printed, but on the expense of the 3D printer that suffered from the little to no cooling in the printing process. However, this reactor was wasted in experiments testing its flow rate limitations. The reactor was abandoned in combination with the 3D printer needing a major overhaul in terms of maintenance and replacement of key parts from the heavy use of it while experimenting with the many advanced settings available through the slicer programme.

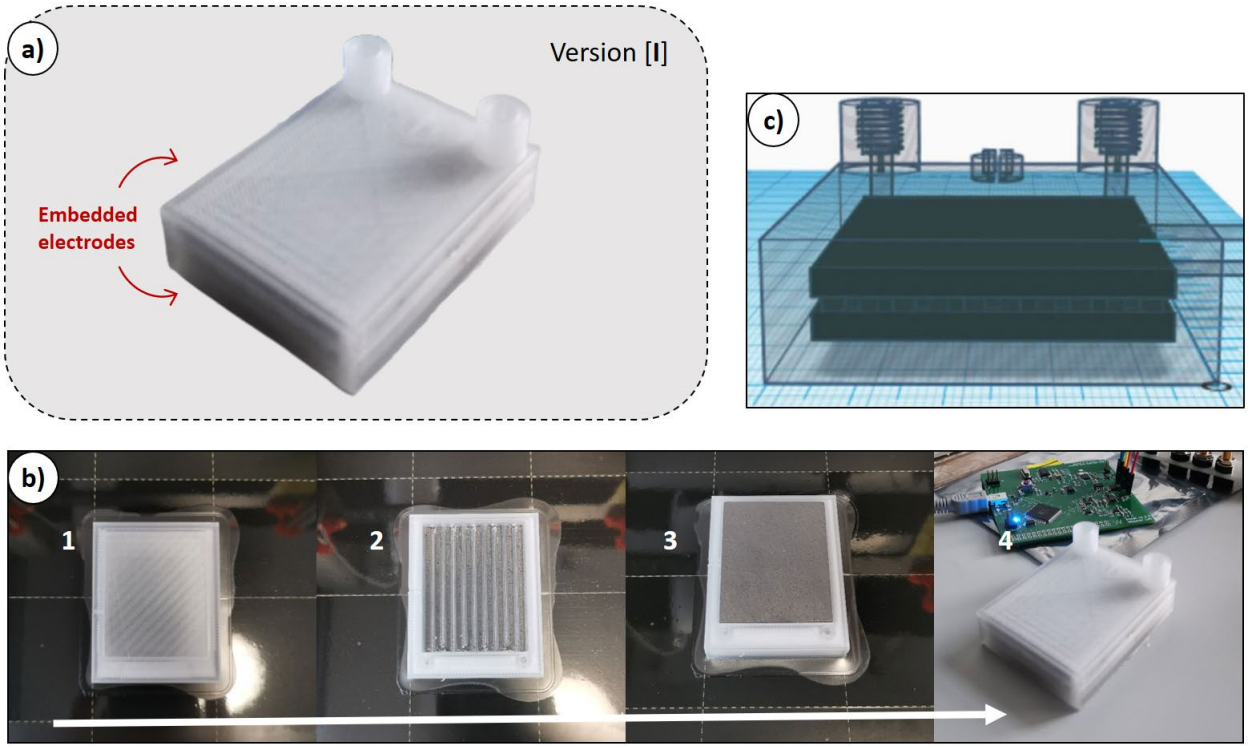

Figure 4.18. *Manufacturing of an enclosed electrochemical millireactor version [I] in PP. The model has a vertical plane of symmetry. a) FDM 3D printed model. b) Printing process with a pause-and-dump method. c) CAD model front view which is adapted from the source that provided the reactor design.*[163]

At this point there was a growing interest in the research group for high-throughput experimentation (HTE) as a way to expedite progress in projects including the aforementioned [2+2] cycloaddition work (see Section 4.5), which moved our research focus away from a flow-based approach. HTE enables the screening of many reaction conditions in parallel resulting in an increased throughput. Therefore we chose to employ an open-source photoreactor designed by A. Ritzén, and fabricated this in PETG using FDM 3D printing (**Figure 4.19**).[191] The photoreactor has four LEDs (4 x 10W) of 440-450 nm wavelength mounted on top of a heatsink at the base of the chamber. The whole photoreactor is dimensioned to fit on top of a standard magnetic stirrer hotplate. A different lid was designed to accommodate LC-MS vials (5 x 5) instead of 20 mL screw neck vials (2 x 2) for increased throughput. The reactor was employed in the investigation of visible light mediated photocatalysis of various alkaloid- and sterol-inspired small-molecule drugs containing aliphatic ketones, following the protocol reported by M. J. Gaunt *et al*.[192] The concept was to generate a library of compounds possessing *N*-heterospirocyclic scaffolds with a high fraction of SP^3 to improve drug-like properties as a consequence of the increased molecular 3-dimensionality. In similar fashion to the previous project related to the synthesis of cyclobutane-containing small-molecules via photochemical [2+2] cycloadditions (*vide supra)*. However, as no product formation was detected for any reaction except the test reaction reproducing the reported conditions with the same reagents, the project was abandoned and further discussion left out of the scope for this thesis.

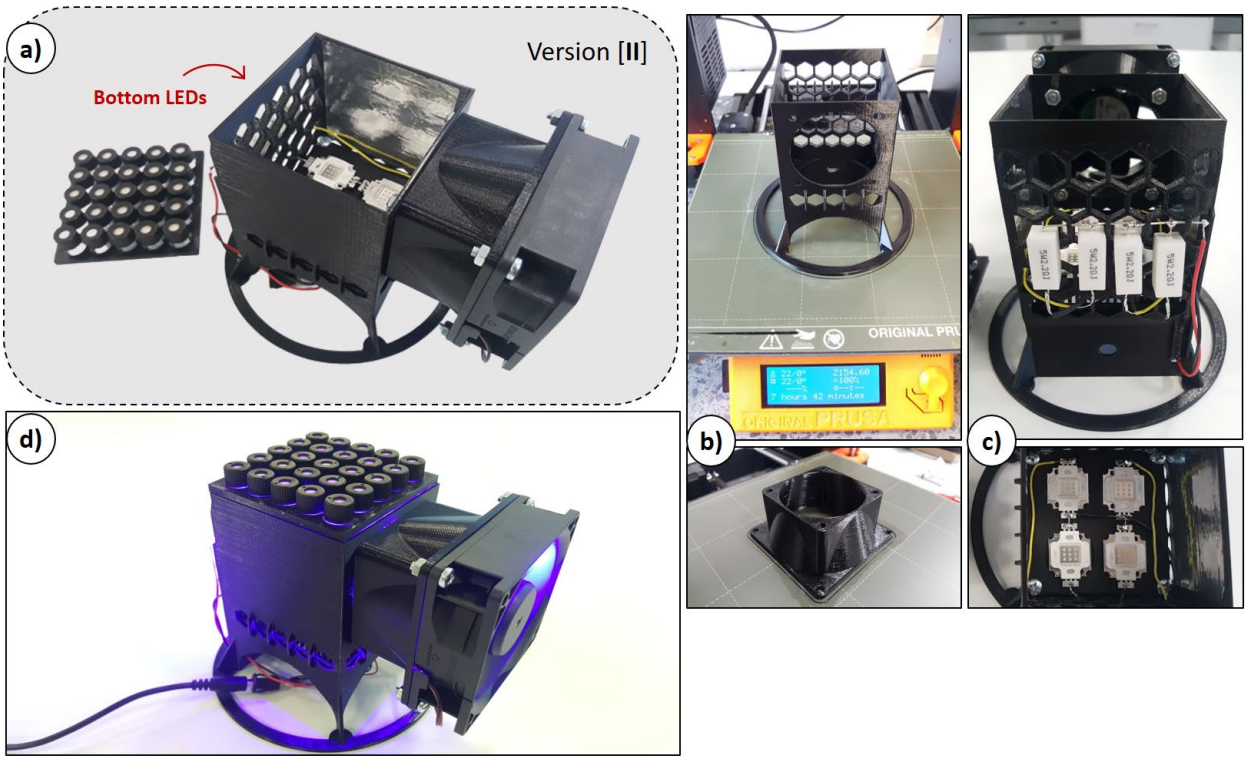

Figure 4.19. *Manufacturing of a photoreactor version [II] in PETG. a) FDM 3D printed model. b) 3D printed objects belonging to the original design by A. Ritzén.*[191] *c) Assembly of photoreactor with 4 x 10 W LEDS connected to power resistors (soldered together) following the procedure by reference.*[191] *A heatsink is placed at the base and fans mounted (bottom and front). d) With the 440-450 nm wavelength LED light on. The lid (own design) can hold 25 x LC-MS vials for parallel screening.*

The photoreactor itself was operational and offered excellent light irradiation of the bottom part of the LC-MS vials. Furthermore, all components combined cost less than 100 euros, which is very cheap compared to commercial alternatives. A major drawback, however, was that stirring was extremely inefficient, and completely irrelevant for inhomogeneous solutions, due to the large distance between the small magnets in the LC-MS vials and the stirrer hotplate. Unfortunately, reducing the distance was not feasible as the LEDs and reaction vials needed the space for proper air cooling and circulation exerted by the big front-mounted fan. Furthermore, the size of the photoreactor also limited the throughput to a 5 x 5 LC-MS vial setup. Hence, we decided on a plate-based approach instead, which addressed the current issues we had with the photoreactor, while providing us with the possibility of automating parts of the process, all of which is the subject of the following chapter.

4.7 CONCLUSION & FUTURE PERSPECTIVES

The fabrication of lab-on-a-chip microfluidic reactors made from silicon is time-consuming and non-trivial requiring specialized tools and training. Hence, reactors are primarily produced in batches to lower the cost and make it worth the effort. However, this conflicts with the interest to enable customizations of the design layout on-the-fly. Furthermore, the reactors are prone to fouling as experienced first-hand, which necessitated the need to produce more reactors. From the studies in our research group employing silicon fabricated microreactors for photochemical [2+2] cycloaddition reactions in flow, a small cyclobutane-containing library was generated, while an unexpected side-product characterized to have a dihydrooxepin-2(3H)-one scaffold was discovered. A tentative reaction mechanism was suggested that follows a homolytic bond cleavage to set up a photochemical [1,3]-sigmatropic rearrangement. Interestingly, this demonstrated the first reported method to prepare the dihydrooxepin-2(3H)-one scaffold.

Additive manufacturing is a convenient alternative to silicon micro processing technologies for the fabrication of microfluidic flow reactors. It lowers the cost and process time significantly, while offering a simple and customizable solution. Hence, with its rapid advancement into the field of flow chemistry as a powerful new fabrication method, we applied it to manufacture various photo- and electrochemical reactors (**Figure 4.20**). In general, designs could easily be modified to fit custom needs, while the cost of one print was less than one euro. However, despite its advantageous, we experienced great difficulty in manufacturing a microreactor that would not leak. The need for a material that was feasible to print while displaying excellent chemical stability limited our options of filaments to polypropylene. This complicated printing, as polypropylene is known for its tendency to contract upon cooling (warping). Unfortunately, none of the 3D printed flow reactors (**Figure 4.20a-e**) exerted an acceptable resolution to afford a non-leaking microreactor, regardless of the approach. Possible solutions going forward will likely include switching to a stereolithography 3D printing technique, which has the benefit of increased resolution. Furthermore, it often handles overhangs and thin parts perfectly well, while the support material is easy to remove in the post processing step. The only real disadvantages are the slight increase in cost as resins are more expensive than their filament counterparts, while the process time also increases by a small margin. A different approach inspired by the many reported electrochemical flow reactors from literature, albeit most are machined, would be to print a two-component body frame to squeeze the entire system together consisting of both the 3D printed reactor and the electrodes or glass plates (**Figure 4.21**). If combined with a stereolithography 3D printing technique, it is very likely that the leakage issue can be solved.

A photoreactor for parallel screening of various reactions or conditions was, however, successfully 3D printed, assembled and applied (**Figure 4.20f**). It neatly, facilitates light irradiation of up to 5 x 5 LC-MS vials at the same time. However, drawbacks included difficulties with stirring due to the large distance to the stirplate, which could not be decreased as it would result in problems with heat management in the photochamber. Intrigued by the capabilities of screening many conditions in parallel, and with in-house knowledge and equipment already established used for rapid screening of large compound libraries against therapeutic targets, we changed direction to focus on a high-throughput experimentation plate-based approach instead, which is the subject of the next chapter.

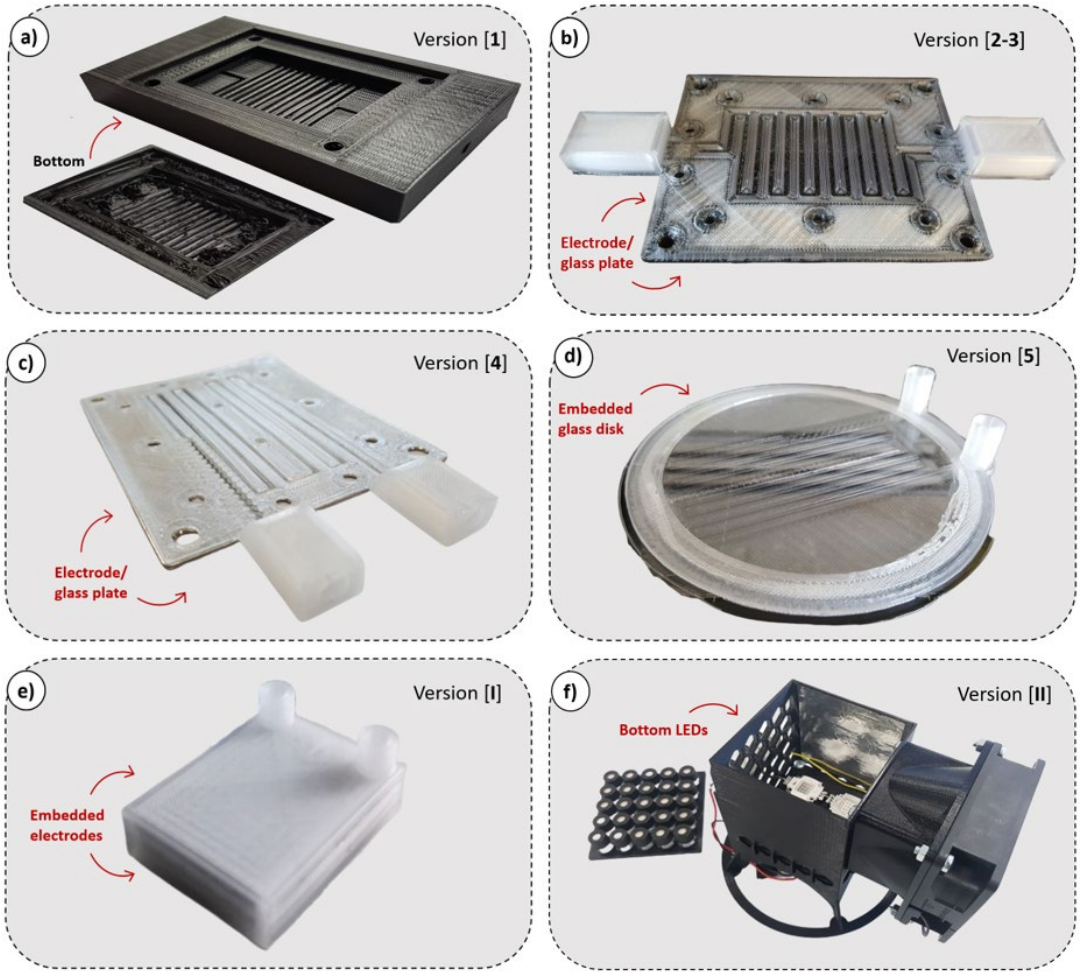

Figure 4.20. *Overview of the various reactors fabricated using additive manufacturing in this project. a) Modular electrochemical millireactor in PLA (test print). b) Multifunctional photo- and electrochemical millireactor in PP. c) Multifunctional photo- and electrochemical microreactor in PP. d) Photochemical microreactor in PP with an embedded glass disk. e) Enclosed electrochemical millireactor in PP with embedded electrodes. Design from reference.*[163] *f) Photoreactor for parallel screening in PETG. Design (except the lid for LC-MS vials) from reference.*[191]

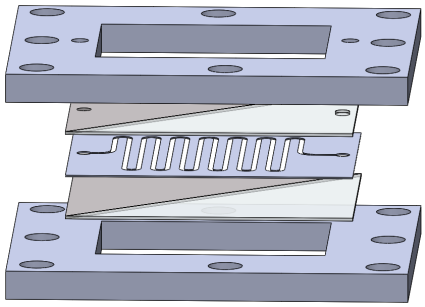

Figure 4.21. *Exploded view of two 3D printed body frames (outer) designed to squeeze the entire system comprising one 3D printed open microreactor (middle) and two electrodes or glass plates (in between) to ensure tight sealing. O-rings can easily be incorporated in the design of the body frames. The inlet and outlet sits on the same (top) face.*

4.8 EXPERIMENTAL

Additive manufacturing (fused deposition modelling) was performed using either a MakerBot Replicator Z18 3D printer for PLA printing (reactor version 1) or a Prusa i3 MK3s having a spring steel sheet with smooth double-sided PEI and hot-end E3D for PLA/PP printing (reactor versions 2-5 and I-II). The bed was prepared with PP tape purchased from billigemballage.dk (part no. TAP210) before printing parts in PP. Filaments of size 1.75 mm diameter were purchased from 3Dstore.dk. All models in this project were designed using SOLIDWORKS Premium 2019 CAD drawing tool and sliced in PrusaSlicer V2.1.

The pump used to drive fluids through the reactors was a New Era model NE-4000 Multi-Phaser Programmable Syringe Pump by KF Technology purchased from syringepump.eu.

Connections between system components were done with Masterflex® PTFE tubing (part no. 06605-27) with dimensions (OD: 3.2 mm; ID: 1.6 mm; thickness: 0.8 mm) purchased from Fischer Scientific. PTFE thread tape (part no. EW-08270-33), female luer ¼" threaded adaptor in PP (part no. EW-45508-66) and male luer lock ¼" threaded adaptor in PP (part no. EW-30505-52) were purchased from Cole-Parmer. PEEK flat bottom fittings for 1/16" OD with P-200 ferules (part no. UP XP230X) were purchased Mikrolab Aarhus. Inlet(s)/outlet hole threads were tapped manually. The aluminium plate (300 x 200 x 3 mm) for sealing and leak testing was acquired from Ebay (part no. 6082 T6).

Electrodes of graphite (50 x 40 x 3 mm) were acquired from Ebay sold by SigmaStore.

Glass plate (Ø100 mm, thickness 0.5 mm) was acquired from DanChip (DTU) (part no. AB 580).

Photoreactor for parallel screening follows the design from reference.[191] The LEDs (10W 440-450 nm) were purchased from Futureeden, while resistors (5W 2.2 Ohm, 5% deviation, part no. 84-453), fan (12 V, 80 mm, part no. 125-220), ventilator (12 V, 70 x 70 x 15 mm, part no. 136-159), heatsink (68 x 68 x 9 mm, part no. 125-304) and switching power supply (12 V, 5 A, 60W, 139-752) was purchased from Elektronik Lavpris.

General directions on chemistry

The following supporting data for compound **15** is published in M. Bargum *et al. Synlett* **2022**, *33*, 1083-1086. For further details please consult the Supporting Information in that paper.[190]

Light-source

Photoirradiation in batch was carried out with an LED from Thorlabs M365L2 (365 nm) with collimator (SM2F32-A) and power supply/driver (LEDD1B).

Specific reaction procedure

3,3-dihydroxy-4,6,6,7,7-pentamethyl-6,7-dihydrooxepin-2(3H)-one (15)

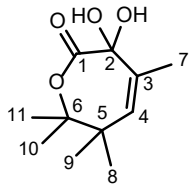

In a round-bottomed flask fitted with a magnetic stir bar was dissolved thioxanthone (53.1 mg, 0.250 mmol) in 25 mL MeCN. Citraconic anhydride (225 µL, 2.50 mmol) and tetramethylethylene (447 µL, 3.75 mmol) were added and the solution degassed for 30 min under nitrogen. The solution was irradiated at 365 nm (700 mA) for 16 h while wrapped in aluminium foil with stirring under a nitrogen atmosphere in which it turned yellow. The solution was concentrated under reduced pressure to yield a residue. The residue was purified by dry column vacuum chromatography (from 100% *n*-heptane to 100% EtOAc with 5% EtOAc increments) yielding a transparent oil (71.6 mg, 15% yield).

TLC: R_f = 0.44 (1:2 EtOAc/*n*-heptane)

^{1}H NMR (400 MHz, $CDCl_3$): δ 6.80 (d, *J* = 1.7 Hz, 1H, C4-H), 1.92 (d, *J* = 1.7 Hz, 3H, C7-H), 1.53 (s, 3H), 1.37 (s, 3H), 1.27 (s, 3H), 1.12 (s, 3H).

^{13}C NMR (101 MHz, $CDCl_3$): δ 171.0 (C1), 142.6 (C4), 133.9 (C3), 113.0 (C2), 86.7 (C6), 47.5 (C5), 25.5, 24.4, 21.4, 18.4, 10.5 (C7).

HRMS-ESI $[M+H]^+$ *m/z* calcd. for $C_{11}H_{19}O_3^+$: 215.1278, *m/z* found: 215.1275 $[M+H]^+$ (Δ ppm = -1.40).

ATR-FTIR: 3459 (broad), 2969, 2933, 2881, 1828, 1763, 1721, 1704, 1666, 1462, 1394 and 1377 cm^{-1}.

3,3-dihydroxy-4,6,6,7,7-pentamethyl-6,7-dihydrooxepin-2(3H)-one (15)

^{1}H NMR

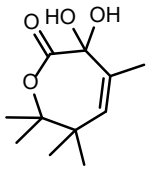

^{13}C NMR

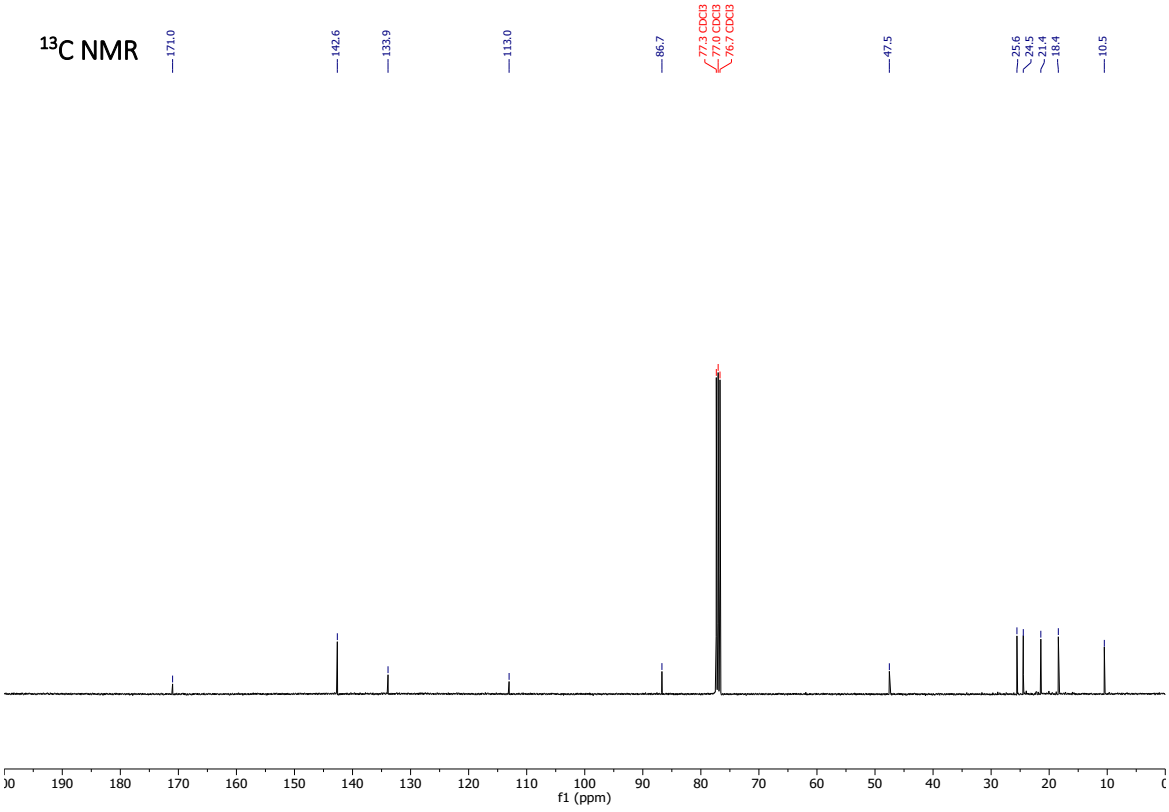

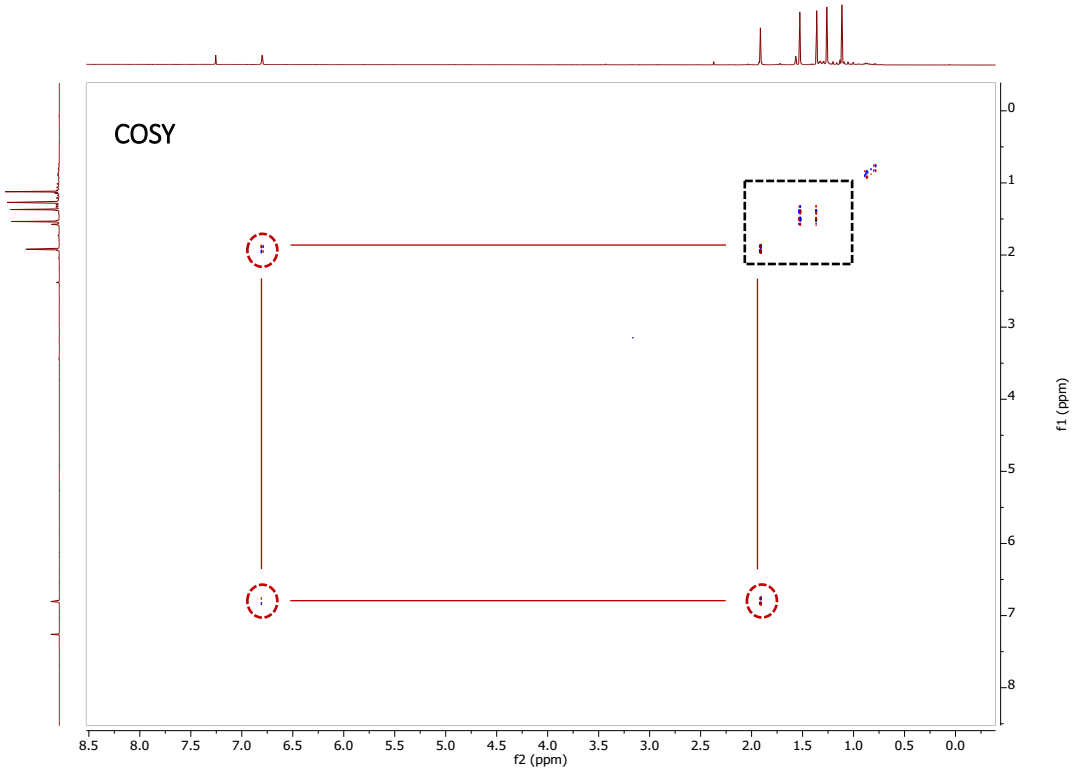
COSY
f1 (ppm)
f2 (ppm)

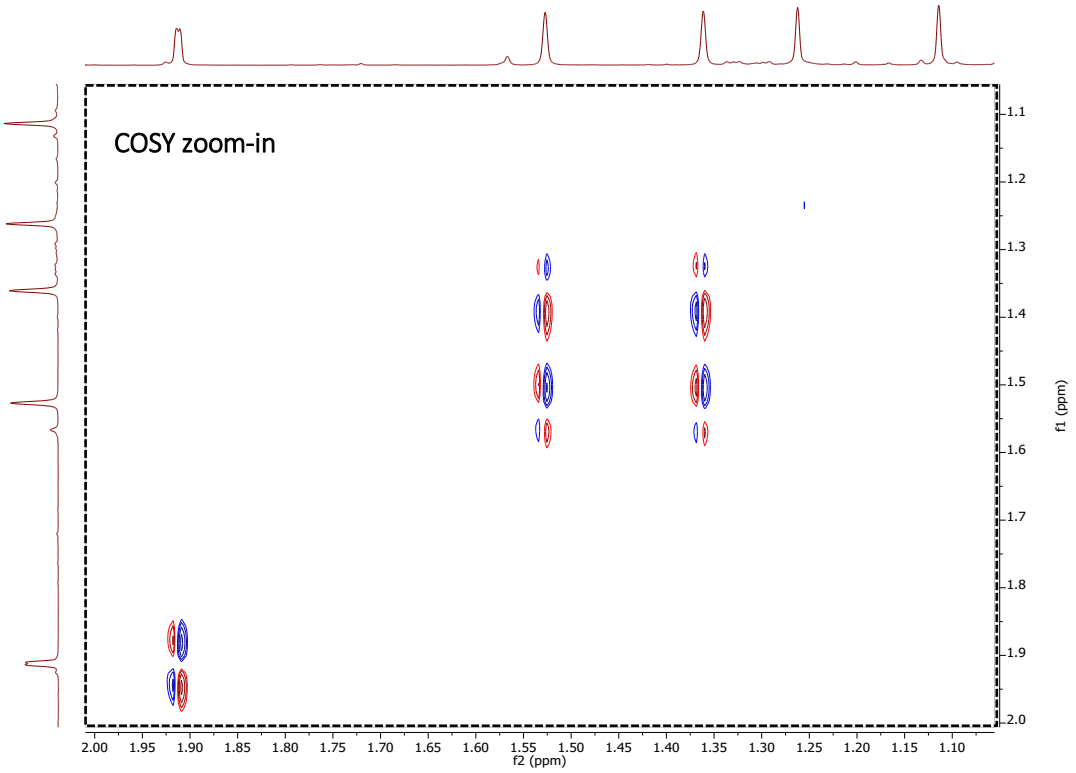
COSY zoom-in
f1 (ppm)
f2 (ppm)

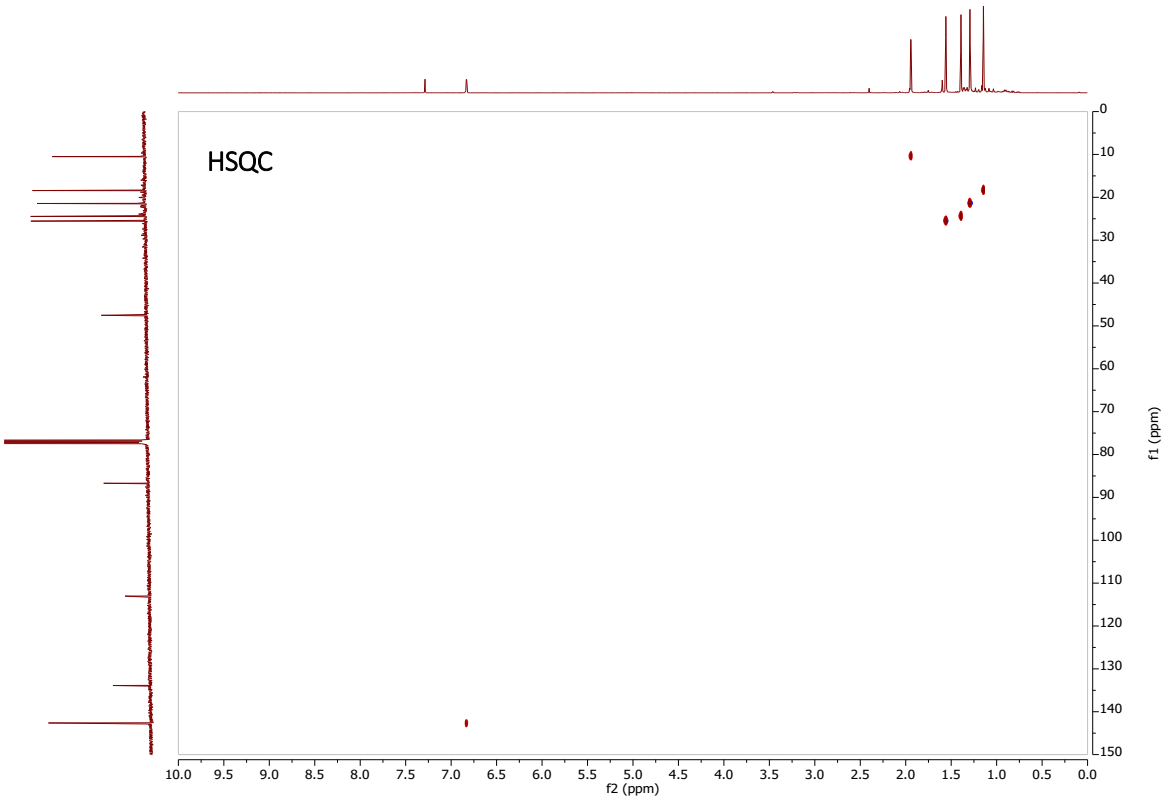
HSQC
f2 (ppm)
f1 (ppm)

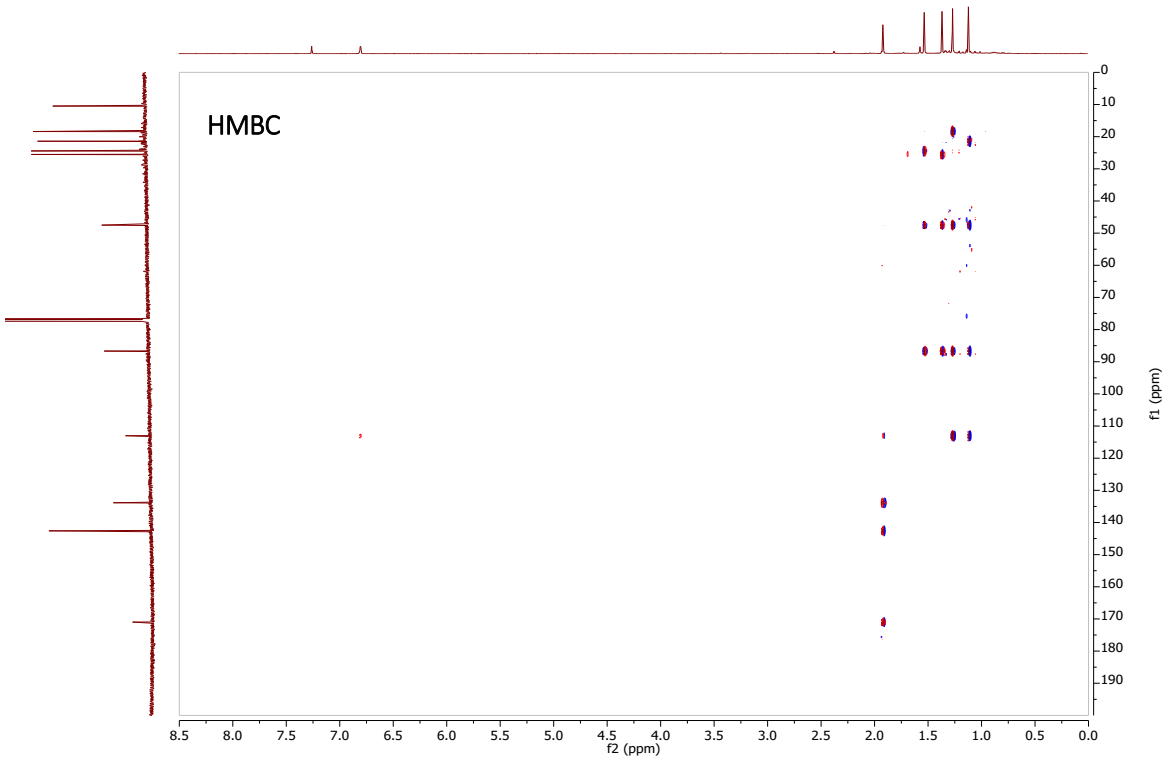
HMBC
f2 (ppm)
f1 (ppm)

ATR-FTIR

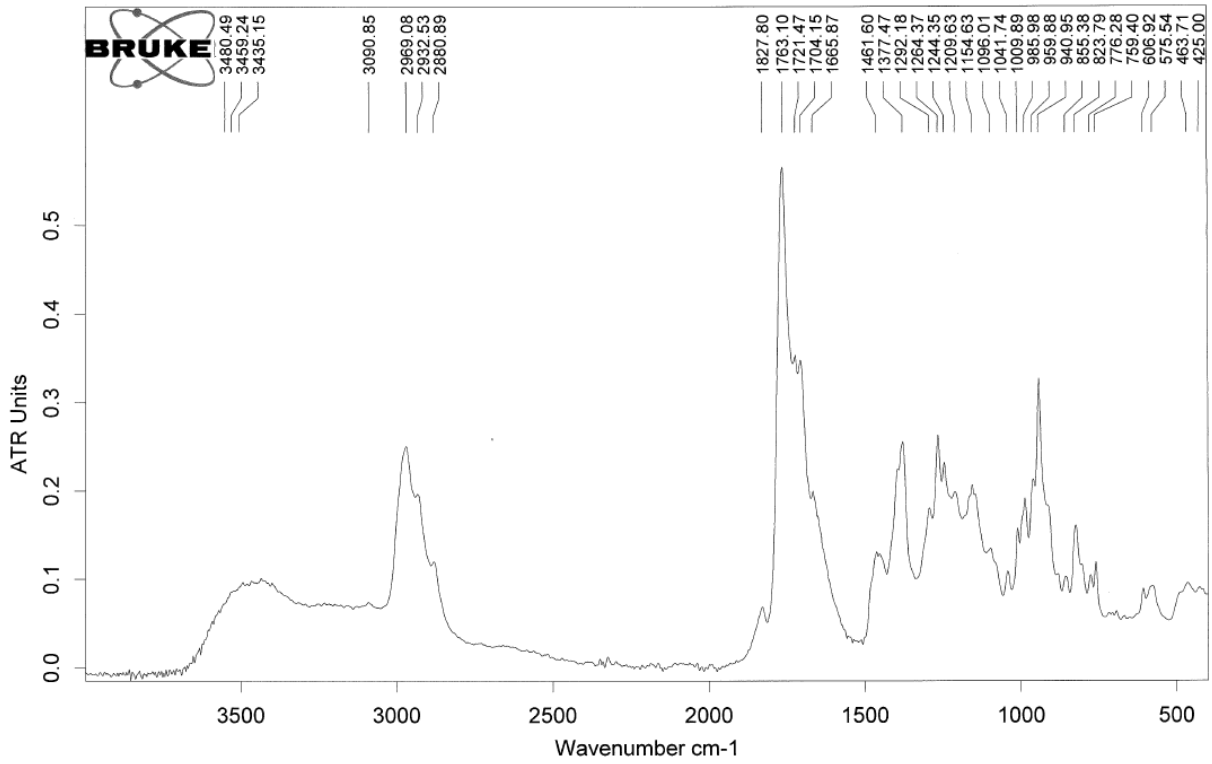
BRUKE
3480.49
3459.24
3435.15
3090.85
2969.08
2932.53
2880.89
1827.80
1763.10
1721.47
1704.15
1665.87
1461.60
1377.47
1292.18
1264.37
1244.35
1209.63
1154.63
1096.01
1041.74
1009.89
985.98
959.88
940.95
855.38
823.79
776.28
759.40
606.92
575.54
463.71
425.00
ATR Units
0.0
0.1
0.2
0.3
0.4
0.5
3500
3000
2500
2000
1500
1000
500
Wavenumber cm-1

5. HIGH-THROUGHPUT PHOTOCHEMICAL SCREENING PLATFORM

Planning and carrying out chemical synthesis requires careful execution of a highly variable series of complex reactions and steps, together with interacting with a wide range of equipment.[193] In general, it is comprehensive and time-consuming, while it most often involves very repetitive steps. Automation may greatly reduce human intervention and increase safety and efficiency by offloading these repetitive steps, leading to increased throughput. Furthermore, material loss can be cut and reproducibility increased as robotic tools offer high precision. Although organic synthesis only recently started to embrace automation in academia with inspiration from industrial practice as front runner, the traditional way of conducting synthesis with one-at-a-time classical batch reactions persist. Partly, due to convenience of it being simple, easy to approach and the way we were trained, but also as a consequence of automation not being very affordable or easy to comprehend how to get started. With the growing demand for delivering robust and efficient manufacturing routes to active pharmaceutical ingredients (APIs) in the industry, a conflict evolves as the academia providing novel chemical transformations can't keep up with the increased demand. [194]

5.1 HIGH-THROUGHPUT EXPERIMENTATION

One approach in response to these challenges and implement automation is high-throughput experimentation (HTE), which is the practice of running up to hundreds or even thousands of chemical reactions in parallel, typically in microtitre plates (MTPs), thereby offering faster experimentation to expedite route optimization or discover new novel reactions without sacrificing the quality of the results.[194,195] Although first developed in the biological space, it has started to win favours within the chemical community in academia as it is relatively inexpensive to set up, given most if not all of the necessary high-cost equipment can be found already in the common chemistry laboratory with emphasis on an LC-MS instrument that can read plates. When combined with a liquid handling dispense system like the Echo (**Figure 5.1**), the prepara-

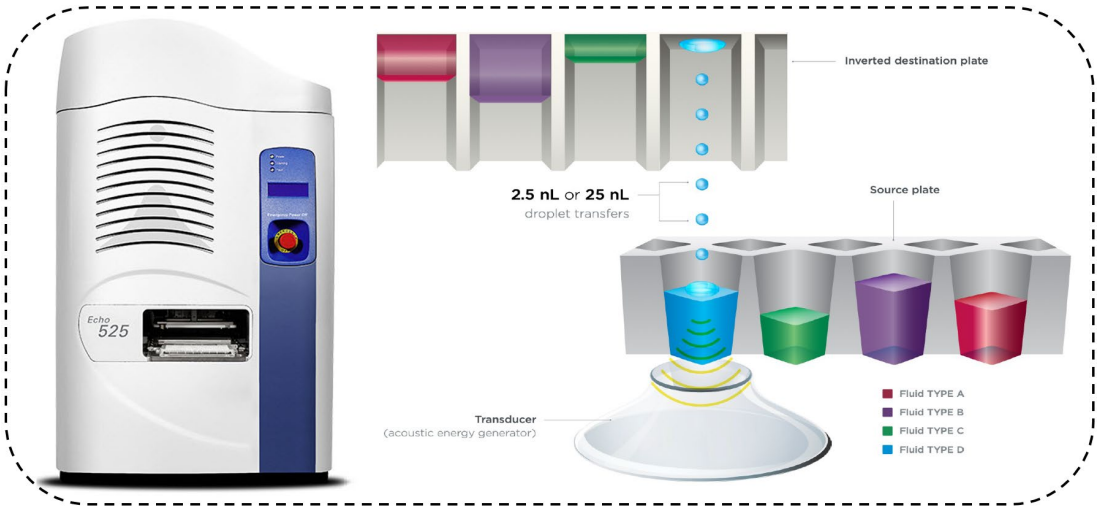

Figure 5.1. *The Echo Liquid Handler dispense system from Labcyte Inc. A Transducer located beneath the microtitre plates transmits soundwaves through the specific solutions to transfer droplets of fluids from the source plate (donor) to the inverted destination plate (acceptor). Adapted from Labcyte Inc.*[196]

tion of plates can be automated to facilitate a process where little effort is required to set up the screening of a large collection of reaction conditions in tandem, which greatly increases the chemical space that can be explored. However, the dispensing robot limits the choice of solvent to DMSO as it is the only solvent with properties compatible with this technique. Furthermore, little material is consumed as the investigation of one set of reaction conditions typically only need the amount which is instrumentally detectable for analysis, or practical to work with if manual pipetting of stock solutions is conducted. To prevent the rate of analysis in becoming a bottleneck, analytical methods should translate the outcome of the reactions, preferably directly from the MTPs, in a timely manner, but without compromising accuracy.[195]

Mass-based techniques currently dominate the analytical methods used in HTE, as these techniques offer rapid sampling and data acquisition depending on equipment in addition to facile product detection, data extraction and handling (**Table 5.1**).[195] However, structural information obtained from a mass-based technique is not as strong as for NMR spectroscopy that provides comprehensive structural elucidation, but at the expense of sampling and acquisition throughput in addition to deconvolution capabilities. IR is an alternative method with rapid acquisition speed, but structural information is only obtained in terms of functional groups. Likewise, deconvolution may prove difficult as overlapping bands will complicate the analysis making IR best suited for relatively clean reactions.

Applying HTE for chemical screening campaigns is already an industry standard in pharmaceutical research and development, and thus provides academic research groups with inspiration for setting up a platform of their own.[194] A neat example is from Astex Pharmaceuticals that developed an HTE photochemical screening platform to elucidate the optimal reaction conditions that facilitated photoredox-mediated synthesis of fragment-based aliphatic heterocyclic precursors enabled through a direct cross-dehydrogenative coupling (**Scheme 5.1**).[197] Reaction conditions were screened on nanoscale using 1536-well MTPs utilizing a liquid dispensing robot to handle the miniscule amounts with subsequent scale-up to micro- and millimolar scale in batch or flow.

Table 5.1. *Qualitative comparison of different analytical techniques for accessing HT analysis suitability. Less favourable (red), moderately favourable (yellow) and most favourable (green). MISER = multiple injections in a single run, MALDI = matrix-assisted laser desorption/ionization, DESI = desorption electrospray ionization. Adapted from R. Grainger & S. Whibleyl.*[195]

	LC-MS	MISER	MALDI/ DESI	Acoustic -MS	NMR	Flow-NMR	IR
Speed of analytical acquisition							
Structural information gained							
Detector sensitivity							
Hardware requirements							
Analytical plate formatting							

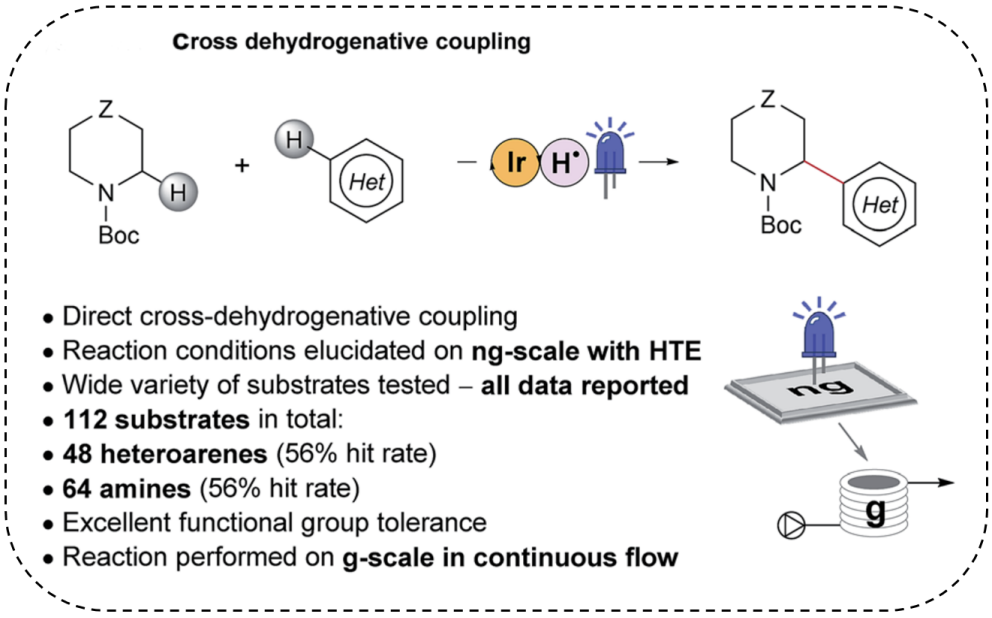

Scheme 5.1. Photoredox-mediated cross-dehydrogenative coupling method elucidated by the development of a high-throughput experimentation photochemical screening platform in Astex Pharmaceuticals. Reproduced from R. Grainger et al.[197]

5.2 PROJECT OUTLINE

In order to address the limitations of the fabricated photoreactor for screening multiple chemical reactions in parallel (see reactor version II in Chapter 4), and to enable the coupling of automation for increased throughput, we decided to develop a plate-based reactor.

Hence, the aim of this project is to establish a semi-automated screening platform to carry out photochemical transformations in microtitre plates similar to high-throughput experimentation (Scheme 5.2). Importantly, the platform should be inexpensive as we already possess most of the necessary instruments, which are currently used as routine for rapid screening of large compound libraries against therapeutic targets in our research group. Reagents will be transferred either by manual multichannel pipetting or through automated acoustic dispensing. The reactions will be analysed directly from the microtitre plates using an LC-MS instrument to which a data analysis tool (script) for rapid processing of the data in an automated way will be developed to ensure fast interpretation and increased throughput of the setup.

The platform will be applied to enable rapid discovery of optimal reaction conditions for photochemical [2+2] cycloadditions to set up the synthesis of an alkaloid-inspired natural product-like compound library with future screening for biological activity. The platform is therefore meant to expedite drug discovery.

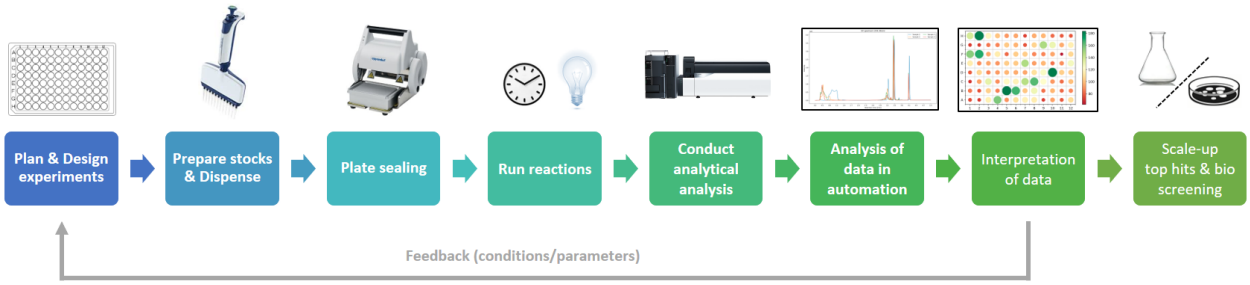

Scheme 5.2. *General workflow of the semi-automated photochemical screening platform to expedite drug discovery.**

*Relevant image references are listed in the reference section.

5.3 ESTABLISHING THE PLATFORM

The first task consisted of figuring out a working setup to facilitate convenient and practical screening of chemical reactions in MTPs, whilst allowing the analysis to be conducted directly from the plates. Therefore, two types of 96-well MTPs were acquired with standard dimensions compatible with an LC-MS (see Section 5.7 in the Experimental).

The first plate type consisted of a standard disposable polypropylene plate with a v-bottom to allow working with smaller reaction volumes easily handled by the needle from the auto-sampler of the LC-MS instrument. The second plate consisted of a re-usable temperature resistant plate made out of borosilicate glass with a flat bottom, thus a larger working volume is needed, but the plate enables chemistry with a broader range of conditions where PP would not be compatible, such as halogenated solvents or irradiation with UV light where PP is highly susceptible to degradation or deformation.

Furthermore, to limit evaporation of solvents from the plates while at the same time allowing light to irradiate the many wells for photochemical transformations, an optical heat-seal was applied using a heat-sealer for strong and even adhesion to the plates. The standard heat-seal for MTPs is made from aluminium, which would not work in our case due to the lack of transparency, but can be convenient if the intended chemistry is thermally allowed.

The next important consideration of the platform was the light-source. As we wanted the platform to facilitate excitation with both UV- and visible light (primarily blue light), two different setups were established. The first setup comprise a 50 W red-green-blue (RGB) LED light-source where the colours are customizable in addition to the intensity, and was employed in a similar setup by R. Grainger *et al*.[197] It is intended for outdoor use, and thus provides a very bright light. It has an integrated heatsink and can be positioned in any orientation for practical purposes. For the second setup, a nail gel-dryer (curing chamber) with integrated 4 x 9 W CFL bulbs with peak wavelength of 365 nm was repurposed to facilitate UV light excitation as it neatly fits the glass MTP inside its curing chamber. It is worth mentioning that this curing device is not meant for prolonged use, and also has an automatic timer that ensures a 30 minute limit likely as a safety percussion to not overheat, for which the light has to be re-activated with the press of a button.

Hence, to better dissipate the heat that will be generated by the light, and cope with potential overheating concerns with extended reaction times, a large desktop fan was integrated and oriented to deliver cooled air across the MTP for the visible light setup and into the curing chamber for the UV light setup. The full setup when reacting can be seen in **Figure 5.2**.

The positions of the plates in both setups are not fixed, but permanent markings guide the placement so it is identical and central to the light source for every screening performed. Similarly, the visible light LED was initially fixed 4 cm above the MTP inspired by the setup established by R. Grainger *et al.*,[197] but will have to be investigated and tested for in-plate variability.

The general workflow that constitutes all elements in the process from design to scale-up and later biological testing is illustrated in **Scheme 5.2** in the outline for this project (see Section 5.2). It is important to not underestimate the 'plan and design experiment' phase as it is this initial step that often determines the success of the screening experiment, and thus requires efforts to be allocated to this key-step.

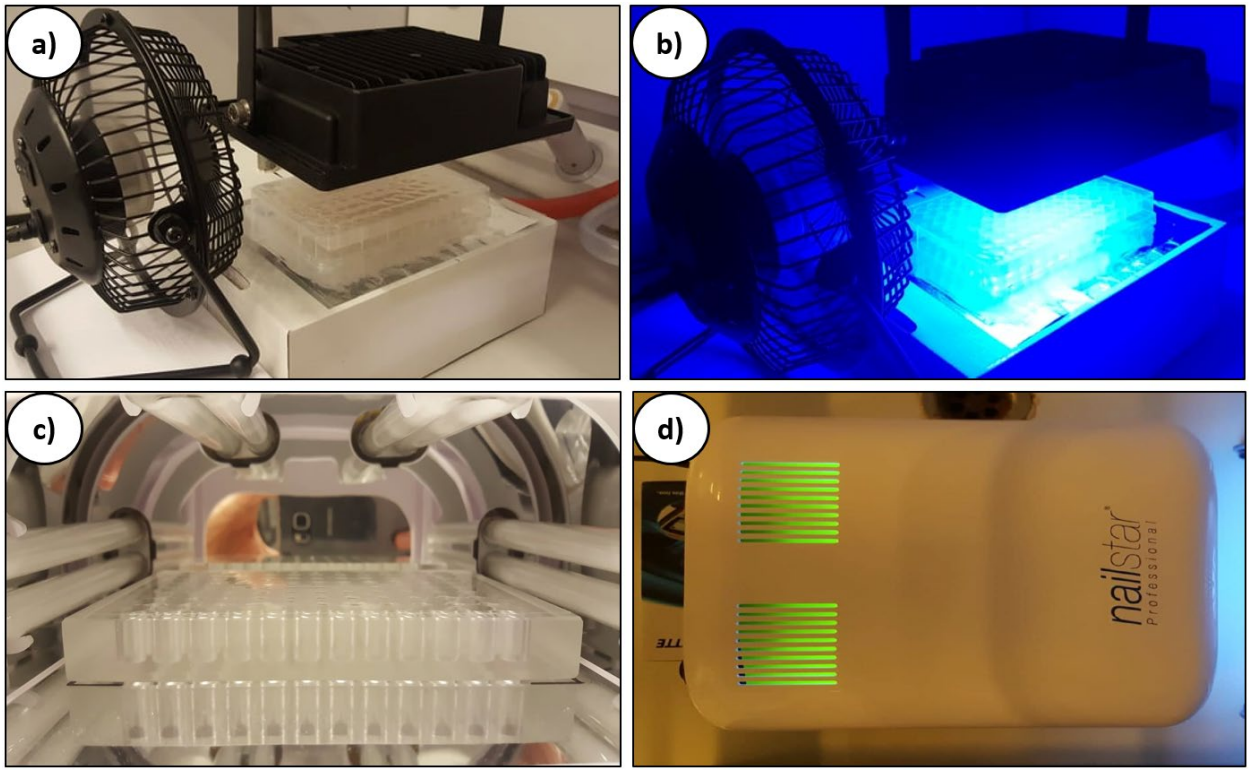

Figure 5.2. *Setup for photochemical reaction screening with a-b) visible (blue) LED light off/on, and b-c) UV light off/on.*

5.3.1 TEST AND VALIDATION USING REFERENCE REACTIONS

Before the HTE platform could be applied to discover new photochemical transformations, its performance and variability needed to be tested and validated. In this context, a known reference reaction reported by Hsu *et al.*[198] in addition to Green *et al.*[199] where an *N*-substituted maleimide (**1**) is photochemically coupled with a trialkyl aniline (**2**) to generate a tetrahydroquinoline (**3**) was employed (Scheme 5.3). It takes place under blue light irradiation without the use of neither photocatalyst nor additives, which simplified the analysis significantly. Furthermore, as we later intended to explore new chemical transformations utilizing maleimides, it provided us with some experience, especially in connection to the LC-MS analysis.

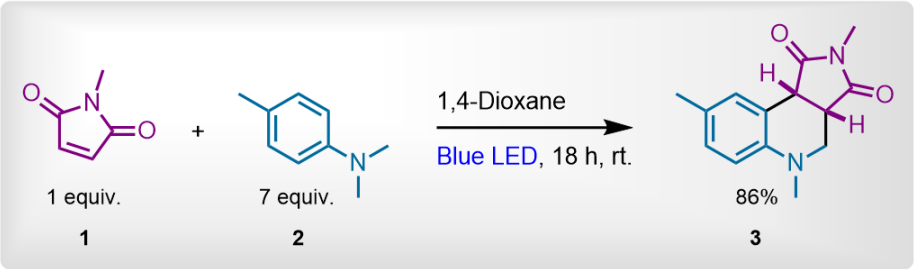

Scheme 5.3. *Original reaction conditions for the literature photochemical oxidative annulation by A. I. Green & G. M. Burslem*[199] *used as a reference to test and validate the developed photochemical screening platform.*

Interestingly, this reaction does not scale favourable, as a large excess of the toxic 4-methylaniline (**2**) is needed,[199] which constitutes a high economic cost besides a safety hazard. Therefore, it was worth investigating alternative reaction conditions to afford the tetrahydroquinoline (**3**).

Commercially available 4-bromobiphenyl (**4**) was added as the internal standard (ISTD) of choice for most screening experiments conducted in this project with inspiration from the literature where it has been applied in previous HTE studies (**Figure 5.3a**).[197] This compound is perfectly suited as an ISTD as it displays strong UV absorbance and resulted in a distinct UV-peak with a retention time close to 4.1 minutes when tested independently with LC-MS analysis. The starting materials were also analysed separately by LC-MS (**Figure 5.3b**), where it was observed that the 4-methylaniline (**2**) afforded a strange and broad initial peak in the beginning of the spectrum (sample 2 with orange colour), in addition to a very distinct and sharp peak close to 2.8 minutes. However, as ^{1}H NMR analysis of the compound afforded a clean spectrum with no evidence of any contamination, we decided to continue with this aniline.

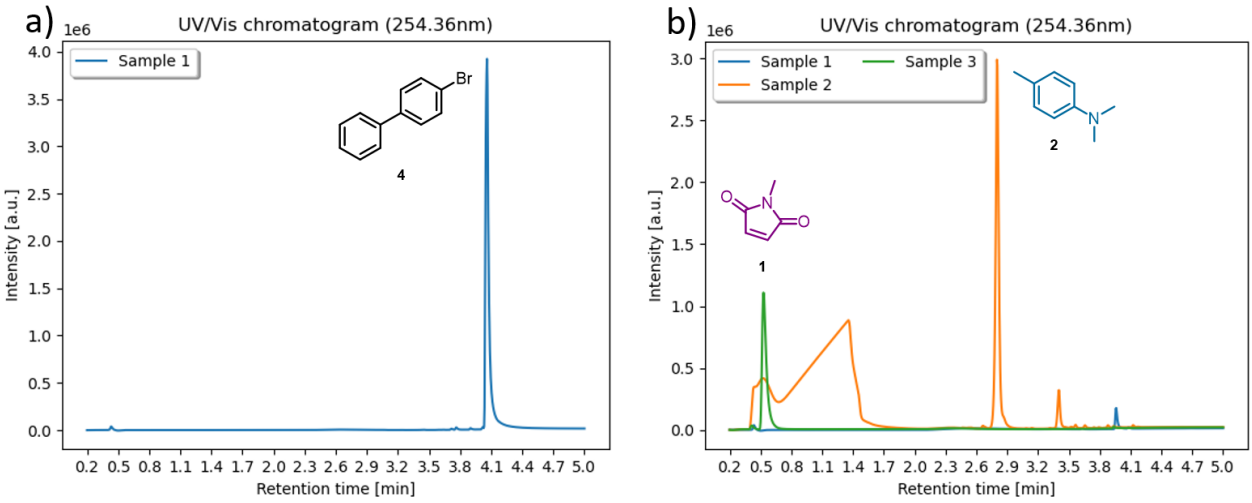

Figure 5.3. *UV-Vis spectra at 254 nm for a) 4-bromobiphenyl (**4**) internal standard (ISTD), and b) starting materials N-methylmaleimide (**1**) (sample 3) and N,N,4-trimethylaniline (**2**) (sample 2) in addition to a blank run (sample 1).*

In order to test the experimental setup of the entire platform and investigate if the reference reaction proceeded as expected, a screen reproducing the initial reaction conditions with either 1,4-dioxane or acetonitrile was performed in triplicates in a 96-well MTP with a 300 µL total volume (**Figure 5.4a**). The product peak was identified with a retention time close to 3.15 minutes, following the apparent detection of its mass peak in positive mode. It was observed that the two solvents performed similarly. It is important to mention that the LC-MS method applied when screening the reference reaction (see Section 5.7 of the Experimental) differs from the one applied to run the starting materials separately (**Figure 5.3b**), and thus produces the observed shift in retention times. In a subsequent screening, we found it important to investigate if the ISTD would interfere with the results. Therefore, two sets of triplicates with and without ISTD in acetonitrile as the solvent were performed with all other conditions reproducing the reference reaction (**Figure 5.4b**). It could be determined that all six reactions performed similarly. The initial test runs further allowed us figure out the LC-MS settings to perform automated analysis of a 96-well plate.

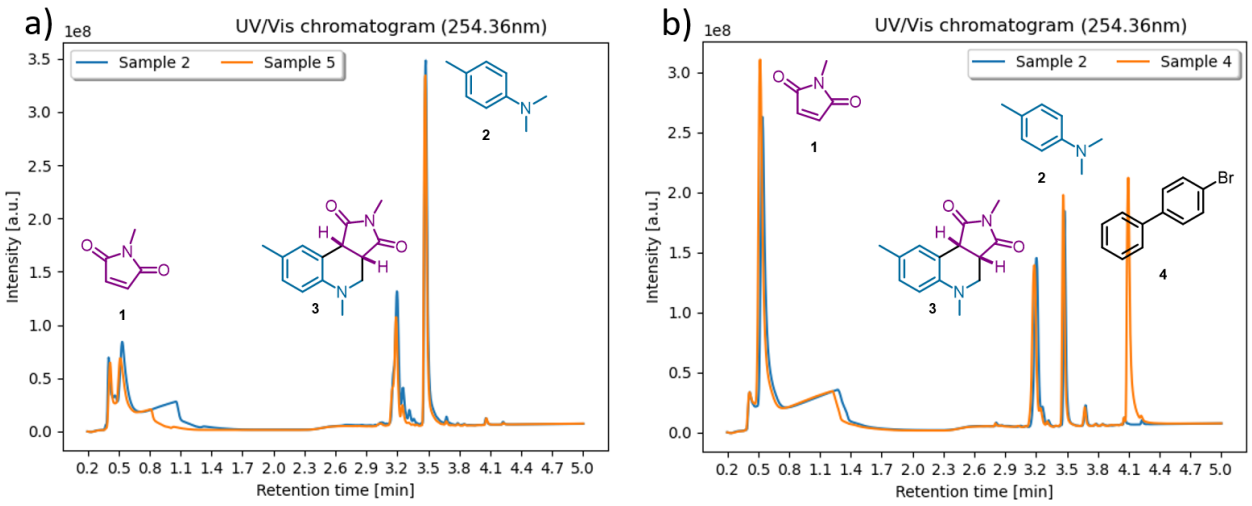

Figure 5.4. *Representative UV-Vis spectra at 254 nm in which the reference reaction in Scheme 5.3 has been reproduced in triplicates with a) 1,4-dioxane (sample 2) or ACN (sample 5) as the solvents, and b) ACN as the solvent without ISTD (sample 2) or with ISTD (sample 4).*

5.3.1.1 SOLVENT SCREEN

To gain some perspective on the utilization of the platform, we decided to run an extended solvent screen on the reference reaction to assess if another solvent would perform better or could substitute the 1,4-dioxane without compromising the conversion, as 1,4-dioxane is not recommended from an environmental perspective. Six different solvents were selected comprising iPrOH, THF, dioxane, ACN, DMF and DMSO, and constitute the only parameter that was varied following the reported conditions.[198,199] The solvents were replicated 16 times and manually pipetted into a 96-well MTP with a total volume of 150 µL in order starting with DMSO having the highest boiling point to limit potential evaporation in the plating process before sealing. The many replicates enable testing of in-plate variability of the platform besides providing statistical power. The positions of the solvents were split into duplicates and divided to extend across the full plate, and thus for this experiment not randomized. The results are visualized with a plate plot (**Figure 5.5**) using an automated data analysis tool developed by Nina R. Hamburger (a former master student in our research group) to allow simple and fast interpretation of the results (see section 5.8 in the Appendix A for script). In the plate plot, the various solvents are represented with a colour code, while the shape size and number represent the conversion (ratio between the integral of the product and the integral of the ISTD normalized to the largest value) in the respective sample wells.

We observe a clear trend with THF (in blue) displaying the highest conversion, which indicates it is the best performing solvent. Besides a distinct physical variation in colour between the samples of different solvent, substantial evaporation of the samples containing THF was noticed upon examining the plate after the 18 hours of blue light irradiation. Hence, the optical heat-seal does not prevent the volatile THF from evaporating when exposed to intense light that likely increase the temperature locally in the wells. Furthermore, from the plate plot is seems that there is some variability between samples with the same solvent, which is suspected to be caused by the evaporation, as samples with other solvents similarly had

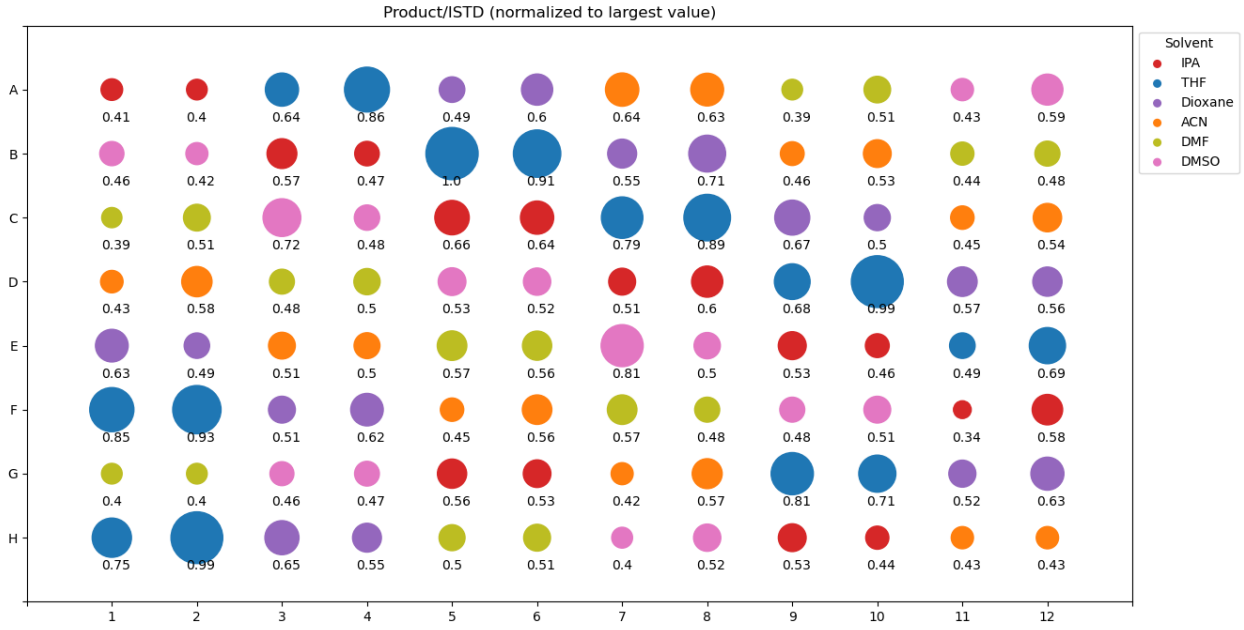

Figure 5.5. *Plate plot of solvent screen conducted on reference reaction from Scheme 5.3. The different solvents and colour codes can be found in the panel (upper right). Number and size represent conversion (product/ISTD) at 254 nm. IPA = isopropyl alcohol.*

their total volumes decreased, although to a lesser extent. When looking at the statistics for the conversion, we observe that the standard deviation (STD) between solvents are comparable, although THF as expected with the most evaporation also displayed the greatest STD (**Table 5.2**). The comparable STDs further implies that human and/or instrumental errors may affect the results almost to the same extent. Despite the higher STD for THF, it also displayed the greatest mean value in correlation with the observed trend from the plate plot, whereas the other solvents performed worse but similarly as is further evident and perhaps easier to comprehend from the box plots (**Figure 5.6**). The box plot for DMSO includes two outliers located outside

Table 5.2. *Mean, STD and compact letter display for the different solvents. Calculated based on 16 replicates.*

Solvent	**Mean** (product/ISTD)	**STD** (product/ISTD)	**Compact letter display**
DMF	0.880	0.112	C, G, I, J
ACN	0.931	0.136	B, E, G, H
IPA	0.944	0.163	A, B, C, D
DMSO	0.954	0.197	D, F, H, I
Dioxane	1.06	0.125	A, E, F, J
THF	**1.49**	**0.265**	

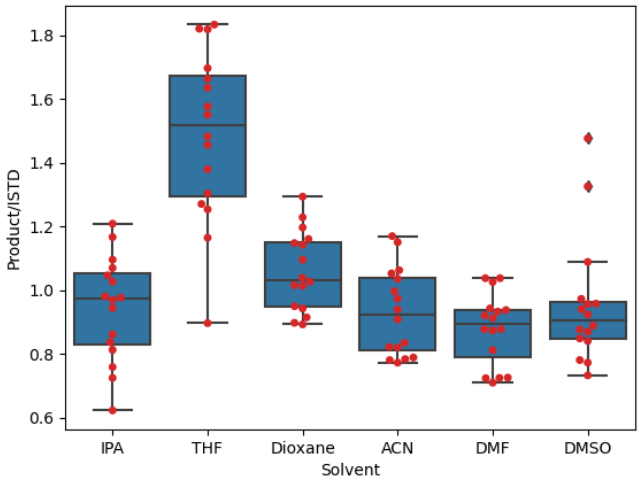

Figure 5.6. *Box plots of solvent screen conducted on reference reaction from Scheme 5.3.*

the maximum whisker. They are numerically distant from the rest of the data as the data points are defined as 1.5 times the interquartile range (IQR, distance from first quartile Q1 to the third quartile Q3) above the upper quartile. These two values correspond to the C3 and E7 plate positions, and no obvious explanation can be provided.

To determine if the solvent had a significant influence on the conversion (product/ISTD) of the reference reaction, an analysis of variance (ANOVA) test was conducted (**Table 5.3**). The null hypothesis (H_0) could be rejected as the p-value was below the significant value of 5%, hence the solvent displayed a significant effect on the formation of product.

Table 5.3. *One-way ANOVA test to examine if solvents differ significantly from one another. The analysis was performed with Python package "statsmodels".*[200] *DF = degrees of freedom. NaN = not a number.*

	DF	Sum of squares	Test-statistic F	P-value (Pr > F)
Solvent	5	4.08	26.86	$1.602e^{-16}$
Residual	90	2.74	NaN	NaN

Furthermore, a quantile-quantile (Q-Q) plot confirmed the model assumption for normality, as the standardized residuals followed a diagonal straight line (**Figure 5.7a**). In addition, the data points were randomly scattered around the 0 line in the residuals vs. fitted plot, which supports a random distribution of residuals having a common variance (**Figure 5.7b**). Therefore, it can be concluded from the ANOVA test that a statistical significance is apparent between the differences displayed by the solvents in the screen, but it is not possible to conclude which solvents that are significantly different from one another. Hence, multiple pairwise post hoc analyses were performed with the compact letter display included in **Table 5.2**. If a pair of solvents (treatments) do not share a common letter, they are determined to be significantly different with a Bonferroni corrected significance level calculated to 0.33%.

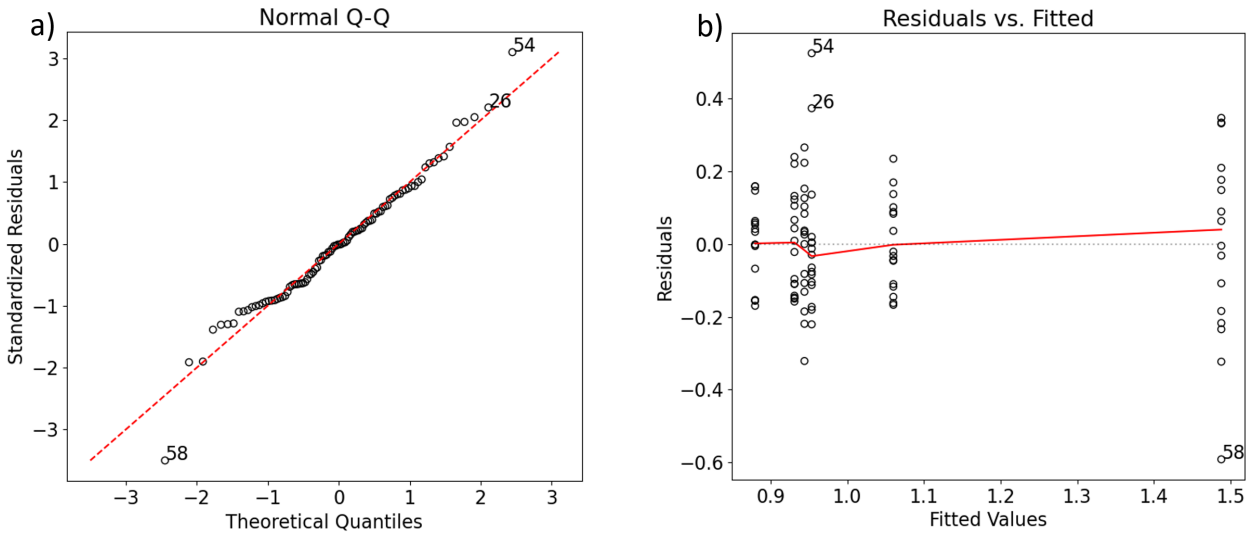

Figure 5.7. *Model assumption validation for the solvent screen. a) Normal quartile-quartile (Q-Q) plot. b) Residuals vs. Fitted plot.*

The analysis thus concludes that THF is significantly different from the other solvents, and can be applied instead of the 1,4-dioxane to achieve a better conversion. However, as already mentioned, the high volatility as a consequence of the low boiling point (66°C) of THF makes it impractical and perhaps not suited for an HTE plate-based approach with manual pipetting. Alternatively, one could use the 2-methyltetrahydrofuran instead, as it possess similar properties to THF, although with a boiling point of 80°C, which makes it more favourable to apply in combination with HTE.

5.3.1.2 EXPANDED OPTIMIZATION SCREEN

Following the success of the initial solvent screen, we decided to design a more comprehensive HTE screen to explore further optimization possibilities, while also providing us with a multivariable dataset to test our data analysis tool. Incorporating the results from the previous screen experiment we included ACN and THF besides the reference dioxane as the solvents. ACN was selected as it will not drag sample components or contaminants from previous LC-MS runs with it, like DMSO is known to do, thus affording a more compatible solvent with the LC-MS instrument and hopefully more clean analysis spectra. Four different reaction conditions were varied comprising of solvent (ACN, THF and dioxane), concentration (0.042 M, 0.083 M and 0.167 M), equivalents of *N,N,4*-trimethylaniline (1-3, 5 and 7 equiv.) and reaction time (2, 4.5 and 18 hours), which corresponds to a total of 45 different combinations tested and screened in duplicates. It is important to note that screening this many conditions necessitates the preparation of a lot of stock solutions, which can be very time consuming. The stock solutions were plated into a 96-well MTP in order of the boiling point of the respective solvent to minimize evaporation. The total volume varied between 150-176 µL in the wells depending on the reaction conditions. After visually inspecting the plate following 18 hours of blue light irradiation, it could be determined that evaporation was noticeable for 13% of the samples conducted in ACN and 57% of the samples conducted in THF. However, it was also observed that

the issue mainly persisted in the bottom left corner of the plate indicating that the optical heat-seal may not have been correctly placed or was not heated properly. It was decided to add 150 µL to all samples with visible evaporation and 100 µL to the remaining samples to ensure proper collection of samples by the autosampler of the LC-MS overnight. This will not affect the analysis of the results as it relies on the product to ISTD ratio, which is not changed. However, the results may be slightly impacted by a change in concentration during the reaction, as a consequence of the observed evaporation. Hence, it is important to have statistical power and run reaction conditions in duplicates or higher to decrease the potential significance of a deviation.

The results of the screen were visualized in a plate plot using the data analysis tool (**Figure 5.8**). Displaying more than two variables as exemplified here with solvent and concentration in the plate plot becomes complicated to visually comprehend, but it is possible to substitute for instance concentration with equivalents of the aniline or reaction time to generate a different plot. Likewise, instead of looking at the product/ISTD, the analysis tool also allows analysing the data based on the starting material/ISTD. It is important to remember when inspecting the plate plot that variables such as equivalents of aniline or reaction time is not visually displayed, but hides underneath the data, and therefore may mislead the interpretation that large variations in the plot is observed between samples of identical reaction conditions. We were pleased to see that the top performing reactions supported our previous discovery that THF seems to be the solvent of choice for increased conversions independent of other variables with this reaction. Another observable trend is that the samples with 0.04 M concentration performed better than the refer-

Figure 5.8. *Plate plot of a screen with different variables (solvent = colours, concentration = shapes, aniline equiv. = not depicted) conducted on reference reaction from Scheme 5.3. The descriptive codes can be found in the panel (upper right). Number and shape size represent conversion (product/ISTD) at 254 nm. Equivalents of the N,N,4-trimethyl-aniline (**2**) screened were 1-3, 5 and 7. N/A (orange) in the panel represent different reaction times performed in ACN (well positions H7-8 = 4.5 h, well positions H9-10 = 2 h), and blank ACN sample runs (well positions H11-12).*

ence reaction conditions of 0.08 M or twice that of 0.16 M. It is difficult to state a reason, but may in part be caused by a possible attenuation effect. When pulling out the top ten reactions from the analysis, it is further evident that a concentration of 0.04 M is favourable as all top reactions contain this condition (Table 5.4). In addition, we observe the aforementioned trend with THF as the solvent for the best performing reactions, while also representing 50% of the top ten results. Interestingly, no clear trend was observed for the equivalents of aniline. Hence, it may be possible to lower the amount of aniline without affecting the conversion to product. The screen further indicated that a reaction time of more than 4.5 hours (orange colour in Figure 5.8) was necessary for efficient conversion, whereas no product could be detected in the samples only reacted for 2 hours. Hence, the results from the screen suggested a few optimized reaction conditions where the concentration is reduced by a factor two and the dioxane solvent is replaced by THF, besides the promising opportunity to reduce the amount of aniline without affecting the conversion.

Table 5.4. Top ten reactions based on conversion (product/ISTD) for the optimization screen with reaction time 18 h. The conversion values are normalized. DO = 1,4-dioxane.

Top (#)	1	2	3	4	5	6	7	8	9	10
Well position	F1	G2	F7	D7	G1	C2	D2	C8	C7	H1
Maleimide conc.	0.04 M	0.04 M	0.04 M	0.04 M	0.04 M	0.04 M	0.04 M	0.04 M	0.04 M	0.04 M
Aniline equiv.	7	3	5	3	3	1	5	7	7	1
Solvent	THF	THF	THF	ACN	THF	DO	ACN	ACN	ACN	THF
Conversion	1.0	0.80	0.72	0.71	0.69	0.68	0.66	0.64	0.63	0.63

5.3.1.3 IN-PLATE & PLATE-TO-PLATE VARIABILITY SCREEN

As variability between samples screened with the same reaction conditions was observed, we sought to estimate the in-plate together with the plate-to-plate variability to test and validate the photochemical screening platform. In order to get reliable results, we thought to minimize potential errors that we might control such as the evaporation of solvent, and thus decided to screen a similar reaction, but where the dioxane is substituted for the less volatile DMF (Scheme 5.4). Furthermore, by replacing the methyl-substituted aniline (**2**) with the chloro-substituted aniline (**5**) multiple issues were addressed. The chloro-substituted aniline (**5**) displayed a better UV-Vis peak for LC-MS integration, thus conversion based on the starting material was an option, while the reported literature reaction in 0.08 M dioxane with 7 equivalents of aniline was obtained in low yields of 37% affording room for improvement with later scale-up in batch or flow.[199]

With prior screening knowledge of a similar reaction (*vide supra*) from the same reported study, we decided to perform the reaction in two 96-well MTP with 3 equivalents of the chloro-substituted aniline (**3**), 0.040 M concentration and a total volume of 150 µL. The two plates were prepared on separate days by two different people. The statistical results based on integrals of product/ISTD is presented in Table 5.5.

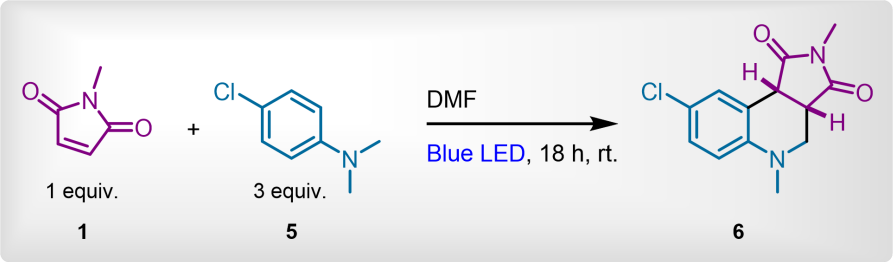

Scheme 5.4. *Literature reaction with altered reaction conditions used as a reference to screen for in-plate and plate-to-plate variability of the developed photochemical screening platform. Original photochemical oxidative annulation reaction by A. I. Green & G. M. Burslem*[199]

We observed close to identical mean, STD and median for both plates, which indicates that there is no plate-to-plate variability (**Table 5.5**). This was further examined with a one-way ANOVA test (**Table 5.6**). The null hypothesis (H_0) could not be rejected as the p-value was above the significant level of 5%, hence no significant difference was displayed on the formation of product between plates prepared on separate days. Q-Q and residuals vs. fitted plots further validated the ANOVA model assumptions (**Figure 5.10**). The spread in the data was visualized with box and scatter plots (**Figure 5.9a-b**). As stock solutions were plated by manual pipetting, human errors cannot be excluded as a potential cause for the observed deviations. It could also be caused by instrumental errors in the injection or detection process. No clear trends were observed from the data, as the spread appeared random and without a pattern, thus it was concluded that neither plate-to-plate nor in-plate variabilities with specific well positions favoured exist for our photochemical screening platform.

Table 5.5. *Mean, STD and median for two screens of identical 96-well MTP.*

	Mean (product/ISTD)	**STD** (product/ISTD)	**Median**
First screen	2.02	0.326	1.97
Second screen	2.03	0.344	1.93

Table 5.6. *One-way ANOVA test to examine if the two identical screens from separate days differ significantly from one another. The analysis was performed with Python package "statsmodels".*[200] *DF = degrees of freedom. NaN = not a number.*

	DF	**Sum of squares**	**Test-statistic F**	**P-value** (Pr > F)
Solvent	1	0.00689	0.0607	0.806
Residual	190	21.6	NaN	NaN

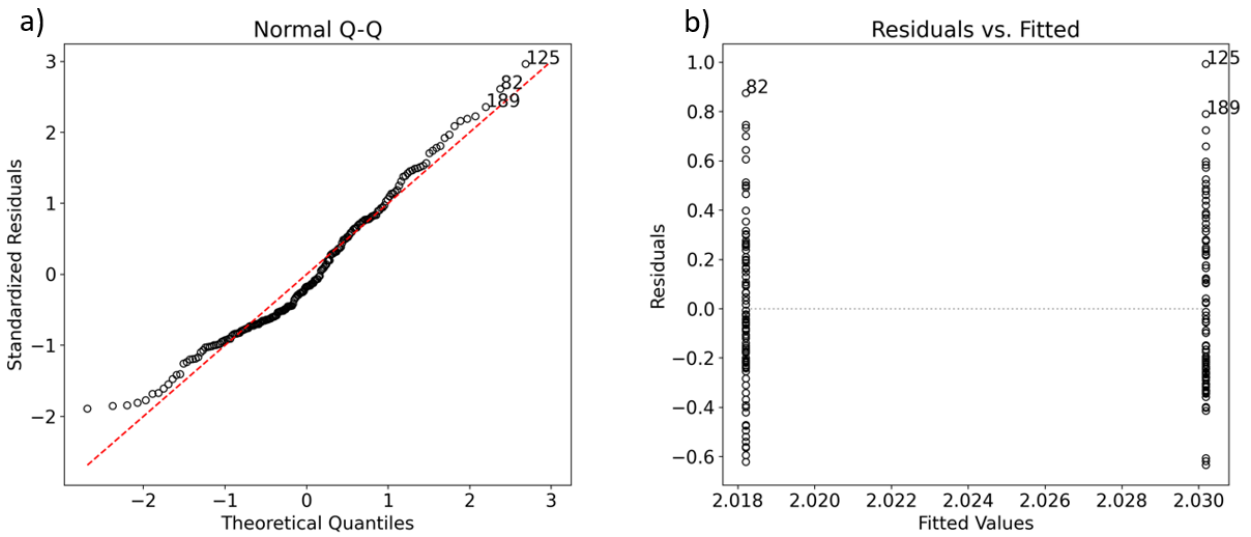

Figure 5.9. Analysis for the two identical 96-well MTP screens performed on separate days with the same reaction conditions for all wells. a) Box plots of the two plates. The integrals for product/ISTD calculation is based on UV-Vis absorbance at 254 nm. b) Scatter plot of the two plates (pate 1 = blue, plate 2 = red).

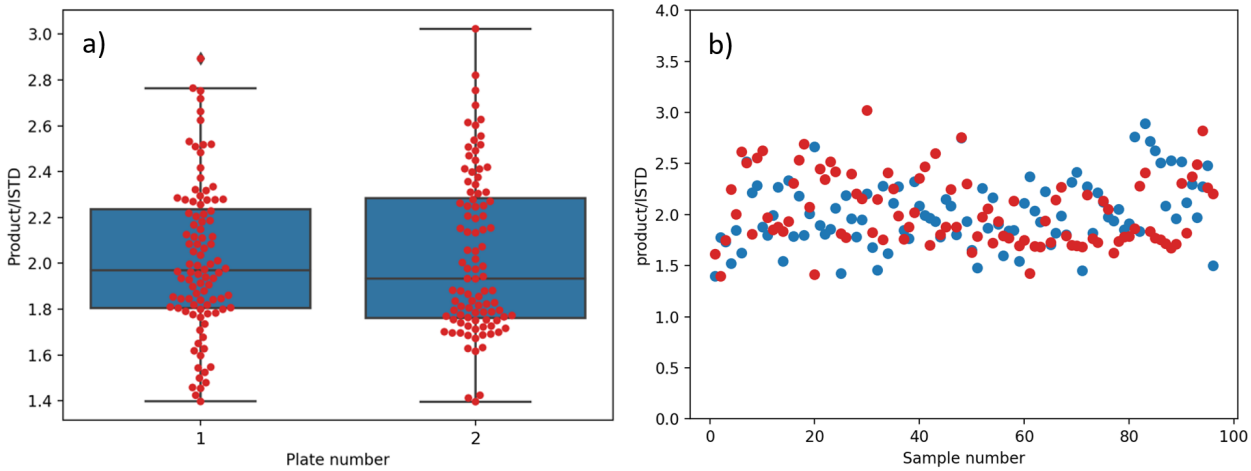

Figure 5.10. Model assumption validation for two identical screens performed on separate days. a) Normal quartile-quartile (Q-Q) plot. b) Residuals vs. Fitted plot.

5.3.1.4 LC-MS PERFORMANCE STABILITY TEST

To investigate the accuracy and performance of the LC-MS instrument, a series of tests were conducted in which three different samples prepared in LC-MS vials (to mitigate evaporation) with ACN (1.5 mL) were analysed (Table 5.7). The samples contained either ISTD, *N*,*N*,4-trimehtylaniline [**2**) or a mixture of the two. A total of 30 injections from each vial was performed, and allowed us to calculate the deviations between the minimum and maximum integrals using their UV-Vis absorbance peaks. Hence, the ISTD displayed up to 12-18% acceptable deviation between sample injections from the same vial irrespective of injection volume (1-5 µL) or if aniline was present. However, the aniline displayed up to 32-34% deviation for the series of samples where the peaks could be reliably determined. A column and needle wash did not affect the results. In this context, conversion based on starting material would not suffice. These results indicate that the observed variations in our data for identical reactions in previous screens, likely arose by instrumental errors.

It is therefore important when comparing reaction conditions to screen with statistical power (for instance in triplicates or higher and take the mean), and not compare subtle changes in reaction conditions as the results of these might not be visible in the data. Furthermore, the parallel screens performed with our platform reliable provided estimates of conversions based on product formation, and when compared to a traditional batch setup with a significantly faster process time.

Table 5.7. *LC-MS instrument performance stability/accuracy. Five samples were prepared in ACN (1.5 mL) and injected 30 times each. Maximum deviations between the 30 injections are represented by the min/max integral ratios. The aniline is N,N,4-trimethylaniline (**2**). In some cases, the UV abs. peak differed too much in shape and intensity to allow for a reliable estimate of the aniline.*

Vial	Compound 1	Compound 2	Injection volume	Min/max (ISTD)	Min/max (aniline)
1	ISTD	N/A	1 µL	13.3%	N/A
2	ISTD	Aniline	1 µL	15.4%	34.0%
3	ISTD	N/A	2 µL	12.6%	N/A
4	ISTD	Aniline	2 µL	18.4%	31.9%
5	ISTD	Aniline	5 µL	14.7%	N/A

5.4 ACCELERATED DISCOVERY OF NEW PHOTOCHEMICAL TRANSFORMATIONS

Having established and validated the photochemical screening platform, we looked towards exploiting its potential in expediting the discovery of new photochemical transformations of interest in our research group. In this context, we wanted to investigate the optimal reaction conditions for photochemical [2+2] cycloadditions intended for an alkaloid-inspired natural product-like compound library. As such, 3-quinuclidinone (**7**) and *N*-boc-nortropinone (**8**) could thus serve as starting materials to set up the cycloadditions with various substituted maleimides to afford a complex compound library with 3d rich spirocyclobutane scaffolds.

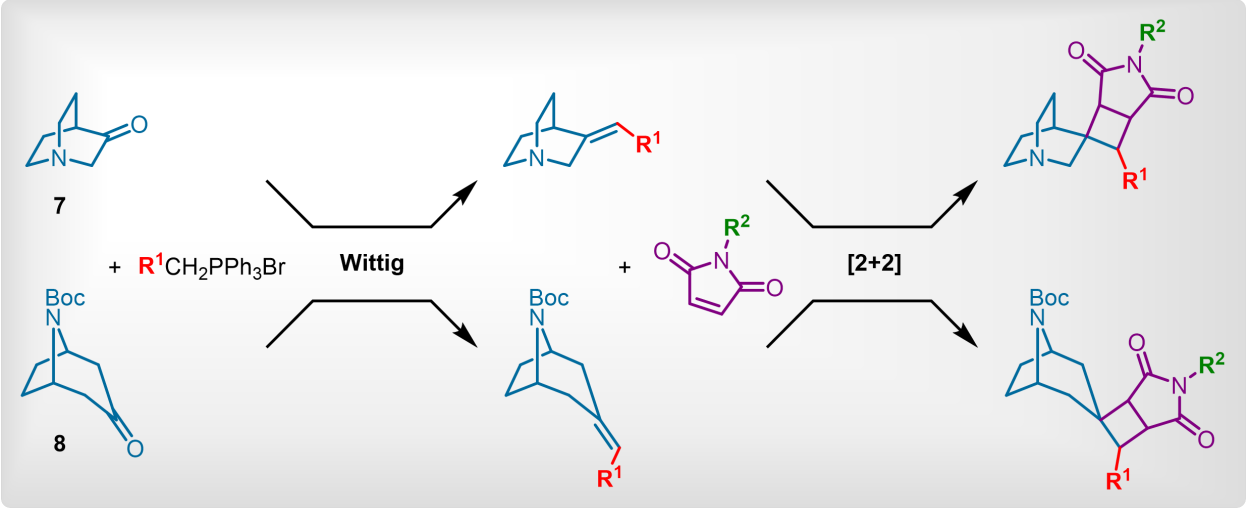

Scheme 5.5. *Overview of an alkaloid-inspired natural product-like compound library enabled through photochemical [2+2] cycloaddition reactions affording scaffolds comprising both spirocycles and cyclobutanes.*

5.4.1 PHOTOCHEMICAL [2+2] CYCLOADDITION

We initiated our photochemical investigations with phenyl-substituted alkene (**10**) and commercially available *N*-methylmaleimide (**11**) (**Scheme 5.6**) with the method inspired by R. Knowles *et al.*[201] The alkene was accessed in 63% yields through a Wittig reaction between commercially available *N*-boc-nortropinone (**8**) and the Wittig reagent benzyltriphenylphosphonium bromide (**9**) (prepared from previously reported methods in 67% yields)[201]. We decided to install and use the phenyl substituted alkene for the optimization studies, as it would absorb sufficient light to produce an easy to analyse UV-Vis absorbance peak. However, it is important to keep in mind that the outcome of the photochemical [2+2] cycloaddition analysed, might result in a mixture of up to eight stereoisomers where four are diastereoisomers together with four pairs of enantiomers all depending on the approach (top or bottom face) of the maleimide that adds with a *syn*-fashion, which may complicate the analysis.

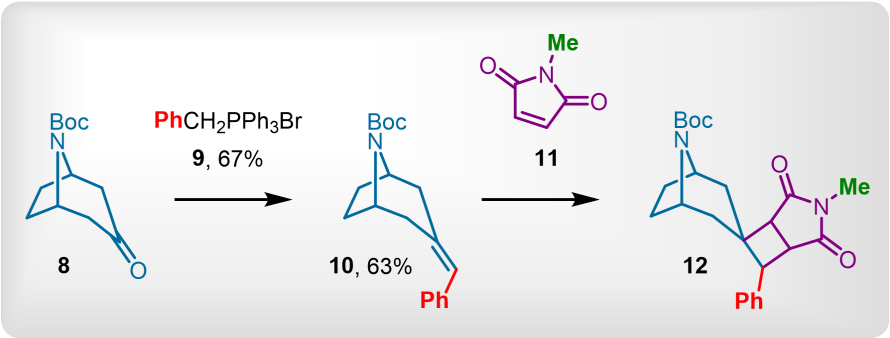

*Scheme 5.6. Overview of the synthesis towards N-boc-nortropinone-derived spirocyclobutane compound **12**.*

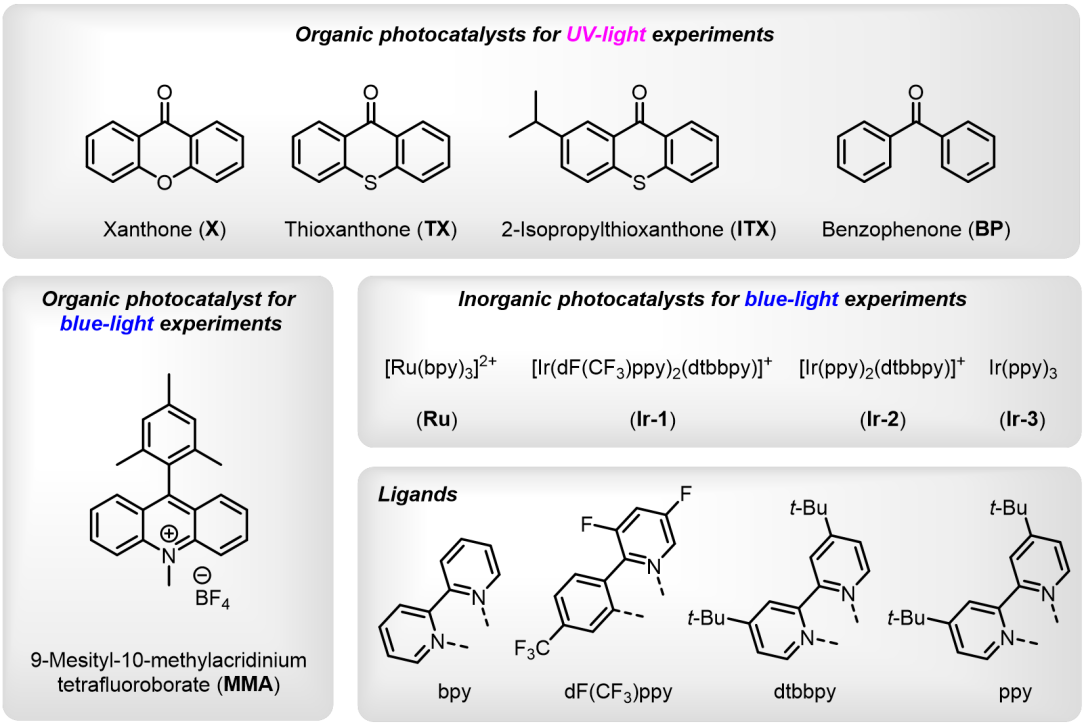

Figure 5.11. Overview of photocatalysts for UV- and visible (blue) light photochemical screening. Bpy = 2,2'-bipyridine, ppy = 2-phenylpyridine, dtbbpy = 4,4'di-tert-butyl-2,2'-dipyridyl.

Most *N*-substituted maleimides exhibit triplet state energies lower than 59.7 kcal/mol, which allows sensitization to take place by a number of suitable, efficient and commercially available sensitizers.[202] Various UV- or visible light absorbing organic carbonyl sensitizers ($n \rightarrow \pi^*$ excited state) and transition metal sensitizers (metal-to-ligand charge-transfer excited state) were selected in the triplet [2+2] cycloaddition screen conducted in this study (Figure 5.11 and Table 5.8).

Table 5.8. Photophysical properties[202–204] of photosensitizers employed in this study.

	X	TX	ITX	BP	MMA	Ru	Ir-1	Ir-2	Ir-3
E_T (kcal/mol)	-	63.3	-	69.0	-	49.0	61.6	-	58.0
$Ø_{ISC}$	-	0.60	-	>0.95	-	>0.95	>0.95	-	>0.95
λ_{max} (nm)	-	420	-	380	430	452	450	410	450
τ (µs)	-	73	-	50	-	1.0	3.0	0.56	2.0

5.4.1.1 UV & VISIBLE LIGHT SCREEN

A total of 48 or 60 different reaction conditions were screened in triplicates in the initial study employing two different platform setups with either UV or blue light excitation with the aforementioned photocatalysts (**Figure 5.11**). Further parameters included equivalents of *N*-methylmaleimide (**11**) (1 or 3 equiv.), loading of photocatalyst (5 or 20 %) and reaction time (3, 6 or 12 hours). The solvent for all reactions was DMF to prevent possible evaporation, and the concentration was 6.67 mM in attempts to prevent substantial dimerization of maleimide (**11**). ISTD (**4**) (0.50 mM) was added to all reaction wells with a total volume of 150 µL, while a script was used to randomize the positions of the reactions in the 96-well MTPs.

The tropinone-derived olefin (**10**) was initially tested separately with LC-MS (**Figure 5.12a**) at 254 nm wavelength detection. However, with detection at 229 nm wavelength the ISTD peak splits into two (**Figure 5.12b**), which is important to realise before product formations are calculated based on ISTD integrals. The detection of product (**12**) was supported by the MS adducts (**Figure 5.13**). Conversion based on the maleimide (**11**) was not possible as it co-eluted in the beginning with the solvent DMF peak.

Product could be detected for all organic photocatalysts using UV light irradiation, but did display significantly higher product/ISTD ratio with xanthone (**X**) as the sensitizer (**Table 5.9**), which was further evident as all top five performing reactions in the screen belonged to reactions with xanthone. Interestingly, the top three reactions all had 3 equivalents of the maleimide (**11**). In addition, it was observed that 20 mol% performed a lot better for most photocatalysts. Illuminating the MTP for longer than 3 hours (6 and 12 hours) only reduced product peak intensities, likely caused by photodegradation.

We initially thought samples with Ir-2 displayed the most product/ISTD ratio for the plate illuminated with blue light. However, based on manual inspection of the top hits from the LC-MS results, we observed that the UV absorbance peak of the catalyst co-eluted on top of the product peak, which resulted in the automated data analysis tool suggesting it was the favourable conditions. After removing the few samples where this was an issue, it could be concluded that no photocatalyst could compete with the samples containing Ir-1 in 20 mol% (**Table 5.10**). In addition, all reactions in the top ten when pulled using the data analysis tool contained Ir-1 with varying maleimide equivalents (1 or 3 equiv.). This indicates that the triplet energies for the other sensitizers are too low to enable energy transfer to the maleimide (**Table 5.8**). The UV absorbance peak intensities were approximately reduced by a factor two with prolonged irradiation of blue light, similar to the UV light irradiation screen. Thus, a reaction time of 3 hours was favoured over 6 or 12 hours.

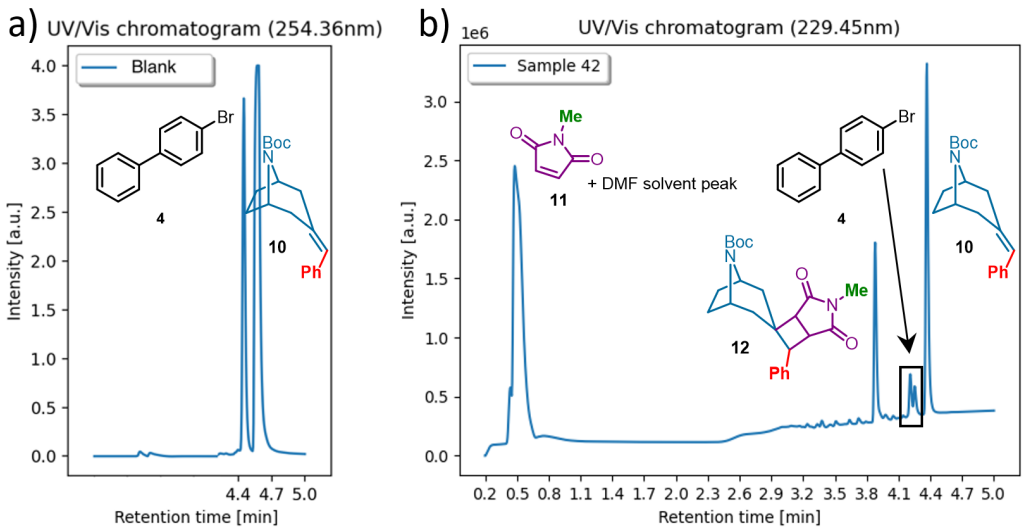

*Figure 5.12. LC-MS chromatograms for a) sample containing the tropinone-derived olefin (**10**) with ISTD with UV detection at 254 nm, and b) sample from initial screens of reaction displayed in Scheme 5.6 (last step) with UV detection at 229 nm. The ISTD peak splits at this wavelength.*

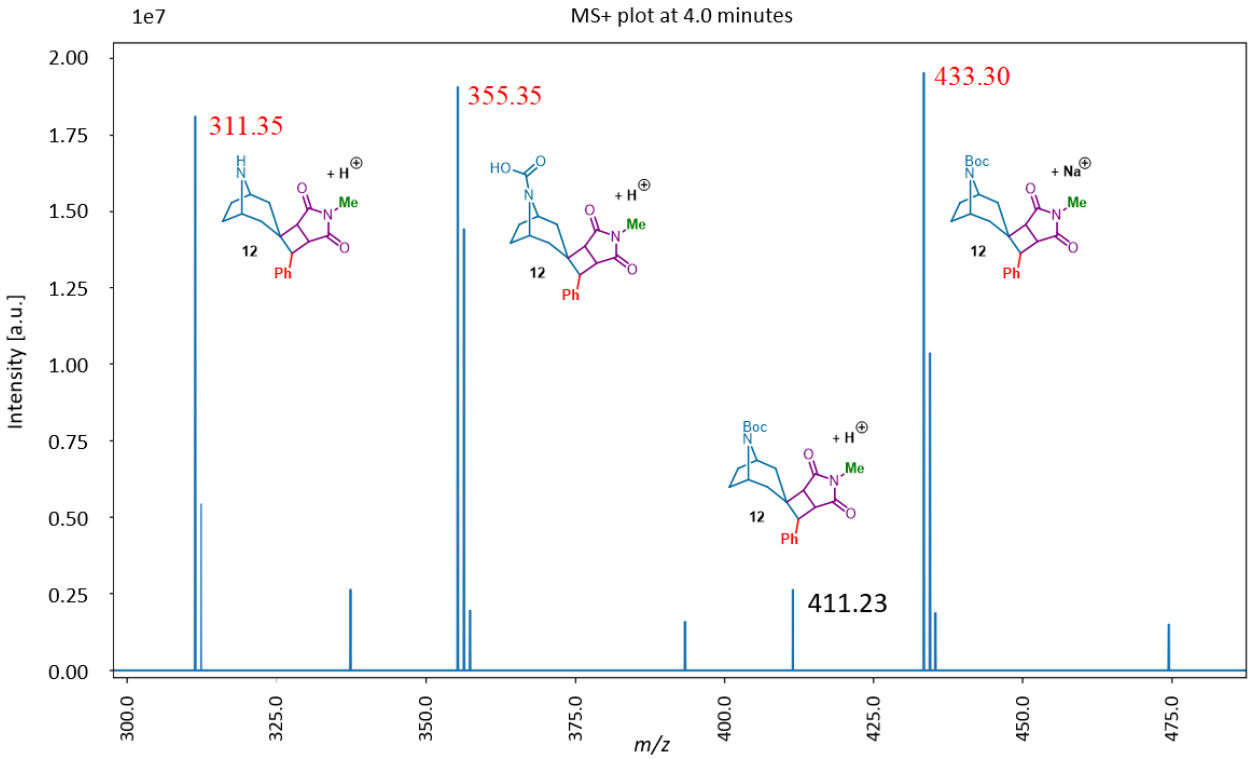

Figure 5.13. LC-MS spectrum for positive mode at retention time 4.0 minutes. Highlighted most abundant MS adducts in m/z range from 300-475.

Table 5.9. *Mean, STD and median for UV light irradiation screen of reaction in Scheme 5.6 (last step) after 6 hours with various organic photocatalysts and loadings (mol%) performed in DMF (6.67 mM) with a 96-well MTP. Calculated based on product/ISTD ratio at 230 nm and independent of the equivalents of N-methylmaleimide (**11**) (1 or 3 equiv.).*

	X (5%)	X (20%)	TX (5%)	TX (20%)	ITX (5%)	ITX (20%)	BP (5%)	BP (20%)
Mean	0.60	**1.77**	0.38	0.92	0.64	0.76	0.72	0.54
STD	0.33	0.52	0.32	0.44	0.26	0.20	0.23	0.05
Median	0.52	1.79	0.38	0.99	0.57	0.68	0.71	0.38

Table 5.10. *Mean, STD and median for blue light irradiation screen of reaction in Scheme 5.6 (last step) after 3 hours with various inorganic and one organic photocatalyst and loadings (mol%) performed in DMF (6.67 mM) with a 96-well MTP. Calculated based on product/ISTD ratio at 230 nm and independent of N-methylmaleimide (**11**) equivalents (1 or 3 equiv.).*

	Ir-1 (5%)	Ir-1 (20%)	Ir-2 (5%)	Ir-2 (20%)	Ir-3 (5%)	Ir-3 (20%)	Ru (5%)	Ru (20%)	MMA (5%)	MMA (20%)
Mean	0.52	**2.71**	0	0.06	0	0	0	0	0	0
STD	0.18	1.52	0	0.14	0	0	0	0	0	0
Median	0.60	2.83	0	0	0	0	0	0	0	0

Interestingly, more than one diastereoisomer was detected in these initial screens as another peak also displaying the product mass eluted with a retention time close to the main product peak. The intensities observed were reproducible. Both xanthone and Ir-1 serve as great candidates in further optimisation studies. Hence, we performed a solvent screen.

5.4.1.2 SOLVENT SCREEN

A total of 7 different solvents were selected (iPrOH, *tert*-BuCN, DMSO, MeTHF, ACN, DMA and DMF) in a follow-up investigation again performed in triplicates with either xanthone (UV light irradiation) or Ir-1 (blue light irradiation) in 20 mol% loadings in addition to 1 or 3 equivalents of maleimide (**4**) with 6.67 mM concentration. ISTD was added (0.50 mM) to all reactions and the total volume kept at 150 µL in each well, while a script was used to randomize the positions of the reactions in the 96-well MTPs.

Similar results were obtained for both screening studies (**Table 5.11** and **Table 5.12**). All samples regardless of solvent afforded the product (**12**) to some extent, but the samples with ACN displayed the best product/ISTD ratio across both studies. To our surprise, was the samples with 1 equivalent of maleimide (**4**) comparably better than the ones with 3 equivalents. The samples containing DMSO for the

blue light screen were removed as it skewed the analysis by pulling contaminants from previous samples on the column with the solvent front. With these results, we decided to move into small scale batch testing as catalyst loadings, concentrations and additives could be adequately tested under an inert atmosphere.

Table 5.11. *Mean, STD and median for solvent and N-methylmaleimide (equiv. 1 or 3) screen of reaction in Scheme 5.6 (last step) following 3 hours of UV light irradiation in a 96-well MTP. Conditions: Xanthone PC (20 mol%) and 6.67 mM concentration. Calculated based on product/ISTD ratio at 254 nm.*

	iPrOH 1 equiv.	*t*BuCN 1 equiv.	DMSO 1 equiv.	MeTHF 1 equiv.	ACN 1 equiv.	DMA 1 equiv.	DMF 1 equiv.
Mean	1.24	**2.22**	**1.88**	0.888	**2.27**	0.063	0.308
STD	0.013	0.122	0.021	0.148	0.159	0.045	0.049
Median	1.24	2.30	1.86	0.949	2.20	0.089	0.321

	iPrOH 3 equiv.	*t*BuCN 3 equiv.	DMSO 3 equiv.	MeTHF 3 equiv.	ACN 3 equiv.	DMA 3 equiv.	DMF 3 equiv.
Mean	0.450	**0.825**	**0.748**	0.389	**0.755**	0.074	0.419
STD	0.049	0.052	0.016	0.08	0.046	0.021	0.120
Median	0.446	0.802	0.373	0.405	0.787	0.066	0.488

5.4.1.3 CATALYST LOADING, CONCENTRATION & REACTION TIME

In continuous efforts towards a methodology that could provide us with means of synthesizing an alkaloid-inspired compound library, we thought it best to move away from the open-air plate-based approach, and instead focus on fine-tuning the conditions in an enclosed batch reactor with an inert atmosphere. We therefore, performed a series of reactions in LC-MS vials under argon. Similarly, was all handling of starting materials and solvent performed under argon. The concentrations were 6.67 mM in ACN (total volume 1 mL) with 1 equivalent of maleimide (**4**) and ISTD added (0.50 mM). The chosen photocatalyst was Ir-1 with three different loadings (1, 5 and 20 mol%). We opted to continue with visible (blue) light LEDs over the UV light as it performed slightly better besides the obvious advantage of being more safe and practical in this case. The reactions were continuously sampled (0.5-8 hours) by taking small aliquots with a syringe.

Table 5.12. Mean, STD and median for solvent and N-methylmaleimide (= MMI) screen of reaction in Scheme 5.6 (last step) following 3 hours of blue light irradiation in a 96-well MTP. Conditions: Ir-1 PC (20 mol%) and 6.67 mM concentration. Calculated based on product/ISTD ratio at 254 nm.

Solvent	iPrOH	*t*BuCN	MeTHF	ACN	DMA	DMF
MMI equiv.	1	1	1	1	1	1
Mean	2.39	2.53	**4.16**	**3.91**	2.61	2.36
STD	0.219	1.55	0.48	0.261	0.349	0.320
Median	2.25	3.58	4.34	4.06	2.82	2.20

Solvent	iPrOH	*t*BuCN	MeTHF	ACN	DMA	DMF
MMI equiv.	3	3	3	3	3	3
Mean	0.967	**2.66**	2.16	**3.06**	1.37	1.43
STD	0.089	0.243	0.249	0.069	0.399	0.184
Median	0.919	2.67	2.05	3.04	1.56	1.31

Samples after 2 hours of blue light irradiation displayed reduced intensities for all peaks in the LC-MS chromatograms, while the product peak intensities did not increase after the first sampling (0.5 hours). The mean value for samples of 5 mol% Ir-1 photocatalyst was 1.18, while the 20 mol% loadings comparably performed much better with a mean value of 5.01 when calculating the integrals of product/ISTD at 254 nm for times 0.5-2.0 hours pooled (**Table 5.13**). A 28% increase in product formation was observed when comparing the previous open-air method with this enclosed inert air study in ACN. However, the need for a high catalyst loading for an acceptable conversion still persisted. Loadings of 1 mol% barely afforded any product. It is unclear at this point, why the conversion of starting material to product is incomplete. Extreme care handling all solids and vials under an inert atmosphere was exercised, although a glove box was not employed to rule out concerns of oxygen rapidly quenching the catalyst.

New test reactions were prepared in LC-MS vials following the same reaction conditions, but with 10 and 20 mol% loadings of Ir-1 photocatalyst to test if we could get away with a compromise. Furthermore, the concentration was varied to include 6.67, 25 and 85 mM. It was observed that the sample with a catalyst loading of 10 mol% (product/ISTD, mean = 2.54) afforded approximately twice the product formation compared to the aforementioned 5 mol%, but it did not provide a solution as 20 mol% was still far better (**Table 5.13**). Intriguingly, increasing the reaction concentration to 25 mM or 85 mM seemed to have a positive effect on product formation, but as it is within the margin for instrumental deviation it cannot be concluded as statistically significant. It was noticed that the UV absorbance peak for the maleimide (**4**)

decreased rather rapidly and was completely gone in the 1 hour samples. Sequential addition of an extra equivalent of maleimide (**4**) starting material after 0.5 hours was attempted, but did not result in any significant change.

***Table 5.13**. Mean values for photocatalyst loading and concentration performed in batch under Ar with samples pooled over 0.5-2 hours. Maleimide (**11**) equivalents (1 equiv.) and solvent (ACN). Total volume (1 mL) and ISTD (**4**) added (0.5 mM). Blue light irradiation. Calculated based on product/ISTD ratio at 254 nm.*

	6.67 mM	25 mM	85 mM
Ir-1 (5 mol%)	1.18	-	-
Ir-1 (10 mol%)	2.54	-	-
Ir-1 (20 mol%)	5.01	5.36	**5.60**

5.4.1.4 ADDITIVE SCREEN

To investigate if product formation could be boosted or the catalytic activity sustained, a range of additives (AcOH, p-TsOH, TEA, DIPEA, DBU, TEMPO and NMO) in 1 or 2 equivalents were screened together with the current optimized reaction conditions with 85 mM concentration. As we did not have much catalyst in stock, and wanted to see if we could boost an otherwise poor reaction, we decided to run the screen with only 5 mol% and a total volume of 25 µL, but still in triplicates for statistical power. A dilution step was necessary prior to analysis as we were concerned if lowering the needle of the autosampler would collide with the bottom of the glass MTP and cause irreversible damage.

Reactions with DBU or TEMPO displayed significantly better means compared to other samples with or without additives (Table 5.14). Hence, an incredible 54% or 45% increase in product formation was observed, respectively. Furthermore, the UV absorbance spectra were very clean without the noisy baseline that was seen for samples without additives (Table 5.14 and Table 5.15). For comparison, was a few reactions without photocatalyst screened, but still with the two aforementioned additives, which resulted in the same clean spectra, but also no product formation observed (Table 5.14b). This may suggest that the baseline noise derives from either the photocatalyst or the product possibly being photodegraded. Both DBU and TEMPO displayed a stabilizing effect on the starting material olefin (10) that remained high, while samples with DBU also had the maleimide (11) peak present. Samples with NMO resulted in the product peak splitting into two diastereoisomers. Other additives or using 2 equivalents instead of 1 had no further positive effects.

Table 5.14. *Mean, STD and median for additive (1 or 2 equiv.) screen of reaction in Scheme 5.6 (last step) following one hour of blue light irradiation in a 96-well MTP. Conditions: Ir-1 PC (5 mol%) and 85 mM concentration. Calculated based on product/ISTD ratio at 254 nm. Asterisk (*) = without PC. Only a representative of additives tested are displayed. DIPEA = diisopropylethylamine, DBU = 1,8-diazabicyclo[5.4.0]undec-7-ene, TEMPO = (2,2,6,6-tetramethyl-piperidin-1-yl)oxyl and NMO = N-methylmorpholine-N-oxide.*

	No additive	DIPEA 1 equiv.	DIPEA 2 equiv.	DBU 1 equiv.	DBU 2 equiv.
Mean	0.996	0.94	1.12	**1.53**	**1.46**
STD	0.096	0.048	0.079	0.016	0.065
Median	0.938	0.917	1.08	1.53	1.49

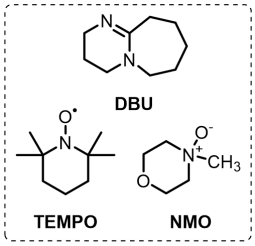

	TEMPO 1 equiv.	TEMPO 2 equiv.	NMO 1 equiv.	NMO 2 equiv.	*TEMPO 1 equiv.	*DBU 1 equiv.
Mean	**1.44**	**1.44**	0.966	0.978	0	0
STD	0.011	0.004	0.033	0.044	0	0
Median	1.44	1.43	0.967	0.971	0	0

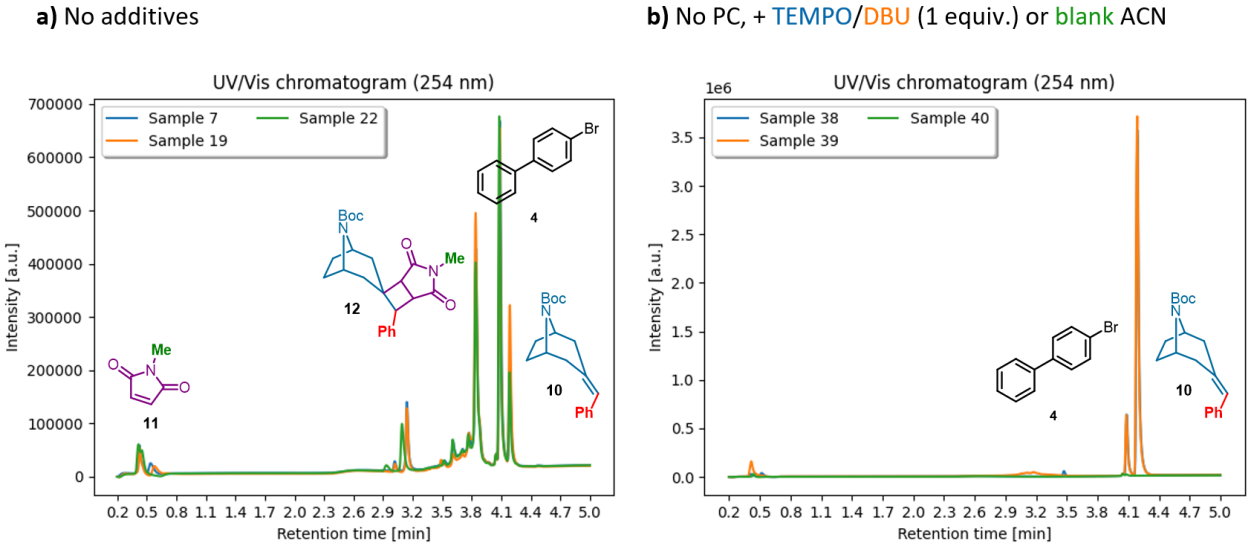

Figure 5.14. *Representative samples of the additive screen a) without additives (triplicate) and b) without PC, but with additives. PC = photocatalyst, DBU = 1,8-diazabicyclo[5.4.0]undec-7-ene and TEMPO = (2,2,6,6-tetramethyl-piperidin-1-yl)oxyl.*

a) + DBU (1-2 equiv.)

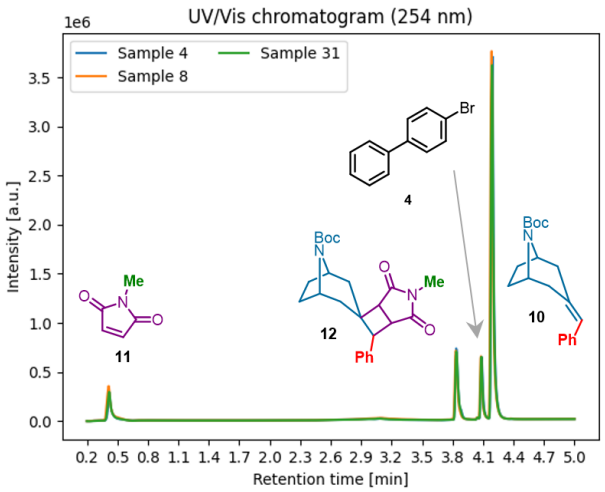

b) + TEMPO (1-2 equiv.)

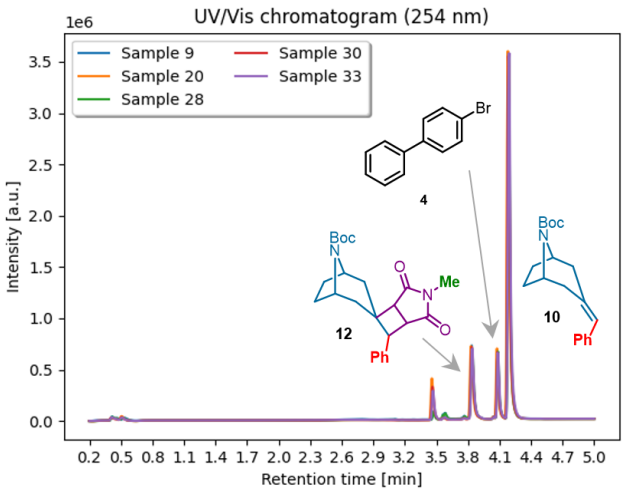

***Figure 5.15**. Representative samples of the additive screen a) with 1 equiv. (sample 4 and 31) and 2 equiv. (sample 8) DBU and b) with 1 equiv. (sample 9 and 28) and 2 equiv. (sample 20, 30 and 33) TEMPO. DBU = 1,8-diazabicyclo-[5.4.0]undec-7-ene and TEMPO = (2,2,6,6-tetramethyl-piperidin-1-yl)oxyl.*

5.4.1.5 WHITE LIGHT SCREEN

One option we still had not explored was the intensity of the blue light, or simply irradiating the samples under white light. As both of these methods provide the means to induce photoexcitation of the iridium triplet sensitizer under more mild conditions, we anticipated less photodegradation of the catalyst, and hence more product formation. Batch reactions were set up in vials under an inert atmosphere with ACN (190 µL, 85 mM) and Ir-1 (5 mol%) in addition to 1 equivalent of both *N*-methylmaleimide (**11**) and DBU. The vials were exposed to either blue (50% or 100% intensity) or white light (100% intensity) (**Table 5.15**).

No effect was observed from reducing the intensity of the blue LEDs (sample 1-3 in **Table 5.15**), despite not having converted all the starting material. However, exposing the samples to white light instead of blue produced a significant change that could be repeated (sample 4-5 in **Table 5.15**). Furthermore, a trend was observed where product formation increased over time, but also at the expense of one presumable diastereoisomer over another, while the starting material peak for the tropinone-derived olefin (**10**) gradually decreased (**Table 5.16a-b**). As the product peaks overlap accurate quantification of product ratio is not possible, but an estimate is given. It is likely that one diastereoisomer is degrading, while another is forming with prolonged irradiation time, but other factors cannot be excluded. All spectra regardless of light setup were once more very clean with little to no baseline noise supporting the use of DBU as an additive.

Table 5.15. Overview of samples performed in batch under an inert atmosphere of reaction in Scheme 5.6 (last step). Values are manually integrated at 254 nm. P = product, SM = starting material, ISTD = internal standard and MMI = N-methylmaleimide. P ratio indicates the ratio (estimate) between two diastereoisomers. Standard method: 190 µL ACN, 85 mM, 1 equiv. MMI, 1 equiv. DBU, 5 mol% Ir-1, blue LED set at maximum intensity.

Sample	P/ISTD	P Ratio	SM/ISTD	Modifications to standard method	Time-point (h)
Blue light experiments					
1	0.581	-	4.46	-	0.25
1	0.569	-	4.46	-	0.50
2	0.578	-	4.37	2 equiv. MMI	0.25
2	0.518	-	3.93	2 equiv. MMI	0.50
3	0.527	-	3.90	50% Light intensity	0.25
3	0.563	-	4.28	50% Light intensity	0.50
3	0.569	-	4.55	50% Light intensity	1.0
White light experiments					
4	0.790	-	4.20	White light, 100% light intensity	0.25
5	0.756	-	3.86	White light, 100% light intensity	0.25
5	0.775	-	3.84	White light, 100% light intensity	0.50
5	0.848	90:10	4.21	White light, 100% light intensity	1.0
5	0.937	74:26	3.75	White light, 100% light intensity	1.5
5	0.988	69:31	2.79	White light, 100% light intensity	2.0
5	1.05	61:39	1.87	White light, 100% light intensity	2.5
5	1.10	56:44	1.06	White light, 100% light intensity	3.0
5	1.15	41:49	0.430	White light, 100% light intensity	3.5
5	1.15	34:66	0.126	White light, 100% light intensity	4.0
5	0.997	28:72	0.066	White light, 100% light intensity	4.5
6	0.478	72:28	4.48	White light, 100% light intensity, DMSO solvent	0.25
6	0.417	67:33	4.58	White light, 100% light intensity, DMSO solvent	0.50
6	0.420	59:41	4.54	White light, 100% light intensity, DMSO solvent	1.00
6	0.424	58:42	4.52	White light, 100% light intensity, DMSO solvent	1.50

a) White light experiments, + DBU (1 equiv.) **b)** Zoom-in of product peaks

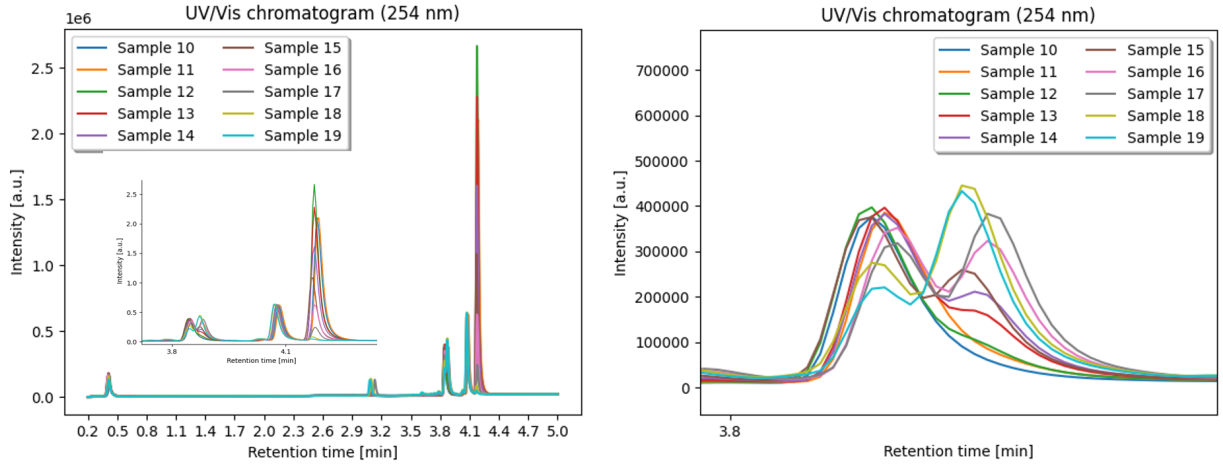

*Figure 5.16. UV absorbance spectra at 254 nm for the white light screen. a) Samples 10-19 correspond to sample 5 (times 0.25-4.5 hours, respectively) in Table 5.15 where reaction conditions can also be found. b) Zoom-in. DBU = 1,8-diazabicyclo-[5.4.0]undec-7-ene. Retention times: Product (**12**) = 3.85-3.90 min, ISTD (**4**) = 4.10 min and SM (**10**) = 4.20 min.*

5.4.1.6 SCALE-UP & CHARACTERIZATION

After substantial screenings had led to clean UV-vis chromatograms with increased conversion, we decided to scale-up the reaction in batch and isolate the spirocyclobutane compound (**12**). In this context, two different reactions were conducted with 150 µmol (45 mg material) of the tropinone-derived alkene (**10**) and either blue or white LEDs (**Scheme 5.7**). The reaction facilitating photoexcitation with blue LEDs was performed prior to the discovery of DBU as an additive.

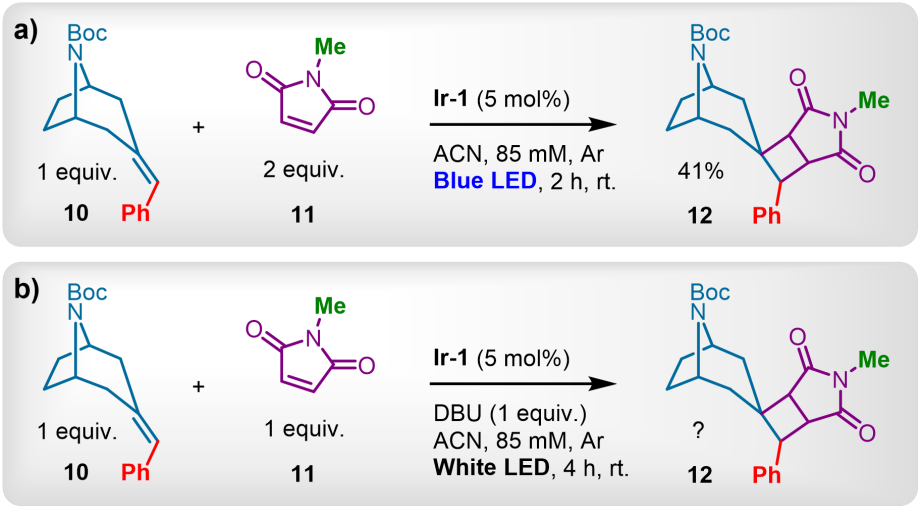

*Scheme 5.7. Scale-up in batch and isolation of the alkaloid-inspired spirocyclobutane compound (**12**).*

The reaction performed under blue LEDs (Scheme 5.7a) could have been stopped already after 15 minutes as no more conversion was observed thereafter, but starting materials still decreased in intensity by LC-MS. While isolating the product with flash column chromatography, it was noticed that the Ir-1 photocatalyst eluted early, but also tailed heavily likely caused by its decomposition on silica. A slow gradient is therefore necessary to not have the compound of interest co-elute with degraded fragments originating from the catalyst. Both fractions comprising a mixture of three diastereoisomers in addition to fractions containing only a single but different diastereoisomer were collected. Unfortunately, a side-product was observed upon analysing the NMR spectra of the supposedly pure fractions where *N*-methylmaleimide (11) had undergone a homo-coupling to produce a dimer (13), which co-eluted with the otherwise pure fractions. This side-product cannot be detected by standard methods like TLC or LC-MS as it is not UV active in the detection range, hence subsequent reactions should have the equivalents of maleimide used lowered. A solution could also be to use maleimides less prone to dimerization or see if it can be monitored by GC-MS.

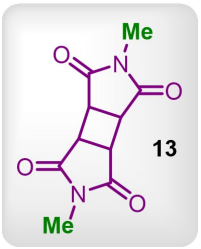

A reaction employing the most optimized reaction condition with DBU (1 equivalent) as additive, lowered amount of maleimide (1 equivalent) and white LEDs was performed once (Scheme 5.7b), but the purification unfortunately failed and the compound was only isolated with enough material to run an LC-MS, which confirmed the product. This will have to be repeated to confirm that the new conditions are favoured.

5.5 CONCLUSION

A semi-automated photochemical screening platform was established from low-cost resources given access to an LC-MS instrument that can read MTPs was already acquired for different screening purposes. The platform was tested and validated employing a reported photochemical reference reaction from the literature (Scheme 5.3 and Scheme 5.4).[199] Both in- and between plate validations were conducted that concluded no statistical significance with respect to neither well-position nor plate-to-plate preparation (Figure 5.10). The performance stability of the LC-MS instrument was also tested where it was observed with multiple injections of the same sample containing an internal standard that up to a 12-18% deviation or difference may occur between the two extremes (minimum and maximum) in the series tested (Table 5.7). Various screens were carried out exploiting the platform to optimize the reference reaction conditions, and the results implied changing the solvent from 1,4-dioxane to THF in order to afford increased product formation, supported by statistical calculations performed on the experimental data (Table 5.2). The screens further suggested that the concentration should be lowered from 80 mM to 40 mM, and that the toxic 4,*N,N*-trimethylaniline starting reagent added in large excess could possibly be reduced from 7 equivalents to 3 equivalents without impacting product formation (Table 5.4). As employing 7 equivalents constitutes a high economic cost besides a safety hazard with the compound being relatively toxic, methods to decrease the stoichiometric amounts needed are favourable.

With the platform established and validated, we exploited it to expedite the discovery of new photochemical transformations. Hence, a photochemical [2+2] cycloaddition reaction (Scheme 5.6) was screened against numerous reaction parameters including photocatalyst, loadings, solvent, stoichiometry, concentration, additives and light-source with the aim of developing a method intended for the synthesis of an alkaloid-inspired spirocyclobutane-containing compound library (Scheme 5.5). The natural product-like compounds in this library are expected to display favourable drug-like properties given their 3-dimensional structures. After hundreds of different reaction conditions were screened in MTPs in triplicates or higher, the reaction conditions with the greatest success of product formation were discovered (Scheme 5.7). Among these was the unexpected surprise of DBU in 1 equivalent as an additive, which afforded neat reactions with vastly improved baseline noise (Figure 5.15a). White light also seemed to outcompete blue light irradiation (Table 5.15), but remains to be validated in a scale-up experiment. However, at an earlier stage of the optimization process, the spirocyclobutane product (12) was isolated in 41% yields (samples with mixed diastereomeric ratio combined) from a batch experiment to confirm the correct structure upon characterization. This platform greatly complements the classical one-at-a-time batch approach for non-trivial optimization studies where more than a few parameters are to be tested.

5.6 FUTURE PERSPECTIVES

In addition to validating the most optimized reaction conditions (**Scheme 5.7b**) by isolating the product without the maleimide dimer and in greater yields, further investigations to elucidate the ratio in which the different stereoisomers are formed is a priority to decipher. In this context, the most convenient method would be to measure crude NMR and compare the integrations to samples containing isolated pure material. Subsequently, the synthesis of a 3d rich spirocyclobutane-containing compound library is of interest. The library will consist of tropinone- (**7**) and quinuclidinone-derived (**8**) fragments combined with various maleimides or other cyclic alkenes that can be excited by the triplet sensitizer for photochemical [2+2] cycloaddition reactions to further increase the scope (**Scheme 5.8**). A structure-activity relationship (SAR) study based on the screening data for biological activity will guide which compounds that are of further interest to chemically modify. Several functionalisation sites exist due to the way the library was designed, and includes deprotecting the *tert*-butoxycarbonyl (boc) group to deliver a reactive secondary amine, modifying the ester functional group or exploiting the chemical handles incorporated via the maleimides. All the tropinone-derived alkenes in addition to the Wittig product with an ester group on the quinuclidinone-derived alkene have been prepared already by employing the standard conditions illustrated in the scheme. Photochemical cycloaddition reactions with the tropinone-derived alkene having a proton in place of the phenyl or ester group, further simplifies the task of deciphering what stereoisomers are formed as the number of potential stereoisomers in the product is reduced. The photochemical screening platform developed herein may also be applied for accelerated discovery of other photochemical or thermal transformations related to other projects in the research group.

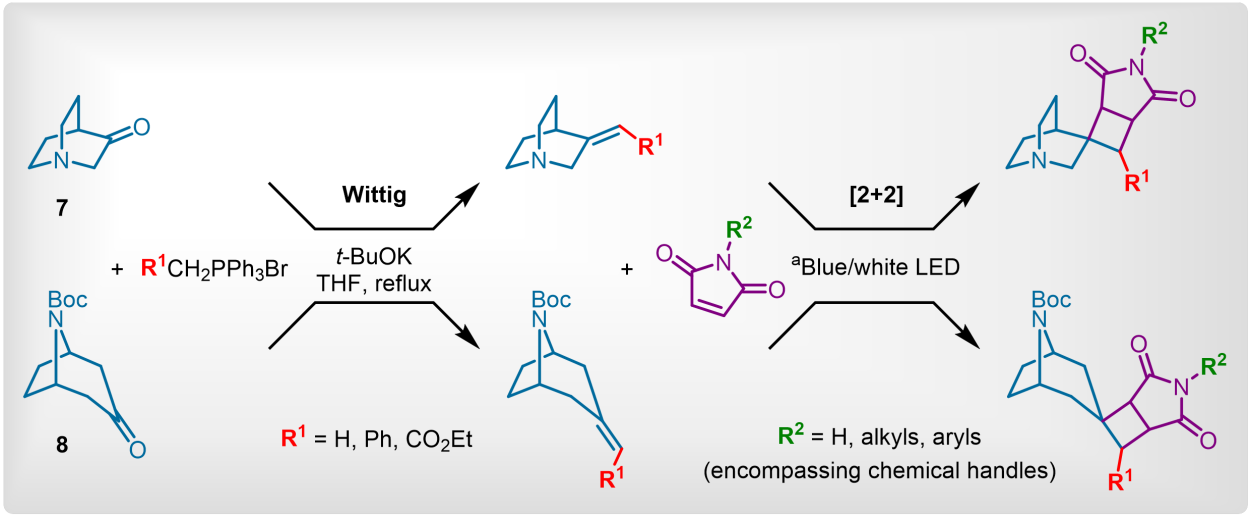

[a]Ir-1 (5 mol%), 85 mM maleimide (1 equiv.), ACN, Ar, rt.

Scheme 5.8. *General scheme for targeting an alkaloid-inspired spirocyclobutane-containing compound library. Encompassing chemical handles will facilitate multiple functionalisation sites for further SAR studies.*

5.7 EXPERIMENTAL

General directions
See Section 3.5 Supporting Information for further details not described here.

Photochemical reactions in batch
All solids were carefully weighed out under a flow of argon. To this, a glass funnel was attached to an argon line via a tube and directed down towards the flask and reagent containers (SI Figure 5.1a). A schlenck-line technique with argon was performed prior to adding degassed solvent to the vial equipped with magnetic stir bar and a balloon with argon (SI Figure 5.1b-e). Both vials and magnets were oven-dried overnight. Light source and fan are the same as for plate screens. Vials were parafilmed and aliquots sampled using a syringe under a positive pressure of argon.

Preparation of stock solutions
Dry solvents of HPLC grade and reagents were purchased from commercial suppliers and used without further purification. Solvent (DMSO, DMF, IPA, ACN and THF) were obtained from a PureSolv Micro Solvent Purification System. Stock solutions with were prepared in an open atmosphere.

Dispensing, sealing, and MTP details
Stock solutions and solvents were dispensed manually with a single- or multi-channel pipette (Thermo Scientific Finnpipette F2, Biohit mLine M1000 or M20) and mixed directly into a 96-well MTP in an open atmosphere. The script "Randomise_plate.py" was applied where specified to randomise the positions of the samples in the MTP. The total sample volume in each well was either 150 µL or 300 µL, unless stated otherwise. The 96-well MTPs applied were single-use polypropylene plastic plates (v-bottom, chimney well, 14.6 x 85.5 x 127.8 mm) from Greiner Bio-One or a re-usable glass plate reactor (standard, 15 x 85 x 127 mm, cat. no. 3600500) from Zinsser Analytic made from special high purity and temperature resistant borosilicate glass. MTPs were sealed with 4titude optical clear heat seals (125 x 78 mm, 4ti-0541 from swab.dk) using a MicroTS (SN 958-1276) plate sealer for 10 seconds.

Light irradiation - plate setup
Sealed plates were reacted under blue- or UV light setups, as shown in figure Figure 5.2a and Figure 5.2b, respectively. For reactions conducted under blue light irradiation, a 50 W LED floodlight lamp (IP65 from Amazon.de) was applied and set to blue with maximum intensity. The distance between the light source and plate was 4 cm. Cooling of the plate was done with either a Satzuma USB 5 V desktop fan or a Goobay fan (cat. no. 20737 from AcXperten.dk). The centre of the MTP was prioritized, if the full plate was not used. For reactions conducted under UV light irradiation, a Nailstar professional 4 x 9 W lamp (NS-01-UK&EU from Amazon.de) with peak 365 nm wavelength was applied. The plate was positioned in the middle of the UV chamber. Note that the UV chamber automatically turns off every 30 minutes. Cooling was carried out with a Goobay fan.

LC-MS analysis - plate setup
LC-MS analysis of 96-well MTPs were acquired on an LC-MS-8045 from Shimandzu equipped with a photodiode array detector and a triple quadrupole mass spectrometer. A Kinetex C18 column (d 2.6 µm, 100 x 2.1 mm) equipped with a security guard (ULTRA Cartridges and Holder) from Phenomenex were applied. In this setup reverse-phase LC was applied, with a flow rate of 0.6 mL/min. Eluents A (H_2O with 0.1% HCO_2H) and B (ACN with 0.1% HCO_2H) were used with the following 5 minute LC method: 5% B for the first 1.25 min, linear gradient (5% B to 50% B) from 1.25 min to 2.00 min, hold for 0.25 min at 50% B,

another linear gradient (50% B to 100% B) from 2.25 min to 3.00 min, hold for 1.00 min at 100% B and then linear gradient (100% B to 5% b) from 4.00 min to 4.50 min, 5% B was held for 0.50 min. The acquisition time interval was from 0.2 minutes to 5.0 minutes. Autosampler temperature was 16°C. Injection volume varied between 1, 2, 4, and 5 µL. MS detection was performed in both positive and negative ionisation mode with a secondary electron multiplier detector. Mass spectra were recorded in the m/z range 100-1000. Absorption wavelengths are reported in nm and are measured in the range 190-700 nm or 210-700 nm.

Blank runs both before and after screening a MTP is recommended.

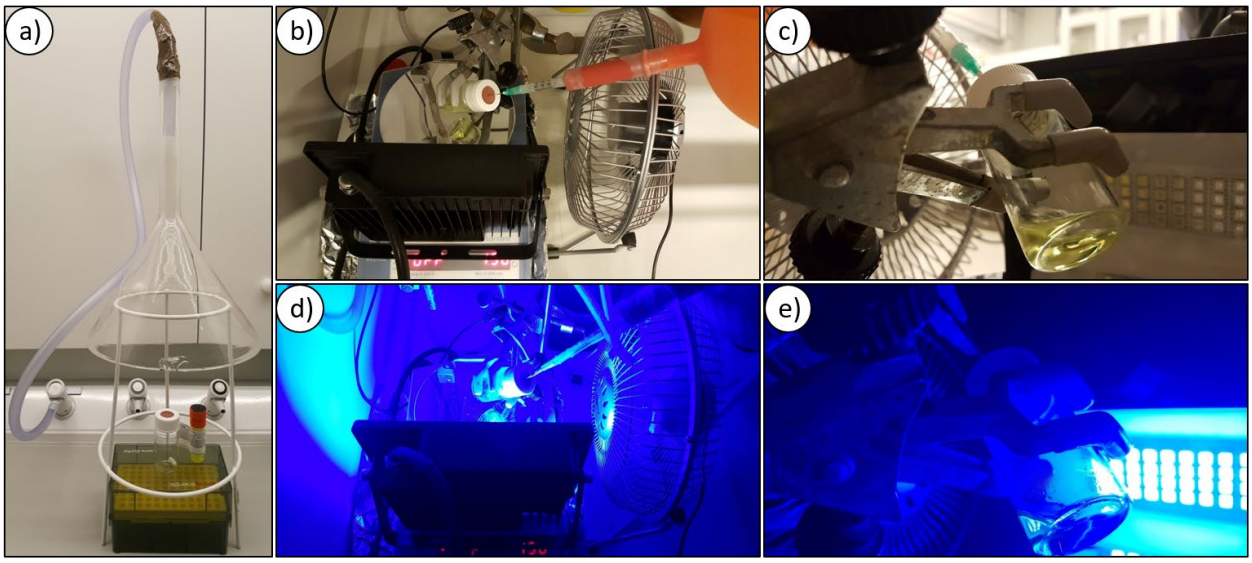

SI Figure 5.1. *Procedure for photochemical batch reactions. a) Preparation of solids under argon atmosphere. b-c) Reaction setup with the LEDs turned off and d-e) turned on.*

Specific reaction procedures

Benzyltriphenylphosphonium bromide (9)

Following the procedure by reference.[201]

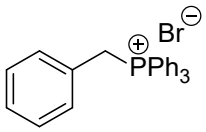

In a pressure vessel fitted equipped a magnetic stir bar were dissolved benzylbromide (347 µL, 2.92 mmol, 1 equiv.) and triphenylphosphane (843 mg, 3.22 mmol, 1.1 equiv.) in chloroform (10 mL). A nitrogen atmosphere was introduced and the vessel capped and heated under stirring at 70°C for 4.5 hours. The solution was cooled and concentrated under reduced pressure by rotary evaporation. The remaining residue was triturated from Et_2O, filtered and dried under high vacuum affording the title compound as a white solid (67% yields). This material was used in the next step as such, without further purification.

LC-MS (ESI) $[M+H]^+$ *m/z* calcd for $C_{25}H_{23}P^+$: 354.1526, *m/z* found: 354.2 $[M+H]^+$

A commercial sample of the same compound afforded the same LC-MS spectrum and mass $[M+H]^+$

tert-Butyl (1R)-3-((Z)-benzylidene)-8-azabicyclo[3.2.1]octane-8-carboxylate (10)

Following the procedure by reference.[201]

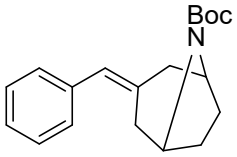

To an oven-dried microwave vial equipped with a magnetic stir bar were added benzyltriphenylphosphonium bromide (**9**) (1.07 g, 2.47 mmol, 1 equiv.) and potassium *tert*-butoxide (277 mg, 2.47 mmol, 1 equiv.) to anhydrous THF (4 mL. The vial was capped and the suspension stirred under an argon atmosphere for 2 hours at ambient temperature in which the solution turned vivid orange. A solution of *N*-boc-nortropinone (500 mg, 2.22 mmol, 0.9 equiv.) in anhydrous THF (2 mL, 0.370 M) was added over 5 min and the reaction mixture heated at 75°C for 12 hours under stirring in an argon atmosphere. Demineralized water (15 mL) was added and the aqueous phase extracted with Et_2O (3 x 15 mL). The combined organic extracts were dried under anhydrous Na_2SO_4, filtered and concentrated under reduced pressure by rotary evaporation. Purification by flash column chromatography on silica gel (1:9 EtOAc/*n*-hexane) afforded the title compound as a white solid (464 mg, 63%).

The data is in accordance with previously reported work.[205]

$[M+H]^+$ *m/z* calcd for $C_{19}H_{26}NO_2^+$: 300.1958

TLC: R_f = 0.38 (1:6 EtOAc/*n*-hexane)

^{1}H NMR (400 MHz, $CDCl_3$): δ 7.36 – 7.28 (m, 2H), 7.24 – 7.14 (m, 3H), 6.46 – 6.40 (m, 1H), 4.30 (dt, *J* = 6.3, 2.7 Hz, 1H), 4.19 (dt, *J* = 6.5, 3.1 Hz, 1H), 2.80 – 2.67 (m, 1H), 2.67 – 2.56 (m, 1H), 2.52 – 2.40 (m, 1H), 2.21 – 2.11 (m, 1H), 1.96 – 1.78 (m, 2H), 1.73 – 1.63 (m, 1H), 1.50 (s, 9H), 1.48 – 1.40 (m, 1H).

^{13}C NMR (101 MHz, $CDCl_3$): δ 153.7, 137.7, 135.8, 129.0, 128.7, 128.3, 126.4, 79.4, 54.5, 54.0, 42.7, 36.1, 28.7, 28.6, 28.3.

tert-Butyl 3-methyl-2,4-dioxo-7-phenyl-3,8'-diazaspiro[bicyclo[3.2.0]heptane-6,3'-bicyclo[3.2.1]octane]-8'-carboxylate (12)

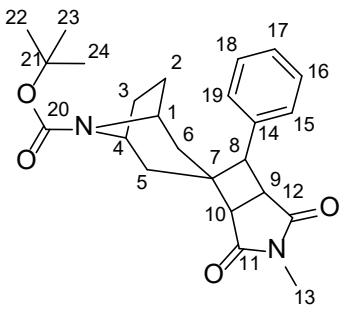

A solution of alkene (**10**) (44.9 mg, 150 µmol, 1 equiv.), *N*-methylmaleimide (**11**) (33.3 mg, 300 µmol, 3 equiv.) and $[Ir(dF(CF_3)ppy)_2(dtbbpy)]PF_6$ (**Ir-1**) (8.41 mg, 7.5 µmol, 0.05 equiv.) was irradiated with blue light in ACN (1.77 mL, 85 mM) for 2 hours. The solution was concentrated under reduced pressure by rotary evaporation. Purification by flash column chromatography on silica gel (1:4 EtOAc/DCM) afforded the title compound as a white solid (25.1 mg, 41%).

TLC: R_f = 0.25 (1:4 EtOAc/DCM)

LC-MS (ESI) $[M+H]^+$ *m/z* calcd for $C_{24}H_{31}N_2O_4^+$: 411.2279, *m/z* found: 411.1 $[M+H]^+$
R_f: 2.76 min (total run time: 5 min)

^{1}H NMR (400 MHz, $CDCl_3$): δ 7.35 – 7.28 (m, 3H, **H-14-19**), 7.06 – 6.93 (m, 2H, **H-14-19**), 4.29 – 4.19 (m, 1H, **H-1/4**), 3.94 (d, *J* = 11.0 Hz, 1H, **H-8**), 3.91 – 3.81 (m, 1H, **H-1/4**), 3.64 (dd, *J* = 11.0, 7.0 Hz, 1H, **H-9**), 3.06 (s, 3H, **H-13**), 2.95 (d, *J* = 7.0 Hz, 1H, **H-10**), 2.40 – 2.28 (m, 1H, **H-5/6**), 2.28 – 2.21 (m, 1H, **H-5/6**), 2.07 (dd, *J* = 14.9, 3.8 Hz, 1H, **H-5/6**), 2.00 – 1.91 (m, 1H, **H-5/6**), 1.77 (tdd, *J* = 12.5, 7.7, 4.2 Hz, 1H, **H-2/3**), 1.67 – 1.57 (m, 1H, **H-2/3**), 1.45 (s, 9H, **H-22-24**), 1.35 – 1.27 (m, 1H, **H-2/3**), 0.25 (ddd, *J* = 13.2, 9.3, 4.1 Hz, 1H, **H-2/3**).

^{13}C NMR (101 MHz, $CDCl_3$): δ 177.4 (**C-11/12**), 174.9 (**C-20**), 137.1 (**C-14**), 129.6 (**C-15-19**), 128.9 (**C-15-19**), 128.2 (**C-15-19**), 79.6 (**C-21**), 54.8 (**C-8**), 52.9(**C-1/4**), 52.4 (**C-1/4**), 49.2 (**C-10**), 48.7 (**C-5/6**), 42.9 (**C-7**), 40.7 (**C-9**), 31.1 (**C-5/6**), 28.6 (**C-22-24**), 26.2 (**C-2-3**), 24.9 (**C-13**).

Note: Dimerization side-product of *N*-methylmaleimide (**11**) integrating 0.33 is present in the NMR spectra.

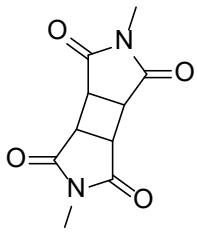

Not previously reported in the literature by NMR spectroscopy in $CDCl_3$.

^{1}H NMR (400 MHz, $CDCl_3$): δ 3.40 (s, 4H), 3.10 (s, 6H)
^{13}C NMR (101 MHz, $CDCl_3$): δ 176.7, 41.6, 25.9.

Note: The reported yields is with the dimer impurity included in addition to another sample containing the product (13 mg) with *d.r.* 1:0.37:0.24 calculated by integrating the proton signals from the *tert*-butyl group.

Nuclear magnetic resonance spectroscopy

^{1}H NMR, ^{13}C NMR

tert-Butyl (1R)-3-((Z)-benzylidene)-8-azabicyclo[3.2.1]octane-8-carboxylate (10)

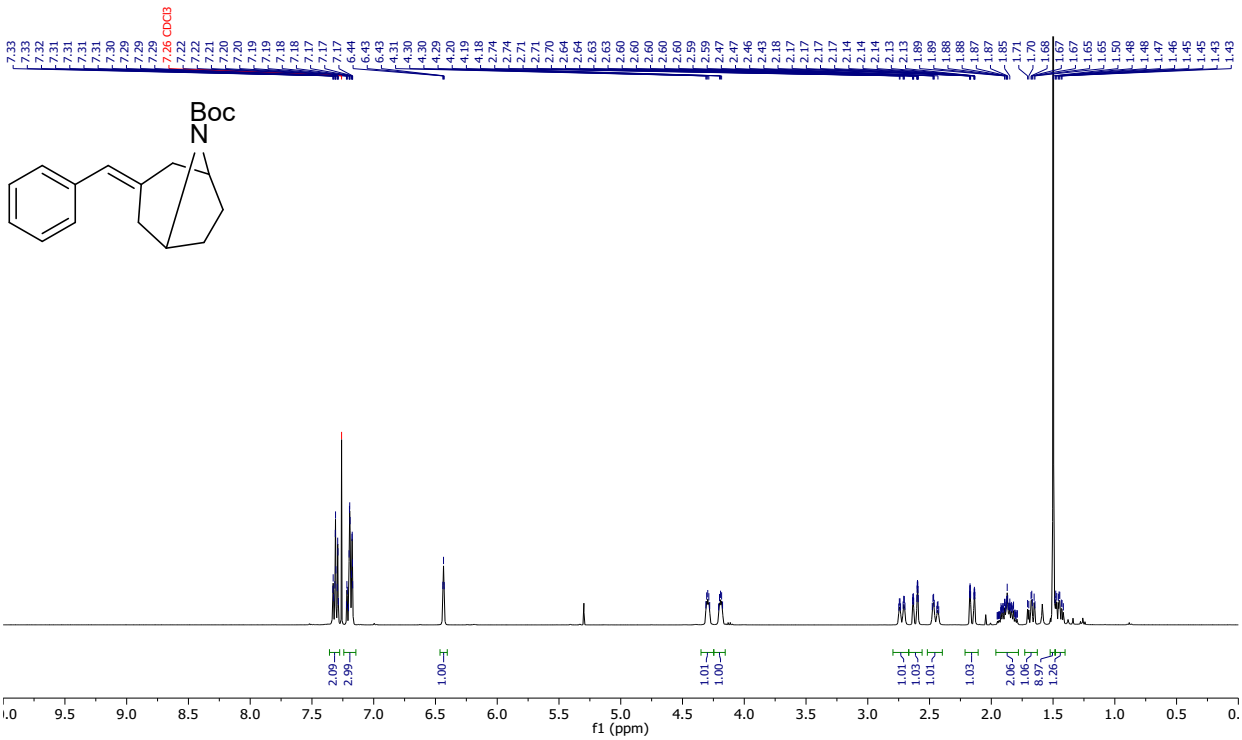

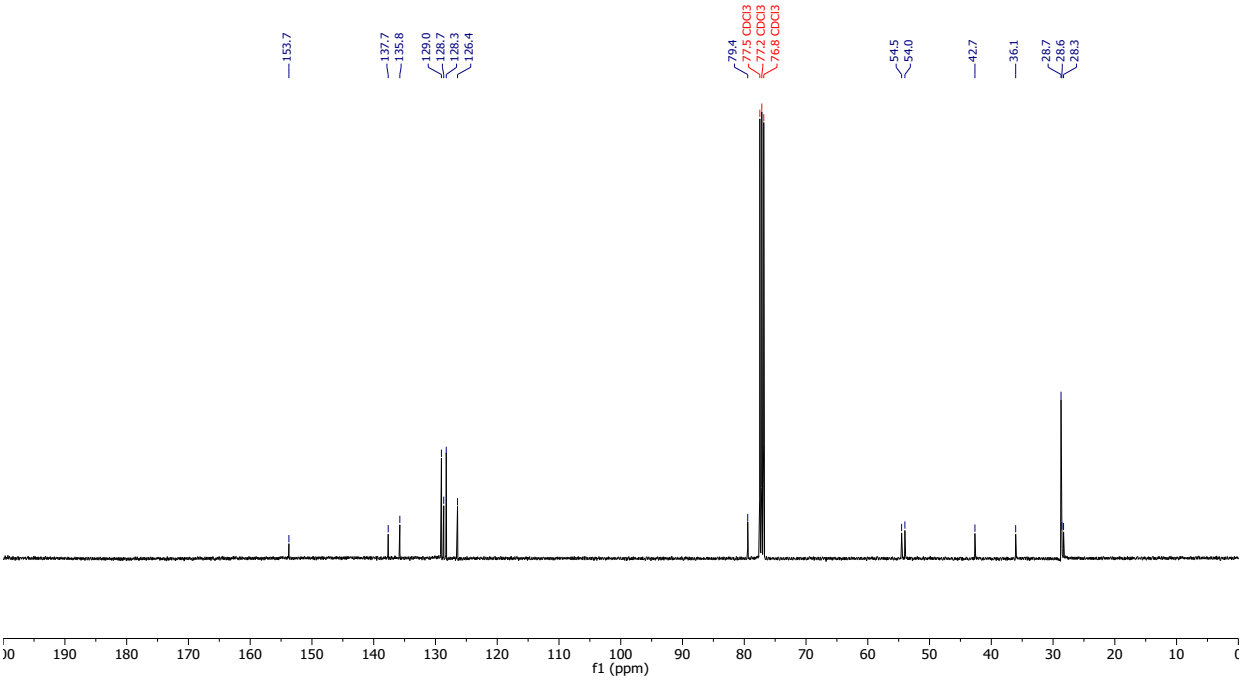

tert-Butyl 3-methyl-2,4-dioxo-7-phenyl-3,8'-diazaspiro[bicyclo[3.2.0]heptane-6,3'-bicyclo[3.2.1]octane]-8'-carboxylate (12)

^{1}H NMR, ^{13}C NMR

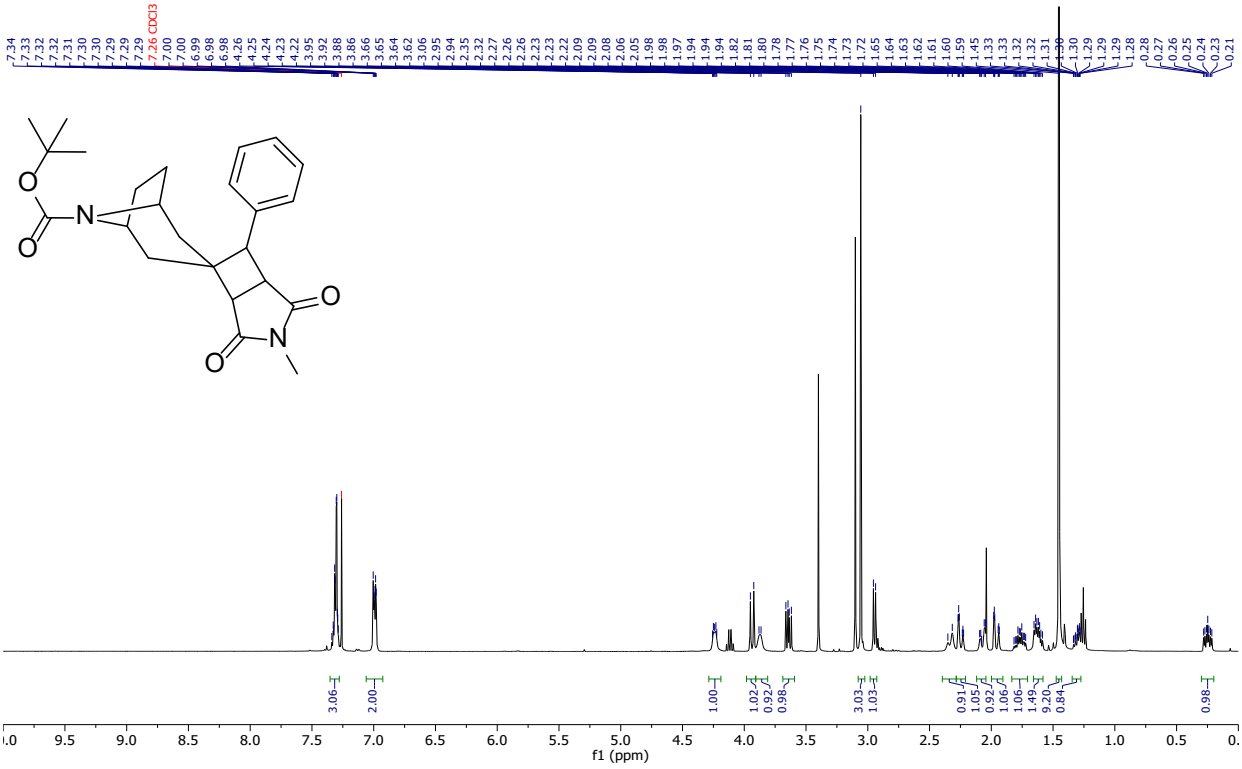

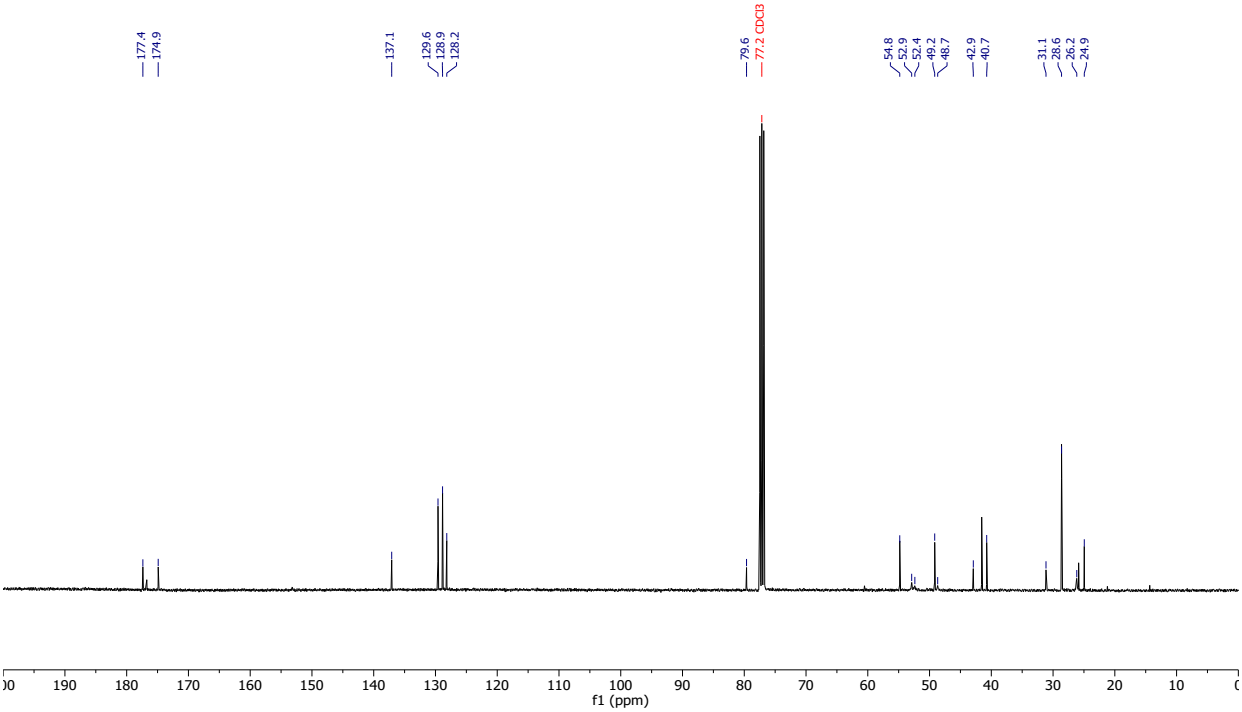

5.8 APPENDIX A

```
# MAIN SCRIPT
# User-inputs are labeled with '# Input'

#%% Data mining
### Import packages
import os
import numpy as np

### Set up path
# Define path to common folder containing all scripts and all plate
folders
path = ('/OneDrive/DTU/MSc_project/HTE_analysis_tool') # Input
os.chdir(path)

### Insert plate number(s) in plate-vector
plates = [1,2,3] # Input

### Remove extra numbering from files (if present)
# Import functions from 'Data_mining.py'
from Data_mining import remove_xxx_from_filename, move_files, load_data
# Remove xxx from filename
#for P in plates:
#    remove_xxx_from_filename(P, path)

### Arrange files in folders
# Create folder and move files
for P in plates:
    move_files(P, path)

### Import data
# Define empty dictionary
data = {}
# Import data from selected plate(s)
for P in plates:
    data['Plate_{}'.format(P)] = {}
    load_data(P, path, data)
    print('Data from plate {} loaded.'.format(P))

### Create tensors
# Set path
os.chdir(path)
# Import function from 'Tensor.py'
from Tensor import tensor_generator
# Generate tensors
for P in plates:
    vars()['P{}_UV_tensor'.format(P)],
vars()['P{}_MS_pos_tensor'.format(P)],
vars()['P{}_MS_neg_tensor'.format(P)] = tensor_generator(P, data, path)

# Set directory to main folder.
os.chdir(path)
```

```
#%% Integration

### Import functions from 'Integration.py'
from IntegrationKopi import calculate_UV_integrals, conversion_product,
conversion_starting_material

P = 1 # Input
wavelength = 254 # Input, see comments below.
# If wavelength=-1, UV integrals is calulated based on all wavelengths.
# If wavelength≠-1, UV integrals are calculated based on one specific
wavelngth, closet to the input value.

# Find integrals for plate P
vars()['P{}_peak_information'.format(P)] = calculate_UV_integrals(P,
wavelength, vars()['P{}_UV_tensor'.format(P)], data)

# Define retention times
RT_ISTD = 4.1 # Input
RT_product =3.3 # Input
RT_SM = 0.45 # Input
# It is possible to search for two starting materials by running the
script two times and change RT_SM to RT_SM1 and RT_SM2 etc.
# Remember to change in line 68 as well, e.g. P{}_conversion_SM1 and
RT_SM1.

# Calculate conversion of product, based on retention times.
vars()['P{}_conversion_product'.format(P)] = conversion_product(P,
wavelength, RT_ISTD, RT_product, vars()['P{}_peak_information'.format(P)],
data)

# Calculate conversion of starting material, based on retention times.
vars()['P{}_conversion_SM'.format(P)] = conversion_starting_material(P,
wavelength, RT_ISTD, RT_SM, vars()['P{}_peak_information'.format(P)],
data)

#%% Visualisation of data
### Description of the different visualisation functions:
# UV_chromatogram: Plots intensity as a function of retention time for one
or more samples.
# UV_plot_specific_wavelength: Plots intensity as a function of retention
time for one or more samples at one specific wavelength.
# MS_chromatogram: Plots intensity as a function of retention time for one
or more samples.
# MS_spectrum: Plots intensity as a function of m/z-values for one or more
samples at one rentention time.
# heatmap_UV_sample: UV heatmap for one sample.
# heatmap_UV_RT: UV heatmap for one retention time.
# heatmap_UV_wavelength: UV heatmap for one wavelength.
# heatmap_MS_sample_binned: MS heatmap for one sample with binned m/z-
values.
# heatmap_MS_RT_binned: MS heatmap for one retention time with binned m/z-
values.
# heatmap_MS_mz: MS heatmap for one m/z-value.
```

```
# It is recommended to generate the plots one by one.

### Import visualisation functions from 'Visualisation.py'
from Visualisation import UV_chromatogram, UV_plot_specific_wavelength,
MS_chromatogram, MS_spectrum, heatmap_UV_sample, heatmap_UV_RT,
heatmap_UV_wavelength, heatmap_MS_sample_binned, heatmap_MS_mz,
heatmap_MS_RT_binned

### Select plate
P = 1 # Input

###### 2D plots ######
## UV chromatogram
samples = [1,2,3,4,5] # Input, select sample(s) of interest
UV_chromatogram(samples, P, vars()['P{}_UV_tensor'.format(P)], data)

## UV plot for one specific wavelength
samples = [8,11] # Input, select sample(s) of interest
# If all samples should be selected run the code below
# samples = np.arange(1, np.shape(UV_tensor)[0]+1) # Input, select all
samples
wavelength = 254 # Input, select wavelength
UV_plot_specific_wavelength(samples, P, wavelength,
vars()['P{}_UV_tensor'.format(P)], data)

## MS(+/-) chromatogram
samples = [1,2,3,4] # Input, select sample(s) of interest
MS_mode = 'pos' # Input, select MS mode, can only take 'pos' or 'neg' as
input
MS_chromatogram(samples, P, MS_mode,
vars()['P{}_MS_{}_tensor'.format(P,MS_mode)], data)

## MS(+/-) plot at one specific retention time
samples = [1,2,3,4] # Input, select sample(s) of interest
RT_mz =3.9 # Input, select retention time in minutes
MS_mode = 'pos' # Input, select MS mode, can only take 'pos' or 'neg' as
input
MS_spectrum(samples, P, RT_mz, MS_mode,
vars()['P{}_MS_{}_tensor'.format(P,MS_mode)], data)


###### Heat maps ######
## UV heat map for one sample
sample = 42 # Input, select sample
heatmap_UV_sample(sample, P, vars()['P{}_UV_tensor'.format(P)], data)

## UV heat map for one retention time
samples = [1,2,3,4,5,6] # Input, select specific samples
RT_value = 4.1 # Input, select retention time in minutes
heatmap_UV_RT(RT_value, P, samples, vars()['P{}_UV_tensor'.format(P)],
data)
```

```
## UV heat map for one wavelength
samples = [1,2,3,4,5,6] # Input, select specific samples
wavelength = 254 # Input
heatmap_UV_wavelength(wavelength, P, samples,
vars()['P{}_UV_tensor'.format(P)], data)

## MS heat map for one sample with binned m/z-values
sample = 1 # Input, select sample
MS_mode = 'pos' # Input, select MS mode, can only take 'pos' or 'neg' as
input
bin_numbers = 200 # Input, select number of bins for the m/z-values
heatmap_MS_sample_binned(sample, P, bin_numbers, MS_mode,
vars()['P{}_MS_{}_tensor'.format(P, MS_mode)], data)

## MS heat map for one retention time with binned m/z-values
RT_value = 4.1
samples = [1,2,3,4] # Input, select specific samples
MS_mode = 'pos' # Input, select MS mode, can only take 'pos' or 'neg' as
input
bin_numbers = 20 # Input, select number of bins for the m/z-values
heatmap_MS_RT_binned(RT_value, P, samples, bin_numbers, MS_mode,
vars()['P{}_MS_{}_tensor'.format(P,MS_mode)], data)

## MS heat map for one m/z-value
samples = [1,2,3,4] # Input, select specific samples
MS_mode = 'pos' # Input, select MS mode, can only take 'pos' or 'neg' as
input
mz_value = 145.15 # Input, select m/z-value
heatmap_MS_mz(mz_value, P, samples, MS_mode,
vars()['P{}_MS_{}_tensor'.format(P,MS_mode)], data)
```

#%% Visualisation of 96-microwell plate for starting materials and product

```
### Import functions from 'Plot_plate.py'
from Plot_plate import plot_96_plate_product,
plot_96_plate_starting_material

P = 1 # Input
variable1 = 'PC' # Input, need to be string which is present in the header
in the meta data file.
variable2 = 'PC_mol%' # Input, If only one variable should be illustrated
set variable2 ='''.
# If variable2 = '', the mean, STD and median will be calculated for the
indivoudal groups in variable1.
# The result is shown in the Console (left lower window).

# Plot plate for conversion of product.
plot_96_plate_product(data, P, variable1, variable2,
vars()['P{}_conversion_product'.format(P)])
# Plot plate for conversion of starting material.
plot_96_plate_starting_material(data, P, variable1, variable2,
vars()['P{}_conversion_SM'.format(P)])
```

```
#%% Top n reaction information saved in CSV file

### Import function from 'Top_reactions.py'.
from Top_reactions import top_reactions_file

n = 10 # Input, number of top reactions.
P = 1 # Input

# Save the top n reactions in a CSV file in the outer path/folder.
# The file is called 'Plate_P_top_reactions.csv'.
top_reactions_file(n, P, vars()['P{}_conversion_product'.format(P)], data)

#%% Detection of new significant peaks

### Import function from 'Significant_peak_search.py'
from Significant_peak_search import new_significent_peaks

P = 13 # Input
threshold = 2000000 # Input
RT_list = [RT_ISTD, RT_product, RT_SM] # Input, write the retention times
of known peaks (RT_ISTD, RT_product, RT_SM, 3.3, etc.)

# Search for new significant peaks above a set threshold for the integral
new_significent_peaks(P, vars()['P{}_peak_information'.format(P)] ,
threshold, RT_list)

#%% m/z search

### Import functions from 'mz_search.py'
from Mz_search import mz_search_top_n, plot_96_plate_detected_product,
mz_search_threshold

P =13 # Input
mz_value = 354.3 # Input, define the m/z value of compound.
MS_mode = 'pos' # Input
n = 1 # Input, number of top m/z-value in one peak.
mz_threshold = 70000000 # Input
mz_search_range = 0.25 # Input, searches in range mz_value+/-
mz_search_range.

# m/z search based on threshold m/z-value in a peak.
# mz_search_result = mz_search_threshold(P, mz_value, mz_search_range,
MS_mode, mz_threshold, vars()['P{}_peak_information'.format(P)],
vars()['P{}_MS_{}_tensor'.format(P,MS_mode)], data)

# m/z search baed on n top m/z-values in a peak.
mz_search_result = mz_search_top_n(P, mz_value, mz_search_range, MS_mode,
n, vars()['P{}_peak_information'.format(P)],
vars()['P{}_MS_{}_tensor'.format(P,MS_mode)], data)

# Plot 96-microwell plate (blue = detected and red = not detected m/z-
value).
plot_96_plate_detected_product(data, P, mz_value, mz_search_result)
```

LIST OF REFERENCES

[1] Phil Davis, "How big is the solar system," https://solarsystem.nasa.gov/news/1164/, 2020. Date accessed 04/04/2022.

[2] B. Wardle, *Principles and Applications of Photochemistry*, John Wiley & Sons Ltd, West Sussex, 2009.

[3] P. Klán, J. Wirz, *Photochemistry of Organic Compounds: From Concepts to Practice*, John Wiley & Sons Ltd, West Sussex, 2009.

[4] Y.-Y. Fan, X.-H. Gao, J.-M. Yue, *Science China Chemistry* 2016, *59*, 1126–1141.

[5] Q. Li, K. Zhao, A. Peuronen, K. Rissanen, D. Enders, Y. Tang, *J Am Chem Soc* 2018, *140*, 1937–1944.

[6] K. C. Nicolaou, S. Sanchini, D. Sarlah, G. Lu, T. R. Wu, D. K. Nomura, B. F. Cravatt, B. Cubitt, J. C. de La Torre, A. J. Hessell, D. R. Burton, *Proceedings of the National Academy of Sciences of the United States of America* 2010.

[7] A. Sergeiko, V. v Poroikov, L. O. Hanu, V. M. Dembitsky, *The Open Medicinal Chemistry Journal* 2008, *2*, 26–37.

[8] M. R. Kolk, M. A. C. H. Janssen, F. P. J. T. Rutjes, D. Blanco-Ania, *ChemMedChem* 2022.

[9] F. Lovering, J. Bikker, C. Humblet, *Journal of Medicinal Chemistry* 2009, *52*, 6752–6756.

[10] Y. A. Skalenko, T. v Druzhenko, A. v Denisenko, M. v Samoilenko, O. P. Dacenko, S. A. Trofymchuk, O. O. Grygorenko, A. A. Tolmachev, P. K. Mykhailiuk, *The Journal of Organic Chemistry* 2018, *83*, 6275–6289.

[11] J. Clayden, N. Greeves, S. Warren, *Organic Chemistry*, Oxford University Press Inc., New York, 2012.

[12] P. Y. Bruice, *Organic Chemistry*, Pearson Education, Inc. Prentice Hall, Hoboken, 2011.

[13] H. Bouas-Laurent, H. Dürr, *Pure and Applied Chemistry* 2001, *73*, 639–665.

[14] A. Goulet-Hanssens, F. Eisenreich, S. Hecht, *Advanced Materials* 2020, *32*.

[15] J. Boelke, S. Hecht, *Advanced Optical Materials* 2019, *7*.

[16] S. Wiedbrauk, H. Dube, *Tetrahedron Letters* 2015, *56*, 4266–4274.

[17] R. S. H. Liu, G. S. Hammond, *Proc Natl Acad Sci U S A* 2000, *97*, 11153–11158.

[18] K. Hüll, J. Morstein, D. Trauner, *Chemical Reviews* 2018, *118*, 10710–10747.

[19] J. Broichhagen, J. A. Frank, D. Trauner, *Accounts of Chemical Research* 2015, *48*, 1947–1960.

[20] M. J. Fuchter, *Journal of Medicinal Chemistry* 2020, *63*, 11436–11447.

[21] S. W. Hell, *Physics Letters, Section A: General, Atomic and Solid State Physics* 2004, *326*, 140–145.

[22] B. N. Sunil, M. Monika, G. Shanker, G. Hegde, V. Prasad, *Frontiers in Physics* 2021, *9*.

[23] Z. Wang, P. Erhart, T. Li, Z. Y. Zhang, D. Sampedro, Z. Hu, H. A. Wegner, O. Brummel, J. Libuda, M. B. Nielsen, K. Moth-Poulsen, *Joule* 2021, *5*, 3116–3136.

[24] J. Orrego-Hernández, A. Dreos, K. Moth-Poulsen, *Accounts of Chemical Research* 2020, *53*, 1478–1487.

[25] C. L. Sun, C. Wang, R. Boulatov, *ChemPhotoChem* 2019, *3*, 268–283.

[26] L. Stricker, M. Böckmann, T. M. Kirse, N. L. Doltsinis, B. J. Ravoo, *Chemistry - A European Journal* 2018, *24*, 8639–8647.

[27] R. J. Li, J. Tessarolo, H. Lee, G. H. Clever, *J Am Chem Soc* 2021, *143*, 3865–3873.

[28] H. Dube, J. Rebek, *Angewandte Chemie Int. Ed.* 2012, *51*, 3207–3210.

[29] S. L. Xiang, Q. X. Hua, P. J. Zhao, W. L. Gong, C. Li, M. Q. Zhu, *Chemistry of Materials* 2019, *31*, 5081–5088.

[30] D. Habault, H. Zhang, Y. Zhao, *Chemical Society Reviews* 2013, *42*, 7244–7256.

[31] M. Kathan, P. Kovaříček, C. Jurissek, A. Senf, A. Dallmann, A. F. Thünemann, S. Hecht, *Angewandte Chemie* 2016, *128*, 14086–14090.

[32] A. Gerwien, P. Mayer, H. Dube, *Nature Communications* 2019, *10*.

[33] D. R. S. Pooler, A. S. Lubbe, S. Crespi, B. L. Feringa, *Chemical Science* 2021, *12*, 14964–14986.

[34] A. S. Lubbe, Q. Liu, S. J. Smith, J. W. de Vries, J. C. M. Kistemaker, A. H. de Vries, I. Faustino, Z. Meng, W. Szymanski, A. Herrmann, B. L. Feringa, *J Am Chem Soc* 2018, *140*, 5069–5076.

[35] M. Baroncini, S. Silvi, A. Credi, *Chemical Reviews* 2020, *120*, 200–268.

[36] Y. Huang, Y. Du, L. Yuan, Z. Chu, L. He, *Journal of Macromolecular Science, Part A: Pure and Applied Chemistry* 2021, *58*, 717–724.

[37] C. Petermayer, H. Dube, *Accounts of Chemical Research* 2018, *51*, 1153–1163.

[38] W. R. Brode, G. M. Wyman, *Journal of Research of the National Bureau of Standards* 1951, *47*, 170–178.

[39] G. M. Wyman, *Chemical Reviews* 1955, *55*, 625–657.

[40] C. Y. Huang, A. Bonasera, L. Hristov, Y. Garmshausen, B. M. Schmidt, D. Jacquemin, S. Hecht, *J Am Chem Soc* 2017, *139*, 15205–15211.

[41] J. Pina, D. Sarmento, M. Accoto, P. L. Gentili, L. Vaccaro, A. Galvão, J. S. Seixas De Melo, *Journal of Physical Chemistry B* 2017, *121*, 2308–2318.

[42] Š. Budzák, J. Jovaišaitė, C. Huang, P. Baronas, K. Tulaitė, S. Juršėnas, D. Jacquemin, S. Hecht, *Chemistry – A European Journal* 2022.

[43] J. Volarić, W. Szymanski, N. A. Simeth, B. L. Feringa, *Chemical Society Reviews* 2021, *50*, 12377–12449.

[44] B. Koeppe, F. Römpp, *Chemistry - A European Journal* 2018, *24*, 14382–14386.

[45] H. M. D. Bandara, S. C. Burdette, *Chemical Society Reviews* 2012, *41*, 1809–1825.

[46] D. H. Waldeck, *Chemical Reviews* 1991, *91*, 415–436.

[47] D. Bléger, S. Hecht, *Angewandte Chemie Int. Ed.* 2015, *54*, 11338--11349.

[48] W. Szymański, J. M. Beierle, H. A. V. Kistemaker, W. A. Velema, B. L. Feringa, *Chemical Reviews* 2013, *113*, 6114–6178.

[49] C. Knie, M. Utecht, F. Zhao, H. Kulla, S. Kovalenko, A. M. Brouwer, P. Saalfrank, S. Hecht, D. Bléger, *Chemistry - A European Journal* 2014, *20*, 16492–16501.

[50] A. A. Beharry, O. Sadovski, G. A. Woolley, *J Am Chem Soc* 2011, *133*, 19684–19687.

[51] S. Samanta, C. Qin, A. J. Lough, G. A. Woolley, *Angewandte Chemie Int. Ed.* 2012, *51*, 6452–6455.

[52] R. Siewertsen, H. Neumann, B. Buchheim-Stehn, R. Herges, C. Näther, F. Renth, F. Temps, *J Am Chem Soc* 2009, *131*, 15594–15595.

[53] F. A. Jerca, V. V. Jerca, R. Hoogenboom, *Nature Reviews Chemistry* 2022, *6*, 51–69.

[54] H. B. Cheng, S. Zhang, J. Qi, X. J. Liang, J. Yoon, *Advanced Materials* 2021, *33*.

[55] I. Tochitsky, M. A. Kienzler, E. Isacoff, R. H. Kramer, *Chemical Reviews* 2018, *118*, 10748–10773.

[56] B. M. Gaub, M. H. Berry, A. E. Holt, A. Reiner, M. A. Kienzler, N. Dolgova, S. Nikonov, G. D. Aguirre, W. A. Beltran, J. G. Flannery, E. Y. Isacoff, *Proc Natl Acad Sci U S A* 2014, *111*, E5574–E5583.

[57] J. Karcher, Z. L. Pianowski, *Chemistry - A European Journal* 2018, *24*, 11605–11610.

[58] B. Maerz, S. Wiedbrauk, S. Oesterling, E. Samoylova, A. Nenov, P. Mayer, R. de Vivie-Riedle, W. Zinth, H. Dube, *Chemistry - A European Journal* 2014, *20*, 13984–13992.

[59] K. Hoffmann, M. Guentner, P. Mayer, H. Dube, *Organic Chemistry Frontiers* 2019, *6*, 1244–1252.

[60] S. Wiedbrauk, T. Bartelmann, S. Thumser, P. Mayer, H. Dube, *Nature Communications* 2018, *9*.

[61] F. Kink, M. P. Collado, S. Wiedbrauk, P. Mayer, H. Dube, *Chemistry - A European Journal* 2017, *23*, 6237–6243.

[62] M. Guentner, E. Uhl, P. Mayer, H. Dube, *Chemistry - A European Journal* 2016, *22*, 16433–16436.

[63] G. Moncelsi, L. Escobar, H. Dube, P. Ballester, *Chemistry - An Asian Journal* 2018, *13*, 1632–1639.

[64] M. Guentner, M. Schildhauer, S. Thumser, P. Mayer, D. Stephenson, P. J. Mayer, H. Dube, *Nature Communications* 2015, *6*.

[65] L. Köttner, M. Schildhauer, S. Wiedbrauk, P. Mayer, H. Dube, *Chemistry - A European Journal* 2020, *26*, 10712–10718.

[66] R. Wilcken, M. Schildhauer, F. Rott, L. A. Huber, M. Guentner, S. Thumser, K. Hoffmann, S. Oesterling, R. de Vivie-Riedle, E. Riedle, H. Dube, *J Am Chem Soc* 2018, *140*, 5311–5318.

[67] A. Gerwien, P. Mayer, H. Dube, *J Am Chem Soc* 2018, *140*, 16442–16446.

[68] K. Hoffmann, P. Mayer, H. Dube, *Organic and Biomolecular Chemistry* 2019, *17*, 1979–1983.

[69] E. Uhl, P. Mayer, H. Dube, *Angewandte Chemie* 2020, *132*, 5779–5786.

[70] L. A. Huber, K. Hoffmann, S. Thumser, N. Böcher, P. Mayer, H. Dube, *Angewandte Chemie* 2017, *129*, 14728–14731.

[71] S. Wiedbrauk, B. Maerz, E. Samoylova, A. Reiner, F. Trommer, P. Mayer, W. Zinth, H. Dube, *J Am Chem Soc* 2016, *138*, 12219–12227.

[72] A. Sailer, F. Ermer, Y. Kraus, R. Bingham, F. H. Lutter, J. Ahlfeld, O. Thorn-Seshold, *Beilstein Journal of Organic Chemistry* 2020, *16*, 125–134.

[73] A. Sailer, J. O. M. M. Eiring, N. Pettersson, A. Akhmanova, J. Thorn-Seshold, O. Thorn-Seshold, *Angewandte Chemie Int. Ed.* 2021, *60*, 23695–23704.

[74] A. Sailer, F. Ermer, Y. Kraus, F. H. Lutter, C. Donau, M. Bremerich, J. Ahlfeld, O. Thorn-Seshold, *ChemBioChem* 2019, *20*, 1305–1314.

[75] L. Zhang, G. Linden, O. Vázquez, *Beilstein Journal of Organic Chemistry* 2019, *15*, 2500–2508.

[76] S. Kitzig, M. Thilemann, T. Cordes, K. Rück-Braun, *ChemPhysChem* 2016, *17*, 1252–1263.

[77] T. Lougheed, V. Borisenko, T. Hennig, K. Rück-Braun, G. A. Woolley, *Organic and Biomolecular Chemistry* 2004, *2*, 2798–2801.

[78] S. Herre, T. Schadendorf, I. Ivanov, C. Herrberger, W. Steinle, K. Rück-Braun, R. Preissner, H. Kuhn, *ChemBioChem* 2006, *7*, 1089–1095.

[79] R. G. Snodgrass, B. Brüne, *Frontiers in Pharmacology* 2019, *10*.

[80] X. Su, S. Voskian, R. P. Hughes, I. Aprahamian, *Angewandte Chemie Int. Ed.* 2013, *52*, 10734–10739.

[81] X. Su, I. Aprahamian, *Organic Letters* 2011, *13*, 30–33.

[82] S. M. Landge, E. Tkatchouk, D. Benítez, D. A. Lanfranchi, M. Elhabiri, W. A. Goddard, I. Aprahamian, *J Am Chem Soc* 2011, *133*, 9812–9823.

[83] S. M. Landge, I. Aprahamian, *J Am Chem Soc* 2009, *131*, 18269–18271.

[84] J. T. Foy, D. Ray, I. Aprahamian, *Chemical Science* 2015, *6*, 209–213.

[85] X. Su, I. Aprahamian, *Organic Letters* 2013, *15*, 5952–5955.

[86] M. L. Croteau, X. Su, D. E. Wilcox, I. Aprahamian, *Chempluschem* 2014, *79*, 1214–1224.

[87] X. Su, I. Aprahamian, *Chemical Society Reviews* 2014, *43*, 1963–1981.

[88] J. D. Harris, M. J. Moran, I. Aprahamian, *Proc Natl Acad Sci U S A* 2016, *115*, 9414–9422.

[89] M. J. Moran, M. Magrini, D. M. Walba, I. Aprahamian, *J Am Chem Soc* 2018, *140*, 13623–13627.

[90] H. Qian, S. Pramanik, I. Aprahamian, *J Am Chem Soc* 2017, *139*, 9140–9143.

[91] S. Kassem, A. T. L. Lee, D. A. Leigh, A. Markevicius, J. Solà, *Nature Chemistry* 2016, *8*, 138–143.

[92] F. Yu, X. Cao, J. Du, G. Wang, X. Chen, *ACS Applied Materials and Interfaces* 2015, *7*, 24023–24031.

[93] A. Ryabchun, Q. Li, F. Lancia, I. Aprahamian, N. Katsonis, *J Am Chem Soc* 2019, *141*, 1196–1200.

[94] M. Irie, T. Fukaminato, K. Matsuda, S. Kobatake, *Chemical Reviews* 2014, *114*, 12174–12277.

[95] H. Cheng, S. Zhang, E. Bai, X. Cao, J. Wang, J. Qi, J. Liu, J. Zhao, L. Zhang, J. Yoon, *Advanced Materials* 2022, 2108289.

[96] N. Nishitani, T. Hirose, K. Matsuda, *Chemical Communications* 2019, *55*, 5099–5102.

[97] J. Koo, Y. Jang, L. Martin, D. Kim, H. Jeong, K. Kang, W. Lee, J. Kim, W. T. Hwang, D. Xiang, E. Scheer, M. Kabdulov, T. Huhn, F. Pauly, T. Lee, *ACS Applied Materials and Interfaces* 2019, *11*, 11645–11653.

[98] P. Ferreira, B. Ventura, A. Barbieri, J. P. da Silva, C. A. T. Laia, A. J. Parola, N. Basílio, *Chemistry - A European Journal* 2019, *25*, 3477–3482.

[99] G. Liu, Y. M. Zhang, X. Xu, L. Zhang, Q. Yu, Q. Zhao, C. Zhao, Y. Liu, *Advanced Optical Materials* 2017, *5*.

[100] H. B. Cheng, B. Qiao, H. Li, J. Cao, Y. Luo, K. M. Kotraiah Swamy, J. Zhao, Z. Wang, J. Y. Lee, X. J. Liang, J. Yoon, *J Am Chem Soc* 2021, *143*, 2413–2422.

[101] S. Fredrich, A. Bonasera, V. Valderrey, S. Hecht, *J Am Chem Soc* 2018, *140*, 6432–6440.

[102] Z. Li, X. Liu, G. Wang, B. Li, H. Chen, H. Li, Y. Zhao, *Nature Communications* 2021, *12*.

[103] J. J. Li, H. Y. Zhang, G. Liu, X. Dai, L. Chen, Y. Liu, *Advanced Optical Materials* 2021, *9*.

[104] J. Qi, C. Chen, X. Zhang, X. Hu, S. Ji, R. T. K. Kwok, J. W. Y. Lam, D. Ding, B. Z. Tang, *Nature Communications* 2018, *9*.

[105] Y. Mi, H. B. Cheng, H. Chu, J. Zhao, M. Yu, Z. Gu, Y. Zhao, L. Li, *Chemical Science* 2019, *10*, 10231–10239.

[106] Y. Qin, L. J. Chen, F. Dong, S. T. Jiang, G. Q. Yin, X. Li, Y. Tian, H. B. Yang, *J Am Chem Soc* 2019, *141*, 8943–8950.

[107] X. Chai, H. H. Han, A. C. Sedgwick, N. Li, Y. Zang, T. D. James, J. Zhang, X. le Hu, Y. Yu, Y. Li, Y. Wang, J. Li, X. P. He, H. Tian, *J Am Chem Soc* 2020, *142*, 18005–18013.

[108] L. Kortekaas, W. R. Browne, *Chemical Society Reviews* 2019, *48*, 3406–3424.

[109] R. Klajn, *Chemical Society Reviews* 2014, *43*, 148–184.

[110] H. Dürr, H. Bouas-Laurent, *Elsevier Science* 2003, *1st edn, Amsterdam*.

[111] F. Jonsson, T. Beke-Somfai, J. Andréasson, B. Nordén, *Langmuir* 2013, *29*, 2099–2103.

[112] S. K. Rastogi, Z. Zhao, M. B. Gildner, B. A. Shoulders, T. L. Velasquez, M. O. Blumenthal, L. Wang, X. Li, T. W. Hudnall, T. Betancourt, L. Du, W. J. Brittain, *Tetrahedron* 2021, *80*.

[113] J. R. Nilsson, S. Li, B. Önfelt, J. Andréasson, *Chemical Communications* 2011, *47*, 11020–11022.

[114] Y. Yokoyama, *Chemical Reviews* 2000, *100*, 1717–1739.

[115] N. Sivasankaran, K. Palaninathan, *Polymer Degradation and Stability* 2013, *98*, 1852–1861.

[116] Y. Kohno, Y. Tamura, R. Matsushima, *Journal of Photochemistry and Photobiology A: Chemistry* 2009, *201*, 98–101.

[117] M. Filatov, M. Paolino, S. K. Min, K. S. Kim, *Journal of Physical Chemistry Letters* 2018, *9*, 4995–5001.

[118] J. Andréasson, U. Pischel, S. D. Straight, T. A. Moore, A. L. Moore, D. Gust, *J Am Chem Soc* 2011, *133*, 11641–11648.

[119] M. Bälter, S. Li, J. R. Nilsson, J. Andréasson, U. Pischel, *J Am Chem Soc* 2013, *135*, 10230–10233.

[120] K. ustler, G. aleeva, A. omila, P. Gorostiza, P. Bregestovski, andBurkhard Kçnig, *Chemistry - A European Journal* 2020, *26*, 12722–12727.

[121] D. Lachmann, C. Studte, B. Männel, H. Hübner, P. Gmeiner, B. König, *Chemistry - A European Journal* 2017, *23*, 13423–1343.

[122] D. Lachmann, A. Konieczny, M. Keller, B. König, *Organic and Biomolecular Chemistry* 2019, *17*, 2467–2478.

[123] S. Helmy, F. A. Leibfarth, S. Oh, J. E. Poelma, C. J. Hawker, J. R. de Alaniz, *J Am Chem Soc* 2014, *136*, 8169–8172.

[124] M. M. Lerch, W. Szymański, B. L. Feringa, *Chemical Society Reviews* 2018, *47*, 1910–1937.

[125] I. M. Welleman, M. W. H. Hoorens, B. L. Feringa, H. H. Boersma, W. Szymański, *Chemical Science* 2020, *11*, 11672–11691.

[126] S. O. Poelma, S. S. Oh, S. Helmy, A. S. Knight, G. L. Burnett, H. T. Soh, C. J. Hawker, J. Read De Alaniz, *Chemical Communications* 2016, *52*, 10525–10528.

[127] S. Singh, K. Friedel, M. Himmerlich, Y. Lei, G. Schlingloff, A. Schober, *ACS Macro Letters* 2015, *4*, 1273–1277.

[128] J. R. Hemmer, S. O. Poelma, N. Treat, Z. A. Page, N. D. Dolinski, Y. J. Diaz, W. Tomlinson, K. D. Clark, J. P. Hooper, C. Hawker, J. Read De Alaniz, *J Am Chem Soc* 2016, *138*, 13960–13966.

[129] B. P. Mason, M. Whittaker, J. Hemmer, S. Arora, A. Harper, S. Alnemrat, A. McEachen, S. Helmy, J. Read De Alaniz, J. P. Hooper, *Applied Physics Letters* 2016, *108*.

[130] S. Ulrich, J. R. Hemmer, Z. A. Page, N. D. Dolinski, O. Rifaie-Graham, N. Bruns, C. J. Hawker, L. F. Boesel, J. Read De Alaniz, *ACS Macro Letters* 2017, *6*, 738–742.

[131] S. Jia, J. D. Du, A. Hawley, W. K. Fong, B. Graham, B. J. Boyd, *Langmuir* 2017, *33*, 2215–2221.

[132] M. M. Lerch, M. J. Hansen, W. A. Velema, W. Szymanski, B. L. Feringa, *Nature Communications* 2016, *7*.

[133] Y. J. Diaz, Z. A. Page, A. S. Knight, N. J. Treat, J. R. Hemmer, C. J. Hawker, J. Read de Alaniz, *Chemistry - A European Journal* 2017, *23*, 3562–3566.

[134] S. Yang, J. Liu, Z. Cao, M. Li, Q. Luo, D. Qu, *Dyes and Pigments* 2018, *148*, 341–347.

[135] J. Ahrens, T. Bian, T. Vexler, R. Klajn, *ChemPhotoChem* 2017, *1*, 230–236.

[136] J. E. Zweig, T. R. Newhouse, *J Am Chem Soc* 2017, *139*, 10956–10959.

[137] J. E. Zweig, T. A. Ko, J. Huang, T. R. Newhouse, *Tetrahedron* 2019, *75*.

[138] T. Fehrentz, M. Schönberger, D. Trauner, *Angewandte Chemie - Int. Ed.* 2011, *50*, 12156–12182.

[139] T. Kawai, T. Sasaki, M. Irie, *Chemical Communications* 2001, 711–712.

[140] H. Dong, H. Zhu, Q. Meng, X. Gong, W. Hu, *Chemical Society Reviews* 2012, *41*, 1754–1808.

[141] L. Peng, M. You, C. Wu, D. Han, I. Öçsoy, T. Chen, Z. Chen, W. Tan, *ACS Nano* 2014, *8*, 2555–2561.

[142] T. T. T. Nguyen, D. Türp, D. Wang, B. Nölscher, F. Laquai, K. Müllen, *J Am Chem Soc* 2011, *133*, 11194–11204.

[143] R. Weissleder, *Nature Biotechnology* 2001, *19*, 316–317.

[144] W. A. Velema, W. Szymanski, B. L. Feringa, *J Am Chem Soc* 2014, *136*, 2178–2191.

[145] D. Wu, M. Dong, C. v. Collins, A. Babalhavaeji, G. A. Woolley, *Advanced Optical Materials* 2016, *4*, 1402–1409.

[146] T. Dohi, K. Morimoto, A. Maruyama, Y. Kita, *Organic Letters* 2006, *8*, 2007–2010.

[147] J. K. Johnson, E. M. Skoda, J. Zhou, E. Parrinello, D. Wang, K. O'Malley, B. R. Eyer, M. Kazancioglu, K. Eisermann, P. A. Johnston, J. B. Nelson, Z. Wang, P. Wipf, *ACS Medicinal Chemistry Letters* 2016, *7*, 785–790.

[148] J. Ostapko, K. Nawara, M. Kijak, J. Buczyńska, B. Leśniewska, M. Pietrzak, G. Orzanowska, J. Waluk, *Chemistry – A European Journal* 2016, *22*, 17311–17320.

[149] T. Dohi, K. Morimoto, A. Maruyama, Y. Kita, *Organic Letters* 2006, *8*, 2007–2010.

[150] T. B. Nguyen, P. Retailleau, *Organic Letters* 2018, *20*, 186–189.

[151] M. B. Plutschack, B. Pieber, K. Gilmore, P. H. Seeberger, *Chemical Reviews* 2017, *117*, 11796–11893.

[152] S. Kobayashi, *Chemistry – An Asian Journal* 2016, *11*, 425–436.

[153] F. M. Akwi, P. Watts, *Chemical Communications* 2018, *54*, 13894–13928.

[154] L. D. Elliott, J. P. Knowles, P. J. Koovits, K. G. Maskill, M. J. Ralph, G. Lejeune, L. J. Edwards, R. I. Robinson, I. R. Clemens, B. Cox, D. D. Pascoe, G. Koch, M. Eberle, M. B. Berry, K. I. Booker-Milburn, *Chemistry – A European Journal* 2014, *20*, 15226–15232.

[155] T. Hu, I. R. Baxendale, M. Baumann, *Molecules* 2016, *21*, 918.

[156] C. J. Mallia, I. R. Baxendale, *Organic Process Research & Development* 2016, *20*, 327–360.

[157] I. R. Baxendale, *Chemical Engineering & Technology* 2015, *38*, 1713–1716.

[158] I. Atodiresei, C. Vila, M. Rueping, *ACS Catalysis* 2015, *5*, 1972–1985.

[159] A. Puglisi, M. Benaglia, R. Porta, F. Coccia, *Current Organocatalysis* 2015, *2*.

[160] V. Sans, L. Cronin, *Chemical Society Reviews* 2016, *45*, 2032–2043.

[161] B. J. Reizman, K. F. Jensen, *Accounts of Chemical Research* 2016, *49*, 1786–1796.

[162] R. H. Sahoo, J. G. Kralj, K. F. Jensen, *Angewandte Chemie Int. Ed.* 2007, *46*, 5704–5708.

[163] C. G. W. van Melis, M. R. Penny, A. D. Garcia, A. Petti, A. P. Dobbs, S. T. Hilton, K. Lam, *ChemElectroChem* 2019, *6*, 4144–4148.

[164] G. Laudadio, W. de Smet, L. Struik, Y. Cao, T. Noël, *Journal of Flow Chemistry* 2018, *8*, 157–165.

[165] E. J. Horn, B. R. Rosen, P. S. Baran, *ACS Central Science* 2016, *2*, 302–308.

[166] M. Yan, Y. Kawamata, P. S. Baran, *Chemical Reviews* 2017, *117*, 13230–13319.

[167] T. Noël, Y. Cao, G. Laudadio, *Accounts of Chemical Research* 2019, *52*, 2858–2869.

[168] J. ichi Yoshida, H. Kim, A. Nagaki, *Journal of Flow Chemistry* 2017, *7*, 60–64.

[169] A. A. Folgueiras-Amador, T. Wirth, *Journal of Flow Chemistry* 2017, *7*, 94–95.

[170] A. A. Folgueiras-Amador, K. Philipps, S. Guilbaud, J. Poelakker, T. Wirth, *Angewandte Chemie - Int. Ed.* 2017, *129*, 15648–15653.

[171] A. Kjar, Y. Huang, *Pharmaceutics* 2019, *11*.

[172] S. Shakibania, M. Khakbiz, C. K. Bektas, L. Ghazanfari, M. T. Banizi, K.-B. Lee, *Molecular Systems Design & Engineering* 2022, *7*, 315–324.

[173] M. Sakin, Y. C. Kiroglu, *Energy Procedia* 2017, *134*, 702–711.

[174] Z. Faraji Rad, P. D. Prewett, G. J. Davies, *Microsystems and Nanoengineering* 2021, *7*, 71.

[175] F. Burmeister, U. D. Zeitner, S. Nolte, A. Tünnermann, *Optics Express* 2012, *20*, 7994–8005.

[176] B. Redwood, S. Filemon, G. Brian, *The 3D Printing Handbook Technologies, Design and Applications*, Coers & Roest, Amsterdam, 2017.

[177] S. v Murphy, A. Atala, *Nature Biotechnology* 2014, *32*, 773–785.

[178] B. Zhang, B. Seong, V. Nguyen, D. Byun, *Journal of Micromechanics and Microengineering* 2016, *26*, 025015.

[179] S. Rossi, A. Puglisi, M. Benaglia, *ChemCatChem* 2018, *10*, 1512–1525.

[180] P. J. Kitson, S. Glatzel, W. Chen, C. G. Lin, Y. F. Song, L. Cronin, *Nature Protocols* 2016, *11*, 920–936.

[181] J. M. Neumaier, A. Madani, T. Klein, T. Ziegler, *Beilstein Journal of Organic Chemistry* 2019, *15*, 558–566.

[182] D. H. Ko, K. W. Gyak, D. P. Kim, *Journal of Flow Chemistry* 2017, *7*, 72–81.

[183] H. van Nguyen, H. Q. Nguyen, V. D. Nguyen, T. S. Seo, *Sensors and Actuators, B: Chemical* 2019, *296*.

[184] D. L. Walmsley, E. Sellier, *EngrXiv [Preprint]* 2020.

[185] A. S. Booeshaghi, E. da V. Beltrame, D. Bannon, J. Gehring, L. Pachter, *Scientific Reports* 2019, *9*.

[186] H. Agrawaal, J. E. Thompson, *Talanta Open* 2021, *3*, Article 100036.

[187] J. H. Bannock, S. H. Krishnadasan, M. Heeney, J. C. de Mello, *Materials Horizons* 2014, *1*, 373–378.

[188] M. Michalec, Ł. Tymecki, *Talanta* 2018, *190*, 423–428.

[189] F. Menzel, T. Klein, T. Ziegler, J. M. Neumaier, *Reaction Chemistry and Engineering* 2020, *5*, 1300–1310.

[190] M. Bargum, M. Krell-Jorgensen, M. Nielsen, K. Qvortrup, L. Laraia, *Synlett* 2022, *33*, 1083–1086.

[191] Andreas Ritzén, "3D Printed Photoreactor," https://www.thingiverse.com/thing:4203672, 08/02/2020, date accessed 11/02/2021.

[192] N. J. Flodén, A. Trowbridge, D. Willcox, S. M. Walton, Y. Kim, M. J. Gaunt, *J Am Chem Soc* 2019, *141*, 8426–8430.

[193] M. Christensen, L. P. E. Yunker, P. Shiri, T. Zepel, P. L. Prieto, S. Grunert, F. Bork, J. E. Hein, *Chemical Science* 2021, *12*, 15473–15490.

[194] S. M. Mennen, C. Alhambra, C. L. Allen, M. Barberis, S. Berritt, T. A. Brandt, A. D. Campbell, J. Castañón, A. H. Cherney, M. Christensen, D. B. Damon, J. Eugenio De Diego, S. García-Cerrada, P. García-Losada, R. Haro, J. Janey, D. C. Leitch, L. Li, F. Liu, P. C. Lobben, D. W. C. Macmillan, J. Magano, E. McInturff, S. Monfette, R. J. Post, D. Schultz, B. J. Sitter, J. M. Stevens, I. I. Strambeanu, J. Twilton, K. Wang, M. A. Zajac, *Organic Process Research and Development* 2019, *23*, 1213–1242.

[195] R. Grainger, S. Whibley, *Organic Process Research and Development* 2021, *25*, 354–364.

[196] LABCYTE, "Echo Acoustic Liquid Handling Technology." Webpage. https://www.labcyte.com/echoliquid- handling (2021). Date accessed 14/9/2021.

[197] R. Grainger, T. D. Heightman, S. v. Ley, F. Lima, C. N. Johnson, *Chemical Science* 2019, *10*, 2264–2271.

[198] C. W. Hsu, H. Sundén, *Organic Letters* 2018, *20*, 2051–2054.

[199] A. I. Green, G. M. Burslem, *RSC Medicinal Chemistry* 2021, *12*, 1780–1786.

[200] J. Perktold, S. Seabold, j. Taylor, Statsmodels-developers, "Statsmodels". https://www.statsmodels.org/stable/index.html (2021). Date accessed 5/2/2022.

[201] P. R. D. Murray, W. M. M. Bussink, G. H. M. Davies, F. W. van der Mei, A. H. Antropow, J. T. Edwards, L. A. D'Agostino, J. M. Ellis, L. G. Hamann, F. Romanov-Michailidis, R. R. Knowles, *J Am Chem Soc* 2021, *143*, 4055–4063.

[202] S. Jonsson, K. Viswanathan, *Journal of Photopolymer Science and Technology* 2000, *13*, 125–144.

[203] F. Strieth-Kalthoff, F. Glorius, *Chem* 2020, *6*, 1888–1903.

[204] E. R. Welin, "Mac Millan Group Meeting February 12th, 2015". https://macmillan.princeton.edu/wp-content/uploads/ERW_Behind_the_Scenes.pdf. Date accessed 03/05/2022.

[205] L. Chen, A. R. Lear, P. Gao, M. K. Brown, *Angewandte Chemie - Int. Ed.* 2019, *131*, 11072–11076.

[206] J. C. Splitstoser, T. D. Dillehay, J. Wouters, A. Claro, *Science Advances* 2016, *2*, e1501623.

References to images included in the high-throughput experimentation general workflow (Scheme 5.2):

i. 96-Well MTP: Wikipedia. https://en.wikipedia.org/wiki/File:96-Well_plate.svg. Date accessed 5/2/2022.

ii. Multichannel pipette: ShopRainin. Pipet-Lite Multi Pipette L12-2000XLS+.

https://www.shoprainin.com/Products/Pipettes-and-Tips/Pipettes/Multichannel-Manual-Pipettes/Pipet-Lite-XLS%2B/Pipet-Lite-Multi-Pipette-L12-200XLS%2B/p/17013810. Date accessed 5/2/2022.

iii. Eppendorf plate sealing machine: Eppendorf. HeatSealer – Plate Sealing. https://onlineshop.eppendorf.dk/NC-en/PCR-44553/PCR-Accessories-44558/HeatSealer-PF-94436.html. Date accessed 5/2/2022.

iv. LC-MS: Shimadzu. Triple Quadrupole LC-MS/MS. https://www.shimadzu.com/an/products/liquidchromatograph-mass-spectrometry/lc-ms-system/lcmsms-method-package-for-dl-aminoacids/option.html. Date accessed 5/2/2022.

v. Erlenmeyer flask: Frisenette. Erlenmeyer Flasks – Glass. https://frisenette.dk/en/produkter/erlenmeyerflasks-glass.FZ45.010.005. Date accessed 5/2/2022.

CO-AUTHOR STATEMENTS

Declaration of co-authorship at DTU

If a PhD thesis contains articles (i.e. published journal and conference articles, unpublished manuscripts, chapters, etc.) written in collaboration with other researchers, a co-author statement verifying the PhD student's contribution to each article should be made.

If an article is written in collaboration with three or less researchers (including the PhD student), all researchers must sign the statement. However, if an article has more than three authors the statement may be signed by a representative sample, cf. article 12, section 4 and 5 of the Ministerial Order No. 1039, 27 August 2013. A representative sample consists of minimum three authors, which is comprised of the first author, the corresponding author, the senior author, and 1-2 authors (preferably international/non-supervisor authors).

DTU has implemented the Danish Code of Conduct for Research Integrity, which states the following regarding attribution of authorship:

"Attribution of authorship should in general be based on criteria a-d adopted from the Vancouver guidelines[1], and all individuals who meet these criteria should be recognized as authors:

Substantial contributions to the conception or design of the work, or the acquisition, analysis, or interpretation of data for the work, and drafting the work or revising it critically for important intellectual content, and final approval of the version to be published, and agreement to be accountable for all aspects of the work in ensuring that questions related to the accuracy or integrity of any part of the work are appropriately investigated and resolved."[2]

For more information regarding definition of co-authorship and examples of authorship conflicts, we refer to DTU Code of Conduct for Research Integrity (pp. 19-22).

By signing this declaration, co-authors permit the PhD student to reuse whole or parts of co-authored articles in their PhD thesis, under the condition that co-authors are acknowledged in connection with the reused text or figure.

It is **important** to note that it is the responsibility of the PhD student to obtain permission from the publisher to use the article in the PhD thesis[3]

1 International Committee of Medical Journal Editors – Recommendations for the Conduct, Reporting, Editing, and Publication of Scholarly Work in Medical Journals, updated December 2016

2 DTU Code of Conduct for Research Integrity (E-book p. 19)

3 Many journals will allow you to use only the post-print version of your article, meaning the accepted version of the article, without the publisher's final formatting. In the event that your article is submitted, but still under review, you should of course use the latest submitted version of your article in your thesis. Always remember to check your publisher's guidelines on reuse of published articles. Most journals, unless open access, have an embargo period on published articles, meaning that within this period you cannot freely use the article. Check your publisher's rules on this issue.

Title of article
Programmable Synthesis of Redshifted and Thermally Bistable One-Way Quantitative Hemithioindigo-derived Photoswitches Enabled by Isomer-Specific Excited State Intramolecular Proton Transfer
Journal/conference
N/A
Author(s)
Mikkel Krell-Jørgensen, Habiburrahman Zulfikri, Magnus Grage Bonnevie, Asmus Ougaard Dohn and Luca Laraia
Name (capital letters) and signature of PhD student
MIKKEL POUL VESTERGAARD KRELL-JØRGENSEN
PhD student's date of birth
20/05/91
Declaration of the PhD student's contribution

For each category in the table below, please specify the PhD student's contribution to the article as appropriate (please do not fill in with names or x's)

Category	Minor contribution to the work *(please specify the nature of the PhD student's contribution)*	Substantial contribution to the work *(please specify the nature of the PhD student's contribution)*
Formulation of the conceptual framework and/or planning of the design of the study including scientific questions		Contributed with relevant scientific input throughout the project and discussed the direction of the project with the authors. Planned the design of synthesis routes and photophysical experiments (for all compounds).
Carrying out of experiments/data collection and analysis/interpretation of results		Carried out synthesis of compound 6 (building-block) and final compounds 10-11 and 14-15, structural characterizations and investigation of photophysical properties (for all compounds), in addition to analysis of data and interpretation of results (for all compounds).
Writing of the article/revising the manuscript for intellectual content		Wrote manuscript in its entirety and developed the scheme and all figures (except figure 3.5).

Signatures			
Date	**Name**	**Title**	**Signature**
27/06/22	Mikkel Krell-Jørgensen	PhD student	
28/06/22	Habiburrahman Zulfikri	Postdoc	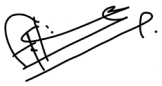
27/06/22	Magnus Grage Bonnevie	Master student	
28/06/22	Asmus Ougaard Dohn	Assistant Professor	
27/06/22	Luca Laraia	Associate Professor	

Please note that by signing this declaration, co-authors permit the PhD student to reuse whole or parts of co-authored articles in their PhD thesis, under the condition that co-authors are acknowledged in connection with the reused text or figure.